Skin-Friction Drag Reduction by Dilute Polymer Solutions in Turbulent Channel Flow

by

Dong-Hyun Lee

A dissertation submitted in partial fulfillment
of the requirements for the degree of
Doctor of Philosophy
(Mechanical Engineering)
in The University of Michigan
2010

Doctoral Committee:

Associate Professor Rayhaneh Akhavan, Chair
Professor Steven J. Wright
Associate Professor Jeremy D. Semrau
Assistant Professor Jianping Fu

To my wife, daughter and parents

Acknowledgements

I express my sincere gratitude and respect to my advisor, Professor Rayhaneh Akhavan for her great inspiration and gentle guidance during my doctoral study at the University of Michigan, Ann Arbor.

Table of Contents

Dedication . . . . . **ii**

Acknowledgements . . . . . **iii**

List of Figures . . . . . **vii**

List of Tables . . . . . **xxi**

List of Symbols . . . . . **xxii**

Abstract . . . . . **xxx**

Chapter

I. Introduction 1

1.1 Early experimental studies 1
1.1.1 Onset of drag reduction 2
1.1.2 Saturation of drag reduction 3
1.1.3 Maximum drag reduction 4
1.2 Recent experimental studies 5
1.2.1 Homogeneous polymer solutions 6
1.2.2 Heterogeneous polymer solutions 8
1.3 Numerical studies 10
1.4 Theoretical studies 20
1.4.1 Elongational viscosity theory (Lumley, 1969, 1973) . 20
1.4.2 Elastic theory (de Gennes, 1986) 22
1.4.3 Comparison of the two theories to experimental and DNS data 23
1.5 The structural view 24
1.6 Objectives of the present study 25

II. Governing Equations and Numerical Methods 27

2.1 Governing equations 27

2.2 Numerical methods 29
2.2.1 Hydrodynamics 29
2.2.2 Polymer dynamics 31
2.2.3 Implementation on parallel computers 35
2.3 Simulation parameters 40
2.4 Verification of the numerical methods 46
2.4.1 Convergence studies 46
2.4.2 Effect of interpolation scheme and comparison to conventional Eulerian schemes 50
2.4.3 Effect of domain size 57
2.5 Assessment of the mixed Eulerian-Lagrangian scheme 66

III. Flow statistics 68

3.1 Effect of polymer concentration on the flow statistics 68
3.2 Effect of Weissenberg number on the flow statistics 88
3.3 Effect of polymer extensibility parameter on the flow statistics 94
3.4 Effect of averaging time on the flow statistics at MDR 97

IV. Scaling of Drag Reduction with Polymer and Flow Parameters 100

4.1 Onset of drag reduction 100
4.2 de Gennes's theory of polymer drag reduction revisited 104
4.2.1 Estimation of r^* 104
4.2.2 Estimation of r^{**} 105
4.2.3 Onset criteria based on the revised de Gennes's theory 108
4.2.4 Comparison to DNS data 109
4.3 Saturation of drag reduction 111
4.4 Criteria for maximum drag reduction (MDR) 113
4.5 Range of affected scales 114

V. Mechanism of Drag Reduction 123

5.1 Data analysis 123
5.1.1 Polymer and turbulence energetics 123
5.1.2 Anisotropy-invariant maps 126
5.1.3 Comparison to predictions of classical theories . . . 128
5.2 Some key features of polymer drag reduction 130
5.2.1 Minimal exchange of energy between turbulence and polymer 131
5.2.2 Highly anisotropic structure of turbulence in drag-reduced flow 136
5.3 Comparison to classical theories of polymer drag reduction . . 143
5.4 Role of pressure-strain in establishing anisotropy 150
5.5 Effect of polymer concentration 161
5.6 Summary of the mechanism of drag reduction 179

VI. Summary and Conclusions 181

Bibliography **186**

List of Figures

Figure

2.1 The channel geometry and coordinate system. 30

2.2 The backward tracking of particles: ∘, particle positions, $r_P^{(n)}$, at t_n; •, particle positions, r_G, at t_{n+1}. 32

2.3 The parallelization scheme used in the simulations. The data is distributed among processors in sets of planes along y-direction in the physical-space and in sets of planes along the x-direction in the spectral-space. 36

2.4 (a) The time per iteration and (b) speedup in DNS of turbulent channel flow performed on IBM e1350 (Big Red) with the number of processors increased from 1 to 128 . △, Newtonian flow with $128\times128\times129$ resolution; ∘, Newtonian flow with $256 \times 256 \times 257$ resolution; ▲, viscoelastic flow with $128 \times 128 \times 129$ resolution; ⧫, viscoelastic flow with $512 \times 256 \times 129$ resolution; ——, ideal linear speedup. 39

2.5 Effect of mesh size at $We_{\tau_b} \approx 35$, $n_p k_B T/(\rho u_{\tau_b}^2) \approx 1 \times 10^{-3}$, $b = 45,000$ on (a) time evolution of the skin friction coefficient; (b) mean velocity profiles; (c) r.m.s. of velocity fluctuations; (d) Reynolds ($\langle\tau_{R,xz}\rangle^+$) and polymer ($\langle\tau_{p,xz}\rangle^+$) shear stresses. ·····, Newtonian (case N); −·−, $64 \times 64 \times 65$ resolution in $\frac{80\pi}{27}h \times \frac{8\pi}{5}h \times 2h$ channel; −−−, $128 \times 128 \times 129$ resolution in $\frac{80\pi}{27}h\times\frac{8\pi}{5}h\times2h$ channel; ——, $256\times256\times257$ resolution in $\frac{80\pi}{27}h\times\frac{8\pi}{5}h\times2h$ channel. 47

2.6 Effect of time-step size at $We_{\tau_b} \approx 35$, $n_p k_B T/(\rho u_{\tau_b}^2) \approx 1\times10^{-3}$, $b = 45,000$ on (a) time evolution of the skin friction coefficient; (b) mean velocity profiles; (c) r.m.s. of velocity fluctuations; (d) Reynolds ($\langle\tau_{R,xz}\rangle^+$) and polymer ($\langle\tau_{p,xz}\rangle^+$) shear stresses. ·····, Newtonian (case N); −−−, $\Delta t^* = 0.1\Delta x/U_o$; ——, $\Delta t^* = 0.05\Delta x/U_o$. 49

2.7 Effect of numerical scheme on the predicted flow statistics at $We_{\tau_b} \approx 35$: (a) time evolution of the skin friction coefficient; (b) mean velocity profiles; (c) turbulence intensities; (d) Reynolds shear stresses and polymer stresses. $\cdots\cdots$, Newtonian (case N); $--$, mixed Eulerian-Lagrangian scheme with linear interpolation (case C3-l); ——, mixed Eulerian-Lagrangian scheme with quadratic interpolation (case C3-q); $-\cdot\cdot-$, Eulerian scheme (case C3-e). 52

2.8 Effect of numerical scheme on the predicted flow statistics at $We_{\tau_b} \approx 100$: (a) time evolution of the skin friction coefficient; (b) mean velocity profiles; (c) turbulence intensities; (d) Reynolds shear stresses and polymer stresses. $\cdots\cdots$, Newtonian (case N); $--$, mixed Eulerian-Lagrangian scheme with linear interpolation (case E3-l); ——, mixed Eulerian-Lagrangian scheme with quadratic interpolation (case E3-q); $-\cdot\cdot-$, Eulerian scheme (case E3-e). 54

2.9 Effect of numerical scheme on the predicted one-dimensional energy spectra at (a-b) $We_{\tau_b} \approx 35$ and (c-d) $We_{\tau_b} \approx 100$: (a), (c) streamwise spectra at $z^+ \approx 30$; (b), (d) spanwise spectra at $z^+ \approx 30$. (a-b) Line types same as in figure 2.7. (c-d) Line types same as in figure 2.8. 56

2.10 Effect of domain size on the predicted flow statistics at $We_{\tau_b} \approx 35$: (a) time evolution of the skin friction coefficient; (b) mean velocity profiles; (c) turbulence intensities; (d) Reynolds shear stresses and polymer stresses. $\cdots\cdots$, Newtonian in small domain (case N); ---, Newtonian in large domain (case NN); ——, mixed Eulerian-Lagrangian scheme with quadratic interpolation in small domain (case C3-q); ——$\cdot$——, mixed Eulerian-Lagrangian scheme with quadratic interpolation in large domain (case CC3-q). . . . 58

2.11 Effect of domain size on the predicted flow statistics at $We_{\tau_b} \approx 100$: (a) time evolution of the skin friction coefficient; (b) mean velocity profiles; (c) turbulence intensities; (d) Reynolds shear stresses and polymer stresses. $\cdots\cdots$, Newtonian in small domain (case N); ---, Newtonian in large domain (case NN); ——, mixed Eulerian-Lagrangian scheme with quadratic interpolation in small domain (case E3-q); ——$\cdot$——, mixed Eulerian-Lagrangian scheme with quadratic interpolation in large domain (case EE3-q). . . . 59

2.12 Effect of domain size on the predicted flow statistics at $We_{\tau_b} \approx 150$: (a) time evolution of the skin friction coefficient; (b) mean velocity profiles; (c) turbulence intensities; (d) Reynolds shear stresses and polymer stresses. $\cdots\cdots$, Newtonian in small domain (case N); ---, Newtonian in large domain (case NN); ——, mixed Eulerian-Lagrangian scheme with quadratic interpolation in small domain (case F3-q); ——$\cdot$——, mixed Eulerian-Lagrangian scheme with quadratic interpolation in large domain (case FF3-q). 60

2.13 Effect of domain size on the predicted one-dimensional energy spectra in (a-b) Newtonian flow and (c-d) viscoelastic flow at $We_{\tau_b} \approx 35$: (a), (c) streamwise spectra at $z^+ \approx 30$; (b), (d) spanwise spectra at $z^+ \approx 30$. Line types same as in figure 2.10. 62

2.14 Effect of domain size on the predicted one-dimensional energy spectra in (a-b) viscoelastic flow at $We_{\tau_b} \approx 100$ and (c-d) $We_{\tau_b} \approx 150$: (a), (c) streamwise spectra at $z^+ \approx 30$; (b), (d) spanwise spectra at $z^+ \approx 30$. (a-b) Line types same as in figure 2.11. (c-d) Line types same as in figure 2.12. 63

2.15 Effect of domain size on the predicted two-point correlations in (a-b) Newtonian flow and (c-d) viscoelastic flow at $We_{\tau_b} \approx 35$: (a), (c) streamwise correlations at $z^+ \approx 30$; (b), (d) spanwise correlations $z^+ \approx 30$. – – –, R_{uu} in small domain; —— ——, R_{uu} in large domain; – · –, R_{vv} in small domain; —— · ——, R_{vv} in large domain; – ·· –, R_{ww} in small domain; —— ·· ——, R_{ww} in large domain. 64

2.16 Effect of domain size on the predicted two-point correlations in (a-b) viscoelastic flow at $We_{\tau_b} \approx 100$ and (c-d) $We_{\tau_b} \approx 150$: (a), (c) streamwise correlations at $z^+ \approx 30$; (b), (d) spanwise correlations $z^+ \approx 30$. – – –, R_{uu} in small domain; —— ——, R_{uu} in large domain; – · –, R_{vv} in small domain; —— · ——, R_{vv} in large domain; – ·· –, R_{ww} in small domain; —— ·· ——, R_{ww} in large domain. 65

3.1 Effect of polymer concentration on the predicted flow statistics at $We_{\tau_b} \approx 10$: (a) time evolution of the skin friction coefficient; (b) mean velocity profiles; (c) r.m.s. of streamwise and spanwise velocity fluctuations; (d) r.m.s. of wall-normal velocity fluctuations. ·····, Newtonian (case N); ---, $\beta \approx 0.999989$ (case A6-l); – ·· –, $\beta \approx 0.99989$ (case A5-l); – · –, $\beta \approx 0.9989$ (case A4-l); – – –, $\beta \approx 0.989$ (case A3-l); ——, $\beta \approx 0.9$ (case A2-l); •, experiments of Warholic, *et al.*(1999) Newtonian. 70

3.2 Effect of polymer concentration on the predicted flow statistics at $We_{\tau_b} \approx 10$: (a) Reynolds shear stresses ($\langle \tau_{R,xz} \rangle^+$), viscous shear stresses ($\langle \tau_v \rangle^+$), and sum of Reynolds, viscous and polymer shear stresses ($\langle \tau_t \rangle^+$); (b) polymer shear stresses ($\langle \tau_{p,xz} \rangle^+$) and polymer extensions; (c) effective viscosities normalized with respect to ν_s; (d) effective viscosities normalized with respect to λu_τ^2. Line types same as in figure 3.1. 71

3.3 Effect of polymer concentration on the predicted flow statistics at $We_{\tau_b} \approx 35$: (a) time evolution of the skin friction coefficient; (b) mean velocity profiles; (c) r.m.s. of streamwise and spanwise velocity fluctuations; (d) r.m.s. of wall-normal velocity fluctuations. ····, Newtonian (case N); ---, $\beta \approx 0.999996$ (case C7-l); $-\cdots-$, $\beta \approx 0.9996$ (case C5-l); $-\cdot-$, $\beta \approx 0.996$ (case C4-l); $--$, $\beta \approx 0.98$ (case C4.1-l); ——, $\beta \approx 0.96$ (case C3-l); —○—, $\beta \approx 0.89$ (case C3.1-l); —△—, $\beta \approx 0.80$ (case C3.2-l); —▽—, $\beta \approx 0.72$ (case C2-l); •, experiments of Warholic, *et al.*(1999) Newtonian; ■, experiments of Warholic, *et al.*(1999) at 14%DR; ♦, experiments of Warholic, *et al.*(1999) at 33%DR. 72

3.4 Effect of polymer concentration on the predicted flow statistics at $We_{\tau_b} \approx 35$: (a) Reynolds shear stresses ($\langle\tau_{R,xz}\rangle^+$), viscous shear stresses ($\langle\tau_v\rangle^+$), and sum of Reynolds, viscous and polymer shear stresses ($\langle\tau_t\rangle^+$); (b) polymer shear stresses ($\langle\tau_{p,xz}\rangle^+$) and polymer extensions; (c) effective viscosities normalized with respect to ν_s; (d) effective viscosities normalized with respect to λu_τ^2. Line types same as in figure 3.3. 73

3.5 Effect of polymer concentration on the predicted flow statistics at $We_{\tau_b} \approx 100$: (a) time evolution of the skin friction coefficient; (b) mean velocity profiles; (c) r.m.s. of streamwise and spanwise velocity fluctuations; (d) r.m.s. of wall-normal velocity fluctuations. ·····, Newtonian (case NN); ---, $\beta \approx 0.9999989$ (case E8-q); $-\cdots-$, $\beta \approx 0.99989$ (case E6-q); $-\cdot-$, $\beta \approx 0.9989$ (case E5-q); —— ——, $\beta \approx 0.98$ (case EE4-q); ——, $\beta \approx 0.90$ (case EE3-q); •, experiments of Warholic *et al.*(1999) Newtonian; ■, experiments of Warholic *et al.*(1999) at 14%DR; ♦, experiments of Warholic *et al.*(1999) at 33%DR; □, experiments of Ptasinski *et al.*(2001) at 63%DR. 76

3.6 Effect of polymer concentration on the predicted flow statistics at $We_{\tau_b} \approx 100$: (a) Reynolds shear stresses ($\langle\tau_{R,xz}\rangle^+$), viscous shear stresses ($\langle\tau_v\rangle^+$), and sum of Reynolds, viscous and polymer shear stresses ($\langle\tau_t\rangle^+$); (b) polymer shear stresses ($\langle\tau_{p,xz}\rangle^+$) and polymer extensions; (c) effective viscosities normalized with respect to ν_s; (d) effective viscosities normalized with respect to λu_τ^2. Line types same as in figure 3.5. 77

3.7 Effect of polymer concentration on the predicted flow statistics at $We_{\tau_b} \approx 150$: (a) time evolution of the skin friction coefficient; (b) mean velocity profiles; (c) r.m.s. of streamwise and spanwise velocity fluctuations; (d) r.m.s. of wall-normal velocity fluctuations. ·····, Newtonian (case NN); ---, $\beta \approx 0.999998$ (case F8-q); $-\cdots-$, $\beta \approx 0.9998$ (case F6-q); —$-\cdot-$——, $\beta \approx 0.998$ (case FF5-q); —— ——, $\beta \approx 0.98$ (case FF4-q); ——, $\beta \approx 0.86$ (case FF3-q); •, experiments of Warholic, *et al.*(1999) Newtonian; ■, experiments of Warholic, *et al.*(1999) at 14%DR; ♦, experiments of Warholic, *et al.*(1999) at 38%DR; ▽, experiments of Ptasinski, *et al.*(2001) at 65%DR; △, experiments of Ptasinski, *et al.*(2001) at 70%DR. 78

3.8 Effect of polymer concentration on the predicted flow statistics at $We_{\tau_b} \approx 150$: (a) Reynolds shear stresses ($\langle \tau_{R,xz} \rangle^+$), viscous shear stresses ($\langle \tau_v \rangle^+$), and sum of Reynolds, viscous and polymer shear stresses ($\langle \tau_t \rangle^+$); (b) polymer shear stresses ($\langle \tau_{p,xz} \rangle^+$) and polymer extensions; (c) effective viscosities normalized with respect to ν_s; (d) effective viscosities normalized with respect to λu_τ^2. Line types same as in figure 3.7. 79

3.9 Effect of polymer concentration on the one-dimensional energy spectra at $We_{\tau_b} \approx 35$: (a-c) streamwise spectra at $z^+ \approx 30$; (d-f) spanwise spectra at $z^+ \approx 30$. Line types same as in figure 3.3. 81

3.10 Effect of polymer concentration on the one-dimensional energy spectra at $We_{\tau_b} \approx 100$: (a-c) streamwise spectra at $z^+ \approx 30$; (d-f) spanwise spectra at $z^+ \approx 30$. Line types same as in figure 3.5. 82

3.11 Effect of polymer concentration on the one-dimensional energy spectra at $We_{\tau_b} \approx 150$: (a-c) streamwise spectra at $z^+ \approx 30$; (d-f) spanwise spectra at $z^+ \approx 30$. Line types same as in figure 3.7. 83

3.12 Effect of polymer concentration on the one-dimensional energy spectra at $We_{\tau_b} \approx 35$: (a-c) streamwise spectra at $z^+ \approx 100$; (d-f) spanwise spectra at $z^+ \approx 100$. Line types same as in figure 3.3. 85

3.13 Effect of polymer concentration on the one-dimensional energy spectra at $We_{\tau_b} \approx 100$: (a-c) streamwise spectra at $z^+ \approx 100$; (d-f) spanwise spectra at $z^+ \approx 100$. Line types same as in figure 3.5. 86

3.14 Effect of polymer concentration on the one-dimensional energy spectra at $We_{\tau_b} \approx 150$: (a-c) streamwise spectra at $z^+ \approx 100$; (d-f) spanwise spectra at $z^+ \approx 100$. Line types same as in figure 3.7. 87

3.15 Effect of Weissenberg number on the predicted flow statistics at $10 \lesssim We_{\tau_b} \lesssim 150$ and $n_p k_B T/(\rho u_{\tau_b}^2) \approx 1 \times 10^{-3}$: (a) time evolution of the skin friction coefficient; (b) mean velocity profiles; (c) r.m.s. of streamwise and spanwise velocity fluctuations; (d) r.m.s. of wall-normal velocity fluctuations. $\cdots\cdots$, Newtonian (case NN); $-\cdot\cdot-$, $We_{\tau_b} \approx 10$ (case A3-l); $-\cdot-$, $We_{\tau_b} \approx 20$ (case B3-l); $---$, $We_{\tau_b} \approx 35$ (case C3-l); ——, $We_{\tau_b} \approx 70$ (case DD3-q); ——$\cdot$——, $We_{\tau_b} \approx 100$ (case EE3-q); ——$\cdot\cdot$——, $We_{\tau_b} \approx 150$ (case FF3-q); •, experiments of Warholic, *et al.*(1999) Newtonian; ■, experiments of Warholic, *et al.*(1999) at 14%DR; ♦, experiments of Warholic, *et al.*(1999) at 33%DR); □, experiments of Ptasinski, *et al.*(2001) at 63%DR; ▽, experiments of Ptasinski, *et al.*(2001) at 65%DR. 89

3.16 Effect of Weissenberg number on the predicted flow statistics at $10 \lesssim We_{\tau_b} \lesssim 150$ and $n_p k_B T/(\rho u_{\tau_b}^2) \approx 1 \times 10^{-3}$: (a) Reynolds shear stresses ($\langle \tau_{R,xz} \rangle^+$), viscous shear stresses ($\langle \tau_v \rangle^+$), and sum of Reynolds, viscous and polymer shear stresses ($\langle \tau_t \rangle^+$); (b) polymer shear stresses ($\langle \tau_{p,xz} \rangle^+$) and polymer extensions; (c) effective viscosities normalized with respect to ν_s; (d) effective viscosities normalized with respect to λu_τ^2. Line types same as in figure 3.15. 90

3.17 Effect of Weissenberg number on the one-dimensional energy spectra at $10 \lesssim We_{\tau_b} \lesssim 150$ and $n_p k_B T/(\rho u_{\tau_b}^2) \approx 1 \times 10^{-3}$: (a-c) streamwise spectra at $z^+ \approx 30$; (d-f) spanwise spectra at $z^+ \approx 30$. Line types same as in figure 3.15. 92

3.18 Effect of Weissenberg number on the one-dimensional energy spectra at $10 \lesssim We_{\tau_b} \lesssim 150$ and $n_p k_B T/(\rho u_{\tau_b}^2) \approx 1 \times 10^{-3}$: (a-c) streamwise spectra at $z^+ \approx 100$; (d-f) spanwise spectra at $z^+ \approx 100$. Line types same as in figure 3.15. 93

3.19 Effect of extensibility parameter on the predicted flow statistics at $We_{\tau_b} \approx 35$ and $n_p k_B T/(\rho u_{\tau_b}^2) \approx 1 \times 10^{-3}$: (a) time evolution of the skin friction coefficient; (b) mean velocity profiles; (c) r.m.s. of streamwise and spanwise velocity fluctuations; (d) r.m.s. of wall-normal velocity fluctuations. $\cdots\cdots$, Newtonian (case N); $- - -$, $b = 4,500$ (case C3.3-*l*); ——, $b = 45,000$ (case C3-*l*); $-\cdot-$, $b = 450,000$ (case C3.4-*l*). 95

3.20 Effect of extensibility parameter on the predicted flow statistics at $We_{\tau_b} \approx 35$ and $n_p k_B T/(\rho u_{\tau_b}^2) \approx 1 \times 10^{-3}$: (a) Reynolds shear stresses ($\langle \tau_{R,xz} \rangle^+$), viscous shear stresses ($\langle \tau_v \rangle^+$), and sum of Reynolds, viscous and polymer shear stresses ($\langle \tau_t \rangle^+$); (b) polymer shear stresses ($\langle \tau_{p,xz} \rangle^+$) and polymer extensions; (c) effective viscosities normalized with respect to ν_s; (d) effective viscosities normalized with respect to λu_τ^2. Line types same as in figure 3.19. 96

3.21 Effect of averaging time on the predicted flow statistics at $We_{\tau_b} \approx 150$ and $n_p k_B T/(\rho u_{\tau_b}^2) \approx 1 \times 10^{-3}$: (a) time evolution of the skin friction coefficient; (b) mean velocity profiles; (c) r.m.s. of streamwise velocity fluctuations; (d) r.m.s. of wall-normal velocity fluctuations; (e) Reynolds shear stresses ($\langle \tau_{R,xz} \rangle^+$), viscous shear stresses ($\langle \tau_v \rangle^+$), and sum of Reynolds, viscous and polymer shear stresses ($\langle \tau_t \rangle^+$); (f) polymer shear stresses ($\langle \tau_{p,xz} \rangle^+$) and polymer extensions. $\cdots\cdots$, Newtonian (case NN); ——$\cdot\cdot$——, $We_{\tau_b} \approx 150$ (case FF3-*q* with statistics averaged over $450 \leq t \leq 650$); •, experiments of Warholic, *et al.*(1999) Newtonian; ▼, experiments of Warholic, *et al.*(1999) at $64\%DR$; ▲, experiments of Warholic, *et al.*(1999) at $69\%DR$. 98

4.1 (a) Drag reduction as a function of the viscosity ratio, β, from DNS: —♦—, DNS at $We_{\tau_b} \approx 10$; —■—, DNS at $We_{\tau_b} \approx 35$; —▼—, DNS at $We_{\tau_b} \approx 100$; —▲—, DNS at $We_{\tau_b} \approx 150$. (b) Onset conditions observed in DNS compared to predictions of the elastic theory of de Gennes (1986): •, onset data from DNS; ---, $\frac{n_p k_B T}{\rho u_\tau^2}|_{onset} = (z^+)^{(\frac{15n}{8}-\frac{1}{2})} We_\tau^{-\frac{15n}{4}}$ (eqn. 4.2) with $n = 2/3$ and $z^+ = 10$. 101

4.2 (a) Onset of drag reduction observed in DNS compared to revised theory of de Gennes: •, onset data from DNS; ——, $\langle \Xi \rangle^{3/2} \frac{n_p k_B T}{\rho u_\tau^2}|_{onset} = A_E \, (\kappa z^+)^{(\frac{3n}{4}-\frac{1}{2})} We_\tau^{-\frac{3n}{2}} A_k^{\frac{4-3n}{4}} \frac{F(k^{**}/k_d)}{\{F(k^*/k_d)\}^{\frac{3n}{4}}}$ (eqn. 4.17) with $A_E = 0.03$ and $n = 2/3$. (b) Onset of drag reduction observed in DNS compared to revised theory of de Gennes: •, onset data from DNS; – – –, $\frac{n_p k_B T}{\rho u_\tau^2}|_{onset} = \frac{A_E \, (\kappa z^+)^{(\frac{3n}{4}-\frac{1}{2})} We_\tau^{-\frac{3n}{2}} A_k^{\frac{4-3n}{4}}}{\left(We_\tau \frac{dU^+}{dz^+} + \frac{We_\tau^{\frac{3n}{2}}}{(\kappa z^+)^{\frac{3n}{4}}} A_K^{\frac{3n}{4}} \{F(k^*/k_d)\}^{\frac{3n}{4}} \right)^{3/2}} \frac{F(k^{**}/k_d)}{\{F(k^*/k_d)\}^{\frac{3n}{4}}}$ (eqn. 4.18) with $A_E = 0.03$ and $n = 2/3$. 110

4.3 Saturation of drag reduction with increasing polymer concentration: (a) drag reduction as a function of the viscosity ratio, β, from DNS; (b) drag reduction as a function of the viscosity ratio, β, from experiments of Hoyt (1966) at $Re_{\tau_b} \approx 420$. —♦—, DNS at $We_{\tau_b} \approx 10$; —■—, DNS at $We_{\tau_b} \approx 35$; —▼—, DNS at $We_{\tau_b} \approx 100$; —▲—, DNS at $We_{\tau_b} \approx 150$; —□—, PEO of $M_w \approx 3.4 \times 10^6$ ($We_{\tau_b} \approx 1360$); —▽—, PEO of $M_w \approx 5.8 \times 10^6$ ($We_{\tau_b} \approx 3520$); —△—, PEO of $M_w \approx 7.0 \times 10^6$ ($We_{\tau_b} \approx 4930$); —◇—, PEO of $M_w \approx 8.0 \times 10^6$ ($We_{\tau_b} \approx 6260$); —○—, PAM of $M_w \approx 1.6 \times 10^6$ ($We_{\tau_b} \approx 230$); (c) Saturation of drag reduction observed in DNS compared to elastic theory of de Gennes (1986) and revised theory of de Gennes: ○, saturation data from DNS; – · · –, $\frac{n_p k_B T}{\rho u_\tau^2}|_{sat} = We_\tau^{-1}$ (eqn. 4.20); —— · ——, $\frac{n_p k_B T}{\rho u_\tau^2}|_{sat} = (1-\beta) We_\tau^{-1}$ (eqn. 4.19) with $\beta = 0.98$. 112

4.4 The largest streamwise and spanwise scales, r_x and r_y, damped by the polymer in the E_{uu} spectra (a,d) with varying the concentration at $We_{\tau_b} \approx 35$, (b,e) with varying the concentration at $We_{\tau_b} \approx 100$, and (c,f) with varying the concentration at $We_{\tau_b} \approx 150$, compared to predictions of Lumley's theory (Lumley, 1969, 1973) (eqn.4.7) and the revised theory of de Gennes (eqn.4.16): (a-c) r_i compared to r^* (eqn.4.7); (d-f) r_i compared to r^{**} (eqn.4.16) with $n = 2/3$ and $A_E = 0.03$. Line types in (a,d) same as in figure 3.3; line types in (b,e) same as in figure 3.5; line types in (c,f) same as in figure 3.7; thin lines, r_x; thick lines, r_y. 115

4.5 Effect of Weissenberg number on the largest streamwise and spanwise scales, r_x and r_y, damped by the polymer in the E_{uu} spectra at $10 \lesssim We_{\tau_b} \lesssim 150$ and saturation concentration of $n_p k_B T/(\rho u_{\tau_b}^2) \approx 1 \times 10^{-3}$: (a) r_i compared to r^* (eqn.4.7); (b) r_i compared to r^{**} (eqn.4.16) with $n = 2/3$ and $A_{turb} = 0.03$. Line types same as in figure 3.15; thin lines, r_x; thick lines, r_y. 117

4.6 Effect of polymer concentration on the largest streamwise and spanwise scales, r_x and r_y, damped by the polymer in the E_{uu} spectra at (a,d) $We_{\tau_b} \approx 35$, (b,e) $We_{\tau_b} \approx 100$, (c,f) $We_{\tau_b} \approx 150$: (a-c) r_i in outer scaling; (d-f) r_i in inner scaling. Line types in (a,d) same as in figure 3.3; line types in (b,e) same as in figure 3.5; line types in (c,f) same as in figure 3.7; thin lines, r_x; thick lines, r_y. 119

4.7 Effect of polymer concentration on the largest streamwise and spanwise scales, r_x and r_y, damped by the polymer in the E_{uu} spectra at (a,d) $We_{\tau_b} \approx 35$, (b,e) $We_{\tau_b} \approx 100$, (c,f) $We_{\tau_b} \approx 150$: (a-c) r_i normalized using ν_{eff} and u_τ; (d-f) r_i normalized using λ and u_τ. Line types in (a,d) same as in figure 3.3; line types in (b,e) same as in figure 3.5; line types in (c,f) same as in figure 3.7; thin lines, r_x; thick lines, r_y. 120

4.8 Effect of Weissenberg number on the largest streamwise and spanwise scales, r_x and r_y, damped by the polymer in the E_{uu} spectra at $10 \lesssim We_{\tau_b} \lesssim 150$ and saturation concentration of $n_p k_B T/(\rho u_{\tau_b}^2) \approx 1 \times 10^{-3}$: (a) r_i in outer scaling; (b) r_i in inner scaling; (c) r_i normalized using ν_{eff} and u_τ; (d) r_i normalized using λ and u_τ. Line types same as in figure 3.15; thin lines, r_x; thick lines, r_y. 121

5.1 Anisotropy-invariant maps showing (a) limiting states of turbulence and (b) data from Newtonian turbulent channel flow at $Re_{\tau_b} \approx 230$ (case NN). 127

5.2 (a-b) Time histories of the volume-averaged turbulence kinetic energy, $\langle E_{ii}(t)\rangle_V$, and polymer elastic energy originating from turbulence, $\langle E_{p,tur}(t)\rangle_V$, normalized by $U_{bulk}^2/2$; (c-d) time histories of the volume-averaged rates of turbulence production, $\langle P_{ii}(t)\rangle_V$, viscous dissipation, $\langle \varepsilon_{ii}(t)\rangle_V$, and energy transfer from turbulence to the polymer, $\langle T_{ii}(t)\rangle_V$, normalized by U_{bulk}^3/h; (e-f) time histories of the skin friction coefficient, in (a,c,e) LDR regime (case CC3-q, 33%DR) and (b,d,f) HDR regime (case FF4-q, 56%DR). The times O, k, K, p, P denote start of viscoelastic simulations, minima and maxima of $\langle E_{ii}(t)\rangle_V$, and minima and maxima of $\langle E_{p,tur}(t)\rangle_V$ during the first cycle of turbulence suppression and regeneration, respectively. ——, viscoelastic flow; ·····, Newtonian flow. 132

5.3 (a-b) Time histories of the volume-averaged turbulence kinetic energy, $\langle E_{ii}(t)\rangle_V$, and polymer elastic energy originating from turbulence, $\langle E_{p,tur}(t)\rangle_V$, normalized by $u_\tau^2(t)/2$; (c-d) time histories of the volume-averaged rates of turbulence production, $\langle P_{ii}(t)\rangle_V$, viscous dissipation, $\langle \varepsilon_{ii}(t)\rangle_V$, and energy transfer from turbulence to the polymer, $\langle T_{ii}(t)\rangle_V$, normalized by $u_\tau^4(t)/\nu_w(t)$ in (a,c) LDR regime (case CC3-q, 33%DR) and (b,d) HDR regime (case FF4-q, 56%DR). ——, viscoelastic flow; ·····, Newtonian flow. 135

5.4 One-point flow statistics in stationary viscoelastic flow in LDR and HDR regimes compared to Newtonian flow: (a) mean velocity profiles; (b) Reynolds, $\langle \tau_{R,xz}\rangle^+$, and viscous, $\langle \tau_v\rangle^+$, shear stresses; (c) polymer shear stresses; (d) streamwise turbulence intensities; (e) spanwise turbulence intensities; (f) wall-normal turbulence intensities. ·····, Newtonian flow (case NN); – – –, viscoelastic flow at low drag reduction (case CC3-q, 33%DR); ——, viscoelastic flow at high drag reduction (case FF4-q, 56%DR). 137

5.5 Anisotropy-invariant maps for (a) Newtonian flow (case NN), (b) viscoelastic flow in the LDR regime (case CC3-q, 33%DR) and (c) viscoelastic flow in the HDR regime (case FF4-q, 56%DR). 139

5.6 The one-dimensional energy spectra in LDR (case CC3-q, 33%DR) and HDR (case FF4-q, 56%DR) regimes compared to Newtonian flow (case NN) at $z^+ \approx 30$. ·····, Newtonian flow (case NN); – – –, viscoelastic flow at low drag reduction (case CC3-q, 33%DR); ——, viscoelastic flow at high drag reduction (case FF4-q, 56%DR). 140

5.7 The one-dimensional energy spectra in LDR (case CC3-q, 33%DR) and HDR (case FF4-q, 56%DR) regimes compared to Newtonian flow (case NN) at $z^+ \approx 50$. ·····, Newtonian flow (case NN); – – –, viscoelastic flow at low drag reduction (case CC3-q, 33%DR); ——, viscoelastic flow at high drag reduction (case FF4-q, 56%DR). 141

5.8 The one-dimensional energy spectra in LDR (case CC3-q, 33%DR) and HDR (case FF4-q, 56%DR) regimes compared to Newtonian flow (case NN) at $z^+ \approx 100$. ·····, Newtonian flow (case NN); – – –, viscoelastic flow at low drag reduction (case CC3-q, 33%DR); ——, viscoelastic flow at high drag reduction (case FF4-q, 56%DR). 142

5.9 The characteristic strain-rate, $s^+(k_i^+, z^+)$, in Newtonian flow (case NN) at (a-b) low drag reduction (case CC3-q, 33%DR) and (c-d) high drag reduction (case FF4-q, 56%DR) compared to $1/T^{*+}$ of Lumley's theory (Lumley, 1969, 1973). – · –, $1/T^{*+}$ from Lumley's theory. 144

5.10 The characteristic strain-rate, $s^+(k_i^+, z^+)$, in viscoelastic flow at (a-b) low drag reduction (case CC3-q, 33%DR) and (c-d) high drag reduction (case FF4-q, 56%DR) compared to $1/T^{*+}$ of Lumley's theory (Lumley, 1969, 1973) and $1/T^{**+}(z^+)$ of the revised version of de Gennes's theory. $-\cdot\cdot-$, $1/T^{*+}$ from Lumley's theory; $-\cdot-$, lowest $1/T^{**+}(z^+)$ from the revised version of de Gennes's theory; ---, scales with $s^+(k_i^+, z^+) > 1/T^{**+}(z^+)$; ——, scales with $s^+(k_i^+, z^+) < 1/T^{**+}(z^+)$. 145

5.11 The characteristic strain-rates in LDR (case CC3-q, 33%DR) and HDR (case FF4-q, 56%DR) regimes compared to Newtonian flow (case NN) at (a-b) $z^+ \approx 10$ and (c-d) $z^+ \approx 30$. $\cdots\cdots$, Newtonian flow (case NN); $--$, viscoelastic flow at low drag reduction (case CC3-q, 33%DR); ——, viscoelastic flow at high drag reduction (case FF4-q, 56%DR). 148

5.12 The characteristic strain-rates in LDR (case CC3-q, 33%DR) and HDR (case FF4-q, 56%DR) regimes compared to Newtonian flow (case NN) at (a-b) $z^+ \approx 50$ and (c-d) $z^+ \approx 100$. $\cdots\cdots$, Newtonian flow (case NN); $---$, viscoelastic flow at low drag reduction (case CC3-q, 33%DR); ——, viscoelastic flow at high drag reduction (case FF4-q, 56%DR). 149

5.13 The normalized one-dimensional spectral density of the diagonal components of strain-rate in LDR (case CC3-q, 33%DR) and HDR (case FF4-q, 56%DR) regimes compared to Newtonian flow (case NN) at $z^+ \approx 30$. $\cdots\cdots$, Newtonian flow (case NN); $---$, viscoelastic flow at low drag reduction (case CC3-q, 33%DR); ——, viscoelastic flow at high drag reduction (case FF4-q, 56%DR). 151

5.14 The normalized one-dimensional spectral density of the diagonal components of strain-rate in LDR (case CC3-q, 33%DR) and HDR (case FF4-q, 56%DR) regimes compared to Newtonian flow (case NN) at $z^+ \approx 50$. $\cdots\cdots$, Newtonian flow (case NN); $---$, viscoelastic flow at low drag reduction (case CC3-q, 33%DR); ——, viscoelastic flow at high drag reduction (case FF4-q, 56%DR). 152

5.15 The normalized one-dimensional spectral density of the diagonal components of strain-rate in LDR (case CC3-q, 33%DR) and HDR (case FF4-q, 56%DR) regimes compared to Newtonian flow (case NN) at $z^+ \approx 100$. $\cdots\cdots$, Newtonian flow (case NN); $---$, viscoelastic flow at low drag reduction (case CC3-q, 33%DR); ——, viscoelastic flow at high drag reduction (case FF4-q, 56%DR). 153

5.16 Components of turbulence kinetic energy budgets in LDR (case CC3-q, 33%DR) and HDR (case FF4-q, 56%DR) regimes compared to Newtonian flow (case NN): (a-c) pressure-strain correlation, $\langle \Pi_{\alpha\alpha} \rangle^+$; (d-f) turbulence production, $\langle P_{\alpha\alpha} \rangle^+$, and viscous dissipation, $\langle \varepsilon_{\alpha\alpha} \rangle^+$. (a,d) streamwise direction; (b,e) spanwise direction; (c,f) wall-normal direction. $\cdots\cdots$, Newtonian flow (case NN); $---$, viscoelastic flow at low drag reduction (case CC3-q, 33%DR); ——, viscoelastic flow at high drag reduction (case FF4-q, 56%DR). 155

5.17 Components of turbulence kinetic energy budgets in LDR (case CC3-q, 33%DR) and HDR (case FF4-q, 56%DR) regimes compared to Newtonian flow (case NN): (a-c) sum of transport terms, $\langle t_{\alpha\alpha}^{(\Sigma)} \rangle^+ = \langle t_{\alpha\alpha}^{(v)} + t_{\alpha\alpha}^{(press)} + t_{\alpha\alpha}^{(R)} + t_{\alpha\alpha}^{(p)} \rangle^+$; (d-f) energy transfer from turbulence to the polymer, $\langle T_{\alpha\alpha} \rangle^+$. (a,d) streamwise direction; (b,e) spanwise direction; (c,f) wall-normal direction. $\cdots\cdots$, Newtonian flow (case NN); $---$, viscoelastic flow at low drag reduction (case CC3-q, 33%DR); ——, viscoelastic flow at high drag reduction (case FF4-q, 56%DR). 156

5.18 Turbulence kinetic energy and polymer elastic energy budgets in LDR (case CC3-q, 33%DR) and HDR (case FF4-q, 56%DR) regimes compared to Newtonian flow (case NN): (a) turbulence production, $\langle P_{ii} \rangle^+$, and viscous dissipation, $\langle \varepsilon_{ii} \rangle^+$; (b) energy transfer from turbulence to the polymer, $\langle T_{ii} \rangle^+$; (c) sum of transport terms, $\langle t_{ii}^{(\Sigma)} \rangle^+ = \langle t_{ii}^{(v)} + t_{ii}^{(press)} + t_{ii}^{(R)} + t_{ii}^{(p)} \rangle^+$; (d) energy transfer from the mean flow to the polymer, $\langle T_U \rangle^+$, and polymer dissipation, $\langle \varepsilon_p \rangle^+$; (e) energy transfer from turbulence to the polymer, $\langle T_{ii} \rangle^+$; (f) polymer energy transport, $\langle t_p \rangle^+$. $\cdots\cdots$, Newtonian flow (case NN); $---$, viscoelastic flow at low drag reduction (case CC3-q, 33%DR); ——, viscoelastic flow at high drag reduction (case FF4-q, 56%DR). . . . 157

5.19 (a) total r.m.s. pressure fluctuations, (b) slow part of r.m.s. pressure fluctuations, (c) rapid and polymer parts of r.m.s. pressure fluctuations, (d-f) The diagonal components of normalized r.m.s. strain-rate fluctuation in LDR (case CC3-q, 33%DR) and HDR (case FF4-q, 56%DR) regimes compared to Newtonian flow (case NN). $\cdots\cdots$, Newtonian flow (case NN); $---$, viscoelastic flow at low drag reduction (case CC3-q, 33%DR); ——, viscoelastic flow at high drag reduction (case FF4-q, 56%DR). 160

5.20 Effect of polymer concentration on the predicted second-order turbulence statistics at $We_{\tau_b} \approx 35$: (a) mean velocity profiles; (b) Reynolds shear stresses and polymer shear stresses; (c) streamwise and spanwise turbulence intensities; (d) wall-normal turbulence intensities. $\cdots\cdots$, Newtonian (case N); ---, $\beta \approx 0.999996$ (case C7-l); $-\cdot\cdot-$, $\beta \approx 0.9996$ (case C5-l); $-\cdot-$, $\beta \approx 0.996$ (case C4-l); $--$, $\beta \approx 0.98$ (case C4.1-l); ——, $\beta \approx 0.96$ (case C3-l); —○—, $\beta \approx 0.89$ (case C3.1-l); —△—, $\beta \approx 0.80$ (case C3.2-l); —▽—, $\beta \approx 0.72$ (case C2-l). 162

5.21 Effect of polymer concentration on the predicted second-order turbulence statistics at $We_{\tau_b} \approx 150$: (a) mean velocity profiles; (b) Reynolds shear stresses and polymer shear stresses; (c) streamwise and spanwise turbulence intensities; (d) wall-normal turbulence intensities. $\cdots\cdots$, Newtonian (case NN); ---, $\beta \approx 0.999998$ (case F8-q); $-\cdot\cdot-$, $\beta \approx 0.9998$ (case F6-q); ——$\cdot$——, $\beta \approx 0.998$ (case FF5-q); —— ——, $\beta \approx 0.98$ (case FF4-q); ——, $\beta \approx 0.86$ (case FF3-q). 163

5.22 Effect of polymer concentration on anisotropy-invariant maps at $We_{\tau_b} \approx 35$: (a) $\beta \approx 0.9996$ (case C5-l); (b) $\beta \approx 0.996$ (case C4-l); (c) $\beta \approx 0.96$ (case C3-l); (d) $\beta \approx 0.89$ (case C3.1-l); (e) $\beta \approx 0.80$ (case C3.2-l); (f) $\beta \approx 0.72$ (case C2-l). 166

5.23 Effect of polymer concentration on anisotropy-invariant maps at $We_{\tau_b} \approx 150$: (a) Newtonian (case NN); (b) $\beta \approx 0.9998$ (case F6-q); (c) $\beta \approx 0.998$ (case FF5-q); (d) $\beta \approx 0.98$ (case FF4-q); (e) $\beta \approx 0.86$ (case FF3-q). . . . 167

5.24 Effect of polymer concentration on the characteristic strain-rate at $We_{\tau_b} \approx 35$: (a-b) $\beta \approx 0.9996$ (case C5-l); (c-d) $\beta \approx 0.996$ (case C4-l); (e-f) $\beta \approx 0.96$ (case C3-l). (a,c,e) streamwise spectra; (b,d,f) spanwise spectra. $-\cdot\cdot-$, $1/T^{*+}$ from Lumley's theory; $-\cdot-$, lowest $1/T^{**+}(z^+)$ from the revised version of de Gennes's theory; ---, scales with $s^+(k_i^+, z^+) > 1/T^{**+}(z^+)$; ——, scales with $s^+(k_i^+, z^+) < 1/T^{**+}(z^+)$. 168

5.25 Effect of polymer concentration on the characteristic strain-rate at $We_{\tau_b} \approx 35$: (a-b) $\beta \approx 0.89$ (case C3.1-l); (c-d) $\beta \approx 0.80$ (case C3.2-l); (e-f) $\beta \approx 0.72$ (case C2-l). (a,c,e) streamwise spectra; (b,d,f) spanwise spectra. $-\cdot\cdot-$, $1/T^{*+}$ from Lumley's theory; $-\cdot-$, lowest $1/T^{**+}(z^+)$ from the revised version of de Gennes's theory; ---, scales with $s^+(k_i^+, z^+) > 1/T^{**+}(z^+)$; ——, scales with $s^+(k_i^+, z^+) < 1/T^{**+}(z^+)$. 169

5.26 Effect of polymer concentration on the characteristic strain-rate at $We_{\tau_b} \approx 150$: (a-b) $\beta \approx 0.9998$ (case F6-l); (c-d) $\beta \approx 0.998$ (case FF5-q). (a,c) streamwise spectra; (b,d) spanwise spectra. $-\cdot\cdot-$, $1/T^{*+}$ from Lumley's theory; $-\cdot-$, lowest $1/T^{**+}(z^+)$ from the revised version of de Gennes's theory; ---, scales with $s^+(k_i^+, z^+) > 1/T^{**+}(z^+)$; ——, scales with $s^+(k_i^+, z^+) < 1/T^{**+}(z^+)$. 170

5.27 Effect of polymer concentration on the characteristic strain-rate at $We_{\tau_b} \approx 150$: (a-b) $\beta \approx 0.98$ (case FF4-q); (c-d) $\beta \approx 0.86$ (case FF3-q). (a,c) streamwise spectra; (b,d) spanwise spectra. $-\cdot\cdot-$, $1/T^{*+}$ from Lumley's theory; $-\cdot-$, lowest $1/T^{**+}(z^+)$ from the revised version of de Gennes's theory; ---, scales with $s^+(k_i^+, z^+) > 1/T^{**+}(z^+)$; ——, scales with $s^+(k_i^+, z^+) < 1/T^{**+}(z^+)$. 171

5.28 Effect of polymer concentration on the predicted turbulence kinetic energy budgets at $We_{\tau_b} \approx 35$: (a-c) pressure-strain correlation, $\langle \Pi_{\alpha\alpha} \rangle^+$; (d) turbulence production, $\langle P_{ii} \rangle^+$, and viscous dissipation, $\langle \varepsilon_{ii} \rangle^+$; (e) energy transfer from turbulence to the polymer, $\langle T_{ii} \rangle^+$; (f) sum of transport terms, $\langle t_{ii}^{(\Sigma)} \rangle^+$. $\cdots\cdots$, Newtonian (case N); ---, $\beta \approx 0.999996$ (case C7-l); $-\cdot\cdot-$, $\beta \approx 0.9996$ (case C5-l); $-\cdot-$, $\beta \approx 0.996$ (case C4-l); $--$, $\beta \approx 0.98$ (case C4.1-l); ——, $\beta \approx 0.96$ (case C3-l); —○—, $\beta \approx 0.89$ (case C3.1-l); —▲—, $\beta \approx 0.80$ (case C3.2-l); —▼—, $\beta \approx 0.72$ (case C2-l). 174

5.29 Effect of polymer concentration on the predicted polymer elastic energy budgets at $We_{\tau_b} \approx 35$: (a) energy transfer from the mean flow to the polymer, $\langle T_U \rangle^+$, and polymer dissipation, $\langle \varepsilon_p \rangle^+$; (b) energy transfer from turbulence to the polymer, $\langle T_{ii} \rangle^+$; (c) polymer energy transport, $\langle t_p \rangle^+$. $\cdots\cdots$, Newtonian (case N); ---, $\beta \approx 0.999996$ (case C7-l); $-\cdot\cdot-$, $\beta \approx 0.9996$ (case C5-l); $-\cdot-$, $\beta \approx 0.996$ (case C4-l); $--$, $\beta \approx 0.98$ (case C4.1-l); ——, $\beta \approx 0.96$ (case C3-l); —○—, $\beta \approx 0.89$ (case C3.1-l); —▲—, $\beta \approx 0.80$ (case C3.2-l); —▼—, $\beta \approx 0.72$ (case C2-l). 175

5.30 Effect of polymer concentration on the predicted turbulence kinetic energy budgets at $We_{\tau_b} \approx 150$: (a-c) pressure-strain correlation, $\langle \Pi_{\alpha\alpha} \rangle^+$; (d) turbulence production, $\langle P_{ii} \rangle^+$, and viscous dissipation, $\langle \varepsilon_{ii} \rangle^+$; (e) energy transfer from turbulence to the polymer, $\langle T_{ii} \rangle^+$; (f) sum of transport terms, $\langle t_{ii}^{(\Sigma)} \rangle^+$. $\cdots\cdots$, Newtonian (case NN); ---, $\beta \approx 0.999998$ (case F8-q); $-\cdot\cdot-$, $\beta \approx 0.9998$ (case F6-q); ——·——, $\beta \approx 0.998$ (case FF5-q); —— ——, $\beta \approx 0.98$ (case FF4-q); ——, $\beta \approx 0.86$ (case FF3-q). 176

5.31 Effect of polymer concentration on the predicted polymer elastic energy budgets at $We_{\tau_b} \approx 150$: (a) energy transfer from the mean flow to the polymer, $\langle T_U \rangle^+$, and polymer dissipation, $\langle \varepsilon_p \rangle^+$; (b) energy transfer from turbulence to the polymer, $\langle T_{ii} \rangle^+$; (c) polymer energy transport, $\langle t_p \rangle^+$. ·····, Newtonian (case NN); ---, $\beta \approx 0.999998$ (case F8-q); $-\cdot\cdot-$, $\beta \approx 0.9998$ (case F6-q); ——·——, $\beta \approx 0.998$ (case FF5-q); —— ——, $\beta \approx 0.98$ (case FF4-q); ——, $\beta \approx 0.86$ (case FF3-q). 177

List of Tables

Table

2.1 Overview of the simulations performed to establish the effect of numerical scheme and domain size. Cases N, C3, E3 and F3 preformed in channels of size $\frac{80\pi}{27}h \times \frac{8\pi}{5}h \times 2h$; cases NN, CC3, EE3 and FF3 preformed in channels of size $\frac{320\pi}{27}h \times \frac{16\pi}{5}h \times 2h$; l denotes simulations performed using the mixed Eulerian-Lagrangian scheme with linear interpolation; q denotes simulations performed using the mixed Eulerian-Lagrangian scheme with quadratic interpolation; e denotes simulations performed using the Eulerian scheme. 42

2.2 Overview of the simulations performed to establish the effect of polymer concentration. Cases N, Ai, Ci, Ei and Fi preformed in channels of size $\frac{80\pi}{27}h \times \frac{8\pi}{5}h \times 2h$; cases NN, EE$i$ and FFi preformed in channels of size $\frac{320\pi}{27}h \times \frac{16\pi}{5}h \times 2h$; l denotes simulations performed using the mixed Eulerian-Lagrangian scheme with linear interpolation; q denotes simulations performed using the mixed Eulerian-Lagrangian scheme with quadratic interpolation. The polymer extensibility parameter was set to $b = 45,000$ in all the viscoelastic simulations 43

2.3 Overview of the simulations performed to establish the effect of Weissenberg number and extensibility parameter. Cases N and Ai, Bi and Ci preformed in channels of size $\frac{80\pi}{27}h \times \frac{8\pi}{5}h \times 2h$; cases NN, DD$i$, EE$i$ and FFi preformed in channels of size $\frac{320\pi}{27}h \times \frac{16\pi}{5}h \times 2h$; l denotes simulations performed using the mixed Eulerian-Lagrangian scheme with linear interpolation; q denotes simulations performed using the mixed Eulerian-Lagrangian scheme with quadratic interpolation. 44

4.1 The onset conditions read from figure 4.1(a) at 0.5% drag reduction. . . . 103

List of Symbols

$\mathbf{A}$	=	conformation tensor ($\langle \mathbf{QQ} \rangle_s$)
A_E	=	fraction of turbulence kinetic energy redirected to the elastic energy of the polymer
A_k	=	Kolmogorov constant
b	=	polymer extensibility parameter
b_{ij}	=	anisotropy tensor
c	=	concentration of the polymer
C_f	=	mean skin friction coefficient
$D^+(k_i^+, z^+)$	=	one-dimensional dissipation spectrum
$E_{\alpha\alpha}$	=	turbulence kinetic energy in α-direction
E_{ii}	=	total turbulence kinetic energy
E_p	=	polymer elastic energy
$E_{p,U}$	=	polymer elastic energy due to the exchanges with the mean flow
$E_{p,tur}$	=	polymer elastic energy due to the exchanges with turbulence
$E(k)$	=	energy spectrum
H	=	spring constant
$\mathcal{H}$	=	heterogeneity index

h	=	channel half height
$\mathbf{I}$	=	identity matrix
II and III	=	scalar invariants of the anisotropy tensor
k	=	wavenumber
k^*	=	wavenumber of scale r^* $(1/r^*)$
k^{**}	=	wavenumber of scale r^{**} $(1/r^{**})$
k_B	=	Boltzmann's constant
k_d	=	Kolmogorov wave number
k_i	=	wavenumber in ith direction
L	=	characteristic length-scale
l	=	average backbone bond length
N	=	number of beads in the chain
N_A	=	Avogadro's number
N_k	=	number of Kuhn steps
NX	=	mesh resolution in streamwise direction
NY	=	mesh resolution in spanwise direction
NZ	=	mesh resolution in wall-normal direction
n	=	dimensionality of the polymer stretching
$\tilde{n}$	=	number of backbone bonds comprising the chain
n_p	=	number density of the polymer
M_w	=	molecular weight of the polymer

P = number of computing processors

$P_{\alpha\alpha}$ = turbulence production in α-direction

P_{ii} = total turbulence production

p = dimensionless pressure

p' = fluctuating pressure

p_{rms} = r.m.s. pressure fluctuation

$p_{r,rms}$ = rapid part of r.m.s. pressure fluctuation

$p_{s,rms}$ = slow part of r.m.s. pressure fluctuation

$p_{p,rms}$ = polymer part of r.m.s. pressure fluctuation

$\mathbf{Q}$ = dimensionless length and orientation vector of two beads

Q_o = maximum extension of the spring

R = pipe radius

R_G = radius of gyration of the polymer in the coiled state

Re = Reynolds number ($\frac{U_o L}{\nu_s}$)

Re_{bulk} = bulk Reynolds number ($\frac{U_{bulk} R}{\nu_s}$ or $\frac{U_{bulk} h}{\nu_s}$)

Re_τ = skin friction Reynolds number of the viscoelastic flow ($\frac{u_\tau \delta}{\nu}$ or $\frac{u_\tau R}{\nu}$ or $\frac{u_\tau h}{\nu}$)

Re_{τ_b} = skin friction Reynolds number of the base Newtonian flow ($\frac{u_{\tau_b} \delta}{\nu_s}$ or $\frac{u_{\tau_b} R}{\nu_s}$ or $\frac{u_{\tau_b} h}{\nu_s}$)

R_{ii} = two-point correlation

r^* = size of eddies whose characteristic time is λ, or
size of the largest turbulent eddies affected by the polymer
in Lumley's theory

r^{**} = size of eddies whose characteristic time is smaller than λ and
has redirected a minimum fraction, A_E, of its turbulent energy
to the elastic energy of the polymer, or
size of the largest turbulent eddies affected by the polymer
in the revised version of de Gennes's theory

$\mathbf{r}_G$ = locations of the particles at the conclusion of each time step

r_x = largest attenuated scale in the x-direction in the E_{uu} spectra

r_y = largest attenuated scale in the y-direction in the E_{uu} spectra

$\mathbf{r}_P^{(n)}$ = starting location of the particle at time t_n

$s^+(k_i^+, z^+)$ = characteristic strain-rate

$s_{\alpha\alpha,rms}$ = diagonal components of r.m.s. strain-rate fluctuation

T = absolute temperature

$T_{\alpha\alpha}$ = energy transfer from turbulence to the polymer in α-direction

T_{ii} = total energy transfer from turbulence to the polymer

T_U = energy transfer from the mean flow to the polymer

T^* = characteristic time at scale r^*

T^{**} = characteristic time at scale r^{**}

t = dimensionless time

$t_{\alpha\alpha}^{(p)}$ = energy transport by the fluctuating polymer stress in α-direction

$t_{ii}^{(p)}$ = total energy transport by the fluctuating polymer stress

$t_{\alpha\alpha}^{(press)}$ = energy transport by the fluctuating pressure in α-direction

$t_{ii}^{(press)}$ = total energy transport by the fluctuating pressure

$t_{\alpha\alpha}^{(R)}$ = energy transport by the fluctuating Reynolds stress in α-direction

$t_{ii}^{(R)}$ = total energy transport by the fluctuating Reynolds stress

$t_{\alpha\alpha}^{(v)}$ = energy transport by the fluctuating viscous stress in α-direction

$t_{ii}^{(v)}$ = total energy transport by the fluctuating viscous stress

$t_{\alpha\alpha}^{(\Sigma)}$ = sum of transport terms in α-direction

$t_{ii}^{(\Sigma)}$ = sum of transport terms in all directions

t_p = energy transport by the polymer

$\tilde{t}$ = dimensional time

U = mean velocity

U_{bulk} = bulk velocity

U_o = characteristic velocity

$U(r^*)$ = characteristic velocity at scale r^*

$U(r^{**})$ = characteristic velocity at scale r^{**}

$u_{i,rms}$ = turbulence intensity

u_τ = friction velocity in viscoelastic flow

u_{τ_b} = friction velocity in base Newtonian flow

u'_α = fluctuating velocity in α-direction

$\mathbf{v}$	=	dimensionless velocity
We	=	Weissenberg number ($\lambda U_o/L$)
We_τ	=	Weissenberg number in viscoelastic flow ($\frac{\lambda u_\tau^2}{\nu}$)
We_{τ_b}	=	Weissenberg number in base Newtonian flow ($\frac{\lambda u_{\tau_b}^2}{\nu_s}$)
wppm	=	weight parts per million
x	=	streamwise direction
y	=	spanwise direction
z	=	wall-normal direction
β	=	viscosity ratio (μ_s/μ_o)
δ	=	characteristic length such as the boundary layer thickness, or channel half height h, or pipe radius R
ε	=	dissipation rate
$\varepsilon_{\alpha\alpha}$	=	viscous dissipation in α-direction
ε_{ii}	=	total viscous dissipation
ε_p	=	polymer dissipation
ζ	=	drag coefficient on each bead
η	=	Kolmogorov length scale
$[\eta]$	=	intrinsic viscosity
λ	=	relaxation time of the polymer

λ_H = Rouse relaxation time of the polymer

λ_z = Zimm relaxation time of the polymer

μ_o = zero shear viscosity of the solution

μ_w = wall shear viscosity ($\frac{\nu_w}{\rho}$)

ν = kinematic viscosity of the polymer solution

ν_{eff} = effective viscosity

ν_s = kinematic viscosity of the solvent

ν_w = wall shear viscosity ($\langle \frac{\tau_w}{\rho(dU/dz)_w} \rangle$)

$\Xi(r^{**})$ = polymer stretch due to stretching by scale r^{**}

Ξ = total polymer stretch

ξ = polymer root-mean-square end-to-end extension

Π = pressure head ($p + \frac{1}{2}|\mathbf{v}|^2$)

$\Pi_{\alpha\alpha}$ = pressure-strain correlation

ρ = density

τ_p = polymer stress

τ_R = Reynolds shear stress

τ_t = total shear stress

τ_w = wall shear stress

τ_p' = fluctuating polymer stress

$\tau^+(k_i^+, z^+)$ = non-dimensional characteristic time at scale k_i^+ at location z^+

χ = artificial stress diffusivity

$\Phi_{s_{\alpha\alpha}s_{\alpha\alpha}}$ = one-dimensional spectral density of

the diagonal components of strain-rate

$\%DR$ = percent drag reduction

$\langle\cdot\rangle$ = ensemble-averaged quantity obtained by averaging

the quantity in the homogeneous flow directions and time

$\langle\cdot\rangle_s$ = average over the configuration space of the dumbbell.

superscripts

$+$ = non-dimensional quantity normalized using u_τ and ν_w

Abstract

Skin-friction drag reduction by dilute polymer solutions is investigated using results from direct numerical simulations (DNS) of homogeneous polymer solutions in turbulent channel flow. Simulations were preformed using a novel mixed Eulerian-Lagrangian scheme in a turbulent channel flow at a base Reynolds number of $Re_{\tau_b} \approx 230$ with a FENE-P dumbbell model of the polymer, and covered the range of Weissenberg numbers between $10 \lesssim We_{\tau_b} \lesssim 150$, polymer number densities between $1 \times 10^{-10} \lesssim n_p k_B T/(\rho u_{\tau_b}^2) \lesssim 1 \times 10^{-2}$ (corresponding to viscosity ratios of $0.7 \lesssim \beta \lesssim 1.0$), and polymer extensibility parameters between $4,500 \leq b \leq 450,000$, to clarify the role of each polymer parameter in drag reduction. The full range of drag reduction from onset to Maximum Drag Reduction (MDR) was reproduced in DNS, with statistics in good quantitative agreement with the available experimental data. Onset of drag reduction was found to be a function of both the polymer concentration and Weissenberg number, as originally suggested by de Gennes (1986). However, the onset criteria suggested by de Gennes (1986) were found to be several orders of magnitude higher than DNS data. A revised version of the theory of de Gennes (1986) has been developed, which gives good agreement with DNS results. The magnitude of drag reduction was found to be a universal function of β, increasing monotonically with β for $1.0 > \beta > 0.98$, and saturating at $\beta \approx 0.98$. The magnitude

of drag reduction at saturation is a strong function of the Weissenberg number. A $We_\tau \sim O(Re_\tau/2)$ is needed to reach MDR. Investigation of the mechanism of drag reduction shows that the main effect of the polymer is extraction of a small amount (on the order of 5% on a volume-averaged basis) of turbulence kinetic energy from turbulent scales which have a timescale shorter than the polymer relaxation time. This extraction of energy leads to a decrease in the fluctuating strain-rate at these scales, which in turn, reduces the magnitude of the pressure-strain correlation at these and neighboring scales. This inhibits the turbulence kinetic energy transfer from the streamwise component to the cross-stream directions at these scales. When this drop in pressure-strain correlation extends to the largest turbulent scales, it results in a highly anisotropic state in which the cross-stream turbulence intensities are sharply reduced, leading to a drop in the Reynolds shear stress. This drop in the Reynolds shear stress, in turn, causes a drop in the rate of turbulence production. In addition, the energy trapped in the streamwise direction can no longer cascade to the small scales, leading to further decay of the fluctuating strain-rate and turbulence kinetic energy in the small scales. This decay further amplifies the features described above. Thus the minute extraction of energy by the polymer at the affected turbulent scales starts a self-amplifying sequence of events, which leads to cessation of turbulence production and results in a drag reduction. For effective high drag reduction, the initial minute extraction of energy by the polymer needs to extend to the largest turbulent scales at wall-normal locations where the peak of turbulence production occurs. The above understanding of the mechanism of polymer drag reduction opens up new possibilities for skin-friction drag reduction in wall-bounded flows.

Chapter I

Introduction

It has been known for nearly sixty years, since its original discovery by Toms (1949), that the addition of a few weight parts per million (wppm) of an appropriate, high molecular weight, linear chain polymer to the turbulent flow of a solvent can lead to drag reductions of up to 80% in wall-bounded turbulent flows. Since then, numerous experimental studies in pipe flows, channel flows, and boundary layer flows have verified these findings and revealed various other features of wall-bounded turbulence in the presence of drag reducing polymers. Nevertheless, many aspects of the problem, including the scaling of drag reduction with polymer and flow parameters, and the detailed mechanism of drag reduction remain poorly understand or controversial. General reviews of the current state of knowledge are available in Lumley (1969, 1973), Virk (1975), Hoyt (1990), Gyr & Bewersdorff (1995), Nieuwstadt & den Toonder (2001), and White & Mungal (2008).

1.1 Early experimental studies

Early experimental studies on polymer drag reduction (Hershey & Zakin, 1967; Lumley, 1969, 1973; Hoyt, 1966, 1971, 1972; Kenis & Hoyt, 1971; Hunston, 1974; Frederick, 1975; Berman, 1977; Nadolink, 1987) were focused on measuring the pressure-

drop and mean velocity profiles in dilute polymer solutions with different polymer molecules, molecular weights, and concentrations to determine the scaling of drag reduction with polymer parameters. Three characteristic features of polymer drag reduction borne out from these early experimental studies include the phenomena of onset of drag reduction, saturation of drag reduction, and maximum drag reduction (MDR).

1.1.1 Onset of drag reduction

Onset of drag reduction refers to the criteria which must be met before a given polymer of molecular weight M_w, radius of gyration in the coiled state R_G, relaxation time λ, and number density n_p (or concentration c) can display any drag reducing effects in the turbulent flow of a solvent at a base Reynolds number of $Re_{\tau_b} \equiv u_{\tau_b}\delta/\nu_s$, where u_{τ_b} denotes the friction velocity of the base Newtonian flow, δ denotes the characteristic length of the flow such as the boundary layer thickness, channel half height, or pipe radius, and ν_s is the kinematic viscosity of the solvent. Establishing the onset criteria has been the subject of a number of experimental studies (Hershey & Zakin, 1967; Patterson & Abernathy, 1970; Berman, 1977; Nadolink, 1987; Sreenivasan & White, 2000). Some of these studies (e.g. Hershey & Zakin, 1967; Berman, 1977) have found that the onset of drag reduction depends on the flow time-scale. The onset of drag reduction have been found to occur when

$$We_\tau \equiv \frac{\lambda u_\tau^2}{\nu} \sim O(1) \tag{1.1}$$

(Hershey & Zakin, 1967; Lumley, 1969), where We_τ is the Weissenberg number, and denotes the ratio of the polymer relaxation time, λ, to the shortest time-scale, ν/u_τ^2, in the viscoelastic turbulent flow, where u_τ is the friction velocity, and ν is the kinematic viscosity of the polymer solution, which is typically defined as either μ_o/ρ or as μ_w/ρ, where μ_o is the zero shear viscosity of the solution, and μ_w is the wall shear viscosity, and ρ is the density. While this onset criterion is found to be a function of Weissenberg number only, and independent of polymer concentration, others (Nadolink, 1987; Sreenivasan & White, 2000) observed an onset criterion as a function of both the polymer concentration and Weissenberg number. An expression for this onset criterion was proposed by Sreenivasan & White (2000) based on analysis of experimental data (Patterson & Abernathy, 1970; Berman, 1977; Nadolink, 1987) as

$$\frac{n_p k_B T}{\rho u_\tau^2}|_{onset} \propto We_\tau^{-\frac{5}{2}}, \tag{1.2}$$

where n_p is the polymer number density, k_B is the Boltzmann's constant, and T is the absolute temperature.

1.1.2 Saturation of drag reduction

Saturation of drag reduction refers to the observation that for all polymers, the amount of drag reduction levels off with increasing polymer concentration (Hoyt, 1966, 1971; Kenis & Hoyt, 1971), such that adding more polymer does not lead to any additional drag reduction. As with the onset phenomenon, the saturation criterion is also still the subject of debate. Some investigators (Lumley, 1969, 1973) believe that saturation occurs when the wavenumber corresponding to the peak of the dissipation

spectrum defined using the effective viscosity coincides with the wavenumber of the largest turbulent eddies having a time-scale λ. In contrast, other investigators (de Gennes, 1986) believe that saturation occurs when the unstretched polymer coils begin to overlap.

1.1.3 Maximum drag reduction

Maximum drag reduction (MDR) refers to the observation (Virk, Mickley & Smith, 1970; Virk, 1975) that regardless of polymer concentrations or type of polymer employed, the maximum drag reduction in any given flow is bound by an empirical asymptote. An expression for this MDR asymptote was proposed by Virk, Mickley & Smith (1970) based on analysis of experimental data in pipe flow.

It was observed that the lowest mean skin friction coefficient which can be achieved experimentally with polymer solutions in pipe flows is bound by,

$$C_f^{-1/2} = 19.0 \log_{10}(2Re_{bulk}C_f^{1/2}) - 32.4, \tag{1.3}$$

where C_f is the mean skin friction coefficient in the pipe, and $Re_{bulk} \equiv \frac{U_{bulk}R}{\nu_s}$ is the Reynolds number based on the pipe radius, R, bulk velocity, U_{bulk}, and the viscosity of the solution, ν. The accuracy of equation (1.3) was observed to be $\sim \pm 15\%$ for Reynolds number between $1,000 < Re_{bulk} < 2,500$, and $\sim \pm 10\%$ for $2,500 < Re_{bulk} < 75,000$ (Virk, Mickley & Smith, 1970). While this mean skin friction coefficient is substantially lower than the value, $C_f^{-1/2} = 4.0 \log_{10}(2Re_{bulk}C_f^{1/2}) - 0.4$, in Newtonian turbulent pipe flow, it always exceeds the laminar value, $C_f = 8/Re_{bulk}$, indicating that the polymer cannot fully relaminarize the flow. Subsequent

experimental measurements were found to conform to this limiting asymptote.

Given the form of the friction coefficient given by (1.3), Virk, Mickley & Smith (1970) argued that at maximum drag reduction (MDR), the mean velocity profile should become asymptotic to

$$U^+ = 11.7 \ln z^+ - 17.0, \tag{1.4}$$

which they called the ultimate profile. As with the onset and saturation phenomena, the criterion for MDR is also still the subject of debate. Some investigators (Lumley, 1969, 1973) believe that MDR is achieved when the edge of the viscous sublayer based on the saturation value of the effective viscosity extends all the way to the core of the pipe or channel or the outer edge of the boundary layer. Thus MDR occurs when $\delta u_\tau/(0.1\lambda u_\tau^2) \approx 10$, or $\delta \sim O(\lambda u_\tau)$ or $We_\tau \sim O(Re_\tau)$, where $Re_\tau \equiv u_\tau \delta/\nu$. In contrast, other investigators (de Gennes, 1986) believe that MDR is achieved when the time criterion of Lumley (1969, 1973) is satisfied by the largest turbulent eddies. This corresponds to $\delta \approx (\varepsilon^3 \lambda)^{1/2}$. With $\varepsilon \approx u_\tau^3/z$ and $z = \delta$, this gives the MDR criterion in wall-bounded flows as $\delta \sim O(\lambda u_\tau)$ or $We_\tau \sim O(Re_\tau)$, which is the same as that in Lumley's theory (Lumley, 1969, 1973).

1.2 Recent experimental studies

With the advent of non-invasive optical measurement techniques such as laser doppler velocimetry (LDV), more detailed measurements of the flow features such as the turbulence intensities and the Reynolds shear stress have become available. Studies have been performed both with homogeneous and heterogeneous polymer

solutions in pipe flows (McComb & Rabie, 1979; Usui, Maeguchi & Sano, 1988; Pinho & Whitelaw, 1990; den Toonder, *et al.*, 1997; Hoyer & Gyr, 1996; Ptasinski, *et al.*, 2001), channel flows (Willmarth, Wei & Lee, 1987; Walker & Tiederman, 1990; Harder & Tiederman, 1991; Wei & Willmarth, 1992; Warholic, Massah & Hanratty, 1999), and boundary layer flows (Fontaine, Petrie & Brungart, 1992; Koskie & Tiederman, 1991; White, Somandepalli & Mungal, 2004; Hou, Somandepalli & Mungal, 2008).

1.2.1 Homogeneous polymer solutions

Detailed experimental measurements with homogeneous polymer solutions have been reported in both pipe flows (Pinho & Whitelaw, 1990; den Toonder, *et al.*, 1997; Ptasinski, *et al.*, 2001) and channel flows (Willmarth, Wei & Lee, 1987; Gampert & Yong, 1990; Harder & Tiederman, 1991; Wei & Willmarth, 1992; Warholic, Massah & Hanratty, 1999).

In the low drag reduction (LDR) regime defined as drag reductions below 35% (Warholic, Massah & Hanratty, 1999), introducing the polymer into turbulent flow resulted in a thickening of the buffer layer, and a contraction and upward shift of the inertial sublayer in the mean velocity profile. In addition, measurements of the turbulence intensities and the Reynolds shear stress showed that the peak of the normalized streamwise turbulence intensity becomes larger than the Newtonian value, whereas the peak of the normalized spanwise and wall normal turbulence intensities and the Reynolds shear stress drop below the Newtonian values. These features become increasingly more pronounced as drag reduction increases.

In the high drag reduction (HDR) regime defined as drag reduction above 35%

(Warholic, Massah & Hanratty, 1999), detailed measurements have been reported by Gampert & Yong (1990) and Warholic, Massah & Hanratty (1999) in channel flow, and by Ptasinski, *et al.* (2001) in pipe flow. Gampert & Yong (1990) performed their experiments in a turbulent channel flow at MDR for $4800 < Re_{bulk} < 16000$. MDR was observed at $49\% - 71\%DR$, depending on the Reynolds number. All the mean velocity profiles conformed to Virk's ultimate profile (eqn.1.4). They observed normalized streamwise turbulence intensities which were below Newtonian values, cross-stream turbulence intensities which were significantly lower than Newtonian values, and Reynolds shear stress significantly lower than Newtonian values, but non-zero. Warholic, Massah & Hanratty (1999) performed their experiments in a turbulent channel flow at $Re_{\tau_b} \approx 1000$. At MDR ($69\%DR$), they observed a mean velocity profile which also conformed to Virk's ultimate profile. They observed normalized turbulence intensities which had peaks below those for Newtonian flow for the streamwise component of velocity, while the wall-normal component of the velocity were drastically reduced compared to Newtonian flow. However, in these experiments, the Reynolds shear stress was observed to be near zero. These features led the investigators to suggest that at MDR the turbulence is maintained by polymer fluctuations. Ptasinski, *et al.* (2001) performed their experiments in a pipe flow at $Re_{\tau_b} \approx 300$. At maximum drag reduction ($70\%DR$), they observed mean velocity profiles which also confirmed the Virk's ultimate profile. The normalized streamwise turbulence intensities had a peak comparable to that for Newtonian flow, while the wall-normal component of turbulence intensities and Reynolds shear stresses were significantly lower than Newtonian, but non-zero. A major difference between the experiments of

Ptasinski, *et al.* (2001) and Warholic, Massah & Hanratty (1999) is the manner in which the polymer was introduced into the flow. Ptasinski, *et al.* (2001) used well premixed polymer solutions, while Warholic, Massah & Hanratty (1999) injected their polymer as a highly concentrated solution into the flow and relied on the turbulent flow to mix it in the test section. Warholic, Massah & Hanratty (1999) mention that with their method of injection, the polymer forms filament aggregates whose size increases with the concentration of the master solution. These aggregates were not dismembered in the channel flow and their presence was found to significantly enhance the effectiveness of polymer drag reduction. In addition to this, Ptasinski, *et al.* (2001) and Warholic, Massah & Hanratty (1999) show a noticeable difference in the experimental setup. The test section in the experiment of Ptasinski, *et al.* (2001) was located at $26m$ ($L_x/R \approx 1288$, where L_x denotes the location of the test section from the entrance or the injection of the polymer) from the entrance of the pipe. In contrast, the test section in the experiment of Warholic, Massah & Hanratty (1999) was located at $11m$ ($L_x/h \approx 433$, where h denotes the channel half height) from the injection slot of the polymer. The length of the channel in the experiments of Warholic, Massah & Hanratty (1999) was much shorter than the length of the pipe in the experiments of Ptasinski, *et al.* (2001).

1.2.2 Heterogeneous polymer solutions

Drag reduction in heterogeneous polymer solutions has been studied experimentally by a number of investigators in pipe flows (McComb & Rabie, 1979; Usui, Maeguchi & Sano, 1988; Hoyer & Gyr, 1996), channel flows (Walker & Tiederman,

1990), and boundary layer flows (Fontaine, Petrie & Brungart, 1992; White, Somandepalli & Mungal, 2004; Hou, Somandepalli & Mungal, 2008). In pipe and channel flow studies, the polymer was injected either at the centerline of the pipe (McComb & Rabie, 1979; Usui, Maeguchi & Sano, 1988; Hoyer & Gyr, 1996) or at the wall of the channel (Walker & Tiederman, 1990). In boundary layer flow studies, the polymer was injected at the wall of the flat-plate (Fontaine, Petrie & Brungart, 1992; White, Somandepalli & Mungal, 2004; Hou, Somandepalli & Mungal, 2008). It was found that if the polymer is injected in the buffer layer then it affects the flow immediately (Walker & Tiederman, 1990), but if it is injected in the viscous sublayer (Fontaine, Petrie & Brungart, 1992) or in the core (McComb & Rabie, 1979), then it needs time to reach the buffer layer before it can affect the flow. The mean velocity profiles observed with heterogeneous polymer solutions were found to be different from those in homogeneous solutions. Instead of the upward shift of the logarithmic layer observed with homogeneous solutions in the low drag reduction (LDR) regime, here the slope of the logarithmic layer increases from the Newtonian value (≈ 2.5) to the Virk's asymptotic value (≈ 11.7) as the drag reduction increases. Generally, it had been believed that drag reduction cannot reach Virk's MDR asymptotic values in heterogeneous polymer solutions. However, Hou, Somandepalli & Mungal (2008) have recently shown that the drag reduction can approach Virk's MDR asymptote with heterogeneous polymer solutions.

1.3 Numerical studies

In the recent years, direct numerical simulations (DNS) have provided an alternative avenue of inquiry, and a number of DNS studies of viscoelastic turbulent flows have been reported in channel flows (Orlandi, 1995; Sureshkumar & Beris, 1995; Sureshkumar, Beris & Handler, 1997; Baron & Sibilla, 1998; Dimitropoulos, Sureshkumar & Beris, 1998; Beris & Dimitropoulos, 1999; Dimitropoulos, *et al.*, 2001; de Angelis, Casciola, & Piva, 2002; de Angelis, *et al.*, 2003, 2004; Housiadas & Beris, 2003; Min, *et al.*, 2003; Min, Yoo & Choi, 2003; Ptasinski, *et al.*, 2003; Dubief, *et al.*, 2004, 2005; Benzi, *et al.*, 2006; Li, Sureshkumar & Khomami, 2006), pipe flows (den Toonder, *et al.*, 1997), boundary layer flows (Dimitropoulos, *et al.*, 2005, 2006; Tamanoa, *et al.*, 2007), shear driven turbulence (Vaithianathan, *et al.*, 2007), and homogeneous, isotropic turbulence (de Angelis, *et al.*, 2005). Earlier studies were performed using generalized Newtonian models of the polymer (Orlandi, 1995). The more recent studies have employed Oldroyd-B (Hookean dumbbell) (Sureshkumar & Beris, 1995; den Toonder, *et al.*, 1997; Min, *et al.*, 2003; Min, Yoo & Choi, 2003; Li, Sureshkumar & Khomami, 2006; Tamanoa, *et al.*, 2007), Giesekus (Dimitropoulos, Sureshkumar & Beris, 1998; Beris & Dimitropoulos, 1999; Housiadas & Beris, 2003; Tamanoa, *et al.*, 2007) or FENE-P dumbbell (Sureshkumar, Beris & Handler, 1997; Baron & Sibilla, 1998; Dimitropoulos, Sureshkumar & Beris, 1998; Beris & Dimitropoulos, 1999; Dimitropoulos, *et al.*, 2001; de Angelis, Casciola, & Piva, 2002; de Angelis, *et al.*, 2003, 2004, 2005; Housiadas & Beris, 2003; Ptasinski, *et al.*, 2003; Dubief, *et al.*, 2004, 2005; Dimitropoulos, *et al.*, 2005, 2006; Benzi, *et al.*, 2006; Li, Sureshkumar & Khomami,

2006; Vaithianathan, *et al.*, 2007) models of the polymer. A summary of these results is given below.

Baron & Sibilla (1998) performed simulations at $Re_{\tau_b} \approx 169$ in a minimal channel size of $4h \times 1.25h \times 2h$ in streamwise, spanwise and wall-normal directions, respectively. Their simulations were performed with a 2nd order finite difference scheme. The FENE-P dumbbell model was used with a realistic extensibility parameter of $b \approx 30,000$. They observed a maximum of 10% drag reduction in their simulations which were performed for $We_{\tau_b} \leq 35.5$. Their DNS results showed qualitative agreement with the experiments of Luchik & Tiederman (1988) and Wei & Willmarth (1992). Their simulations showed that the spacing between the high and low speed streaks in the near wall region becomes larger in drag reduced flow.

Sureshkumar & Beris (1995), Sureshkumar, Beris & Handler (1997), Dimitropoulos, Sureshkumar & Beris (1998), Beris & Dimitropoulos (1999), Housiadas & Beris (2003) and Li, Sureshkumar & Khomami (2006) performed simulations using pseudo-spectral methods at $Re_\tau \equiv u_\tau h/\nu \approx 125$, 180, 395 and 590. Direct numerical simulations were performed in channels of size up to $10h \times 5h \times 2h$ at LDR, in channels of size up to $20h \times 5h \times 2h$ at HDR, and in channels of size up to $40h \times 5h \times 2h$ at MDR. The polymer was modeled using a FENE-P dumbbell with an extensibility parameter of $4 \leq b \leq 14,400$, or using a Giesekus model with $b \sim 2$ and 100 ($\alpha = 1/b = 0.5$ & 0.01), or using Oldroyd-B, which can infinitely extend ($b \sim \infty$). These polymer extensibility parameter do not correspond to any real polymers, as real polymers have $10^4 < b < 10^6$. The bulk of the simulations were performed for viscosity ratio of $\beta = 0.9$, where $\beta = \mu_s/\mu_o$ denotes the ratio of the solvent viscosity to

the zero shear viscosity of the polymer solution, and the range of Weissenberg number between $6.25 \leq We_\tau \leq 200$. Onset of drag reduction was observed at $We_\tau \approx 6.25$. With $We_\tau \approx 100$, $\sim 74\%DR$ was achieved at MDR at $Re_\tau \approx 125$, and $\sim 71\%DR$ was achieved at MDR at $Re_\tau \approx 180$. At $Re_\tau \approx 395$, $\sim 75\%DR$ was achieved at MDR with $We_\tau \approx 200$. The mean velocity profiles at MDR showed good agreement with Virk's ultimate profile (Li, Sureshkumar & Khomami, 2006). The normalized streamwise turbulence intensities showed a monotonic increase with increasing drag reduction at HDR (Li, Sureshkumar & Khomami, 2006). However, this trend stands at odd with the observations in experiments (Warholic, Massah & Hanratty, 1999; Ptasinski, *et al.*, 2001), which showed a decay in streamwise turbulence intensity with increasing drag reduction at HDR. It was found that a large polymer extensibility parameter and high Weissenberg number are required to obtain significant drag reduction (Li, Sureshkumar & Khomami, 2006). In contrast, drag reduction was observed to decrease with increasing Reynolds number (Li, Sureshkumar & Khomami, 2006). The streaks near the wall were observed to be more spaced out, and the near wall coherent structures were observed to become weaker in drag reduced flow (Dimitropoulos, Sureshkumar & Beris, 1998; Li, Sureshkumar & Khomami, 2006). The polymer was observed to generate a body force which opposes the cross-stream components of turbulence, but performs a positive work on streamwise component (Li, Sureshkumar & Khomami, 2006). In addition, Dimitropoulos, *et al.* (2001) studied budgets of Reynolds stress, kinetic energy and streamwise enstrophy based on these simulations. Dimitropoulos, *et al.* (2001) observed a significantly lower magnitude of the turbulence production and velocity-pressure gradient terms in the turbulent

kinetic energy budget compared to Newtonian case. Furthermore, Kim, *et al.* (2007, 2008) found that the polymer suppresses near wall vortices by generating torques which oppose the motions of the vortical structures. Kim, *et al.* (2007, 2008) claimed that this reduction in vortex strength results in the suppression of the autogeneration of new vortices, which attenuates turbulence in drag reduced flow.

de Angelis, Casciola, & Piva (2002), de Angelis, *et al.* (2003, 2004) and Benzi, *et al.* (2006) performed simulations at $Re_\tau \approx 125$ and 212, and $Re_{\tau_b} \approx 195$ in a channel of size $2\pi h \times 1.2\pi h \times 2h$. The channel size was not large enough to accommodate the large structures which develop in drag-reduced viscoelastic turbulent flows. Simulations were preformed using pseudo-spectral methods with a FENE-P dumbbell model of the polymer with $\beta = 0.9$. The extensibility parameter was fixed at $b \approx 5,000$, which is again too small to be realistic. They observed $\sim 30\%$ drag reduction with $We_{\tau_b} \approx 140$ at $Re_{\tau_b} \approx 195$ (de Angelis, Casciola, & Piva, 2002). The turbulence kinetic energy production was observed to decrease (de Angelis, Casciola, & Piva, 2002), and the energy in the energy containing eddies was observed to grow in drag reduced flow rather than dissipated by the polymer (de Angelis, *et al.*, 2003). The spacing between the streaks in drag reduced flow was observed to become more sparse compared to Newtonian in drag reduced flow, and the polymer was observed to generate a body force which opposes the velocity fluctuations to suppress turbulence (de Angelis, Casciola, & Piva, 2002). Based on this database, L'vov, *et al.* (2004), de Angelis, *et al.* (2004) and Benzi, *et al.* (2004) suggested that the presence of the polymer leads to an effective viscosity which increases linearly with the distance from the the wall. It was suggested that this effective viscosity suppresses the Reynolds

stress in the elastic sublayer, resulting in a reduction of the momentum flux from bulk flow to the wall. They claimed that this linear effective viscosity is originated from the polymer extension in the wall-normal direction (Benzi, *et al.*, 2006).

Min, *et al.* (2003) and Min, Yoo & Choi (2003) performed simulations in a turbulent channel of size $7h \times 3.5h \times 2h$ at $Re_{\tau_b} \approx 150$, and in a $2.4h \times 0.9h \times 2h$ minimal channel at $Re_{\tau_b} \approx 590$. These channels are again too small to accommodate the large structures in drag reduced flow. Simulations were performed using a 4th-order compact difference scheme for the polymer-stress derivatives in the hydrodynamic equations, a modified compact upwind difference scheme for the polymer-stress convection term in the polymer dynamic equations, and all other terms were discretized using a 2nd-order center difference scheme. Simulation were performed for $We_{\tau_b} \lesssim 60$ at $Re_{\tau_b} \approx 150$ and for $We_{\tau_b} \lesssim 46$ at $Re_{\tau_b} \approx 590$ with the Hookean dumbbell model of the polymer, which can infinitely extend. In all simulations the viscosity ratio was fixed at $\beta = 0.9$. They observed drag reductions of up to 44% at the low Reynolds number and up to 28% at the high Reynolds number. In addition, 60% drag reduction was observed in the transient period with $We_{\tau_b} \approx 45$ at $Re_{\tau_b} \approx 150$, which confirmed to Virk's MDR asymptote. The DNS results in the LDR regime showed qualitative agreement with the experiments of Luchik & Tiederman (1988) and Wei & Willmarth (1992). Min, *et al.* (2003) observed that the polymer stores the elastic energy from the flow very near the wall and then releases it there when the relaxation time is short, showing no drag reduction. However, when the relaxation time is long enough, the elastic energy stored in the very near-wall region is transported to and released in the buffer and log layers, showing a significant amount of drag reduction.

However, turbulence inside the channel was observed to survive in the MDR state due to the enhanced energy transfer from the polymer elastic energy to the turbulent kinetic energy (Min, Yoo & Choi, 2003).

Ptasinski, *et al.* (2003) performed simulations at $Re_\tau = 180$ in a $3h \times 2h \times 2h$ minimal channel and compared their results with their own pipe flow experiments (Ptasinski, *et al.*, 2001). The size of the channel was again too small to accommodate the large structures in drag reduced flow. Their simulations were performed using Fourier methods in streamwise and spanwise directions and a finite difference method in wall normal direction. Simulations were performed using the FENE-P dumbbell model with $b = 100$ and $1,000$, $We_\tau \leq 72$ and $0.4 \leq \beta \leq 0.8$. The values of extensibility parameter were too small to be realistic, and the range of viscosity ratio was too low to correspond to "dilute" polymer solution. Drag reductions of up to 66%, corresponding to the MDR, were observed. In the LDR regime, their DNS results showed qualitative agreement with experiments. However, in the HDR regime, the DNS results showed a monotonic increase in the peak of streamwise turbulence intensity with increasing drag reduction, which again stands at odd with the trends observed in experiments (Warholic, Massah & Hanratty, 1999; Ptasinski, *et al.*, 2001). Their DNS results showed a significantly lower magnitude of turbulence production and pressure-strain correlation in drag reduced flow compared to Newtonian flow. A substantial part of the energy production by the mean flow was transferred directly into elastic energy of the polymers, and the turbulent velocity fluctuations also contributed energy to the polymers. The elastic energy of the polymers was subsequently dissipated by polymer relaxation. Ptasinski, *et al.* (2003) were explained their sim-

ulation results by two mechanisms. First, as suggested by Lumley (1969, 1973) the polymers damp the cross-stream velocity fluctuations and suppress the bursting in the buffer layer. Secondly, the 'shear sheltering' mechanism which amplifies the streamwise fluctuations in the thickened buffer layer, while reducing and decoupling the motions within and above this layer. The expression for the substantial reduction in the wall drag derived by considering the long time scales of the nonlinear fluctuations of this damped shear layer.

Dubief, *et al.* (2004, 2005) performed simulations at $Re_\tau = 300$ in a channel of size $4\pi h \times 4h \times 2h$. Simulations were performed using a 4th-order compact difference scheme for the polymer-stress derivatives in the hydrodynamic equations, a 3rd-order modified compact upwind difference scheme for the polymer-stress convection term in the polymer dynamic equations, and all other terms were discretized using a 2nd-order center difference scheme. Simulations were preformed with a FENE-P dumbbell model of the polymer at $b \approx 3,600$ or $10,000$, and a viscosity ratio of $\beta = 0.9$. Drag reductions approached 60% with $We_{\tau_b} \leq 120$, corresponding to HDR regime. They observed that the polymer absorbs energy from near-wall vortices and releases it in the near-wall region. In this process, the polymer was observed to generate a force field which opposes the velocity fluctuations in spanwise and wall-normal directions, but provides a positive work in streamwise direction. They argued that the near wall vortices are suppressed and the turbulence kinetic energy in the streamwise direction is enhanced through this event, and the balance of these two opposite actions leads to a self-sustained drag-reduction.

Dimitropoulos, *et al.* (2005, 2006) performed simulations in a boundary layer flow with $Re_{\theta_b} \equiv u_{\tau_b}\theta_{in}/\nu_s = 670$, where θ_{in} is the momentum thickness at the inlet. The size of computational domain was $168.4\theta_{in} \times 32.2\theta_{in} \times 24.5\theta_{in}$. Simulations were performed using a 4th-order compact difference scheme for the polymer-stress derivatives in the hydrodynamic equations, a modified compact upwind difference scheme for the polymer-stress convection term in the polymer dynamic equations, and all other terms in the hydrodynamic and polymer dynamic equations were discretized using a 2nd-order center difference scheme. In addition, the concentration equation was computed using the second-order QUICK scheme (Pierce & Moin, 2004). Simulations were preformed at $We_{\tau_b} = 25$ or 50, $\beta = 0.9$ and $b = 10,000$ with a FENE-P dumbbell model of the polymer in homogeneous and inhomogeneous polymer solutions. In the inhomogeneous case, polymers were introduced at the inlet with a polymer concentration corresponding to a constant Gaussian profile, which varied only in the wall-normal direction. For both homogeneous and inhomogeneous cases, friction drag was observed to increase just after the inlet due to the initial stretching of the polymer, and then it reduced and approached an equilibrium state as the flow proceeded downstream. In the homogeneous case, $40\%DR$ was achieved at $We_{\tau_b} = 25$ in the equilibrium state, while $60\%DR$ was achieved at $We_{\tau_b} = 50$. In the inhomogeneous case, the achieved drag reduction at different streamwise locations was consistent with the polymer concentration near the wall, which was observed to decrease as the flow proceeded downstream. Simulation at $We_{\tau_b} = 50$ with inhomogeneous polymer solution achieved drag reduction of $\sim 50\%DR$ in the equilibrium state, which was smaller than that with homogeneous polymer solution.

de Angelis, *et al.* (2005) performed simulations in homogeneous isotropic turbulence at $Re_f \equiv (L^3 f_o)^{1/2}/\nu = 960$ in a domain of size $L \times L \times L$ using Fourier spectral method, where f_o is the external forcing applied in the largest turbulent scale. Simulations were preformed at $We_f \equiv \lambda(f_o/L)^{1/2} = 0.18$ and $\beta = 0.9$ with the FENE-P dumbbell model of the polymer. Polymer extensibility parameter was fixed at $b = 1,000$, which is again too small to be realistic. Their results showed that an alteration of the cascade in turbulent flows with dilute polymer solution results in a pure damping of the entire range of scales for small values of Weissenberg number, or the depletion of the small scales accompanied by increased fluctuations at large scales for larger values of Weissenberg number.

Vaithianathan, *et al.* (2007) performed simulations in shear-driven turbulence at $Re_T \equiv q^2/3\sqrt{15/\nu\varepsilon} = 15.8$ in a channel of size $4h \times 2h \times 2h$ using finite-difference method, where q denotes the turbulence kinetic energy at Newtonian state. Once again, the channel size was too small to accommodate the large structures in drag reduced flow. In their study, the polymer was introduced as a thin slab concentrated in the middle of the channel to investigate the polymer mixing (corresponding to 9.85 times of bulk average polymer concentration in the channel). Simulations were performed for $1.41 \leq We_S \equiv S\lambda \leq 3.54$, $\beta = 0.95$ with a FENE-P dumbbell model of the polymer, where S denotes the constant mean shear applied in DNS. Polymer extensibility parameters of $b = 10,000$ and $b = 40,000$ were used. The simulations showed that the polymer mixing, the Reynolds stress in mean shear direction, and the turbulence production were suppressed with increasing Weissenberg number and extensibility parameter. They argued that the origin of this suppression at higher

Weissenberg number is not only due to the suppression of vertical velocity fluctuations but also the reduced correlation between vertical velocity fluctuations and polymer concentrations.

These direct numerical simulations all show results which are qualitatively similar to experiments. However, they all suffer from the following limitations: (i) the polymer extensibility parameter in many of these simulations is either too small for the FENE-P (Sureshkumar, Beris & Handler, 1997; Dimitropoulos, Sureshkumar & Beris, 1998; Beris & Dimitropoulos, 1999; Dimitropoulos, *et al.*, 2001; de Angelis, Casciola, & Piva, 2002; de Angelis, *et al.*, 2003, 2004, 2005; Housiadas & Beris, 2003; Ptasinski, *et al.*, 2003; Dubief, *et al.*, 2004, 2005; Dimitropoulos, *et al.*, 2005, 2006; Benzi, *et al.*, 2006) and Giesekus (Dimitropoulos, Sureshkumar & Beris, 1998; Beris & Dimitropoulos, 1999; Housiadas & Beris, 2003) models, or is infinite (Hookean dumbbell model) (Sureshkumar & Beris, 1995; Min, *et al.*, 2003; Min, Yoo & Choi, 2003; Li, Sureshkumar & Khomami, 2006). Realistic polymer extensibility parameters should be in the range $10^4 < b < 10^6$. This makes it difficult to make any 'quantitative' comparisons between experiments and these DNS results; (ii) the simulation domains in many of these studies (Baron & Sibilla, 1998; de Angelis, Casciola, & Piva, 2002; de Angelis, *et al.*, 2003, 2004; Min, Yoo & Choi, 2003; Ptasinski, *et al.*, 2003; Benzi, *et al.*, 2006; Vaithianathan, *et al.*, 2007) are not large enough to accommodate the large structures which develop in drag-reduced viscoelastic turbulent flows; (iii) some of the studies (Sureshkumar & Beris, 1995; Sureshkumar, Beris & Handler, 1997; Dimitropoulos, Sureshkumar & Beris, 1998; Beris & Dimitropoulos, 1999; Dimitropoulos, *et al.*, 2001; Housiadas & Beris, 2003) used coarse mesh resolutions, which cannot resolve the small

scale structure of turbulence even in drag-reduced flow; (iv) the polymer concentration in some of these studies was too high for the simulations to correspond to a dilute polymer solution (Ptasinski, *et al.*, 2003); (v) all simulations had to introduce an 'ad hoc' artificial stress diffusivity to stabilize the numerical methods, which affects the polymer and turbulence dynamics; (vi) even with the artificial diffusivity, simulations could not be performed for high Weissenberg numbers representative of the true MDR regime. We_{τ_b} should be of the same order of Re_{τ_b} at MDR according to the classical theories (Lumley, 1969, 1973; de Gennes, 1986), while in most of simulations to date is $We_{\tau_b} < Re_{\tau_b}/2$; (vii) some of the simulations (Ptasinski, *et al.*, 2003; Li, Sureshkumar & Khomami, 2006) could not fully capture the trends in the streamwise turbulence intensity at HDR observed in experiments; (viii) the MDR results reported in some of the studies (Min, Yoo & Choi, 2003) correspond to a transient state, not to true MDR at steady-state.

1.4 Theoretical studies

Two principal theories have been proposed to explain the phenomenon of polymer drag reduction. One is the so-called time-criteria or elongational viscosity theory suggested by Lumley (1969, 1973); the other is the elastic theory suggested by de Gennes (1986).

1.4.1 Elongational viscosity theory (Lumley, 1969, 1973)

In the elongational viscosity theory of Lumley (1969, 1973), drag reduction is attributed to the additional dissipation introduced by the enhanced elongational vis-

cosity of the polymer. This elongational viscosity is assumed to act only on turbulent eddies whose time-scale is shorter than the polymer relaxation time, λ. Onset of drag reduction is assumed to occur when there exists a turbulent scale whose characteristic time-scale matches the polymer relaxation time, λ. In wall-bounded flows, this translates to the onset criterion $\lambda \sim O(\nu/u_\tau^2)$ or

$$We_\tau|_{onset} \equiv \frac{\lambda u_\tau^2}{\nu} \sim O(1). \tag{1.5}$$

The proposed onset criterion is, therefore, independent of polymer concentration. Saturation is assumed to occur when the wavenumber corresponding to the peak of the dissipation spectrum defined using the effective viscosity coincides with the largest turbulent eddies having a time-scale λ. In wall-bounded flows, the largest turbulent eddies having a time-scale λ would have $kz \sim 1$ and $(k^2\varepsilon)^{-1/3} \sim \lambda$, where z denotes the wall-normal coordinate and it has been assumed that the Reynolds number is large so an inertial spectra can be assumed that the peak of the dissipation spectrum occurs at $k/k_{d,eff} \simeq 0.2$, where $k_{d,eff} = (\varepsilon/v_{eff}^3)^{1/4}$, $\varepsilon \approx u_\tau^3/z$ is the dissipation rate, and v_{eff} is the effective viscosity introduced by the polymer. Equating the above three equations, gives the saturation value of the effective viscosity in wall-bounded flows as

$$\nu_{eff,sat} \sim (0.2)^{4/3}\lambda u_\tau^2 \sim (0.1)\lambda u_\tau^2. \tag{1.6}$$

In his original derivation (Lumley, 1973) gave the condition as $\nu_{eff,sat} \sim O(\lambda u_\tau^2)$. Maximum drag reduction is assumed to be achieved when the edge of the viscous sublayer defined based on the saturation value of the effective viscosity, namely

$zu_\tau/\nu_{eff,sat} \approx 10$, extends all the way to the core of the pipe or channel or the outer edge of the boundary layer. Thus MDR occurs when $\delta u_\tau/(0.1\lambda u_\tau^2) \approx 10$, or $\delta \sim O(\lambda u_\tau)$ or $We_\tau \sim O(Re_\tau)$, where $Re_\tau \equiv u_\tau \delta/\nu$.

1.4.2 Elastic theory (de Gennes, 1986)

In the elastic theory of de Gennes (1986), it is assumed that the turbulence dynamics is affected in a turbulent eddy when the eddy has a characteristic time shorter than λ and it has redirected "all" its turbulence kinetic energy into the elastic energy of the polymer. Onset of drag reduction in wall-bounded flows is assumed to occur when the largest such affected scale equals the Kolmogorov scale just outside the viscous sublayer. It was shown by Sreenivasan & White (2000) that this condition corresponds to the onset criterion

$$\frac{n_p k_B T}{\rho u_\tau^2}|_{onset} = (z^+)^{(\frac{15n}{8}-\frac{1}{2})} We_\tau^{-\frac{15n}{4}} \quad for \quad z^+ \approx 10, \tag{1.7}$$

where k_B is the Boltzmann's constant, T is the absolute temperature, $z^+ \approx 10$ denotes the wall-normal coordinate at the outer edge of the viscous sublayer, and $0 < n \leqslant 2$ denotes the dimensionality of the polymer stretching (de Gennes, 1986). The onset criteria is thus found to be a function of both the Weissenberg number and polymer number density (or concentration). Sreenivasan & White (2000) found $n = 2/3$ by fitting the experimental data (Patterson & Abernathy, 1970; Berman, 1977; Nadolink, 1987), which gives agreement with equation (1.2). Saturation is assumed to occur when the unstretched polymer coils begin to overlap, or when $n_p R_G^3 \sim 1$. Using the relation between R_G and the Zimm relaxation time of the polymer $\frac{1}{\lambda_Z} \approx \frac{k_B T}{\mu_s R_G^3}$ (Flory,

1971), de Gennes's saturation criterion in wall-bounded flows can be expressed as

$$\frac{n_p k_B T}{\rho u_\tau^2}|_{sat} \approx \beta We_\tau^{-1} \approx We_\tau^{-1}. \tag{1.8}$$

de Gennes does not specifically comment on the conditions for achieving MDR, but mentions in passing that when the time criterion of Lumley is satisfied by the largest turbulent eddies, further addition of the polymer becomes less effective (de Gennes, 1986). This corresponds to $\delta \approx (\varepsilon^3 \lambda)^{1/2}$. With $\varepsilon \approx u_\tau^3/z$ and $z = \delta$, this gives the MDR criterion in wall-bounded flows as $\delta \sim O(\lambda u_\tau)$ or $We_\tau \sim O(Re_\tau)$, which is the same as that in Lumley's theory (Lumley, 1969, 1973).

1.4.3 Comparison of the two theories to experimental and DNS data

From the perspective of turbulence dynamics, both Lumley's mechanism and de Gennes's mechanism represent a drain of turbulence kinetic energy at the affected scales. The main difference between the two theories is the range of affective scales and the fate of the energy which has been redirected into the polymer. Lumley's theory predicts a shift of the peak of dissipation spectrum due to the enhanced dissipation introduced through the polymer, while de Gennes's theory predicts a truncation of the turbulent energy cascade for all turbulent eddies which have redirected all their turbulence kinetic energy into the elastic energy of the polymer. The energy spectra observed in viscoelastic flow in experiments (Wei & Willmarth, 1992; Warholic, Massah & Hanratty, 1999) and DNS (de Angelis, *et al.*, 2003, 2005; Housiadas & Beris, 2003; Dubief, *et al.*, 2005) show evidence of enhanced dissipation compared to Newtonian due to the enhanced elongational viscosity as suggested in Lumley's the-

ory, but none of these show the truncation of the cascade which has been proposed by de Gennes. Furthermore, de Genne's theory gives predictions for the criteria for onset and saturation which are orders of magnitude off from observations in both experiments and DNS. However, there are several features which are not explained by either theory. Specifically, the amount of energy redirected from turbulence to the polymer has been found to be minuscule in all numerical studies. Neither theory provides an explanation of how these energetically insignificant exchange can result in the dramatic skin-friction drag reductions which have been observed with polymers. Furthermore, both experiments and DNS show a highly anisotropic state of turbulence near the buffer layer (Walker & Tiederman, 1990; Gampert & Yong, 1990; Gyr & Bewersdorff, 1990) and also in the viscous sublayer (Frohnapfel, *et al.*, 2007) in drag reduced flow. However, neither theory can explain how this anisotropic state is established through either elongational viscosity or elastic energy of the polymer.

1.5 The structural view

An alternative approach to investigating the mechanism of polymer drag reduction is a structural view. Investigation of the effect of the polymer on the near-wall coherent structures have shown that these structures become weaker, more sparse and larger in size compared to Newtonian flow (Oldaker & Tiederman, 1977; Baron & Sibilla, 1998; de Angelis, Casciola, & Piva, 2002; White, Somandepalli & Mungal, 2004; Stone, *et al.*, 2004; Kim, *et al.*, 2007; Li & Graham, 2007). These changes have been attributed to polymer generated body forces (de Angelis, Casciola, & Piva, 2002; Stone, *et al.*, 2004; Dubief, *et al.*, 2005) or torques (Kim, *et al.*, 2007) which oppose

the motions of the vortical structures. Some investigators claim that this reduction in vortex strength results in the suppression of the autogeneration of new vortices (Kim, *et al.*, 2008), while other investigators claim that it suppresses the pressure-strain correlation in the turbulence kinetic energy budget (Stone, *et al.*, 2004; Li & Graham, 2007) due the attenuated pressure fluctuation in the middle of vortices. Neither of these theories has resulted in a comprehensive picture of polymer drag reduction.

1.6 Objectives of the present study

The objectives of the present study are to: (i) Develop the required numerical methods for accurate and efficient Direct Numerical Simulation (DNS) of drag reduction by dilute polymer solutions in wall-bounded flows. (ii) Perform DNS of drag reduction by homogeneous, dilute polymer solutions in turbulent channel flow, and validate the DNS results through 'quantitative' comparisons with available experimental data. (iii) Use the DNS results to investigate the scaling of drag reduction with polymer and flow parameters, such that the 'optimal' polymer parameters for drag reduction in a given turbulent flow can be determined a priori. (iv) Use the DNS results to clarify the detailed mechanism of drag reduction by dilute polymer solutions. The ultimate goal of the studies is to use the knowledge gained from the mechanism of polymer drag reduction to devise strategies for skin-friction drag reduction in wall-bounded flows based on agents other than polymer additives. The organization of the dissertation is as follows. In chapter II, the governing equations and the numerical methods are reviewed. The results from DNS are presented in

chapter III. The scaling of drag reduction with polymer and flow parameters is presented in chapter IV. The mechanism of drag reduction is discussed in chapter V. Summary and conclusions are provided in chapter VI.

Chapter II

Governing Equations and Numerical Methods

2.1 Governing equations

The equations governing the conservation of mass and momentum for isothermal, incompressible flow of a dilute polymer solution, expressed in dimensionless and rotation form, are given by

$$\frac{\partial \mathbf{v}}{\partial t} = \mathbf{v} \times \omega - \nabla \Pi + \frac{1}{Re} \nabla^2 \mathbf{v} + \nabla \cdot \tau_p, \tag{2.1}$$

$$\nabla \cdot \mathbf{v} = 0, \tag{2.2}$$

where $\mathbf{v}$ is the velocity, $\omega = \nabla \times \mathbf{v}$ is the vorticity, $\Pi = p + \frac{1}{2}|\mathbf{v}|^2$ is the pressure head, τ_p is the polymer stress, $Re = U_o L/\nu_s$ is the Reynolds number, and all quantities have been non-dimensionalized with respect to a velocity scale U_o, a length scale L, and the density ρ.

The presence of the polymer introduces an additional body force $\nabla \cdot \tau_p$ in the momentum equations. For the system of equations (2.1)-(2.2) to be closed, the polymer stress τ_p needs to be computed. In the present study, the polymer dynamics is represented using the FENE-P dumbbell closure approximation (Bird, *et al.*, 1987). In this model, the dilute polymer solution is represented as a suspension of non-interacting and free-draining dumbbells convected in a Newtonian solvent. Each dumbbell con-

sists of two identical Brownian beads connected by a spring, and its configuration is described by the length and orientation of the vector $\mathbf{Q}$ connecting the two beads. In the FENE-P dumbbell model of the polymer, the evolution equation for the polymer conformation tensor is given by (Bird, *et al.*, 1987)

$$\frac{\mathrm{D}\mathbf{A}}{\mathrm{D}t} = (\nabla\mathbf{v})^T \cdot \mathbf{A} + \mathbf{A} \cdot (\nabla\mathbf{v}) - \frac{1}{We}\left(\frac{\mathbf{A}}{1 - \mathrm{Tr}(\mathbf{A})/b} - \mathbf{I}\right). \tag{2.3}$$

Here $\mathbf{A} = \langle\mathbf{QQ}\rangle_s$ denotes the conformation tensor non-dimensionalized with respect to k_BT/H, where H is the spring constant of the dumbbell, $b = Q_o^2/(k_BT/H)$ is the dumbbell extensibility parameter, Q_o is the maximum extension of the spring, $We = \lambda U_o/L$ is the Weissenberg number, $\lambda = \frac{\zeta}{4H}$ is the relaxation time of the dumbbell, ζ is the drag coefficient on each bead, $\mathbf{I}$ is an identity matrix, and the brackets $\langle\cdot\rangle_s$ denote an average over the configuration space of the dumbbell. Once $\mathbf{A}$ is known, the polymer stress can be found using Kramers's expression (Bird, *et al.*, 1987) as

$$\tau_p = \frac{n_p k_B T}{\rho U_o^2}\left(\frac{\mathbf{A}}{1 - \mathrm{Tr}(\mathbf{A})/b} - \mathbf{I}\right), \tag{2.4}$$

where n_p is the polymer number density, and the polymer stress has been non-dimensionalized with respect to ρU_o^2 to be consistent with the non-dimensionalization used in equations (2.1)-(2.2). Also of interest is the polymer root-mean-square end-to-end extension which when non-dimensionalized with respect to the maximum extension of the spring is given by

$$\xi = \sqrt{\frac{\mathrm{Tr}(\mathbf{A})}{b}}. \tag{2.5}$$

2.2 Numerical methods

Equations (2.1)-(2.4) are solved using a novel mixed Eulerian-Lagrangian scheme. In this scheme the mass and momentum conservation equations (2.1)-(2.2) are solved in an Eulerian representation using standard pseudo-spectral methods (Canuto, *et al.*, 1988), while the polymer dynamics equations (2.3)-(2.4) are solved in a Lagrangian framework using the Backward-tracking Lagrangian Particle Method (BLPM) suggested by Wapperom, Keunings & Legat (2000).

2.2.1 Hydrodynamics

We consider the solution of the system of equations (2.1)-(2.2) in a channel, assumed to be homogeneous in the streamwise (x) and spanwise (y) directions. A schematic of the channel and the coordinate system is shown in figure 2.1. To proceed with the solution, all flow variables are expanded in terms of discrete Fourier series in the homogeneous directions and Chebyshev polynomials in the wall-normal direction as,

$$\mathbf{v}(\mathbf{x},t) = \sum_{n=-N}^{N} \sum_{m=-M}^{M} \sum_{p=0}^{P} \hat{\mathbf{v}}_{nmp}(t) e^{i\alpha n x} e^{i\beta m y} T_p(z). \tag{2.6}$$

Time advancement is performed using a two-step (Green's function) splitting method (Canuto, *et al.*, 1988). In the first fractional step, the nonlinear terms are advanced in time using a second-order Adams-Bashforth scheme and the polymer body-force terms using a second-order Adams-Moulton (Crank-Nicolson) scheme as,

$$\frac{\mathbf{v}^{*(n+1)} - \mathbf{v}^{(n)}}{\Delta t} = [\frac{3}{2}(\mathbf{v}\times\omega)^{(n)} - \frac{1}{2}(\mathbf{v}\times\omega)^{(n-1)}] + \frac{\nabla\cdot\tau_p^{(n+1)} + \nabla\cdot\tau_p^{(n)}}{2}. \tag{2.7}$$

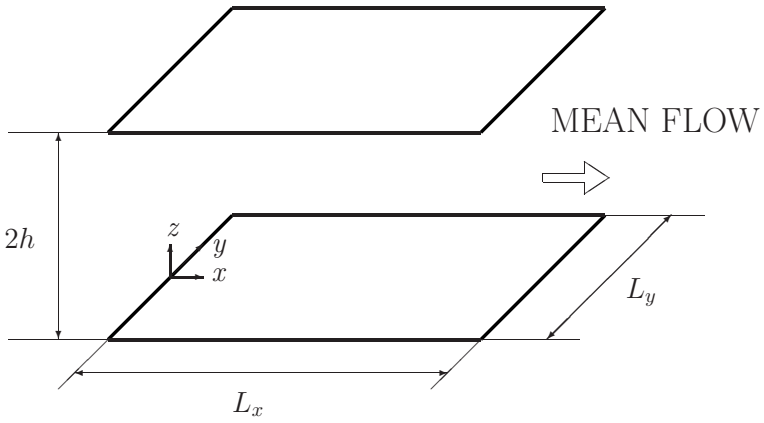

Figure 2.1: The channel geometry and coordinate system.

In the second fractional step, the pressure and viscous terms are incorporated into the solution using a second-order Adams-Moulton (Crank-Nicolson) scheme, subject to the condition of incompressibility and the boundary conditions at the walls

$$\frac{\mathbf{v}^{(n+1)} - \mathbf{v}^{*(n+1)}}{\Delta t} = -\nabla \Pi^{(n+1)} + \frac{1}{Re}\nabla^2\left(\frac{\mathbf{v}^{(n+1)} + \mathbf{v}^{(n)}}{2}\right), \tag{2.8}$$

$$\nabla \cdot \mathbf{v}^{(n+1)} = 0, \tag{2.9}$$

$$\mathbf{v}^{(n+1)} = \mathbf{v}_w \qquad \text{at the boundaries.} \tag{2.10}$$

Equations (2.8) and (2.9) are combined into a single fourth-order equation for the wall-normal component of velocity (w), which is solved using the analytic Green's functions method suggested by Domaradzki (1990). Once w is known, the other components of velocity are found from the remaining equations.

2.2.2 Polymer dynamics

Solution of (2.7) requires knowledge of the polymer stress, τ_p. The polymer dynamics is computed using the Backward-tracking Lagrangian Particle Method (BLPM) suggested by Wapperom, Keunings & Legat (2000). In this scheme, the polymer dynamics is obtained by time integration of the constitutive equations (2.3)-(2.4) along Lagrangian trajectories of discrete particles that are convected by the flow. The locations of the particles at the conclusion of each time step are specified to be the fixed Eulerian grid points, $\mathbf{r}_G$, as shown in figure 2.2. The trajectories leading to these locations are calculated by tracking backwards in time using

$$\mathbf{r}_P^{(n)} = \mathbf{r}_G - \int_{t_n}^{t_{n+1}} \mathbf{v}(\mathbf{r}, t_n)\, dt, \tag{2.11}$$

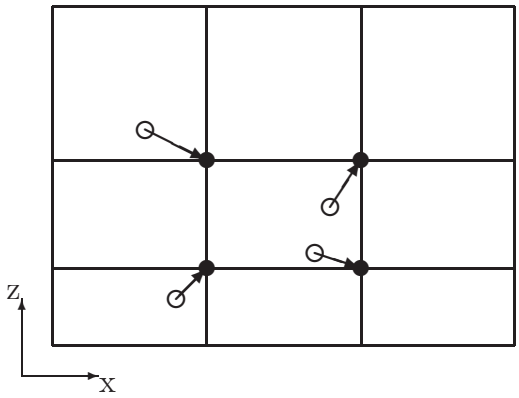

Figure 2.2: The backward tracking of particles: ∘, particle positions, $r_P^{(n)}$, at t_n; •, particle positions, r_G, at t_{n+1}.

where $\mathbf{r}_P^{(n)}$ denotes the starting location of the particle at time t_n, and the integral is evaluated using a second-order Runge-Kutta scheme.

Thus with BLPM, the solution of the FENE-P dumbbell equation (2.3) reduces to time integration of the equation

$$\frac{\mathrm{d}\mathbf{A}}{\mathrm{d}t} = (\nabla\mathbf{v})^T \cdot \mathbf{A} + \mathbf{A} \cdot (\nabla\mathbf{v}) - \frac{1}{We}\left(\frac{\mathbf{A}}{1 - \mathrm{Tr}(\mathbf{A})/b} - \mathbf{I}\right) \tag{2.12}$$

along particle trajectories from $(\mathbf{r}_P^{(n)}, t_n)$ to $(\mathbf{r}_G, t_{n+1})$. Integration of (2.12) requires initial conditions specifying the configuration tensor $\mathbf{A}(\mathbf{r}_P^{(n)}, t_n)$ and the velocity gradient tensor $\nabla\mathbf{v}(\mathbf{r}_P^{(n)}, t_n)$ at $\mathbf{r}_P^{(n)}$ at each time step. These are obtained by polynomial interpolation from the corresponding values, $\mathbf{A}(\mathbf{r}_G, t_n)$ and $\nabla\mathbf{v}(\mathbf{r}_G, t_n)$, at the Eulerian grid points at time t_n.

As noted by Wapperom, Keunings & Legat (2000), the interpolation process for obtaining $\mathbf{A}(\mathbf{r}_P^{(n)}, t_n)$ has to be handled with care. Given an Eulerian field which satisfies $\mathrm{Tr}\{\mathbf{A}(\mathbf{r}_G, t_n)\} < b$ and $A_{ii}(\mathbf{r}_G, t_n) > 0$, where A_{ii} denote the diagonal elements of $\mathbf{A}$, the interpolation process must ensure that

$$A_{ii}(\mathbf{r}_P^{(n)}, t_n) > 0 \tag{2.13}$$

and

$$\mathrm{Tr}\{\mathbf{A}(\mathbf{r}_P^{(n)}, t_n)\} < b. \tag{2.14}$$

Two obvious choices are interpolation based on linear and quadratic schemes. Linear interpolation preserves the constraints (2.13) and (2.14). However, it introduces an artificial stress diffusivity of magnitude $\chi_i(u_i, \lambda)$ in the ith direction. In the simulations of turbulent channel flow reported in this study, χ_i is negligible in the spanwise

and wall-normal directions where only fluctuating velocities are present. However, in the streamwise direction, χ_1 at the center of the channel with high Weissenberg number reaches a value similar to that in the conventional Eulerian schemes, which is typically implemented with an artificial stress diffusivity of $\chi_i/\nu_s \sim 2$ or higher in all three directions (Sureshkumar, Beris & Handler, 1997) across the channel. Therefore, the linear interpolation scheme imposes a smaller artificial diffusivity throughout most for the cross-section of the channel. But towards the center of the channel, its artificial stress diffusivity becomes comparable to that in Eulerian schemes at higher Weissenberg numbers. The quadratic interpolation scheme does not introduce any artificial stress diffusivity, but it can violate the constraint (2.13). In practice, we find if the quadratic interpolation is performed using the three points comprised of the two nearest neighboring grid points and the choice of the third neighboring point which gives the lower curvature in the polynomial interpolation, the constraint (2.13) is satisfied at more than 99.8% of the grid points in the domain. At the remaining 0.2% of the points, the quadratic interpolation is replaced with linear interpolation. We have never observed a violation of the constraint (2.14) during the interpolation process with either the linear or quadratic scheme. The velocity gradient tensor $\nabla\mathbf{v}(\mathbf{r}_P^{(n)}, t_n)$ is interpolated using the same interpolation scheme as that used for $\mathbf{A}$.

Once $\mathbf{A}(\mathbf{r}_P^{(n)}, t_n)$ and $\nabla\mathbf{v}(\mathbf{r}_P^{(n)}, t_n)$ are known, the polymer equations (2.12) are integrated in time using a second-order Runge-Kutta scheme for one time-step, from $(\mathbf{r}_P^{(n)}, t_n)$ to $(\mathbf{r}_G, t_{n+1})$ to obtain $\mathbf{A}(\mathbf{r}_G, t_{n+1})$. Once $\mathbf{A}(\mathbf{r}_G, t_{n+1})$ is known, the polymer stress $\tau_p^{(n+1)} = \tau_p(\mathbf{r}_G, t_{n+1})$ is evaluated using (2.4) and the result is supplied to the hydrodynamics equations (2.7).

2.2.3 Implementation on parallel computers

The numerical methods described above are amenable to efficient parallel implementation on Multiple Instruction and Multiple Data (MIMD) architectures. In parallelizing the code, one can take advantage of the fact that the solution of equations (2.7)-(2.12) involves one of only two classes of operations: (i) operations which are point-wise in the Fourier space, and (ii) operations which are point-wise in the physical space. The first category includes solution the Poisson operators which result from equations (2.8-2.9), as well as all the derivative operations in the Fourier (x or y) directions needed to compute the vorticity ω, the velocity gradient tensor $\nabla\mathbf{v}$, or the polymer body force term $\nabla \cdot \tau_p$. These operations can be performed locally without communication if they are implemented in the Fourier space with the data distributed among different processors such that each processor contains an assigned number of x-planes or y-planes of data, as shown in figure 2.3. Load balance can be achieved by assigning an equal number of planes of data to each processor. The second class of operations includes computation of all the nonlinear terms in equations (2.7) and (2.12), integration of the above equations in time (assuming ω, $\nabla\mathbf{v}$, $\nabla \cdot \tau_p$ and the initial conditions for eqn.2.12 are given), and evaluation of the polymer stress using equation (2.4). These operations can be performed in the physical-space with no communication as long as all the data pertaining to a given physical location is local to each processor. As with the previous case, load balance can be achieved by assigning an equal number of planes of data to each processor. Solving the governing equations in this manner, however, requires that the data be transformed back and

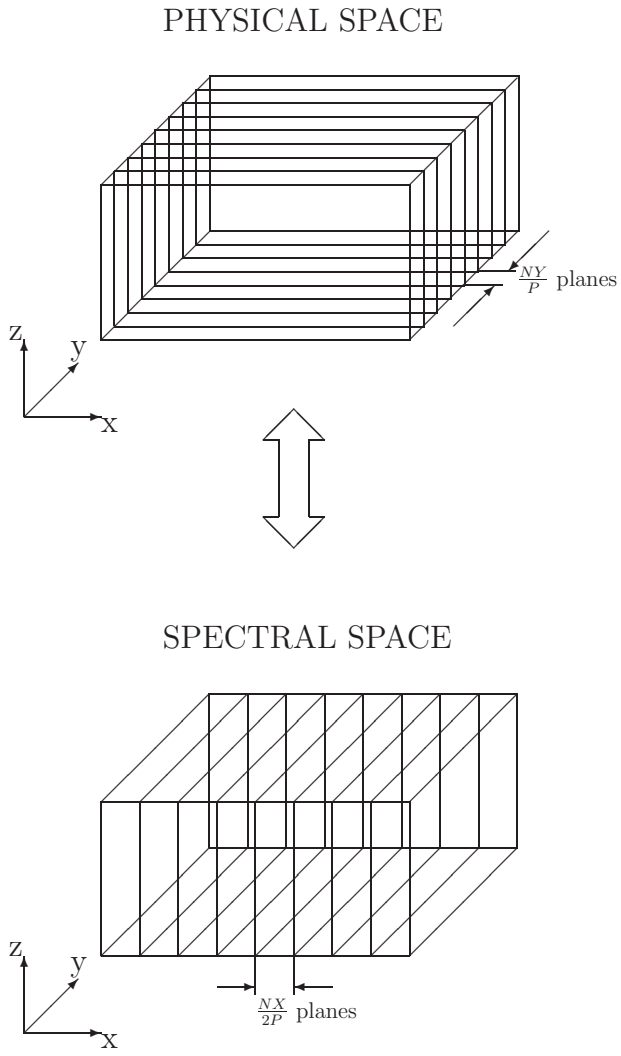

Figure 2.3: The parallelization scheme used in the simulations. The data is distributed among processors in sets of planes along y-direction in the physical-space and in sets of planes along the x-direction in the spectral-space.

forth between the physical-space and the spectral-space. This can be achieved using multi-dimensional FFTs. Using partial summation, these multi-dimensional FFTs can be broken down into a series of one-dimensional FFTs. If the data is distributed such that each processor contains an equal number of y-planes of data in the physical-space, as shown in figure 2.3, the one-dimensional FFTs in the x and z directions can be performed locally without communication. However, for the remaining (y) direction, the data is distributed among different processors. To evaluate the FFT in this direction, one can either: (i) evaluate the FFT using a parallel FFT algorithm, or (ii) rearrange the data among different processors, as shown in figure 2.3, such each processor now contains an equal number of x-planes of data and the FFT in the y-direction can be performed locally. Both approaches involve approximately the same number of operations. However, method (ii) requires less communication and allows the use of highly optimized assembly-coded one-dimensional FFT routines. For these reasons, we have adopted the latter approach in our simulations. The rearrangement of data is performed using the transpose algorithm described in Mangiavacchi & Akhavan (1993).

The only other operation which requires communication is the interpolation procedure needed to evaluate the velocity gradient tensor $\nabla\mathbf{v}(\mathbf{r}_P^{(n)}, t_n)$, and the polymer configuration tensor $\mathbf{A}(r_P^{(n)}, t_n)$ at the particle locations at each time step. Since the interpolation is performed in the physical-space, the data is distributed as shown in figure 2.3. With this configuration, the data required for all the interpolations is local to each processor in the x and z directions. However, in the y-direction, each processor J needs access to information from the $(J-1)NY/P$ and $(J \cdot NY/P + 1)$

or the $(J-1)NY/P-1$, $(J-1)NY/P$, $(J\cdot NY/P+1)$ and $(J\cdot NY/P+2)$ y-planes of data, which reside on its two or four neighboring sub-domains. To provide access to this data, before performing the interpolation, each sub-domain passes the information from its one or two highest and lowest y-planes to the respective neighboring sub-domains. This data is stored as ghost points in the neighboring sub-domains, and used to perform the interpolations.

The above parallelization scheme results in good overall parallel performance on medium-grained, distributed-memory, parallel architectures. The only limitation of the scheme is that the maximum number of processors which can be used in a problem of size $NX \times NY \times NZ$ is the smaller of $NX/2$ or NY (the factor 2 in $NX/2$ arises from the real to complex FFTs which we use in our codes) (Canuto, *et al.*, 1988) . In practice, however, this is not a major limitation, as the best parallel performance is generally obtained when the number of processors is smaller than the limit set by $NX/2$ or NY.

This is shown in figure 2.4, where we plot the speedup realized in DNS of Newtonian flow with $128\times128\times129$ and $256\times256\times257$ mesh resolutions, and viscoelastic flow with $128 \times 128 \times 129$ and $512 \times 256 \times 129$ mesh resolutions as the number of processors is increased from 1 to 128 processors on the Big Red Cluster at Indiana University. It can be seen that the performance remains close to the ideal (linear) up to 64 processors, but significantly degrades at 128 processors. The degradation of performance at 128 processors reflects the enhanced communication to computation ratio as the number of processors is increased. In general, for DNS of viscoelastic flows performed with constitutive closures, we use the largest number of processors

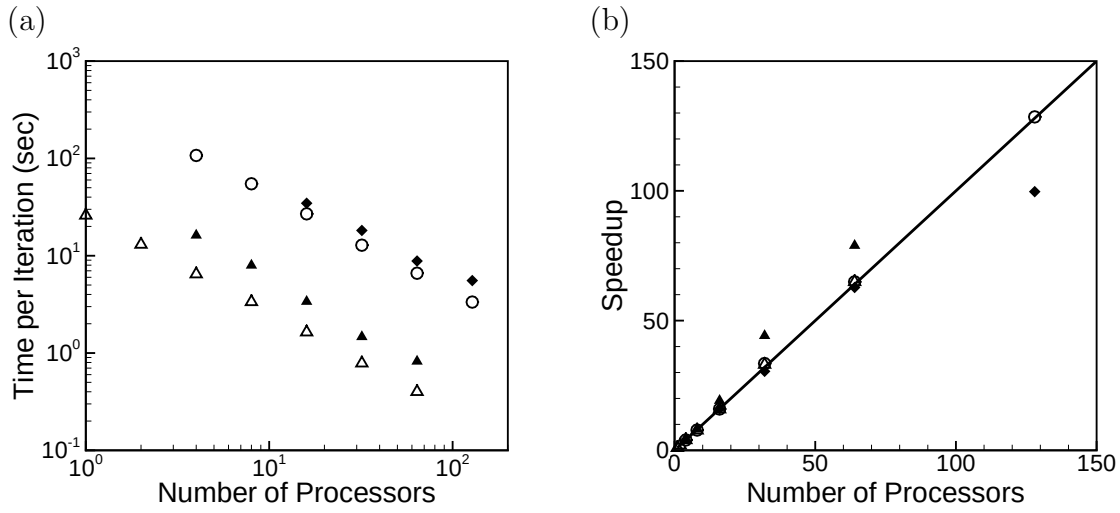

Figure 2.4: (a) The time per iteration and (b) speedup in DNS of turbulent channel flow performed on IBM e1350 (Big Red) with the number of processors increased from 1 to 128 . △, Newtonian flow with $128\times128\times129$ resolution; ○, Newtonian flow with $256 \times 256 \times 257$ resolution; ▲, viscoelastic flow with $128 \times 128 \times 129$ resolution; ⧫, viscoelastic flow with $512 \times 256 \times 129$ resolution; ——, ideal linear speedup.

for which linear speedup can be still achieved. This translates to 64 processors in our simulations.

2.3 Simulation parameters

The choice of flow conditions and polymer parameters employed in the present study were guided by one of the experimental data points of Virk (1975). The experiments were performed in a pipe of diameter $d = 4.57mm$ at a bulk Reynolds number of $Re_{bulk} = U_{bulk}R/\nu_s = 3,500$, corresponding to a friction Reynolds number of $Re_{\tau_b} = u_{\tau_b}R/\nu_s \approx 230$, where R denotes the pipe radius, and U_{bulk} denotes the bulk velocity. The working polymer in the experiments was polyethylene oxide (PEO) of average molecular weight 5.2×10^6, heterogeneity index (molecular weight distribution) of $\mathcal{H} = 3.5$, and concentration of $c = 30$ wppm, corresponding to a polymer number density of $n_p k_B T/(\rho u_{\tau_b}^2) \approx 1 \times 10^{-3}$. A drag reduction of $\sim 60\%$ was observed by Virk (1975) in this flow, which corresponds to maximum drag reduction at this Reynolds number.

Because the precise molecular weight distribution in the poly-disperse sample of PEO in Virk's experiments was unknown, in our DNS studies we consider a mono-disperse sample of PEO of molecular weight 5.2×10^6. The dumbbell extensibility parameter, b, for this mono-disperse PEO sample was estimated from the relation

$$b(N-1) = 3N_k = 3\frac{\tilde{n}^2 l^2 \sin^2[\tan^{-1}(\sqrt{2})]}{6R_G^2}, \tag{2.15}$$

where N denotes the number of beads in the chain ($N = 2$ for a dumbbell), N_k is the number of Kuhn steps, $\tilde{n}$ is the number of backbone bonds comprising the chain,

and l is the average backbone bond length (Larson, 1999). The radius of gyration was estimated from the relation (Flory, 1971)

$$R_G = \left[\frac{\mathcal{H} M_w[\eta]}{31 \times 10^{23}}\right]^{1/3} (cm), \tag{2.16}$$

where M_w is the average molecular weight and $[\eta]$ is the intrinsic viscosity. The intrinsic viscosity $[\eta]$, in turn, was estimated from the correlation

$$[\eta] = K M_w^a, \tag{2.17}$$

where $K = 0.00875 cm^3/g$ and $a = 0.79$ for PEO (Virk, 1975). Based on these results, the extensibility parameter for a mono-disperse sample ($\mathcal{H} = 1$) of PEO of $M_w = 5.2 \times 10^6$ was estimated to be $b \approx 43,000$.

The relaxation time of a FENE-P dumbbell corresponding to this mono-disperse sample of PEO was estimated based on Rouse theory (Bird, *et al.*, 1987) as

$$\lambda_H \approx \frac{[\eta]\, M_w \mu_s}{N_A k_B T}, \tag{2.18}$$

where N_A is Avogadro's number. Using (2.18) and (2.17), the relaxation time for a mono-disperse sample of PEO of $M_w = 5.2 \times 10^6$ was estimated to be $\lambda_H \approx 3 \times 10^{-3}$, which corresponds to a $We_{\tau_b} = \lambda_H u_{\tau_b}^2 / \nu_s \approx 34$ in Virk's experiments.

Based on these data, the baseline polymer parameters for the simulations were chosen as $b = 45,000$, $n_p k_B T/(\rho u_{\tau_b}^2) \approx 1 \times 10^{-3}$ and $We_{\tau_b} \equiv \lambda u_{\tau_b}^2/\nu_s \approx 35$. With these as the baseline parameters, we consider the effect of variation of individual polymer parameters on drag reduction by (i) keeping the polymer extensibility parameter fixed at $b = 45,000$ and varying the polymer number density over the range $1 \times 10^{-7} \lesssim$

$Case$	We_{τ_b}	b	$\frac{n_p k_B T}{\rho u_{\tau_b}^2}$	β	t_{avg}	$\frac{\Delta t_{avg}}{h/u_\tau}$	$\langle C_f \times 10^3 \rangle$	$DR\%$
N				1.00	200-400	8.4	8.03	
NN				1.00	200-300	4.2	8.01	
C3-l	35	45,000	1×10^{-3}	0.96	400-600	6.9	5.41	32.6
C3-q	35	45,000	1×10^{-3}	0.96	400-600	6.9	5.42	32.5
C3-e	35	45,000	1×10^{-3}	0.96	400-600	7.1	5.60	30.3
CC3-q	35	45,000	1×10^{-3}	0.96	400-600	6.9	5.38	32.8
E3-l	100	45,000	1×10^{-3}	0.90	850-1,500	18.2	3.52	56.2
E3-q	100	45,000	1×10^{-3}	0.90	850-1,500	17.9	3.40	57.7
E3-e	100	45,000	1×10^{-3}	0.90	1250-2,000	21.4	3.66	54.4
EE3-q	100	45,000	1×10^{-3}	0.90	600-1,000	11.4	3.67	54.2
F3-q	150	45,000	1×10^{-3}	0.86	850-1,500	13.8	2.04	74.6
FF3-q	150	45,000	1×10^{-3}	0.86	850-1,100	7.1	3.59	55.2

Table 2.1: Overview of the simulations performed to establish the effect of numerical scheme and domain size. Cases N, C3, E3 and F3 preformed in channels of size $\frac{80\pi}{27}h \times \frac{8\pi}{5}h \times 2h$; cases NN, CC3, EE3 and FF3 preformed in channels of size $\frac{320\pi}{27}h \times \frac{16\pi}{5}h \times 2h$; l denotes simulations performed using the mixed Eulerian-Lagrangian scheme with linear interpolation; q denotes simulations performed using the mixed Eulerian-Lagrangian scheme with quadratic interpolation; e denotes simulations performed using the Eulerian scheme.

$Case$	We_{τ_b}	$\frac{n_p k_B T}{\rho u_{\tau_b}^2}$	β	t_{avg}	$\frac{\Delta t_{avg}}{h/u_\tau}$	$\langle C_f \times 10^3 \rangle$	$DR\%$
N			1.00	200-400	8.4	8.03	
NN			1.00	200-300	4.2	8.01	
A7-l	10	1×10^{-7}	0.9999989	400-600	8.4	8.03	0.0
A6-l	10	1×10^{-6}	0.999989	400-600	8.4	8.00	0.4
A5-l	10	1×10^{-5}	0.99989	400-600	8.4	7.98	0.6
A4-l	10	1×10^{-4}	0.9989	400-600	8.4	7.96	0.9
A3-l	10	1×10^{-3}	0.989	400-600	8.4	7.88	1.9
A2-l	10	1×10^{-2}	0.9	400-600	8.4	7.87	2.0
C9-l	35	1×10^{-9}	0.99999996	400-600	8.4	8.03	0.0
C8-l	35	1×10^{-8}	0.9999996	400-600	8.4	8.015	0.2
C7-l	35	1×10^{-7}	0.999996	400-600	8.4	7.98	0.6
C6-l	35	1×10^{-6}	0.99996	400-600	8.3	7.77	3.2
C5-l	35	1×10^{-5}	0.9996	400-600	7.8	6.81	15.2
C4-l	35	1×10^{-4}	0.996	400-600	7.1	5.64	29.8
C4.1-l	35	6×10^{-4}	0.98	400-600	7.0	5.46	32.0
C3-l	35	1×10^{-3}	0.96	400-600	6.9	5.41	32.6
C3.1-l	35	3×10^{-3}	0.89	400-600	7.0	5.44	32.3
C3.2-l	35	7×10^{-3}	0.80	400-600	7.2	5.87	26.9
C2-l	35	1×10^{-2}	0.72	400-600	7.4	6.12	23.8
E10-q	100	1×10^{-10}	0.999999989	400-600	8.4	8.03	0.0
E9-q	100	1×10^{-9}	0.99999989	400-600	8.4	8.015	0.2
E8-q	100	1×10^{-8}	0.9999989	400-600	8.4	8.00	0.4
E7-q	100	1×10^{-7}	0.999989	400-600	8.3	7.84	2.4
E6-q	100	1×10^{-6}	0.99989	400-600	7.9	7.00	12.8
E5-q	100	1×10^{-5}	0.9989	600-1,000	13.1	4.85	39.6
EE4-q	100	2×10^{-4}	0.98	600-800	5.7	3.69	53.9
EE3-q	100	1×10^{-3}	0.90	600-1,000	11.4	3.67	54.2
F10-q	150	1×10^{-10}	0.99999998	400-600	8.4	8.03	0.0
F9-q	150	1×10^{-9}	0.9999998	400-600	8.4	8.015	0.2
F8-q	150	1×10^{-8}	0.999998	400-600	8.4	7.98	0.6
F7-q	150	1×10^{-7}	0.99998	400-600	8.3	7.76	3.4
F6-q	150	1×10^{-6}	0.9998	400-600	7.6	6.58	18.1
FF5-q	150	1×10^{-5}	0.998	450-700	7.9	4.55	43.2
FF4-q	150	1×10^{-4}	0.98	550-800	7.0	3.51	56.2
FF3-q	150	1×10^{-3}	0.86	850-1,100	7.1	3.59	55.2

Table 2.2: Overview of the simulations performed to establish the effect of polymer concentration. Cases N, Ai, Ci, Ei and Fi preformed in channels of size $\frac{80\pi}{27}h \times \frac{8\pi}{5}h \times 2h$; cases NN, EE$i$ and FFi preformed in channels of size $\frac{320\pi}{27}h \times \frac{16\pi}{5}h \times 2h$; l denotes simulations performed using the mixed Eulerian-Lagrangian scheme with linear interpolation; q denotes simulations performed using the mixed Eulerian-Lagrangian scheme with quadratic interpolation. The polymer extensibility parameter was set to $b = 45,000$ in all the viscoelastic simulations

$Case$	We_{τ_b}	b	$\frac{n_p k_B T}{\rho u_{\tau_b}^2}$	β	t_{avg}	$\frac{\Delta t_{avg}}{h/u_\tau}$	$\langle C_f \times 10^3 \rangle$	$DR\%$
N				1.00	200-400	8.4	8.03	
NN				1.00	200-300	4.2	8.01	
A3-l	10	45,000	1×10^{-3}	0.989	400-600	8.4	7.88	1.9
B3-l	20	45,000	1×10^{-3}	0.98	400-600	7.7	6.60	17.8
C3-l	35	45,000	1×10^{-3}	0.96	400-600	6.9	5.41	32.6
DD3-q	70	45,000	1×10^{-3}	0.93	600-800	6.0	4.08	49.2
EE3-q	100	45,000	1×10^{-3}	0.90	600-1,000	11.4	3.67	54.2
FF3-q	150	45,000	1×10^{-3}	0.86	850-1,100	7.1	3.59	55.2
C3.3-l	35	4,500	1×10^{-3}	0.96	400-600	7.1	5.68	29.3
C3-l	35	45,000	1×10^{-3}	0.96	400-600	6.9	5.41	32.6
C3.4-l	35	450,000	1×10^{-3}	0.96	400-600	6.9	5.39	32.9

Table 2.3: Overview of the simulations performed to establish the effect of Weissenberg number and extensibility parameter. Cases N and Ai, Bi and Ci preformed in channels of size $\frac{80\pi}{27}h \times \frac{8\pi}{5}h \times 2h$; cases NN, DD$i$, EE$i$ and FFi preformed in channels of size $\frac{320\pi}{27}h \times \frac{16\pi}{5}h \times 2h$; l denotes simulations performed using the mixed Eulerian-Lagrangian scheme with linear interpolation; q denotes simulations performed using the mixed Eulerian-Lagrangian scheme with quadratic interpolation.

$n_p k_B T/(\rho u_{\tau_b}^2) \lesssim 1 \times 10^{-2}$ at $We_{\tau_b} \approx 10$, over the range $1 \times 10^{-9} \lesssim n_p k_B T/(\rho u_{\tau_b}^2) \lesssim 1 \times 10^{-2}$ at $We_{\tau_b} \approx 35$, and over the range $1 \times 10^{-10} \lesssim n_p k_B T/(\rho u_{\tau_b}^2) \lesssim 1 \times 10^{-3}$ at $We_{\tau_b} \approx 100$ and $We_{\tau_b} \approx 150$, (ii) keeping the polymer extensibility parameter fixed at $b = 45,000$ and polymer number density fixed at $n_p k_B T/(\rho u_{\tau_b}^2) \approx 1 \times 10^{-3}$ and varying the Weissenberg number over the range $10 \lesssim We_{\tau_b} \lesssim 150$, and (iii) keeping the Weissenberg number fixed at $We_{\tau_b} \approx 35$ and the polymer number density fixed at $n_p k_B T/(\rho u_{\tau_b}^2) \approx 1 \times 10^{-3}$ and varying the polymer extensibility parameter over the range $4,500 \leq b \leq 450,000$. In reality, the polymer extensibility parameter and relaxation time (or Weissenberg number) are not independent parameters, as they are both linked to the polymer molecular weight. In the numerical simulations, however, we choose to vary each parameter independently to isolate the effect of each parameter on drag reduction. A summary of all the simulations is given in tables 2.1, 2.2 and 2.3.

The simulations were performed in a 2D channel at a base Reynolds number of $Re_{bulk} \equiv U_{bulk} h/\nu_s = 3600$, corresponding to $Re_{\tau_b} \equiv u_{\tau_b} h/\nu_s \approx 230$ based on Dean's correlation (Dean, 1978), where h denotes the channel half height, and U_{bulk} is the bulk velocity which was kept constant during the course of all simulations. Two different channel sizes were considered; a small channel of size $\frac{80\pi}{27}h \times \frac{8\pi}{5}h \times 2h$, and a large channel of size $\frac{320\pi}{27}h \times \frac{16\pi}{5}h \times 2h$. The simulations in the small channel were performed with a resolution of $128 \times 128 \times 129$ in the streamwise, spanwise and wall-normal directions, respectively, while those in the large channel were performed with a resolution of $512 \times 256 \times 129$. All simulations were de-aliased in the streamwise and spanwise directions using the so-called 2/3 rule (Canuto, *et al.*, 1988).

All computations were performed at constant flow rate and were started at $t = 0$ from Newtonian laminar flow, on which a combination of two and three-dimensional least-stable eigen-modes of the Orr-Sommerfeld equation were superimposed. This flow goes through transition between $50 < t < 100$ and equilibrates to a fully-developed turbulent state by $t \approx 200$, where t denotes the time non-dimensionalized with respect to U_o and h, where $U_o = 3/2U_{bulk}$ is the centerline velocity in the initial Newtonian laminar channel flow. The polymer was introduced in the fully-developed turbulent flow in its equilibrium state ($\mathbf{A} = \frac{b}{b+3}\mathbf{I}$) at $t = 200$, and the simulations were continued until the viscoelastic flow had reached a new fully-developed state. All flow statistics were computed based on spatial averaging in the homogeneous directions and time-averaging over 7 to 21 large-eddy turnover times ($\frac{\Delta \tilde{t}_{avg}}{h/u_\tau}$, where $\tilde{t}$ denotes the dimensional time) in the fully-developed state of the viscoelastic flow, as summarized in tables 2.1, 2.2 and 2.3.

2.4 Verification of the numerical methods

2.4.1 Convergence studies

To investigate the convergence of the mixed Eulerian-Lagrangian scheme, we compare the results obtained with quadratic interpolation scheme in turbulent channel flow at three different mesh resolutions at $We_{\tau_b} \approx 35$, $n_p k_B T/(\rho u_{\tau_b}^2) \approx 1 \times 10^{-3}$ and $b = 45,000$. Simulations were performed with mesh resolutions of $64 \times 64 \times 65$, $128 \times 128 \times 129$, and $256 \times 256 \times 257$ in $\frac{80\pi}{27}h \times \frac{8\pi}{5}h \times 2h$ channel.

Figure 2.5 shows the evolution of the skin friction coefficient, $C_f = \tau_w/(0.5\rho U_{bulk}^2)$, after the introduction of the polymer, along with turbulence and polymer statistics

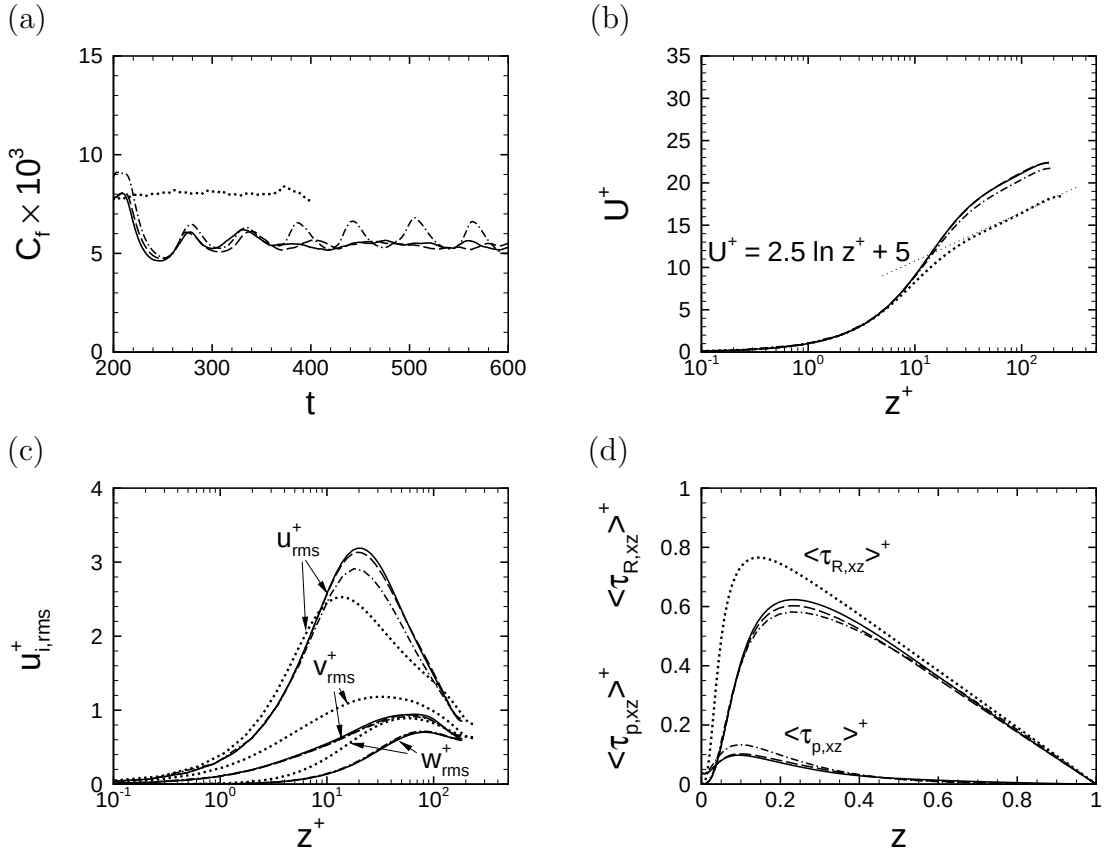

Figure 2.5: Effect of mesh size at $We_{\tau_b} \approx 35$, $n_p k_B T/(\rho u_{\tau_b}^2) \approx 1 \times 10^{-3}$, $b = 45,000$ on (a) time evolution of the skin friction coefficient; (b) mean velocity profiles; (c) r.m.s. of velocity fluctuations; (d) Reynolds ($\langle\tau_{R,xz}\rangle^+$) and polymer ($\langle\tau_{p,xz}\rangle^+$) shear stresses. $\cdots\cdots$, Newtonian (case N); $-\cdot-$, $64 \times 64 \times 65$ resolution in $\frac{80\pi}{27}h \times \frac{8\pi}{5}h \times 2h$ channel; $---$, $128 \times 128 \times 129$ resolution in $\frac{80\pi}{27}h \times \frac{8\pi}{5}h \times 2h$ channel; ——, $256 \times 256 \times 257$ resolution in $\frac{80\pi}{27}h \times \frac{8\pi}{5}h \times 2h$ channel.

obtained at viscoelastic steady-state with various mesh resolutions. Here and throughout this manuscript, the + superscript denotes normalization of the variables using the wall-friction velocity, u_τ, and the wall shear viscosity, $\nu_w = \langle \frac{\tau_w}{\rho(dU/dz)_w} \rangle$, of the polymer solution (Ptasinski, *et al.*, 2003), and $\langle \cdot \rangle$ denotes an ensemble-average over the homogeneous flow directions and time. The value of the wall shear viscosity, ν_w, was found to be within 1.5% of the zero-shear viscosity, ν_o, in all the simulations performed in this study. The average skin friction coefficients obtained with both $128 \times 128 \times 129$ and $256 \times 256 \times 257$ mesh resolutions are $\langle C_f \rangle = 5.42 \times 10^{-3}$ $(32.5\%DR)$, while that obtained with the $64 \times 64 \times 65$ mesh resolution was $\langle C_f \rangle = 5.77 \times 10^{-3}$ $(28.1\%DR)$. The flow statistics, including the mean velocity profile (figure 2.5b), turbulence intensities (figure 2.5c), and Reynolds and polymer shear stresses (figure 2.5d), are nearly identical with both $128 \times 128 \times 129$ and $256 \times 256 \times 257$ mesh resolutions. However the results with the $64 \times 64 \times 65$ mesh resolution are somewhat off. All these results confirm the convergence of the scheme with mesh refinement with $128 \times 128 \times 129$ and $256 \times 256 \times 257$ mesh resolutions. In contrast, the results indicate the inadequacy of the $64 \times 64 \times 65$ mesh resolutions for the present study.

We next compare the results obtained with two different time-step size of $\Delta\tilde{t} = 0.1\Delta x/U_o$ and $\Delta\tilde{t} = 0.05\Delta x/U_o$ to investigate the convergence with time-step size refinement. Figure 2.6 shows a comparison of the results obtained with these two time-step size in the $\frac{80\pi}{27}h \times \frac{8\pi}{5}h \times 2h$ channel with $128 \times 128 \times 129$ mesh resolution. As before, simulations were performed with quadratic interpolation scheme at $We_{\tau_b} \approx 35$, $n_p k_B T/(\rho u_{\tau_b}^2) \approx 1 \times 10^{-3}$ and $b = 45,000$. The case with $\Delta\tilde{t} = 0.1\Delta x/U_o$ corresponds to the case with $128 \times 128 \times 129$ mesh resolution in figure 2.5. An average skin friction

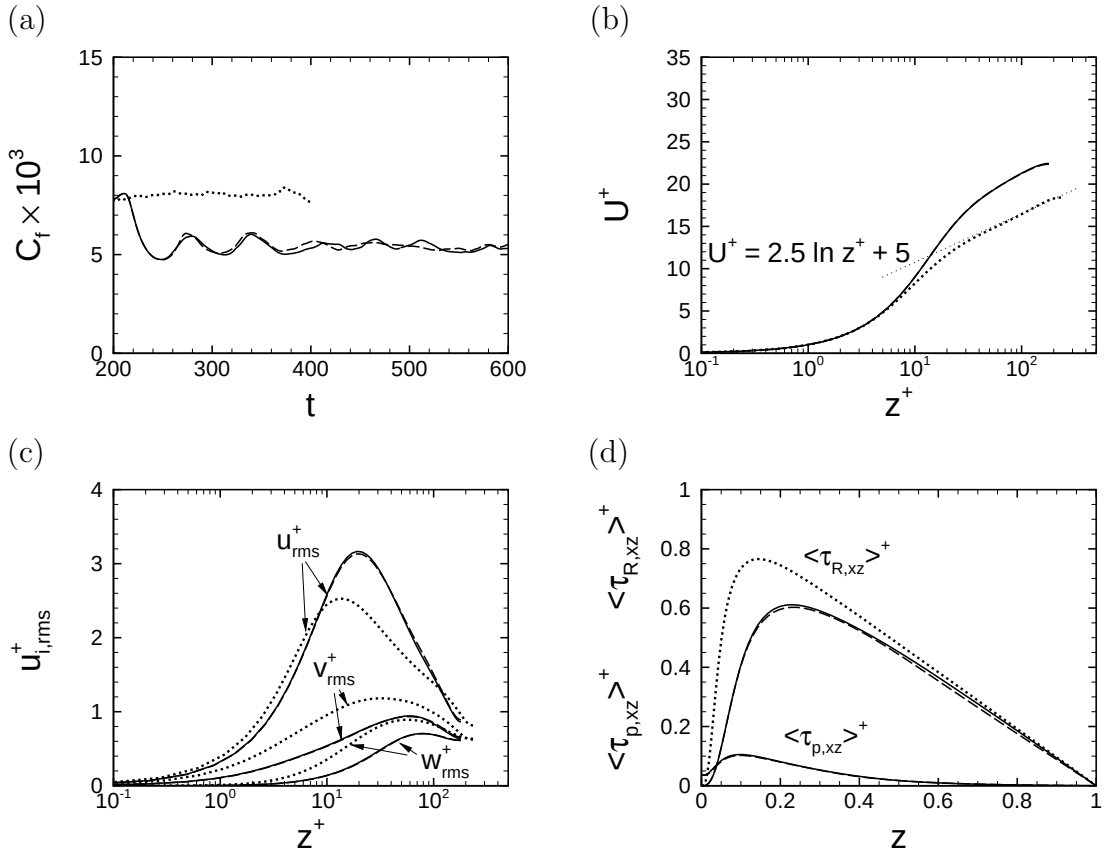

Figure 2.6: Effect of time-step size at $We_{\tau_b} \approx 35$, $n_p k_B T/(\rho u^2_{\tau_b}) \approx 1 \times 10^{-3}$, $b = 45,000$ on (a) time evolution of the skin friction coefficient; (b) mean velocity profiles; (c) r.m.s. of velocity fluctuations; (d) Reynolds ($\langle\tau_{R,xz}\rangle^+$) and polymer ($\langle\tau_{p,xz}\rangle^+$) shear stresses. $\cdots\cdots$, Newtonian (case N); $---$, $\Delta t^* = 0.1\Delta x/U_o$; ——, $\Delta t^* = 0.05\Delta x/U_o$.

coefficient of $\langle C_f \rangle = 5.41 \times 10^{-3}$ $(32.6\%DR)$ is obtained with $\Delta\tilde{t} = 0.05\Delta x/U_o$, which is very close to the average skin friction coefficient of $\langle C_f \rangle = 5.42 \times 10^{-3}$ $(32.5\%DR)$ with $\Delta\tilde{t} = 0.1\Delta x/U_o$. All turbulence statistics (figures 2.6b, 2.6c & 2.6d) show good agreement in these two cases, confirming the convergence of the scheme with time-step size refinement.

2.4.2 Effect of interpolation scheme and comparison to conventional Eulerian schemes

To assess the effect of linear versus quadratic interpolation in the mixed Eulerian-Lagrangian scheme, the predictions obtained with these schemes were compared to each other and to those obtained with conventional Eulerian schemes (Sureshkumar, Beris & Handler, 1997).

In conventional Eulerian scheme, the hydrodynamics is computed using the same methods as those described in § 2.2.1, but the polymer dynamics is computed in an Eulerian framework using

$$\frac{\partial \mathbf{A}}{\partial t} + (\mathbf{v}\cdot\nabla)\mathbf{A} = (\nabla\mathbf{v})^T\cdot\mathbf{A} + \mathbf{A}\cdot(\nabla\mathbf{v}) - \frac{1}{We}\left(\frac{\mathbf{A}}{1-\mathrm{Tr}(\mathbf{A})/b} - \mathbf{I}\right) + \frac{\chi}{U_0 h}\nabla^2\mathbf{A}, \quad (2.19)$$

where all variables have been non-dimensionalized as in equation (2.3) and χ denotes an artificial stress diffusivity which needs to be introduced to keep the computations numerically stable (Sureshkumar, Beris & Handler, 1997). Equation (2.19) is integrated in time using a fractional step method. In the first fractional step, the non-linear terms are advanced using a second-order Adams-Bashforth scheme

$$\frac{\mathbf{A}^{*(n+1)} - \mathbf{A}^{(n)}}{\Delta t} = [\frac{3}{2}\mathcal{F}^{(n)} - \frac{1}{2}\mathcal{F}^{(n-1)}], \quad (2.20)$$

where $\mathcal{F} = -(\mathbf{v}\cdot\nabla)\mathbf{A} + (\nabla\mathbf{v})^T\cdot\mathbf{A} + \mathbf{A}\cdot(\nabla\mathbf{v}) - \frac{1}{We}\left(\frac{\mathbf{A}}{1-\mathrm{Tr}(\mathbf{A})/b} - \mathbf{I}\right)$. In the second fractional step, the artificial stress diffusivity term is incorporated into the solution using a second-order Adams-Moulton (Crank-Nicolson) scheme

$$\frac{\mathbf{A}^{(n+1)} - \mathbf{A}^{*(n+1)}}{\Delta t} = \frac{\chi}{U_0 h}\nabla^2\left(\frac{\mathbf{A}^{(n+1)} + \mathbf{A}^{(n)}}{2}\right). \tag{2.21}$$

The magnitude of the artificial stress diffusivity was set to the lowest value for which the computations remained stable, which by trial and error was found to be $\chi/\nu_s = 2$. While this choice of χ ensures the stability of the simulations, the required positive-definiteness of the polymer conformation tensor is violated in a small fraction (less than 1.5%) of the points within the domain during the course of the simulation. The simulations were allowed to proceed in spite of these unphysical points, because the points occur randomly in space and time and self-correct at later times. One can, of course, entirely eliminate these unphysical points by using a larger χ. However, a larger χ diminishes the magnitude of drag reduction which can be predicted in the simulation.

Comparisons of the different numerical schemes were performed at two Weissenberg numbers corresponding to We_{τ_b} of 35 and 100 or $We = \lambda U_o/h$ of 3.64 and 10.40. The simulations were performed in a channel of size $\frac{80\pi}{27}h \times \frac{8\pi}{5}h \times 2h$ with a resolution of $128\times128\times129$. The polymer extensibility parameter was set to $b = 45,000$, and the polymer number density to $n_p k_B T/(\rho u_{\tau_b}^2) \approx 1\times10^{-3}$ in all the simulations. A summary of the simulation parameters employed in these computations is provided in table 2.1.

Figure 2.7 shows the predictions of different numerical schemes for the time evolu-

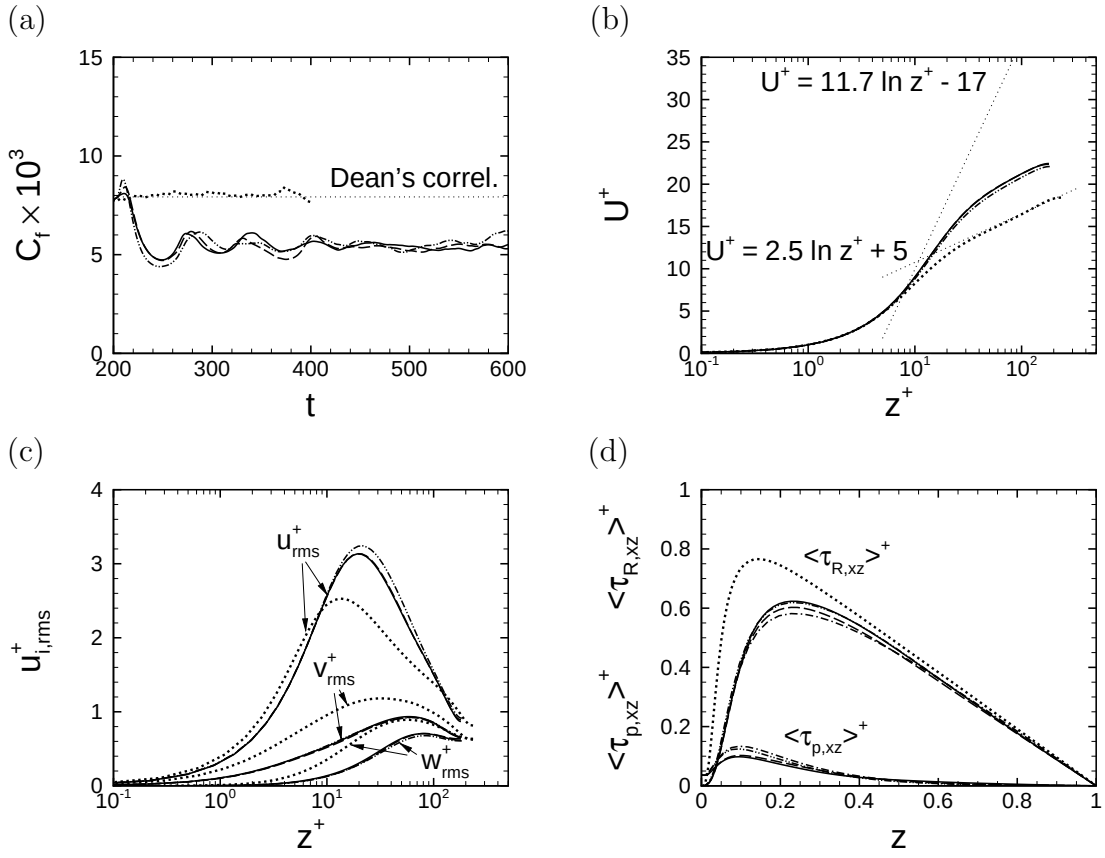

Figure 2.7: Effect of numerical scheme on the predicted flow statistics at $We_{\tau_b} \approx 35$: (a) time evolution of the skin friction coefficient; (b) mean velocity profiles; (c) turbulence intensities; (d) Reynolds shear stresses and polymer stresses. $\cdots\cdots$, Newtonian (case N); $- - -$, mixed Eulerian-Lagrangian scheme with linear interpolation (case C3-l); ——, mixed Eulerian-Lagrangian scheme with quadratic interpolation (case C3-q); $- \cdot\cdot -$, Eulerian scheme (case C3-e).

tion of the skin friction coefficient, C_f, and the turbulence and polymer statistics in the fully-developed state of the viscoelastic flow at $We_{\tau_b} \approx 35$. The average skin friction coefficient predicted for the base Newtonian turbulent flow was $\langle C_f \rangle = 8.03 \times 10^{-3}$, which is within 1.5% of the value 7.92×10^{-3} predicted by Dean's correlation. In the fully-developed viscoelastic turbulent flow, the mixed Eulerian-Lagrangian scheme predicts average skin friction coefficients of $\langle C_f \rangle = 5.42 \times 10^{-3}$ $(32.5\%DR)$ and $\langle C_f \rangle = 5.41 \times 10^{-3}$ $(32.6\%DR)$ with quadratic and linear interpolation, respectively. The close correspondence between the $\langle C_f \rangle$ values predicted by these two schemes indicates the negligible magnitude of the artificial stress diffusivity in the linear interpolation scheme at this Weissenberg number. In contrast, the Eulerian scheme predicts an average skin friction coefficient of $\langle C_f \rangle = 5.60 \times 10^{-3}$ $(30.3\%DR)$, reflecting the higher artificial stress diffusivity in this scheme. The mixed Eulerian-Lagrangian scheme predicts nearly identical flow statistics (figures 2.7b, 2.7c & 2.7d) with both linear and quadratic interpolation at this Weissenberg number. In comparison, the Eulerian scheme predicts a slightly lower mean velocity in the logarithmic layer (figure 2.7b), a slightly higher peak of the streamwise turbulence intensity (figure 2.7c), and a slightly higher peak of Reynolds shear stress (figure 2.7d) compared to the mixed Eulerian-Lagrangian scheme, which is consistent with the lower magnitude of drag reduction in the Eulerian scheme. Furthermore, the Eulerian scheme predicts a more flat distribution of $\tau_{p,yy}$ and $\tau_{p,zz}$ compared to the mixed Eulerian-Lagrangian schemes due to its higher artificial stress diffusivity, as shown in figure 2.7(d).

Figure 2.8 shows the flow statistics predicted by the different numerical schemes at $We_{\tau_b} \approx 100$. At this Weissenberg number, the mixed Eulerian-Lagrangian scheme

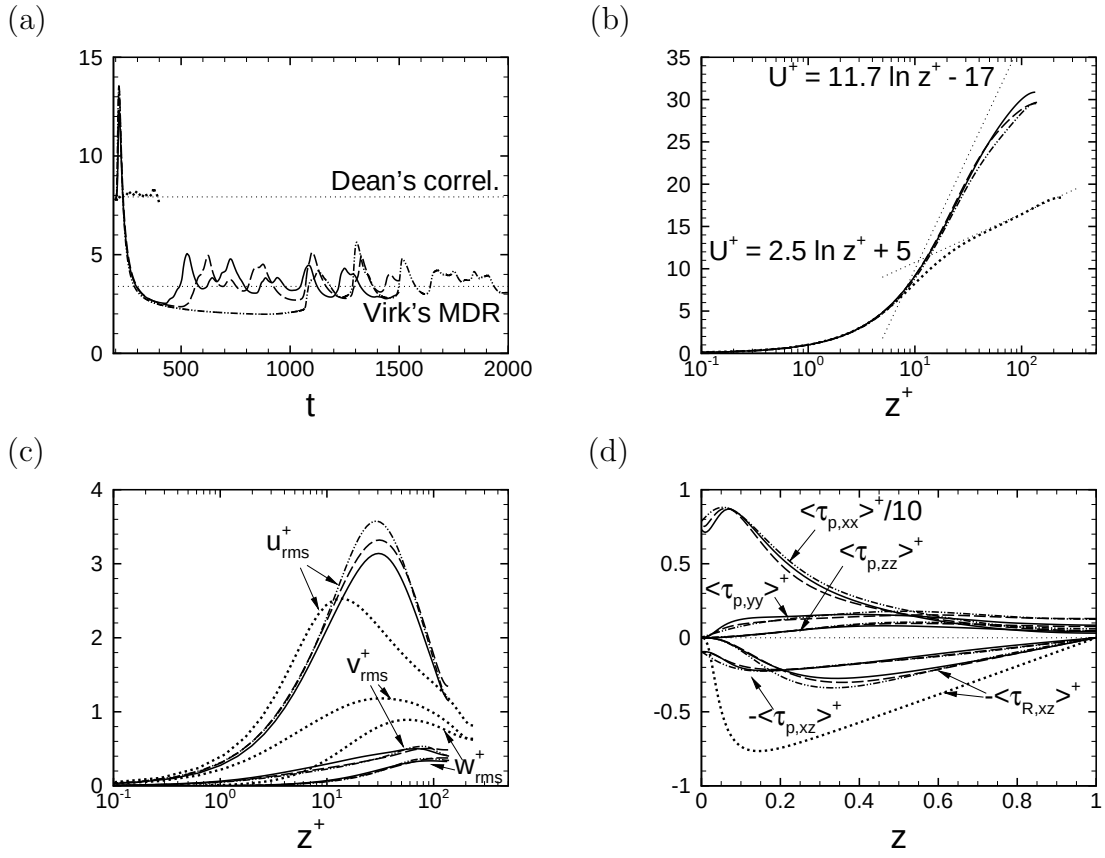

Figure 2.8: Effect of numerical scheme on the predicted flow statistics at $We_{\tau_b} \approx 100$: (a) time evolution of the skin friction coefficient; (b) mean velocity profiles; (c) turbulence intensities; (d) Reynolds shear stresses and polymer stresses. $\cdots\cdots$, Newtonian (case N); $---$, mixed Eulerian-Lagrangian scheme with linear interpolation (case E3-l); ——, mixed Eulerian-Lagrangian scheme with quadratic interpolation (case E3-q); $-\cdots-$, Eulerian scheme (case E3-e).

predicts average skin friction coefficients of $\langle C_f \rangle = 3.40 \times 10^{-3}$ ($57.7\%DR$) and $\langle C_f \rangle = 3.52 \times 10^{-3}$ ($56.2\%DR$) with quadratic and linear interpolation, respectively, while the Eulerian scheme predicts a $\langle C_f \rangle = 3.66 \times 10^{-3}$ ($54.4\%DR$). These results indicate that with increasing Weissenberg number, the magnitude of the artificial stress diffusivity introduced by the linear interpolation scheme becomes more pronounced. However, it remains below that in simulations with traditional Eulerian schemes. The trends in the predictions of the different numerical scheme for the mean velocity profile (figure 2.8b), the streamwise turbulence intensity (figure 2.8c) and the Reynolds shear stress (figure 2.8d) are consistent with the magnitude of drag reduction by each numerical scheme. For the polymer stresses (figure 2.8d), the Eulerian and linear interpolation schemes predict a more flat distribution of the polymer stresses compared to quadratic interpolation due to their higher artificial stress diffusivities.

Figure 2.9 shows the one-dimensional energy spectra obtained by different numerical schemes at $z^+ = 30$, where $k_d = 1/\eta = (\nu^3/\varepsilon)^{-1/4}$ denotes the Kolmogorov wavenumber. The energy spectra obtained using Eulerian scheme at all Weissenberg numbers are the highest, reflecting the lowest magnitude of drag reduction due to its artificial stress diffusivity. The energy spectra obtained using mixed Eulerian-Lagrangian scheme with quadratic and linear interpolation at $We_{\tau_b} \approx 35$ are nearly identical. However, the energy spectra obtained using linear interpolation scheme at $We_{\tau_b} \approx 100$ are slightly different in the large scales but significantly larger in the small scales compared to those obtained using quadratic interpolation scheme, reflecting the presence of small artificial stress diffusivity. These results show that linear interpolation scheme can be used for $We_{\tau_b} \lesssim 35$.

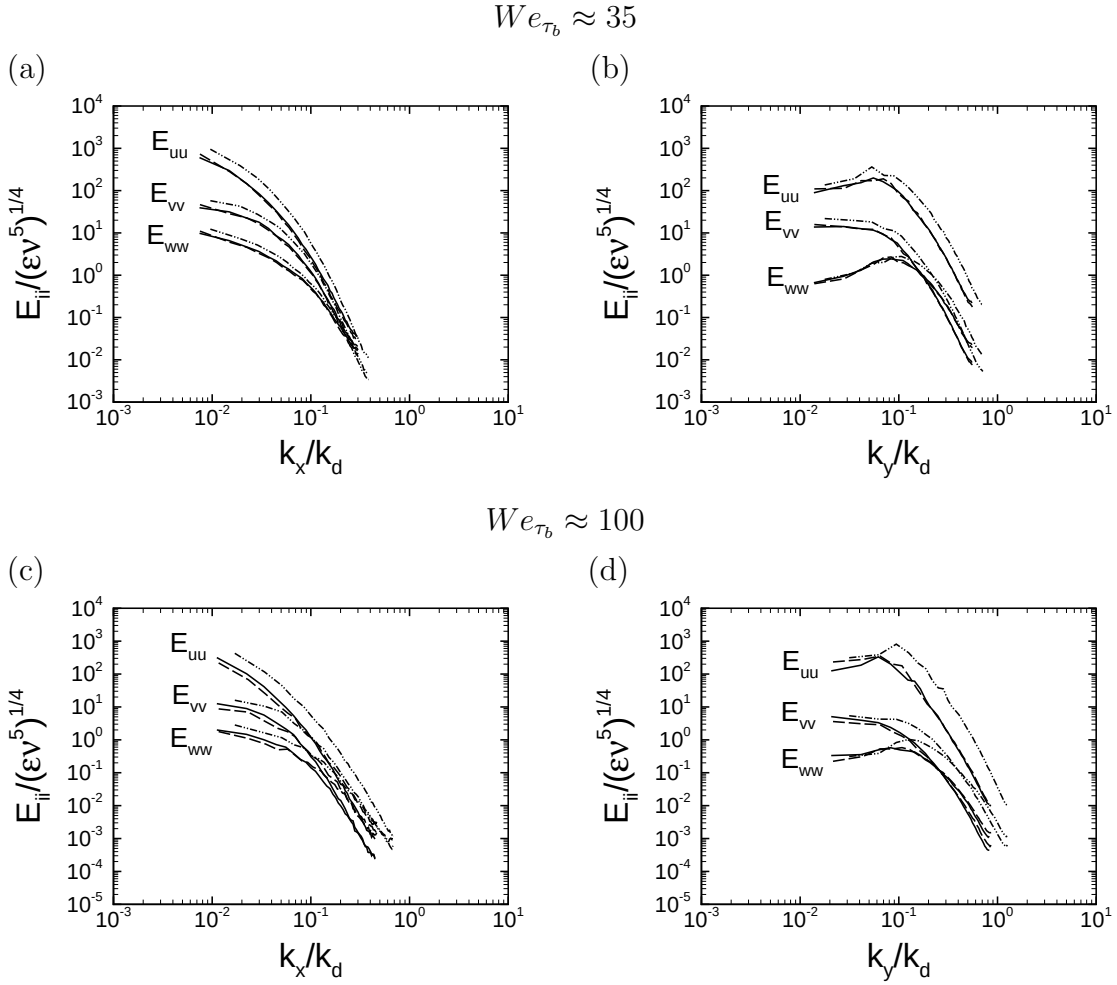

Figure 2.9: Effect of numerical scheme on the predicted one-dimensional energy spectra at (a-b) $We_{\tau_b} \approx 35$ and (c-d) $We_{\tau_b} \approx 100$: (a), (c) streamwise spectra at $z^+ \approx 30$; (b), (d) spanwise spectra at $z^+ \approx 30$. (a-b) Line types same as in figure 2.7. (c-d) Line types same as in figure 2.8.

2.4.3 Effect of domain size

We next investigate the effect of domain size on the predicted flow statistics. Figures 2.10, 2.11 and 2.12 show the flow statistics predicted by the mixed Eulerian-Lagrangian scheme with quadratic interpolation in the large ($\frac{320\pi}{27}h \times \frac{16\pi}{5}h \times 2h$ with a resolution of $512 \times 256 \times 129$) and small ($\frac{80\pi}{27}h \times \frac{8\pi}{5}h \times 2h$ with a resolution of $128 \times 128 \times 129$) channels at $We_{\tau_b} \approx 35$, 100 and 150, respectively. In Newtonian flow (figure 2.10 & table 2.1), the large channel predicts a $\langle C_f \rangle = 8.01 \times 10^{-3}$, which is within 0.3% of the value of $\langle C_f \rangle = 8.03 \times 10^{-3}$ predicted in the small channel. In viscoelastic flow at $We_{\tau_b} \approx 35$ (figure 2.10 & table 2.1), the large channel predicts a $\langle C_f \rangle = 5.38 \times 10^{-3}$, which is within 0.7% of the value of $\langle C_f \rangle = 5.42 \times 10^{-3}$ predicted in the small channel. In viscoelastic flow at $We_{\tau_b} \approx 100$ (figure 2.11 & table 2.1), the small channel predicts a $\langle C_f \rangle = 3.40 \times 10^{-3}$, which is $\sim 7.5\%$ larger than the value of $\langle C_f \rangle = 3.67 \times 10^{-3}$ predicted in the large channel. At $We_{\tau_b} \approx 150$ (figure 2.12 & table 2.1), however, the simulations in the small channel give dramatically different results compared to the large channel. The flow in the small channel relaminarizes, as shown in figure 2.12, which predicts a drag reduction of 74.6%. Instead, the simulations predict a drag reduction of $55.2\%DR$ in the large channel, which is close to Virk's MDR value of $55.7\%DR$. The large and small channels predict nearly identical flow statistics in Newtonian flow and at $We_{\tau_b} \approx 35$ (figures 2.10b, 2.10c & 2.10d), while the flow statistics at $We_{\tau_b} \approx 100$ reflect the 3.5% difference in magnitude of drag reduction between the two channels (figures 2.11b, 2.11c & 2.11d). At $We_{\tau_b} \approx 150$, the mean velocity profile in the large channel begins to approach Virk's MDR, $U^+ =$

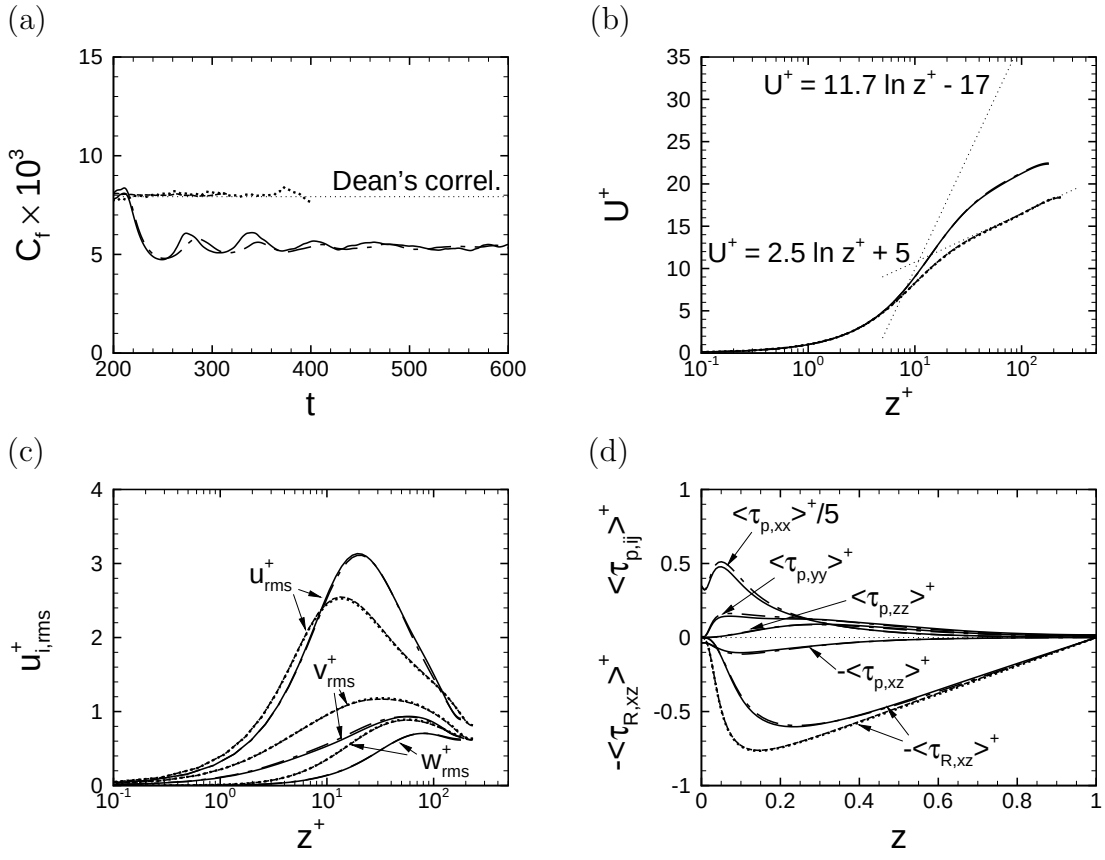

Figure 2.10: Effect of domain size on the predicted flow statistics at $We_{\tau_b} \approx 35$: (a) time evolution of the skin friction coefficient; (b) mean velocity profiles; (c) turbulence intensities; (d) Reynolds shear stresses and polymer stresses. ·····, Newtonian in small domain (case N); ---, Newtonian in large domain (case NN); ——, mixed Eulerian-Lagrangian scheme with quadratic interpolation in small domain (case C3-q); ——·——, mixed Eulerian-Lagrangian scheme with quadratic interpolation in large domain (case CC3-q).

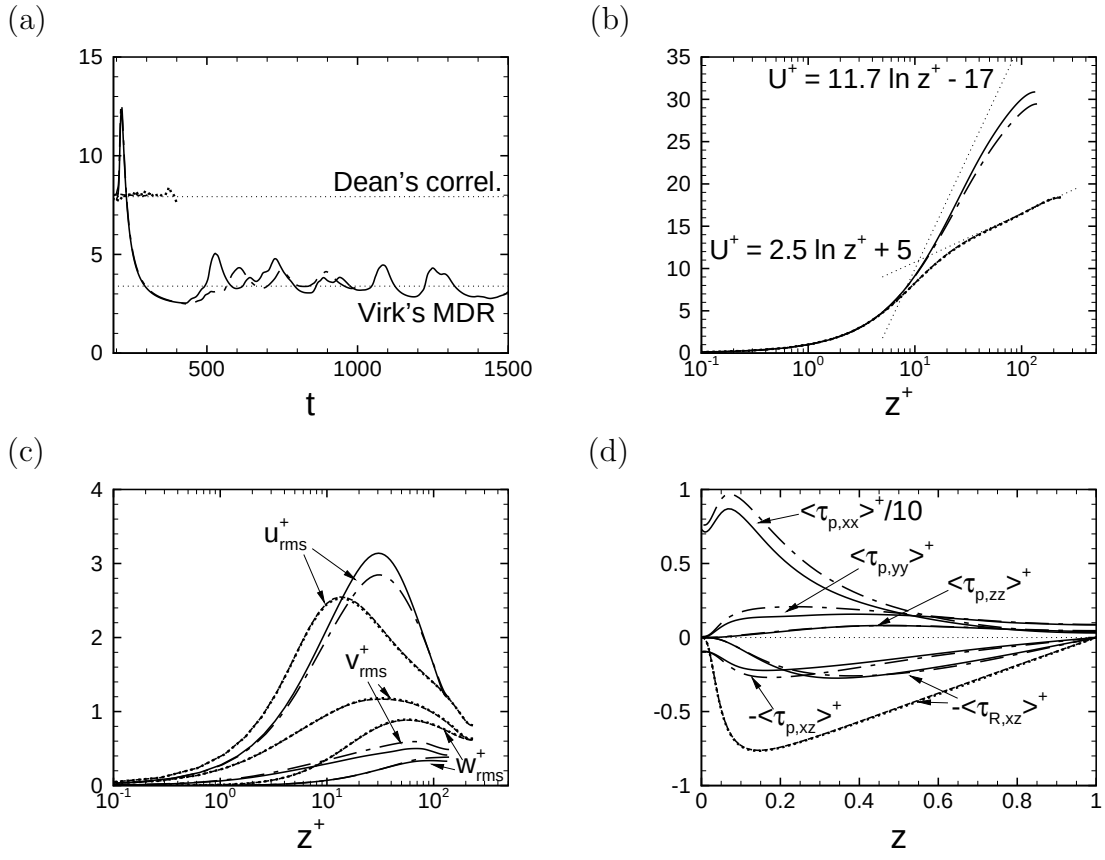

Figure 2.11: Effect of domain size on the predicted flow statistics at $We_{\tau_b} \approx 100$: (a) time evolution of the skin friction coefficient; (b) mean velocity profiles; (c) turbulence intensities; (d) Reynolds shear stresses and polymer stresses. $\cdots\cdots$, Newtonian in small domain (case N); ---, Newtonian in large domain (case NN); ——, mixed Eulerian-Lagrangian scheme with quadratic interpolation in small domain (case E3-q); ——$\cdot$——, mixed Eulerian-Lagrangian scheme with quadratic interpolation in large domain (case EE3-q).

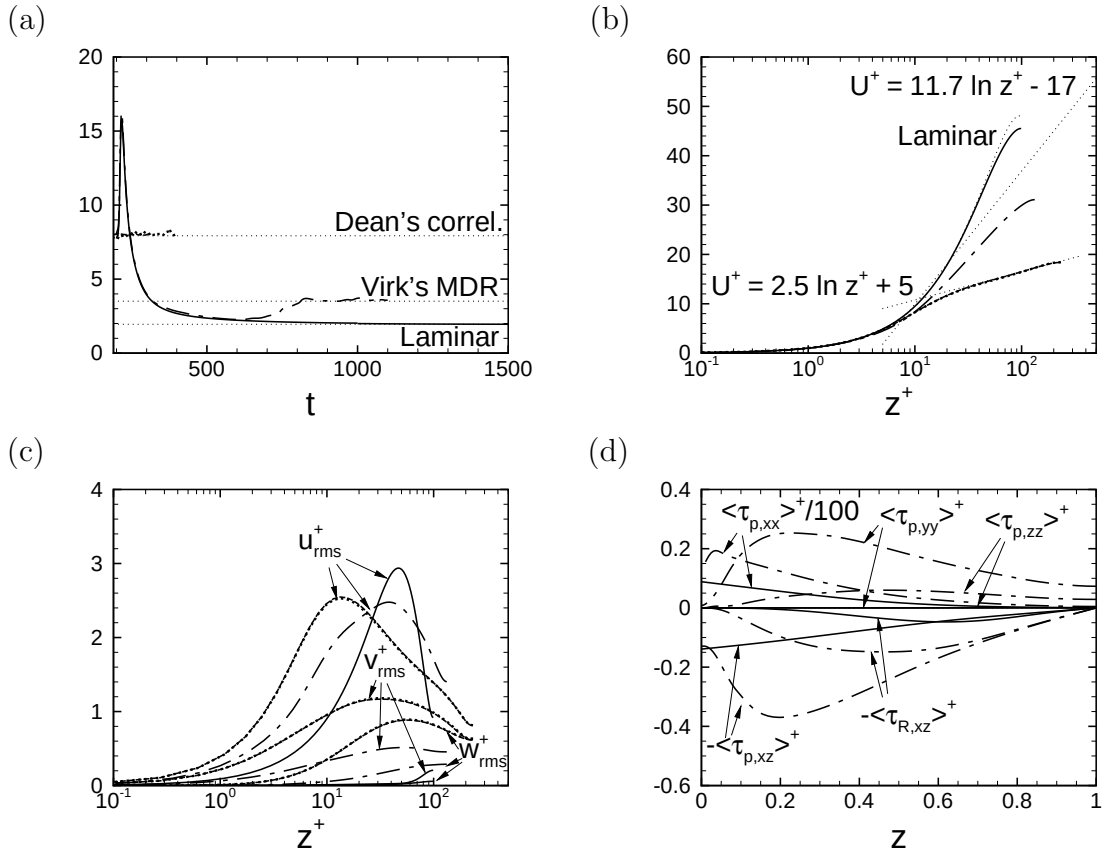

Figure 2.12: Effect of domain size on the predicted flow statistics at $We_{\tau_b} \approx 150$: (a) time evolution of the skin friction coefficient; (b) mean velocity profiles; (c) turbulence intensities; (d) Reynolds shear stresses and polymer stresses. ·····, Newtonian in small domain (case N); ---, Newtonian in large domain (case NN); ——, mixed Eulerian-Lagrangian scheme with quadratic interpolation in small domain (case F3-q); ——·——, mixed Eulerian-Lagrangian scheme with quadratic interpolation in large domain (case FF3-q).

$11.7 \ln z^+ - 17$ (Virk *et al.*1970), and its second-order turbulence statistics show trends consistent with those reported at MDR in experiments (Ptasinski, *et al.*, 2001), as shown in figures 2.12(b-d).

Figures 2.13 and 2.14 shows the one-dimensional energy spectra predicted using the mixed Eulerian-Lagrangian scheme with quadratic interpolation in the large channel compared to those in the small channel at $z^+ = 30$. The energy spectra obtained in Newtonian flow and at $We_{\tau_b} \approx 35$ in both channels are nearly identical. However, those obtained at $We_{\tau_b} \approx 100$ in the large scales are slightly higher in the large channel compared to those in the small channel, reflecting the smaller magnitude of drag reduction in the large channel. The energy spectra obtained in the small channel at $We_{\tau_b} \approx 150$ are significantly lower than those in the large channel, reflecting the relaminarization in the small channel. However, the energy spectra in the large channel at $We_{\tau_b} \approx 150$ are similar to those observed at $We_{\tau_b} \approx 100$, reflecting the similar amount of drag reduction at both Weissenberg numbers.

Figures 2.15 and 2.16 show the streamwise and spanwise two-point correlations of the turbulent velocity fluctuations obtained using mixed Eulerian-Lagrangian scheme with quadratic interpolation in the small and large channels at $z^+ = 30$. In Newtonian flow, the two-point correlations become uncorrelated at a separation of one-half the domain size in both the streamwise and spanwise directions for both channel sizes, indicating the adequacy of both domain sizes in Newtonian flow. In viscoelastic flow, the large channel shows uncorrelated statistics in both directions at all Weissenberg numbers, indicating the adequacy of this domain size at all Weissenberg numbers. In the small channel, the streamwise velocity fluctuations remain correlated in the

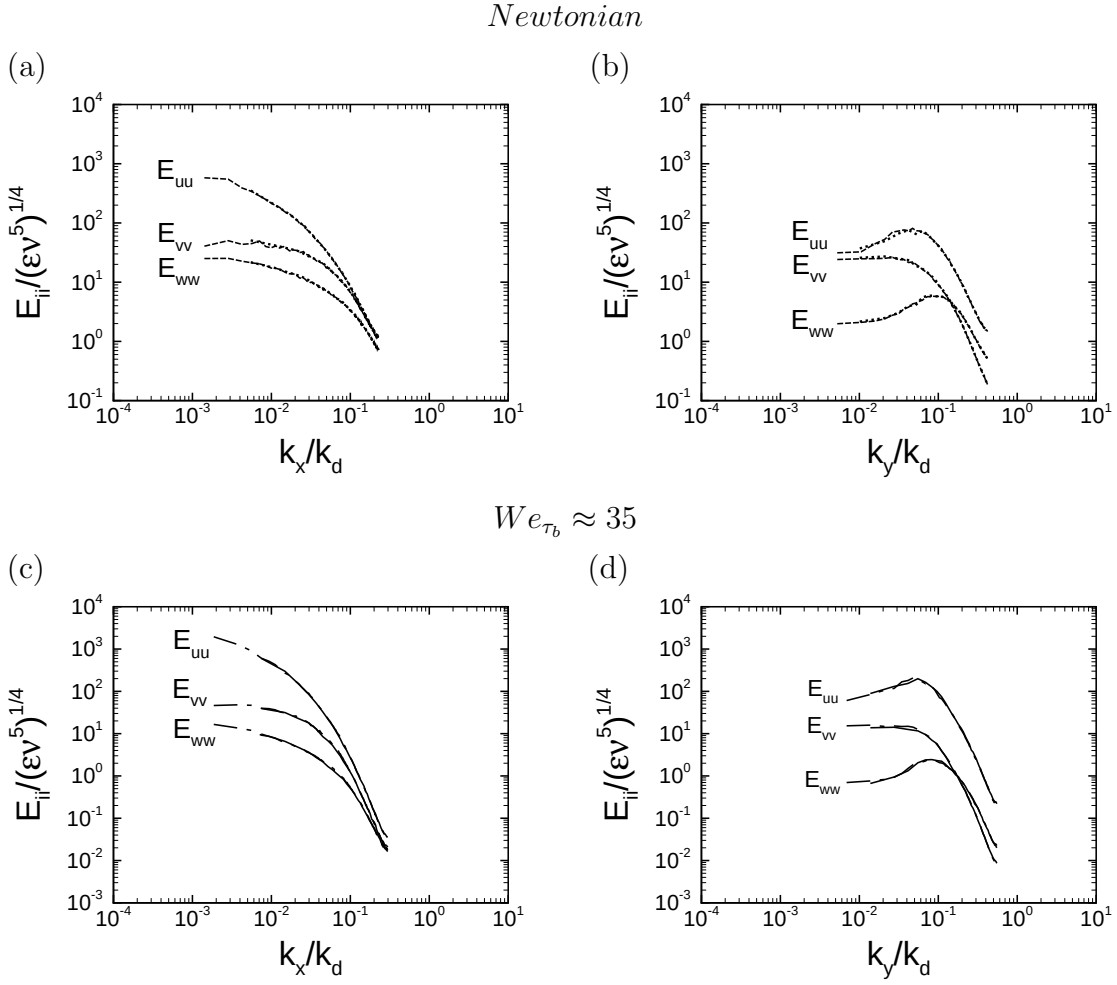

Figure 2.13: Effect of domain size on the predicted one-dimensional energy spectra in (a-b) Newtonian flow and (c-d) viscoelastic flow at $We_{\tau_b} \approx 35$: (a), (c) streamwise spectra at $z^+ \approx 30$; (b), (d) spanwise spectra at $z^+ \approx 30$. Line types same as in figure 2.10.

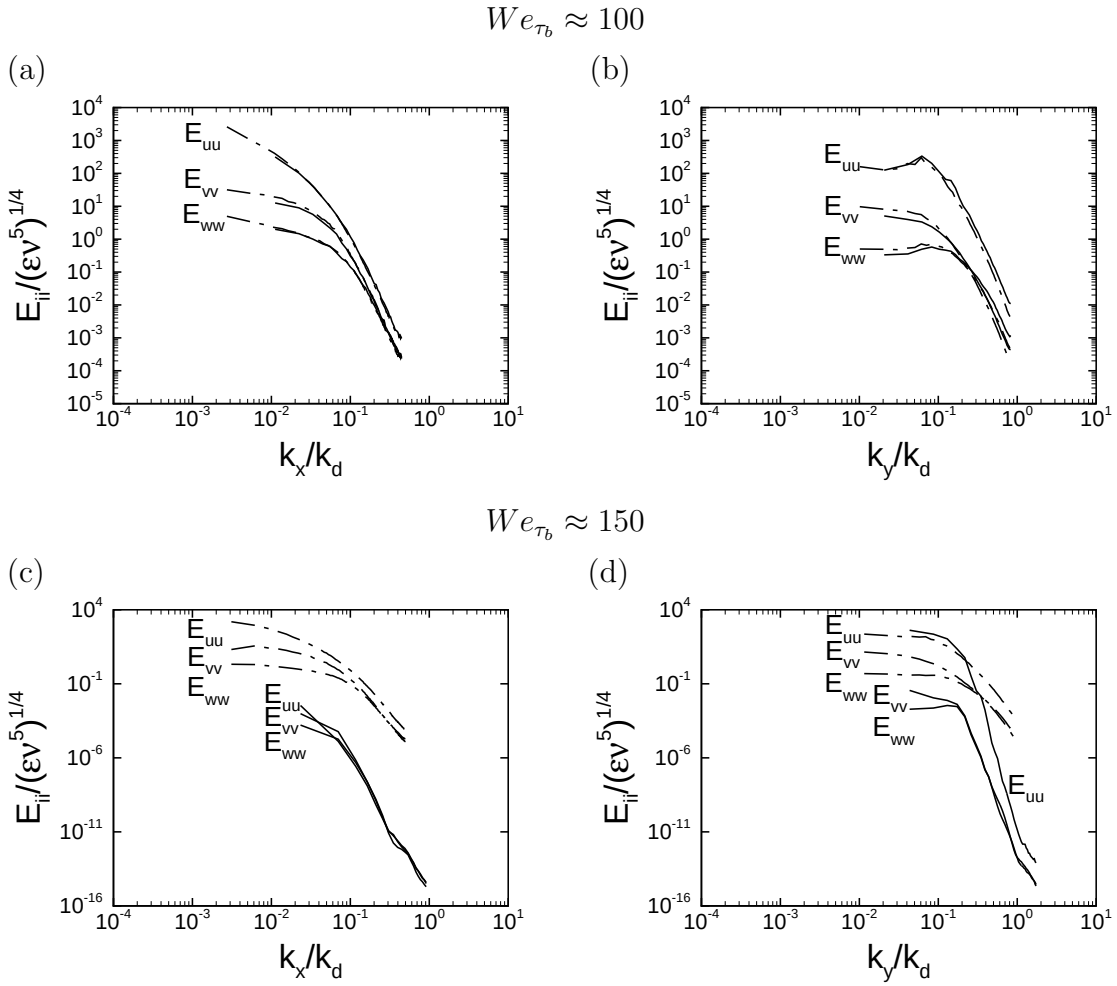

Figure 2.14: Effect of domain size on the predicted one-dimensional energy spectra in (a-b) viscoelastic flow at $We_{\tau_b} \approx 100$ and (c-d) $We_{\tau_b} \approx 150$: (a), (c) streamwise spectra at $z^+ \approx 30$; (b), (d) spanwise spectra at $z^+ \approx 30$. (a-b) Line types same as in figure 2.11. (c-d) Line types same as in figure 2.12.

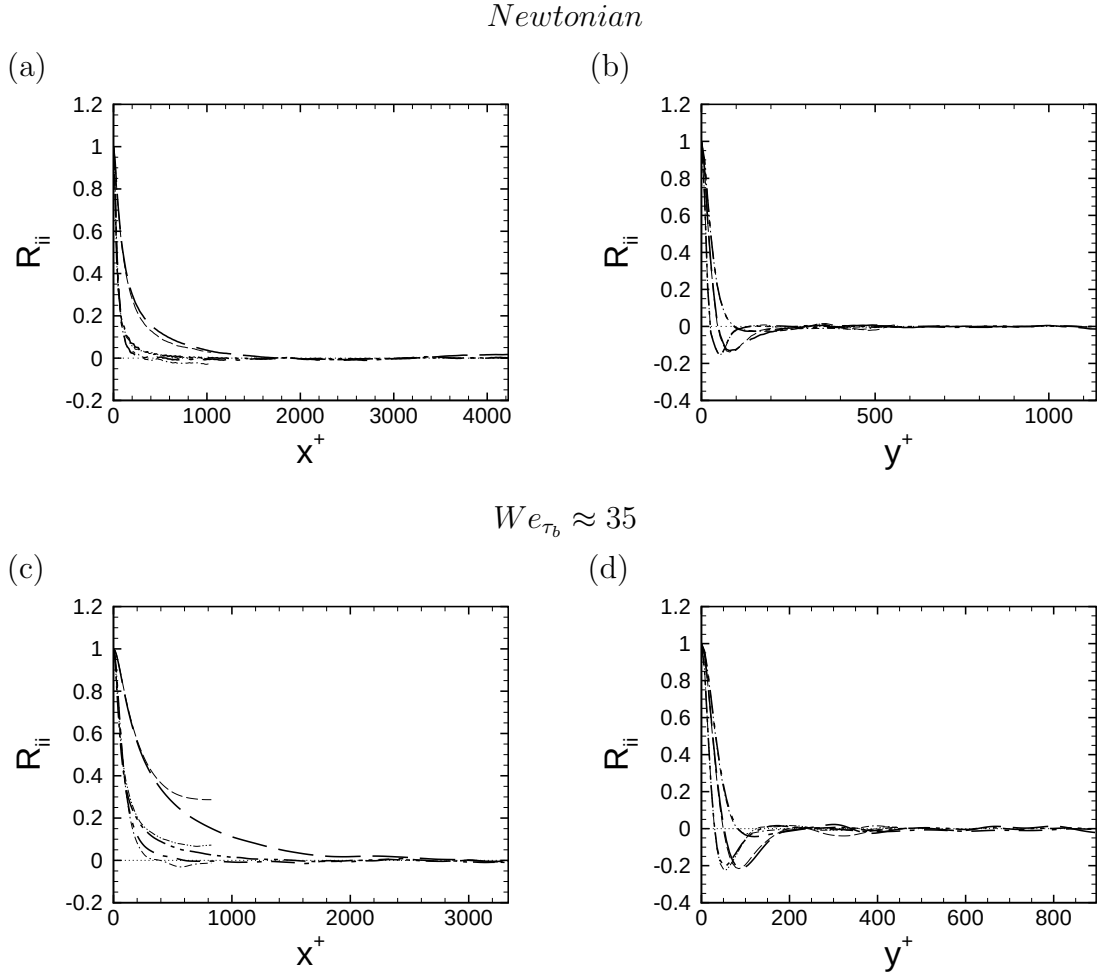

Figure 2.15: Effect of domain size on the predicted two-point correlations in (a-b) Newtonian flow and (c-d) viscoelastic flow at $We_{\tau_b} \approx 35$: (a), (c) streamwise correlations at $z^+ \approx 30$; (b), (d) spanwise correlations $z^+ \approx 30$. – – –, R_{uu} in small domain; —— ——, R_{uu} in large domain; – · –, R_{vv} in small domain; —— · ——, R_{vv} in large domain; – ·· –, R_{ww} in small domain; —— ·· ——, R_{ww} in large domain.

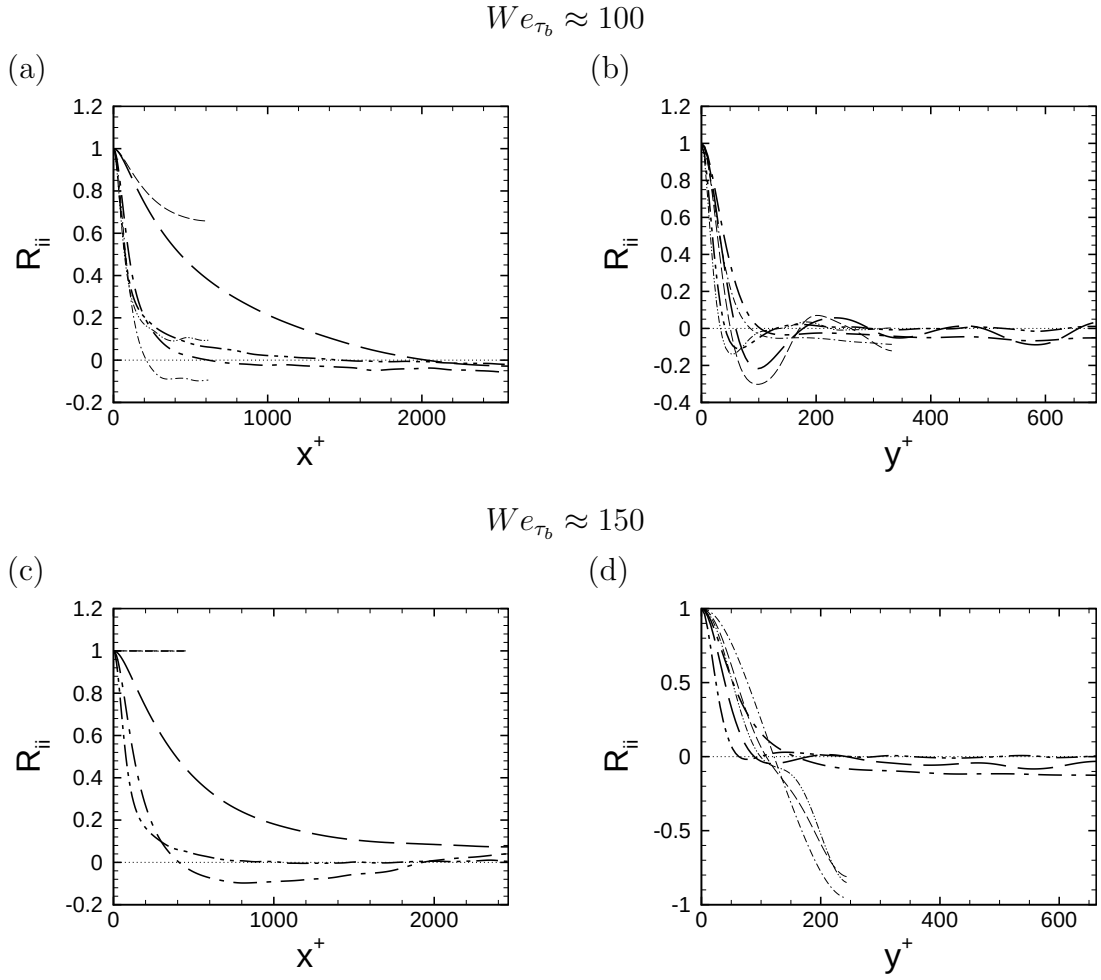

Figure 2.16: Effect of domain size on the predicted two-point correlations in (a-b) viscoelastic flow at $We_{\tau_b} \approx 100$ and (c-d) $We_{\tau_b} \approx 150$: (a), (c) streamwise correlations at $z^+ \approx 30$; (b), (d) spanwise correlations $z^+ \approx 30$. – – –, R_{uu} in small domain; —— ——, R_{uu} in large domain; – · –, R_{vv} in small domain; —— · ——, R_{vv} in large domain; – ·· –, R_{ww} in small domain; —— ·· ——, R_{ww} in large domain.

streamwise direction at all Weissenberg numbers. However, the other statistics show good agreement with the large channel up to $We_{\tau_b} \approx 35$. At $We_{\tau_b} \gtrsim 100$, all two-point correlations remain correlated in both the streamwise and spanwise directions. These results show the inadequacy of the small domain size at drag reductions greater than $\sim 35\%$.

2.5 Assessment of the mixed Eulerian-Lagrangian scheme

Overall, the results presented in this section demonstrate the accuracy and efficiency of mixed Eulerian-Lagrangian scheme. The main advantages of the mixed Eulerian-Lagrangian scheme compared to traditional Eulerian schemes are (i) cost, (ii) the ability to perform the computations with less artificial stress diffusivity, and (iii) the ability to reach Weissenberg numbers and polymer extensibility parameters inaccessible to traditional Eulerian schemes. The mixed Eulerian-Lagrangian scheme with linear and quadratic interpolation incurs a computational cost per time step which is 42% and 75% of the Eulerian scheme, respectively. In addition, computations can be performed with twice as large a time-step size with the mixed Eulerian-Lagrangian scheme compared to traditional Eulerian schemes. This makes the overall cost of the computations with the mixed Eulerian-Lagrangian scheme with linear interpolation 21% of that associated with Eulerian schemes, and the overall cost of the mixed Eulerian-Lagrangian scheme with quadratic interpolation 38% of that associated with Eulerian schemes.

In view of the results in the previous sections, simulations at $We_{\tau_b} \gtrsim 35$ were performed using the mixed Eulerian-Lagrangian scheme with quadratic interpolation.

However, given the close correspondence between the statistics predicted by the linear and quadratic interpolation schemes at $We_{\tau_b} \lesssim 35$, simulations at $We_{\tau_b} \lesssim 35$ were performed using the mixed Eulerian-Lagrangian scheme with linear interpolation to take the advantage of less computational cost in the small channel. Simulations with $DR \gtrsim 35\%$ were performed in the large channel. Once again, simulations with $DR \lesssim 35\%$ were performed in the small channel because the computational cost is significantly less than those with the large channel, while the statistics predicted in both channels are near identical.

Chapter III

Flow statistics

Increasing the polymer concentration and the polymer molecular weight, which relates to the polymer relaxation time and extensibility parameter both, are the most common method for enhancing drag reduction in experimental settings. In this chapter, we present the isolated effect of concentration (or polymer number density), Weissenberg number (or polymer relaxation time), and polymer extensibility parameter on the flow statistics.

3.1 Effect of polymer concentration on the flow statistics

To investigate the effect of polymer concentration on flow statistics, four sets of direct numerical simulations were preformed: (i) at $We_{\tau_b} \approx 10$ for $1 \times 10^{-7} \lesssim n_p k_B T/(\rho u_{\tau_b}^2) \lesssim 1 \times 10^{-2}$ ($0.9 \lesssim \beta \lesssim 0.9999989$), (ii) at $We_{\tau_b} \approx 35$ for $1 \times 10^{-9} \lesssim n_p k_B T/(\rho u_{\tau_b}^2) \lesssim 1 \times 10^{-2}$ ($0.72 \lesssim \beta \lesssim 0.99999996$), (iii) at $We_{\tau_b} \approx 100$ for $1 \times 10^{-10} \lesssim n_p k_B T/(\rho u_{\tau_b}^2) \lesssim 1 \times 10^{-3}$ ($0.9 \lesssim \beta \lesssim 0.999999989$), and (iv) at $We_{\tau_b} \approx 150$ for $1 \times 10^{-10} \lesssim n_p k_B T/(\rho u_{\tau_b}^2) \lesssim 1 \times 10^{-3}$ ($0.86 \lesssim \beta \lesssim 0.99999998$). The polymer extensibility parameter was kept fixed at $b = 45,000$ in all the simulations. The full range of drag reduction from onset to saturation was reproduced at all four Weissenberg numbers. A summary of the simulation parameters employed in these

studies is given in table 2.2.

Figures 3.1 and 3.2 show the effect of concentration on the flow and polymer statistics at $We_{\tau_b} \approx 10$. Increasing the polymer number density by several orders of magnitude from $n_p k_B T/(\rho u_{\tau_b}^2) \approx 1 \times 10^{-7}$ to $n_p k_B T/(\rho u_{\tau_b}^2) \approx 1 \times 10^{-2}$ results in only a slight increase in the magnitude of drag reduction at this Weissenberg number. The largest drag reduction of 2% is achieved at $n_p k_B T/(\rho u_{\tau_b}^2) \approx 1 \times 10^{-2}$ ($\beta \approx 0.9$), as shown in figure 3.1(a) and table 2.2. These small changes in the drag reduction result in minor variations in the first and second-order turbulence statistics, as shown figures 3.1(b-d) and 3.2(a). In addition, the variations in polymer shear stresses and polymer extensions are also observed to be insignificant as shown in figure 3.2(b). Using the computed polymer shear stresses, an effective viscosity can be defined as

$$\langle \nu_{eff} \rangle = \nu_s + \frac{\langle \tau_{p,xz} \rangle}{\rho(dU/dz)}. \tag{3.1}$$

Figures 3.2(c-d) show the predicted effective viscosity normalized by the kinematic viscosity of the solvent, ν_s, and by λu_τ^2, respectively. With either normalization, the effective viscosity monotonically increases with increasing polymer concentration. The peak of ν_{eff} occurs at $z^+ \approx 30$ and has a magnitude of $\sim 1.2\nu_s$ or $\sim 0.13\lambda u_\tau^2$ at saturation. The latter value is consistent with the saturation value of $\nu_{eff,sat} \sim 0.1\lambda u_\tau^2$ predicted by Lumley's theory (egn.1.6).

Figures 3.3 and 3.4 show the effect of polymer concentration on flow and polymer statistics at $We_{\tau_b} \approx 35$. With increasing polymer number density, the drag reduction increases, reaching a peak magnitude of 32.6% at $n_p k_B T/(\rho u_{\tau_b}^2) \approx 1 \times 10^{-3}$ ($\beta \approx 0.96$). Adding more polymer beyond this point only reduces the magnitude of drag reduction,

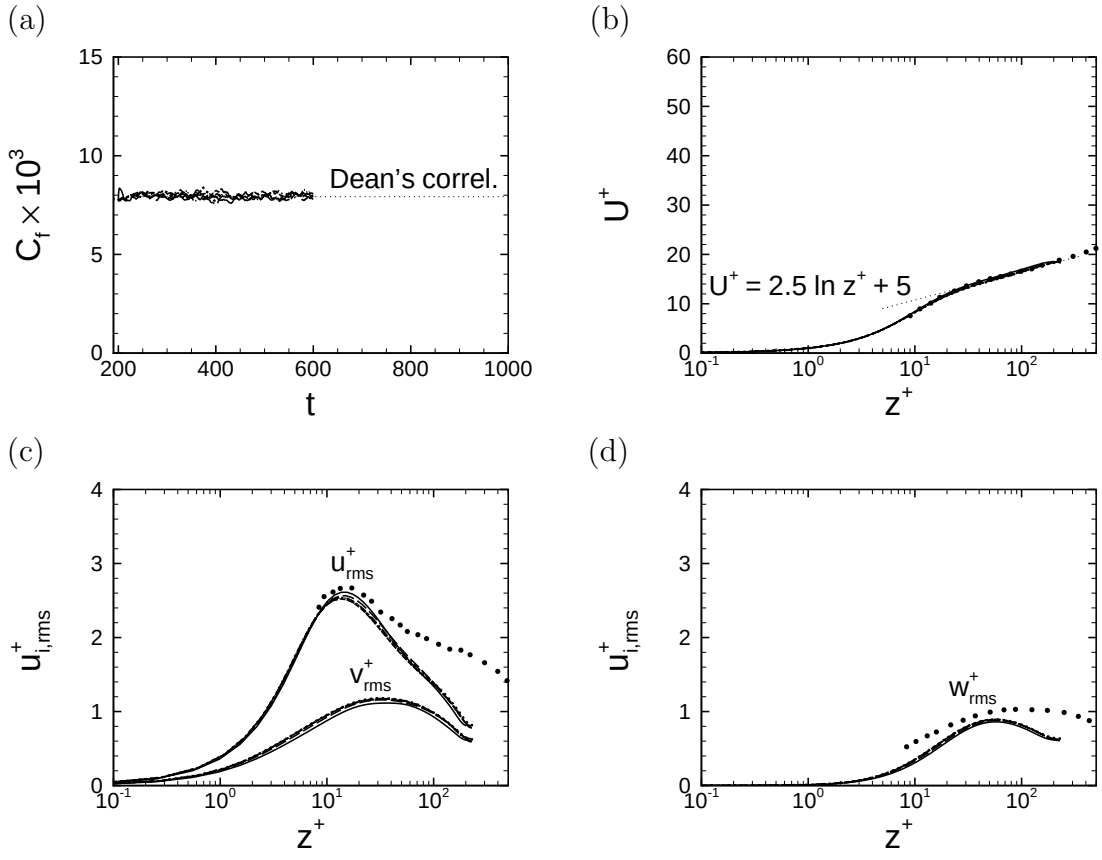

Figure 3.1: Effect of polymer concentration on the predicted flow statistics at $We_{\tau_b} \approx 10$: (a) time evolution of the skin friction coefficient; (b) mean velocity profiles; (c) r.m.s. of streamwise and spanwise velocity fluctuations; (d) r.m.s. of wall-normal velocity fluctuations. $\cdots\cdots$, Newtonian (case N); ---, $\beta \approx 0.999989$ (case A6-l); $-\cdot\cdot-$, $\beta \approx 0.99989$ (case A5-l); $-\cdot-$, $\beta \approx 0.9989$ (case A4-l); $--$, $\beta \approx 0.989$ (case A3-l); ——, $\beta \approx 0.9$ (case A2-l); •, experiments of Warholic, *et al.*(1999) Newtonian.

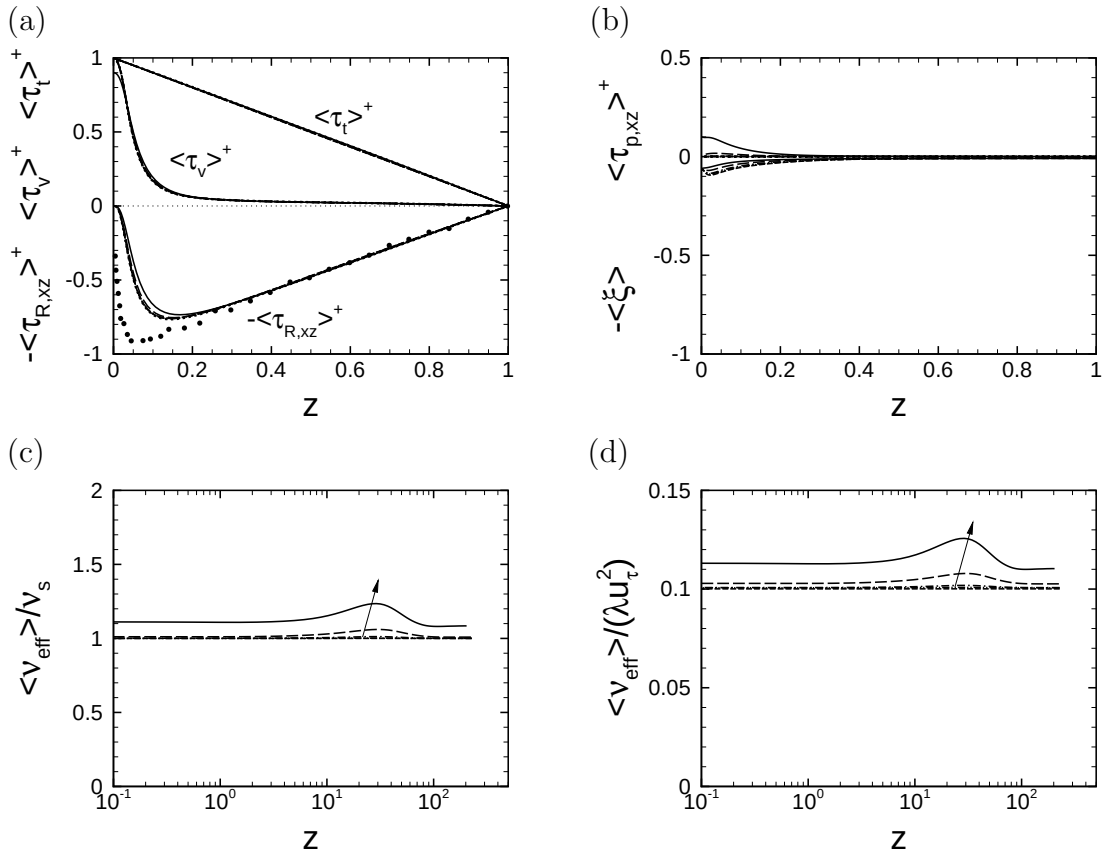

Figure 3.2: Effect of polymer concentration on the predicted flow statistics at $We_{\tau_b} \approx 10$: (a) Reynolds shear stresses ($\langle \tau_{R,xz} \rangle^+$), viscous shear stresses ($\langle \tau_v \rangle^+$), and sum of Reynolds, viscous and polymer shear stresses ($\langle \tau_t \rangle^+$); (b) polymer shear stresses ($\langle \tau_{p,xz} \rangle^+$) and polymer extensions; (c) effective viscosities normalized with respect to ν_s; (d) effective viscosities normalized with respect to λu_τ^2. Line types same as in figure 3.1.

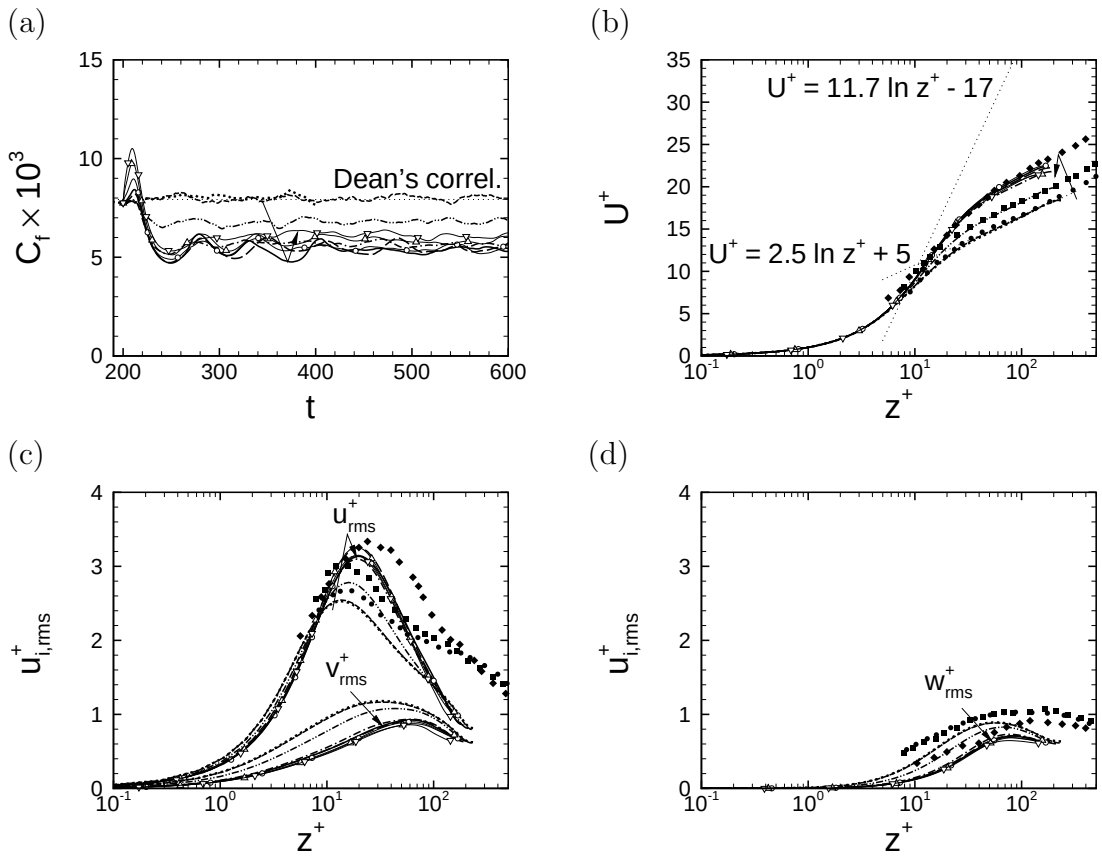

Figure 3.3: Effect of polymer concentration on the predicted flow statistics at $We_{\tau_b} \approx 35$: (a) time evolution of the skin friction coefficient; (b) mean velocity profiles; (c) r.m.s. of streamwise and spanwise velocity fluctuations; (d) r.m.s. of wall-normal velocity fluctuations. ·····, Newtonian (case N); ---, $\beta \approx 0.999996$ (case C7-l); $-\cdot\cdot-$, $\beta \approx 0.9996$ (case C5-l); $-\cdot-$, $\beta \approx 0.996$ (case C4-l); $---$, $\beta \approx 0.98$ (case C4.1-l); ——, $\beta \approx 0.96$ (case C3-l); —○—, $\beta \approx 0.89$ (case C3.1-l); —△—, $\beta \approx 0.80$ (case C3.2-l); —▽—, $\beta \approx 0.72$ (case C2-l); •, experiments of Warholic, *et al.*(1999) Newtonian; ■, experiments of Warholic, *et al.*(1999) at $14\%DR$; ♦, experiments of Warholic, *et al.*(1999) at $33\%DR$.

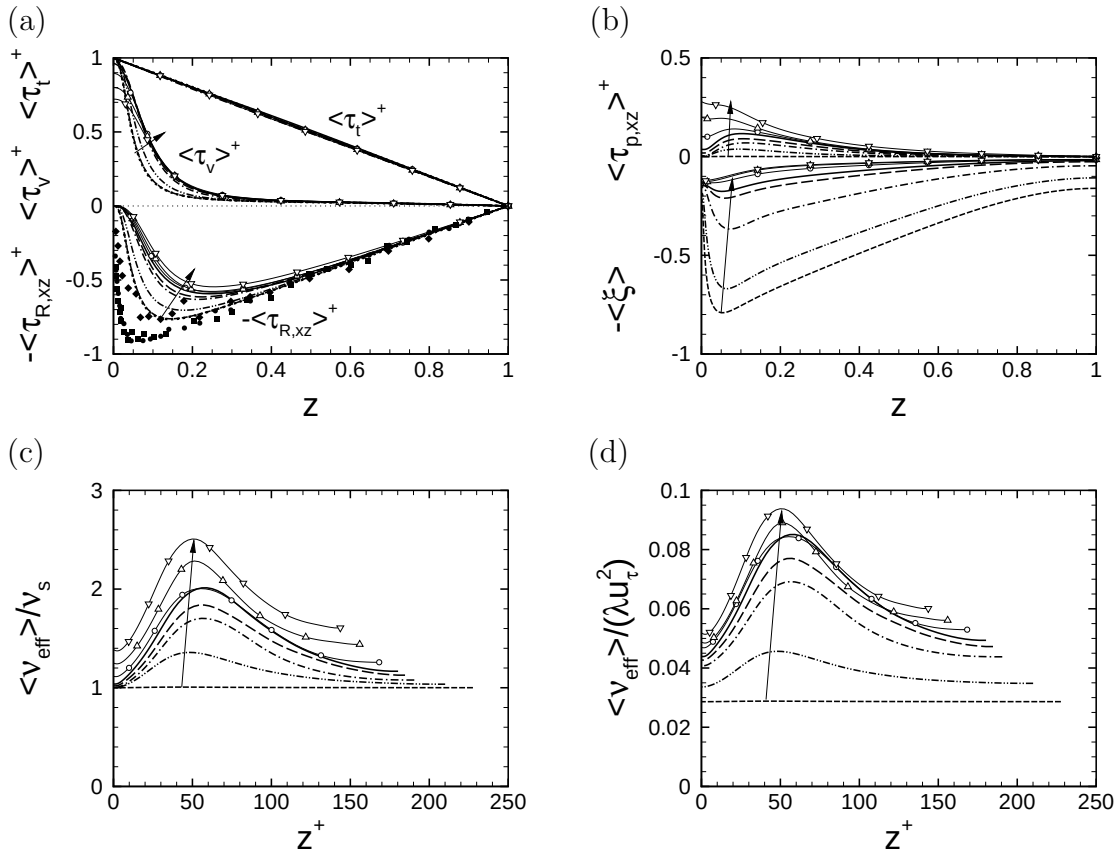

Figure 3.4: Effect of polymer concentration on the predicted flow statistics at $We_{\tau_b} \approx 35$: (a) Reynolds shear stresses ($\langle\tau_{R,xz}\rangle^+$), viscous shear stresses ($\langle\tau_v\rangle^+$), and sum of Reynolds, viscous and polymer shear stresses ($\langle\tau_t\rangle^+$); (b) polymer shear stresses ($\langle\tau_{p,xz}\rangle^+$) and polymer extensions; (c) effective viscosities normalized with respect to ν_s; (d) effective viscosities normalized with respect to λu_τ^2. Line types same as in figure 3.3.

as seen in figure 3.3(a) and table 2.2. The predicted mean velocity profiles show good agreement with the experimental data of Warholic, Massah & Hanratty (1999) at comparable drag reductions, as seen in figure 3.3(b). For $0.96 \lesssim \beta < 1$, increasing the polymer concentration results in a thickening of the buffer layer, and a contraction and upward shift of the inertial sublayer. At higher concentrations ($\beta < 0.96$), the inertial sublayer shifts back downwards, consistent with the lower magnitude of drag reduction observed at these higher concentrations. The normalized turbulence intensities and Reynolds and viscous shear stresses are shown in figures 3.3(c-d) and 3.4(a). With increasing polymer concentration, the peaks of all three turbulence intensities and the Reynolds shear stress shift towards the center of the channel. The peak of the normalized streamwise turbulence intensity rapidly grows for $0.96 \lesssim \beta < 1$, but gradually decays at higher concentrations. The normalized spanwise and wall-normal turbulence intensities and the Reynolds shear stress rapidly decay for $0.96 \lesssim \beta < 1$ but show a more gradual decay at higher concentrations. In contrast, the normalized viscous shear stress rapidly grows near the buffer layer for $0.96 \lesssim \beta < 1$ but slowly grows at higher concentrations. The trends observed in the turbulence intensities and the Reynolds shear stress for $0.96 \lesssim \beta < 1$ are consistent with the experimental data of Warholic, Massah & Hanratty (1999), as seen in figures 3.3(c-d) and 3.4(a). However, the magnitude of the stresses are different due to the different Reynolds number of the experiments ($Re_{\tau_b} \approx 1000$) compared to DNS ($Re_{\tau_b} \approx 230$). The sum of Reynolds, viscous and polymer shear stresses (figure 3.4a) collapses into a line at all concentrations, indicating that all flows are at stationary steady state. Figure 3.4(b) shows the polymer shear stresses and polymer end-to-end extensions. The

polymer shear stress monotonically grows with increasing polymer concentration for $0.96 \lesssim \beta < 1$. At higher concentrations ($\beta < 0.96$), the main increase in the polymer shear stress occurs within the viscous sublayer. This indicates that the solution is no longer dilute at these higher concentrations and explains the drop in drag reduction at these higher concentrations. The peak value of the polymer extension occurs near the buffer layer and varies between $\sim 80\%$ of the full extension at the lowest concentration to $\sim 10\%$ at the highest concentration, as shown in figure 3.4(b). The peak of ν_{eff} occurs at $z^+ \approx 50$ and has a magnitude of $\sim 2\nu_s$ or $\sim 0.08\lambda u_\tau^2$ at saturation, as shown in figures 3.4(c-d). Once again, this is consistent with Lumley's theory as shown in equation (eqn.1.6).

Figures 3.5-3.8 show the effect of polymer concentration at $We_{\tau_b} \approx 100$ and $We_{\tau_b} \approx 150$, respectively, as the polymer number density is varied between $1\times10^{-8} \lesssim n_p k_B T/(\rho u_{\tau_b}^2) \lesssim 1\times10^{-3}$ ($0.86 \lesssim \beta \lesssim 0.999999989$). The magnitude of drag reduction rapidly increases for $0.98 \lesssim \beta < 1$, and saturates to a plateau for $0.86 \lesssim \beta \lesssim 0.98$, as shown in figures 3.5(a), 3.7(a) and table 2.2. The magnitude of drag reduction at saturation is $\sim 54\%DR$ at $We_{\tau_b} \approx 100$ and $\sim 56\%DR$ at $We_{\tau_b} \approx 150$. The maximum drag reduction at $We_{\tau_b} \approx 150$ is comparable to the range of $57 - 60\%DR$ predicted by Virk's MDR asymptote at $Re_{\tau_b} \approx 230$ for $0.9 \lesssim \beta \lesssim 0.98$. At both Weissenberg numbers, the mean velocity profiles at saturation begin to approach Virk's asymptotic profile and the experimental data of Ptasinski, *et al.* (2001) at MDR, as shown in figures 3.5(b) and 3.7(b). The normalized streamwise turbulence intensity shows an increase in its peak magnitude up to $0.998 \lesssim \beta \lesssim 0.9989$ (corresponding to $\sim 40 - 43\%DR$), but decays at higher drag reductions, as shown in figures 3.5(c)

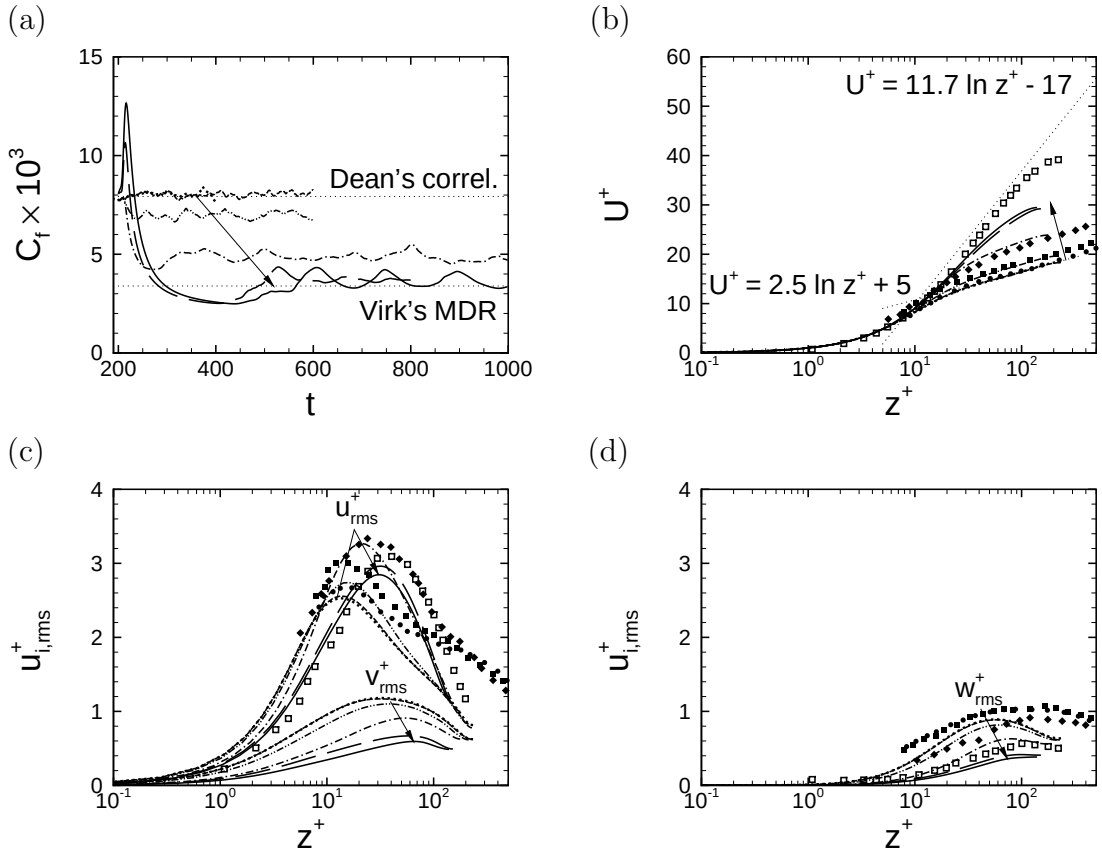

Figure 3.5: Effect of polymer concentration on the predicted flow statistics at $We_{\tau_b} \approx 100$: (a) time evolution of the skin friction coefficient; (b) mean velocity profiles; (c) r.m.s. of streamwise and spanwise velocity fluctuations; (d) r.m.s. of wall-normal velocity fluctuations. $\cdots\cdots$, Newtonian (case NN); ---, $\beta \approx 0.9999989$ (case E8-q); $-\cdots-$, $\beta \approx 0.99989$ (case E6-q); $-\cdot-$, $\beta \approx 0.9989$ (case E5-q); ——, $\beta \approx 0.98$ (case EE4-q); ——, $\beta \approx 0.90$ (case EE3-q); •, experiments of Warholic *et al.*(1999) Newtonian; ■, experiments of Warholic *et al.*(1999) at 14%DR; ♦, experiments of Warholic *et al.*(1999) at 33%DR; □, experiments of Ptasinski *et al.*(2001) at 63%DR.

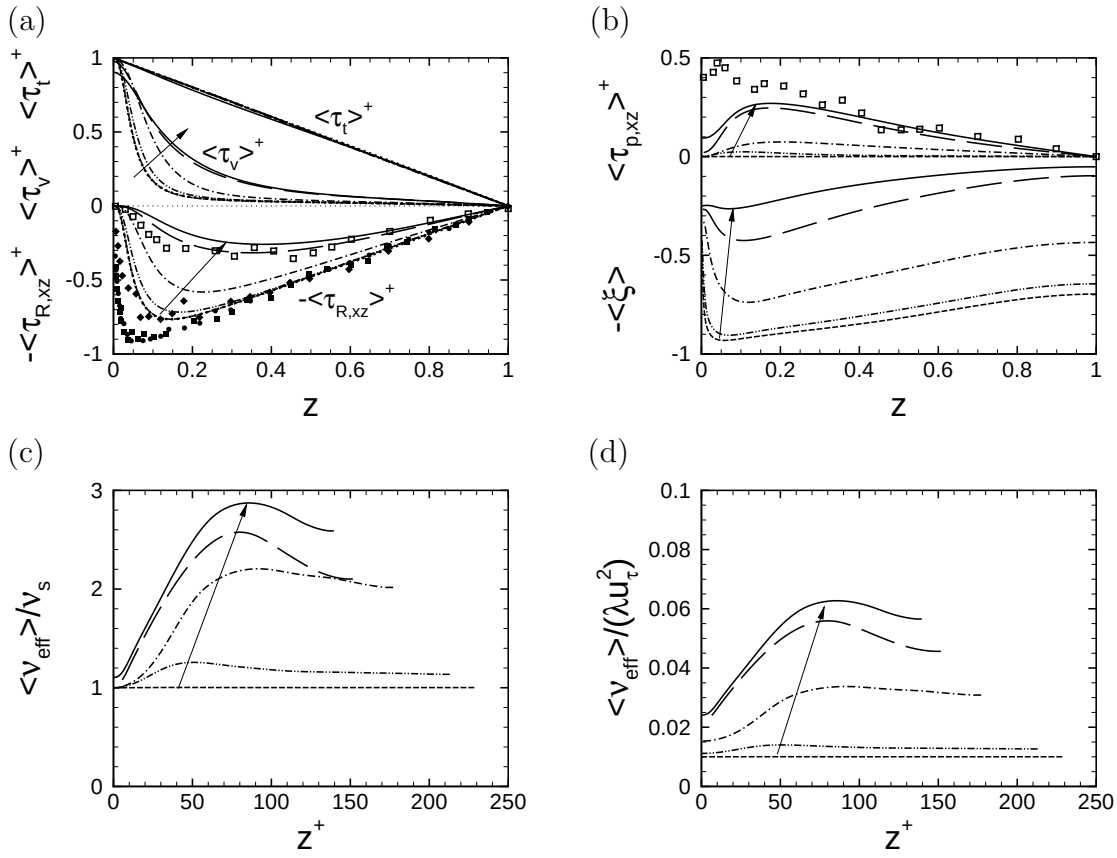

Figure 3.6: Effect of polymer concentration on the predicted flow statistics at $We_{\tau_b} \approx 100$: (a) Reynolds shear stresses ($\langle \tau_{R,xz} \rangle^+$), viscous shear stresses ($\langle \tau_v \rangle^+$), and sum of Reynolds, viscous and polymer shear stresses ($\langle \tau_t \rangle^+$); (b) polymer shear stresses ($\langle \tau_{p,xz} \rangle^+$) and polymer extensions; (c) effective viscosities normalized with respect to ν_s; (d) effective viscosities normalized with respect to λu_τ^2. Line types same as in figure 3.5.

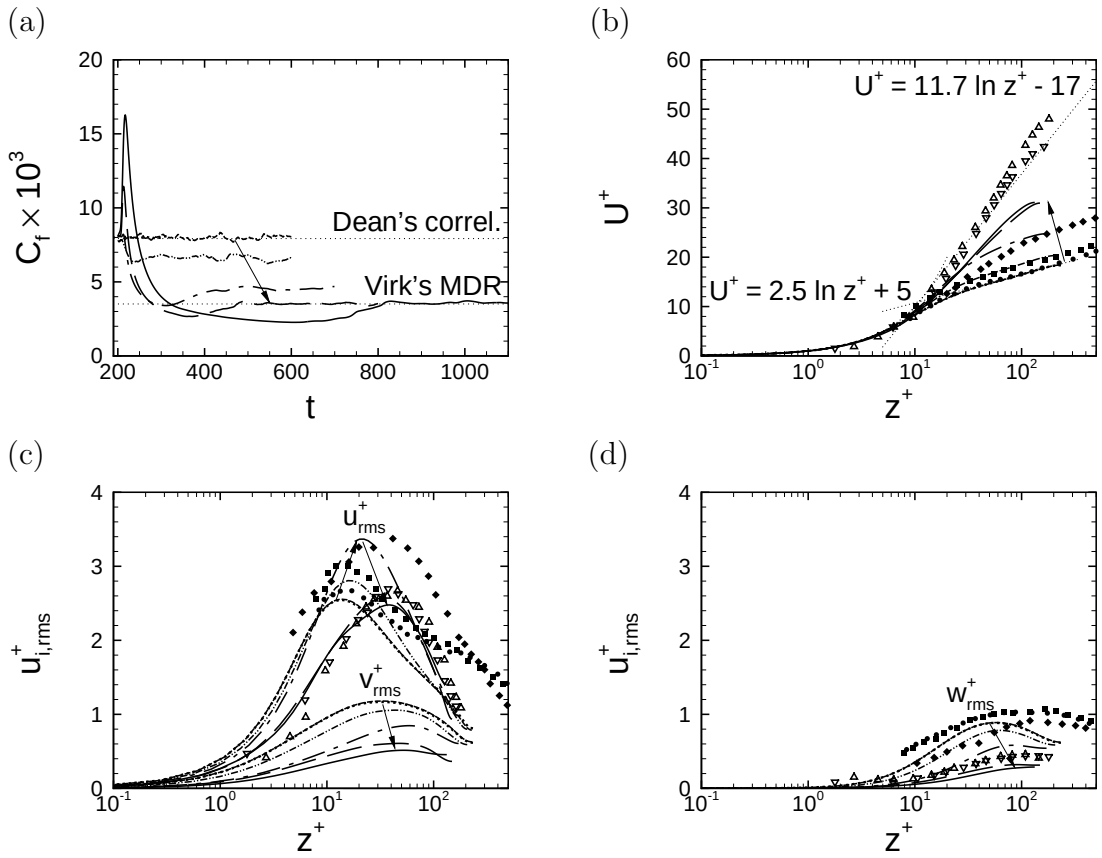

Figure 3.7: Effect of polymer concentration on the predicted flow statistics at $We_{\tau_b} \approx 150$: (a) time evolution of the skin friction coefficient; (b) mean velocity profiles; (c) r.m.s. of streamwise and spanwise velocity fluctuations; (d) r.m.s. of wall-normal velocity fluctuations. $\cdots\cdots$, Newtonian (case NN); ---, $\beta \approx 0.999998$ (case F8-q); $-\cdots-$, $\beta \approx 0.9998$ (case F6-q); ——·——, $\beta \approx 0.998$ (case FF5-q); —— ——, $\beta \approx 0.98$ (case FF4-q); ——, $\beta \approx 0.86$ (case FF3-q); •, experiments of Warholic, *et al.*(1999) Newtonian; ■, experiments of Warholic, *et al.*(1999) at 14%DR; ♦, experiments of Warholic, *et al.*(1999) at 38%DR; ▽, experiments of Ptasinski, *et al.*(2001) at 65%DR; △, experiments of Ptasinski, *et al.*(2001) at 70%DR.

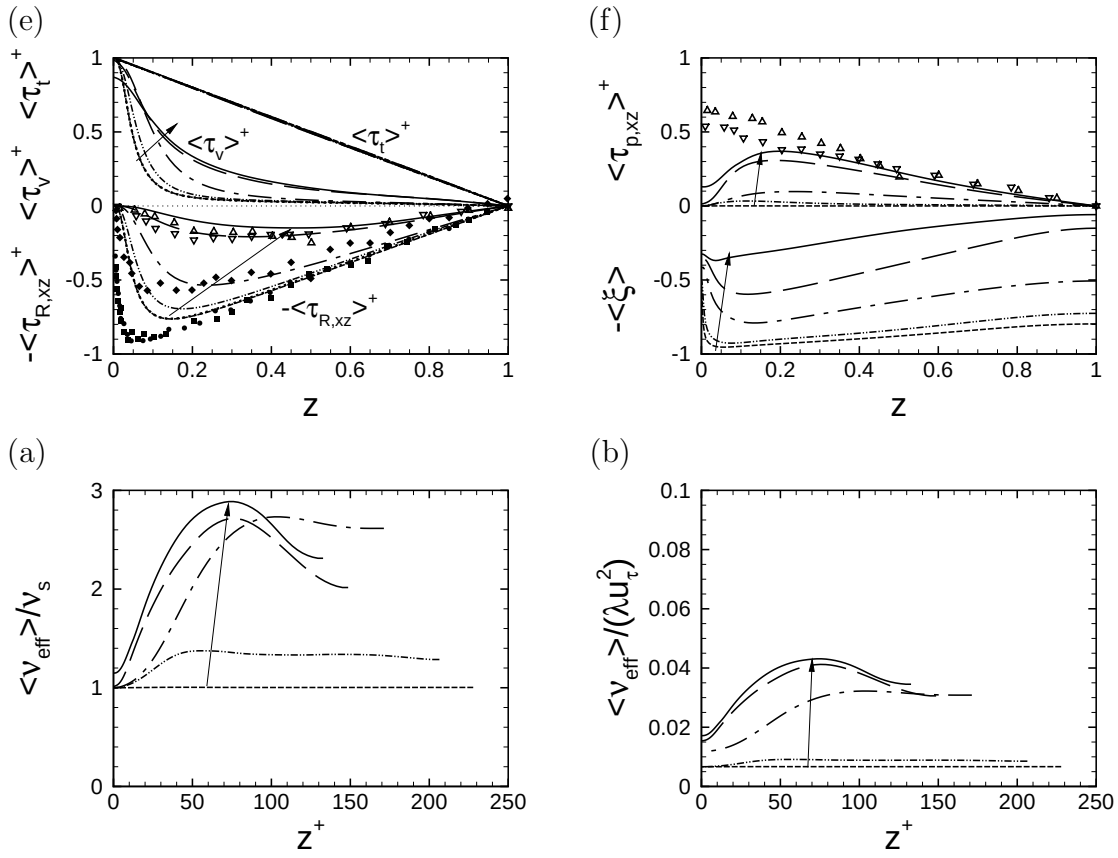

Figure 3.8: Effect of polymer concentration on the predicted flow statistics at $We_{\tau_b} \approx 150$: (a) Reynolds shear stresses ($\langle\tau_{R,xz}\rangle^+$), viscous shear stresses ($\langle\tau_v\rangle^+$), and sum of Reynolds, viscous and polymer shear stresses ($\langle\tau_t\rangle^+$); (b) polymer shear stresses ($\langle\tau_{p,xz}\rangle^+$) and polymer extensions; (c) effective viscosities normalized with respect to ν_s; (d) effective viscosities normalized with respect to λu_τ^2. Line types same as in figure 3.7.

and 3.7(c). At saturation, the peak of the normalized streamwise turbulence intensity is found to be slightly higher than the Newtonian value at $We_{\tau_b} \approx 100$ and slightly lower than the Newtonian value at $We_{\tau_b} \approx 150$. The spanwise and wall-normal turbulence intensities and the Reynolds shear stress strongly decay for $0.98 \lesssim \beta < 1$, but change little for $0.86 \lesssim \beta \lesssim 0.98$ when saturation conditions are reached, as seen in figures 3.5(c-d), 3.6(a), 3.7(c-d) and 3.8(a). At both Weissenberg numbers, the Reynolds shear stress is found to have a small but non-zero magnitude at saturation. Overall, the second-order statistics observed at saturation at $We_{\tau_b} \approx 100$ show agreement with the experimental data of Ptasinski, *et al.* (2001) $63\%DR$, while those for $We_{\tau_b} \approx 150$ show agreement with the experimental data of Ptasinski, *et al.* (2001) at $65 - 70\%DR$, which correspond to MDR conditions in their experiments. The polymer shear stress rapidly grows from near-zero values at the lowest concentrations to values comparable to or surpassing the Reynolds shear stress at saturation, while the polymer extension decays from near full extension at the lowest concentrations to $25 - 35\%$ of full extension at saturation, as shown in figures 3.6(b) and 3.8(b). The effective viscosity, ν_{eff}, reaches peak magnitude of $\sim 3\nu_s$ and $\sim (0.04 - 0.06)\lambda u_\tau^2$ at saturation, as shown in figures 3.6(c-d) and 3.8(c-d). The profile of ν_{eff} grows almost linearly from $0 < z^+ \lesssim 50 - 100$ and remains nearly flat at its peak value for higher z^+. This behavior has been used in recent studies to suggest a modeling approach to polymer drag reduction based on a linear viscosity profile (L'vov, *et al.*, 2004; de Angelis, *et al.*, 2004).

Figures 3.9, 3.10 and 3.11 show the effect of concentration on the one-dimensional energy spectra at $z^+ \approx 30$ at $We_{\tau_b} \approx 35$, 100 and 150, respectively. At all three

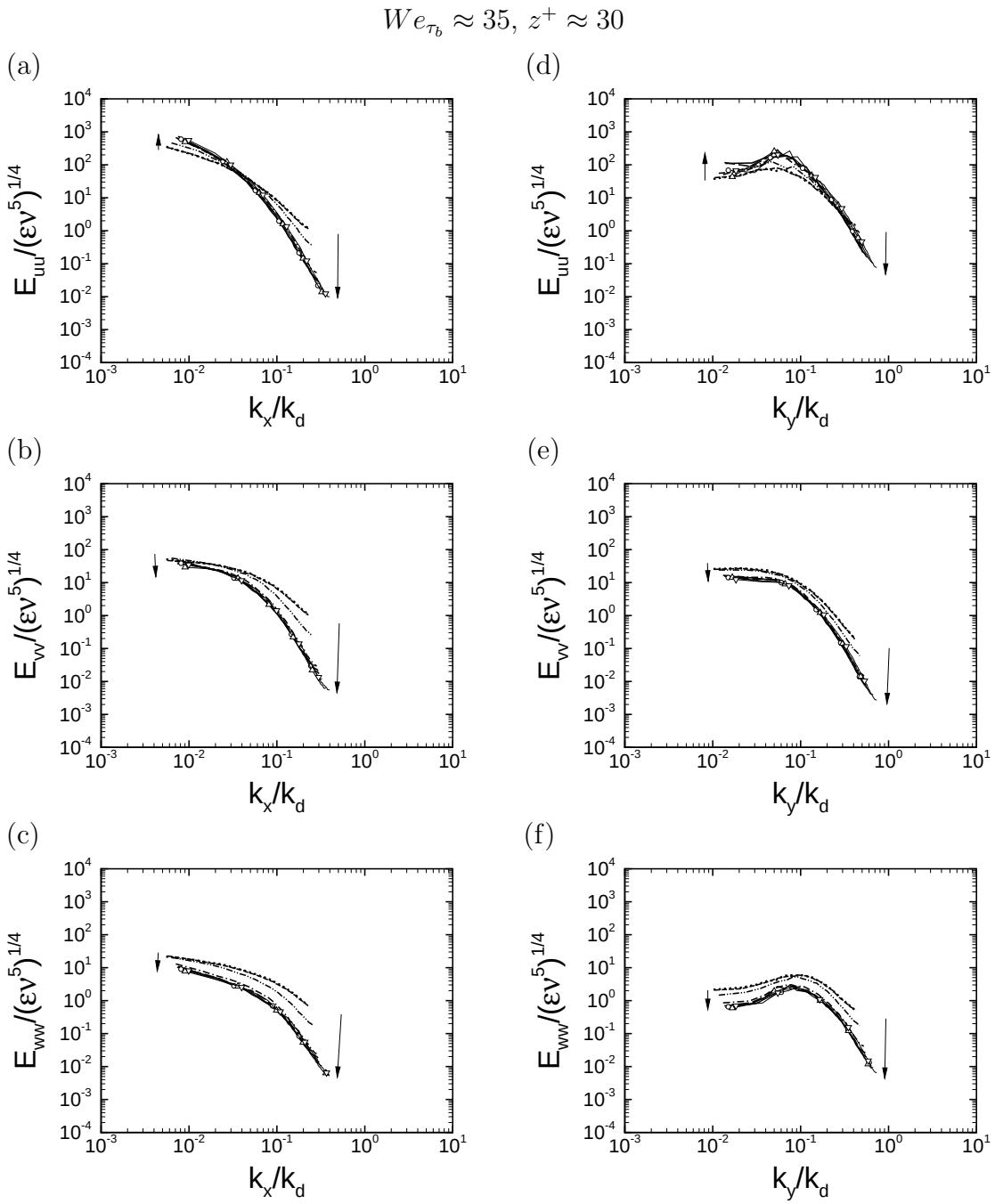

Figure 3.9: Effect of polymer concentration on the one-dimensional energy spectra at $We_{\tau_b} \approx 35$: (a-c) streamwise spectra at $z^+ \approx 30$; (d-f) spanwise spectra at $z^+ \approx 30$. Line types same as in figure 3.3.

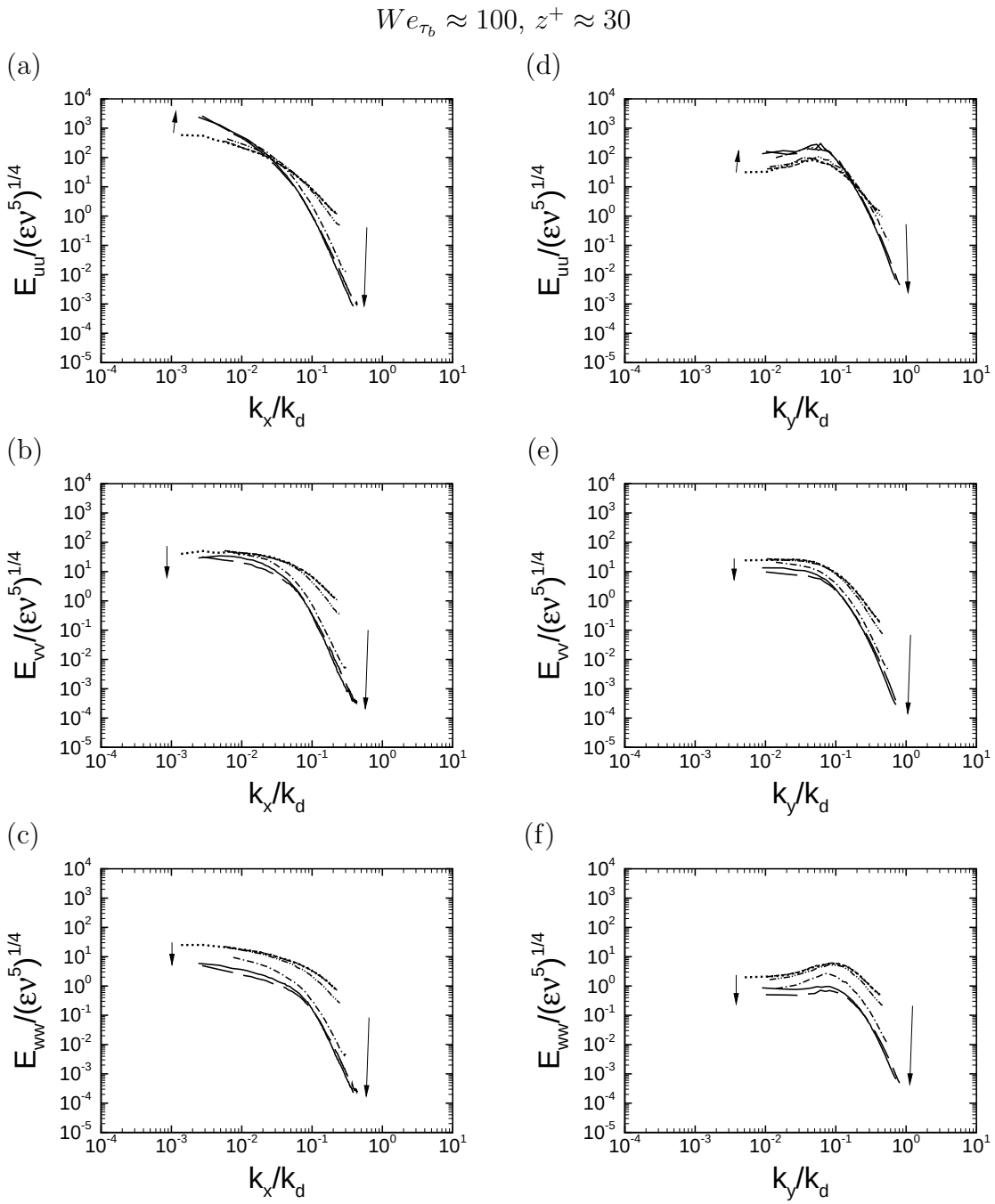

Figure 3.10: Effect of polymer concentration on the one-dimensional energy spectra at $We_{\tau_b} \approx 100$: (a-c) streamwise spectra at $z^+ \approx 30$; (d-f) spanwise spectra at $z^+ \approx 30$. Line types same as in figure 3.5.

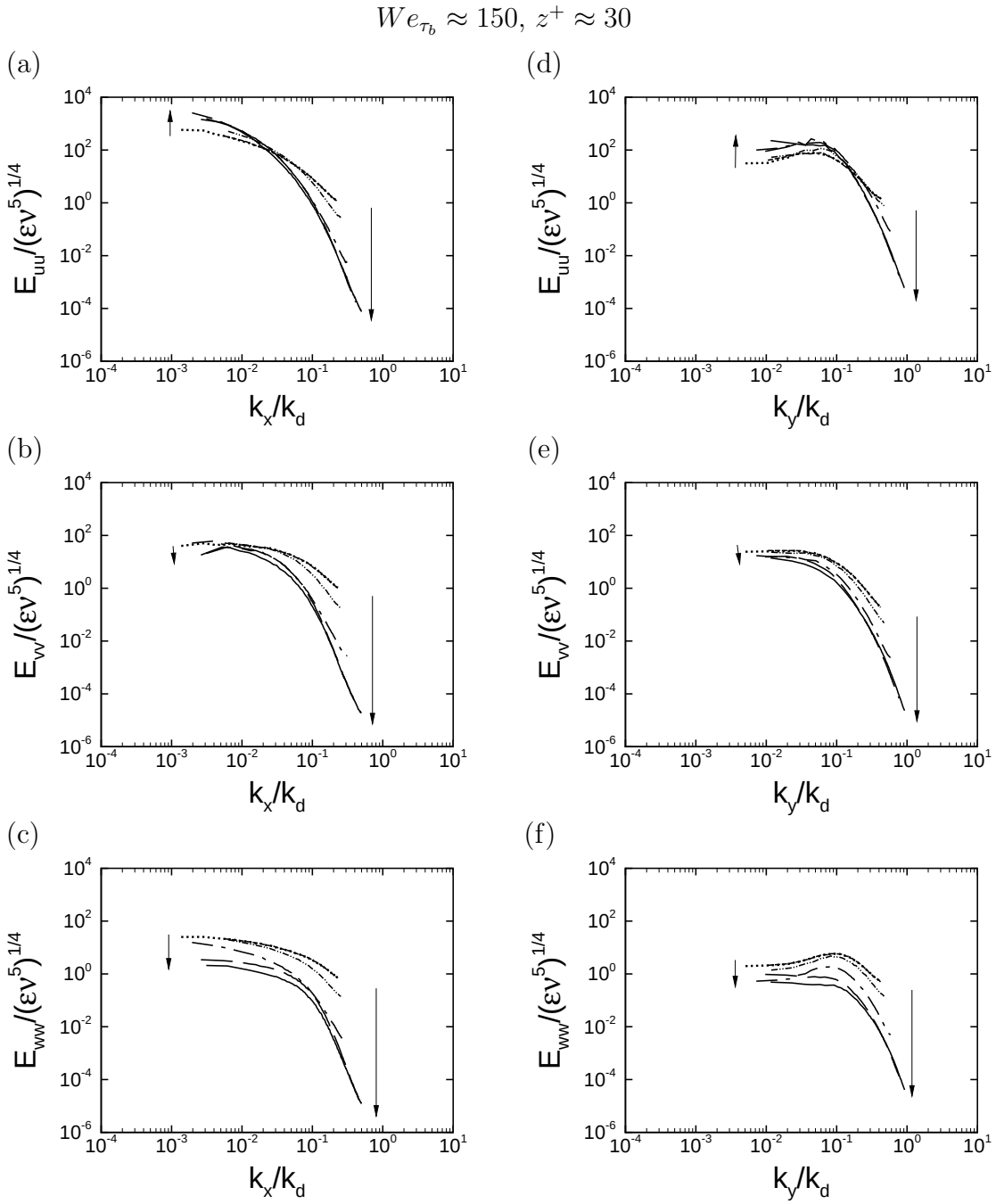

Figure 3.11: Effect of polymer concentration on the one-dimensional energy spectra at $We_{\tau_b} \approx 150$: (a-c) streamwise spectra at $z^+ \approx 30$; (d-f) spanwise spectra at $z^+ \approx 30$. Line types same as in figure 3.7.

Weissenberg numbers, the presence of the polymer results in a drop in the streamwise turbulence kinetic energy (E_{uu}) at the small scales and an increase in the streamwise turbulence kinetic energy at the large scales, along with by a drop in the spanwise (E_{vv}) and wall-normal (E_{ww}) turbulence kinetic energies at all scales. These trends are similar to what has been observed in experiments (Wei & Willmarth, 1992; Warholic, Massah & Hanratty, 1999). The range of scales damped by the polymer and the magnitude of the drop in the turbulence kinetic energy are determined by the polymer concentration and Weissenberg number. At a fixed Weissenberg number, increasing the polymer concentration up to the saturation concentration extends the range of damped scales to lower wavenumbers (larger scales) and enhances the magnitude of the drop in the turbulence kinetic energy. Beyond the saturation concentration, the range of affected scales and the magnitude of the drop remain nearly the same. Increasing the Weissenberg number extends the range of scales damped in the E_{uu} spectra to lower wavenumbers (larger scales).

Figures 3.12, 3.13 and 3.14 show the corresponding one-dimensional energy spectra at $z^+ \approx 100$, respectively. At $We_{\tau_b} \approx 35$, the energy spectra at $z^+ \approx 100$ are little changed from Newtonian flow. However, the minor variations follow the same trends as those observed at $z^+ \approx 30$. In contrast, at $We_{\tau_b} \approx 100$ and $We_{\tau_b} \approx 150$ the same trends as those observed at $z^+ \approx 30$ can also be observed at $z^+ \approx 100$. The main difference is that the range of damped scales at $z^+ \approx 100$ and the magnitude of damping is diminished compared to $z^+ \approx 30$, resulting in a weaker modification of the turbulence kinetic energy away from the wall. These trends are consistent with the behavior of turbulence intensities (figures 3.3, 3.5 & 3.7), and with experimental

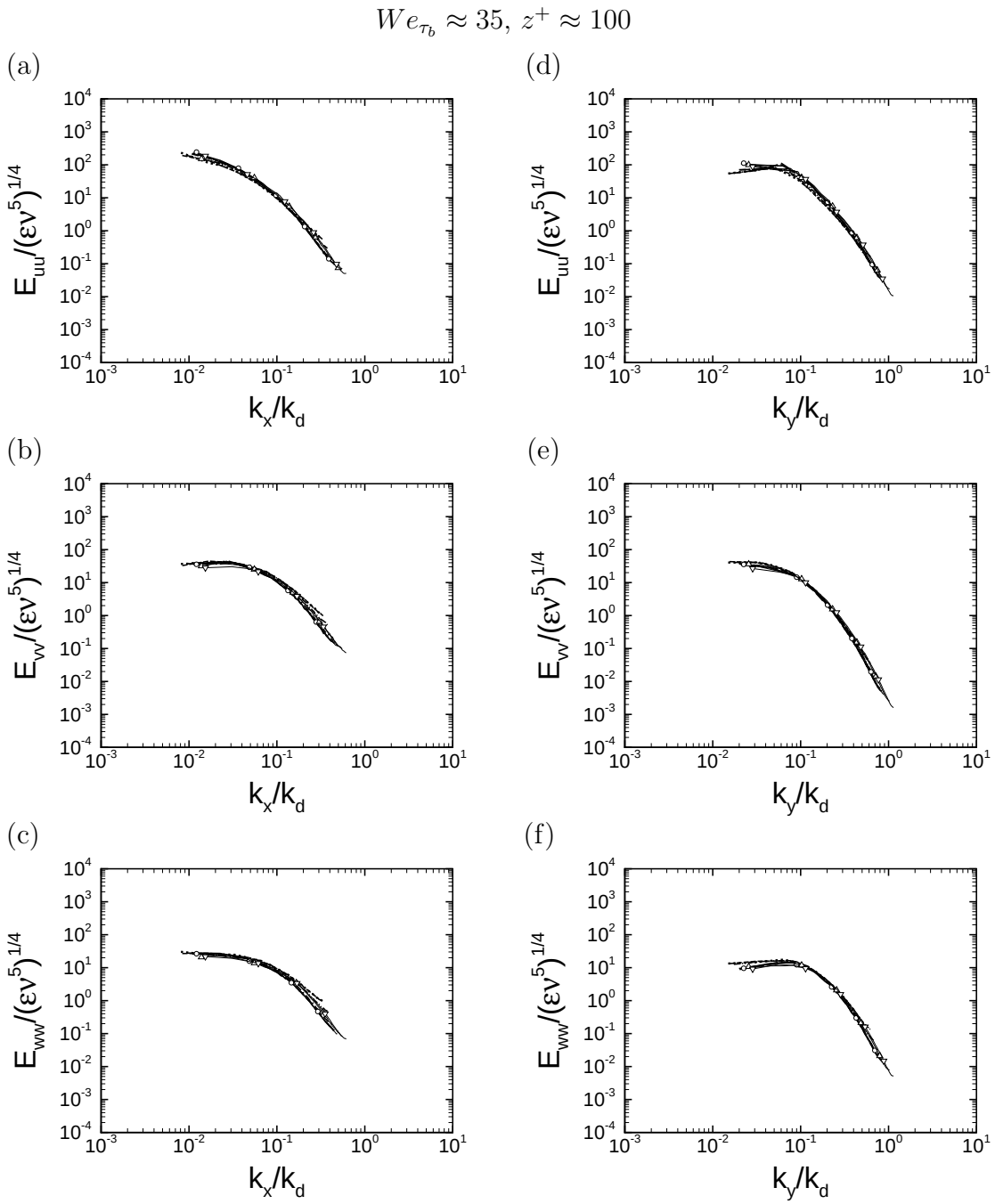

Figure 3.12: Effect of polymer concentration on the one-dimensional energy spectra at $We_{\tau_b} \approx 35$: (a-c) streamwise spectra at $z^+ \approx 100$; (d-f) spanwise spectra at $z^+ \approx 100$. Line types same as in figure 3.3.

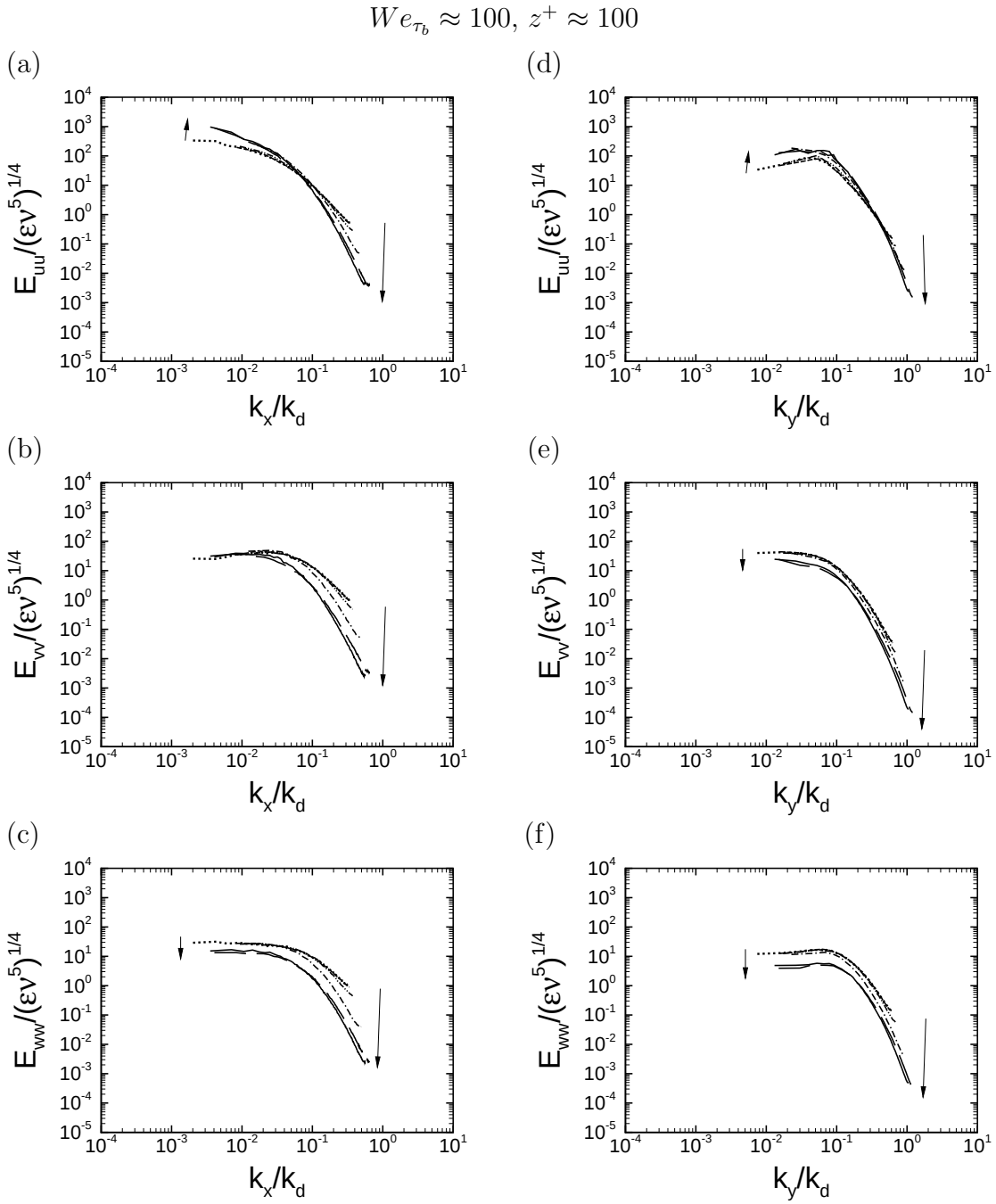

Figure 3.13: Effect of polymer concentration on the one-dimensional energy spectra at $We_{\tau_b} \approx 100$: (a-c) streamwise spectra at $z^+ \approx 100$; (d-f) spanwise spectra at $z^+ \approx 100$. Line types same as in figure 3.5.

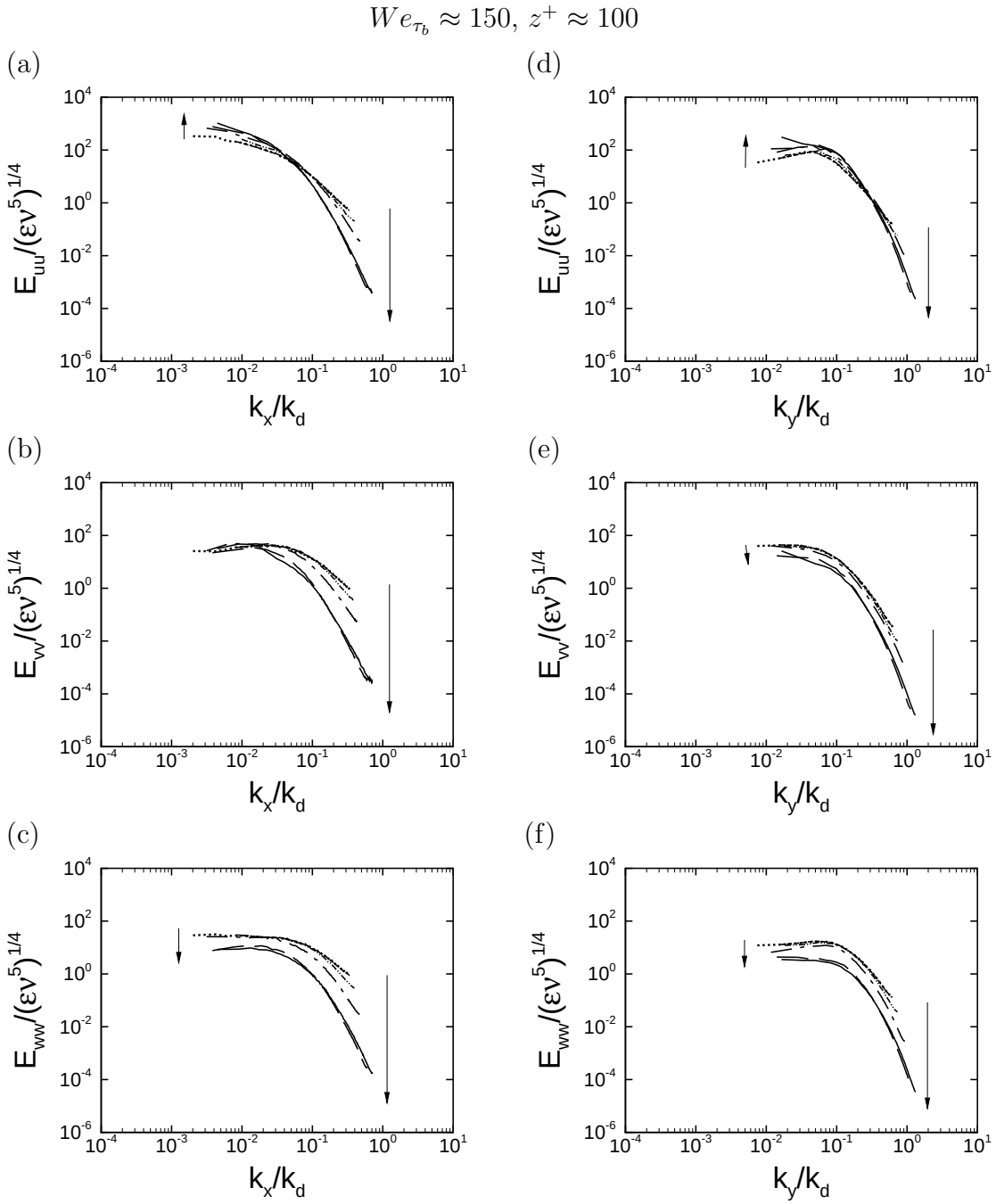

Figure 3.14: Effect of polymer concentration on the one-dimensional energy spectra at $We_{\tau_b} \approx 150$: (a-c) streamwise spectra at $z^+ \approx 100$; (d-f) spanwise spectra at $z^+ \approx 100$. Line types same as in figure 3.7.

data (Wei & Willmarth, 1992; Warholic, Massah & Hanratty, 1999).

These trends in the energy spectra are consistent with the behavior of turbulence intensities observed in figures 3.3(c-d), 3.5(c-d) and 3.7(c-d) which show pileup in streamwise, but drop in spanwise and wall-normal components. However, they stand at odds with the predictions of Lumley's (1969, 1973) and de Gennes's (1986) theories, which describe the effect of the polymer to be an isotropic attenuation of the energy spectra at the small scales (Lumley, 1969, 1973) or a termination of the cascade (de Gennes, 1986). In contrast to the predictions of these theories, the spectra shown in figures 3.9-3.14 show different behaviors for the streamwise, spanwise and wall-normal components. Specially, the pileup of energy in the largest scales of E_{uu} is not explained by either theory.

3.2 Effect of Weissenberg number on the flow statistics

We next investigate the effect of polymer relaxation time on the flow statistics. To this end, direct numerical simulations were performed for $10 \lesssim We_{\tau_b} \lesssim 150$ with the polymer extensibility parameter and polymer number density fixed at $b = 45,000$ and $n_p k_B T/(\rho u_{\tau_b}^2) \approx 1 \times 10^{-3}$ ($0.86 \lesssim \beta \lesssim 0.989$), which correspond to saturation conditions at each Weissenberg number. A summary of the simulation parameters employed in these computations is provided in table 2.3.

Figures 3.15 and 3.16 show the turbulence and polymer statistics predicted in these simulations. With increasing Weissenberg number, the magnitude of drag reduction increases from $1.9\%DR$ at $We_{\tau_b} \approx 10$ to $\sim 55\%DR$ at $We_{\tau_b} \approx 150$ which is comparable to $\sim 56\%DR$ predicted by Virk's MDR at $\beta = 0.86$. For $10 \lesssim We_{\tau_b} \lesssim 70$,

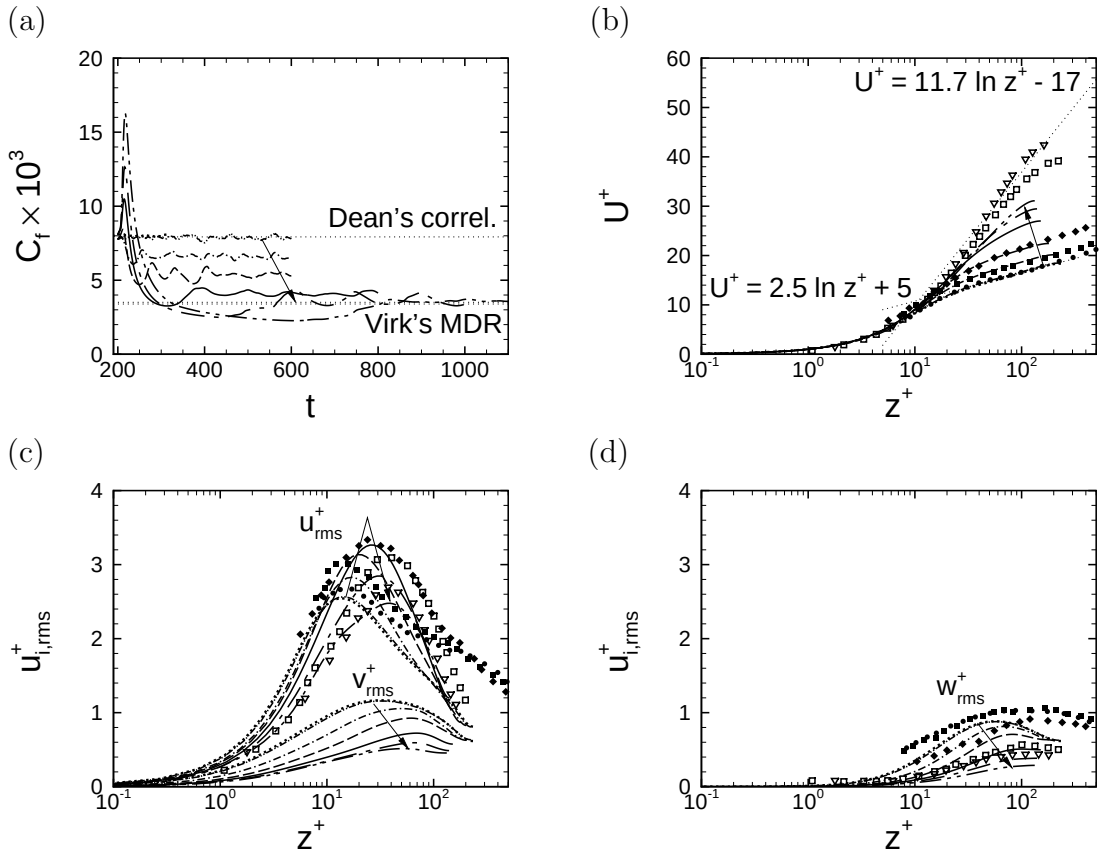

Figure 3.15: Effect of Weissenberg number on the predicted flow statistics at $10 \lesssim We_{\tau_b} \lesssim 150$ and $n_p k_B T/(\rho u^2_{\tau_b}) \approx 1 \times 10^{-3}$: (a) time evolution of the skin friction coefficient; (b) mean velocity profiles; (c) r.m.s. of streamwise and spanwise velocity fluctuations; (d) r.m.s. of wall-normal velocity fluctuations. $\cdots\cdots$, Newtonian (case NN); $-\cdot\cdot-$, $We_{\tau_b} \approx 10$ (case A3-l); $-\cdot-$, $We_{\tau_b} \approx 20$ (case B3-l); $---$, $We_{\tau_b} \approx 35$ (case C3-l); ——, $We_{\tau_b} \approx 70$ (case DD3-q); ——$\cdot$——, $We_{\tau_b} \approx 100$ (case EE3-q); ——$\cdot\cdot$——, $We_{\tau_b} \approx 150$ (case FF3-q); •, experiments of Warholic, *et al.*(1999) Newtonian; ■, experiments of Warholic, *et al.*(1999) at 14%DR; ♦, experiments of Warholic, *et al.*(1999) at 33%DR); □, experiments of Ptasinski, *et al.*(2001) at 63%DR; ▽, experiments of Ptasinski, *et al.*(2001) at 65%DR.

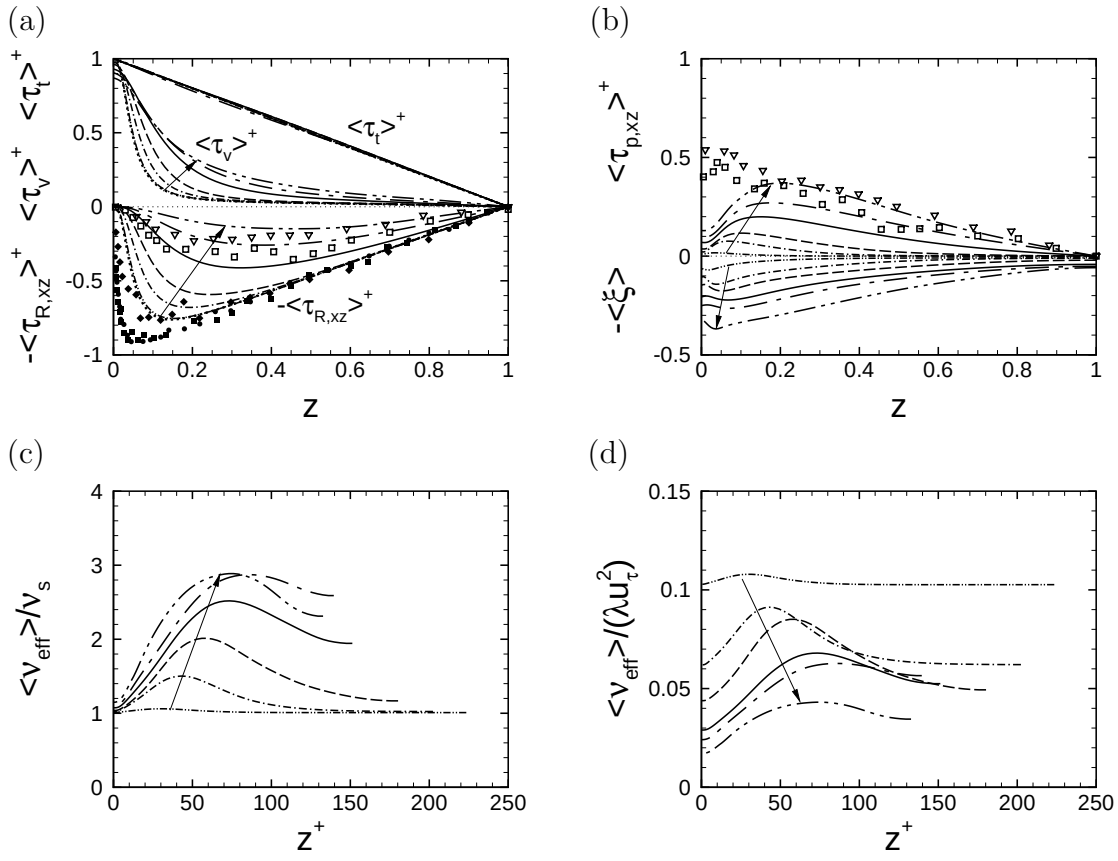

Figure 3.16: Effect of Weissenberg number on the predicted flow statistics at $10 \lesssim We_{\tau_b} \lesssim 150$ and $n_p k_B T/(\rho u_{\tau_b}^2) \approx 1 \times 10^{-3}$: (a) Reynolds shear stresses ($\langle \tau_{R,xz} \rangle^+$), viscous shear stresses ($\langle \tau_v \rangle^+$), and sum of Reynolds, viscous and polymer shear stresses ($\langle \tau_t \rangle^+$); (b) polymer shear stresses ($\langle \tau_{p,xz} \rangle^+$) and polymer extensions; (c) effective viscosities normalized with respect to ν_s; (d) effective viscosities normalized with respect to λu_τ^2. Line types same as in figure 3.15.

where the drag reduction is less than 50%, increasing the Weissenberg number results in a thickening of the buffer layer and an upward shift of the inertial sublayer, as shown in figure 3.15(b). These changes are accompanied by an increase in the streamwise turbulence intensity, and a decay of the spanwise and wall-normal turbulence intensities and the Reynolds shear stress, as shown in figures 3.15(c-d) and 3.16(a). At higher Weissenberg numbers, corresponding to drag reductions of greater than 50%, the mean velocity profiles approach Virk's MDR asymptote, while the peak of the streamwise turbulence intensity decays to values comparable to the Newtonian, and the spanwise and wall-normal turbulence intensities and the Reynolds shear stress continue to decay, as shown in figures 3.15(b-d) and 3.16(a). The polymer extension and the polymer shear stress monotonically increase with increasing Weissenberg number, as shown in figure 3.16(b). The first and second-order turbulence statistics, and polymer shear stresses predicted in DNS show agreement with the experimental data of Warholic, Massah & Hanratty (1999) and Ptasinski, *et al.* (2001) at comparable magnitudes of drag reduction. The magnitude of the effective viscosity normalized by ν_s increases from near Newtonian values at $We_{\tau_b} \approx 10$ to a peak magnitude of $\sim 3\nu_s$ at $We_{\tau_b} \gtrsim 100$, as shown in figure 3.16(c). In contrast, the magnitude of ν_{eff} normalized by λu_τ^2 decreases from $\sim 0.1(\lambda u_\tau^2)$ at $We_{\tau_b} \approx 10$ to $\sim 0.04(\lambda u_\tau^2)$ at $We_{\tau_b} \approx 150$, as shown in figure 3.16(d). These range of ν_{eff} values are comparable to $\nu_{eff,sat} \sim 0.1\lambda u_\tau^2$ predicted by Lumley's theory (eqn.1.6).

Figures 3.17 and 3.18 show the one-dimensional energy spectra predicted in these simulations at $z^+ \approx 30$ and 100, respectively. In the spectra of the streamwise velocity fluctuations, E_{uu}, the presence of the polymer leads to a drop of the turbulence

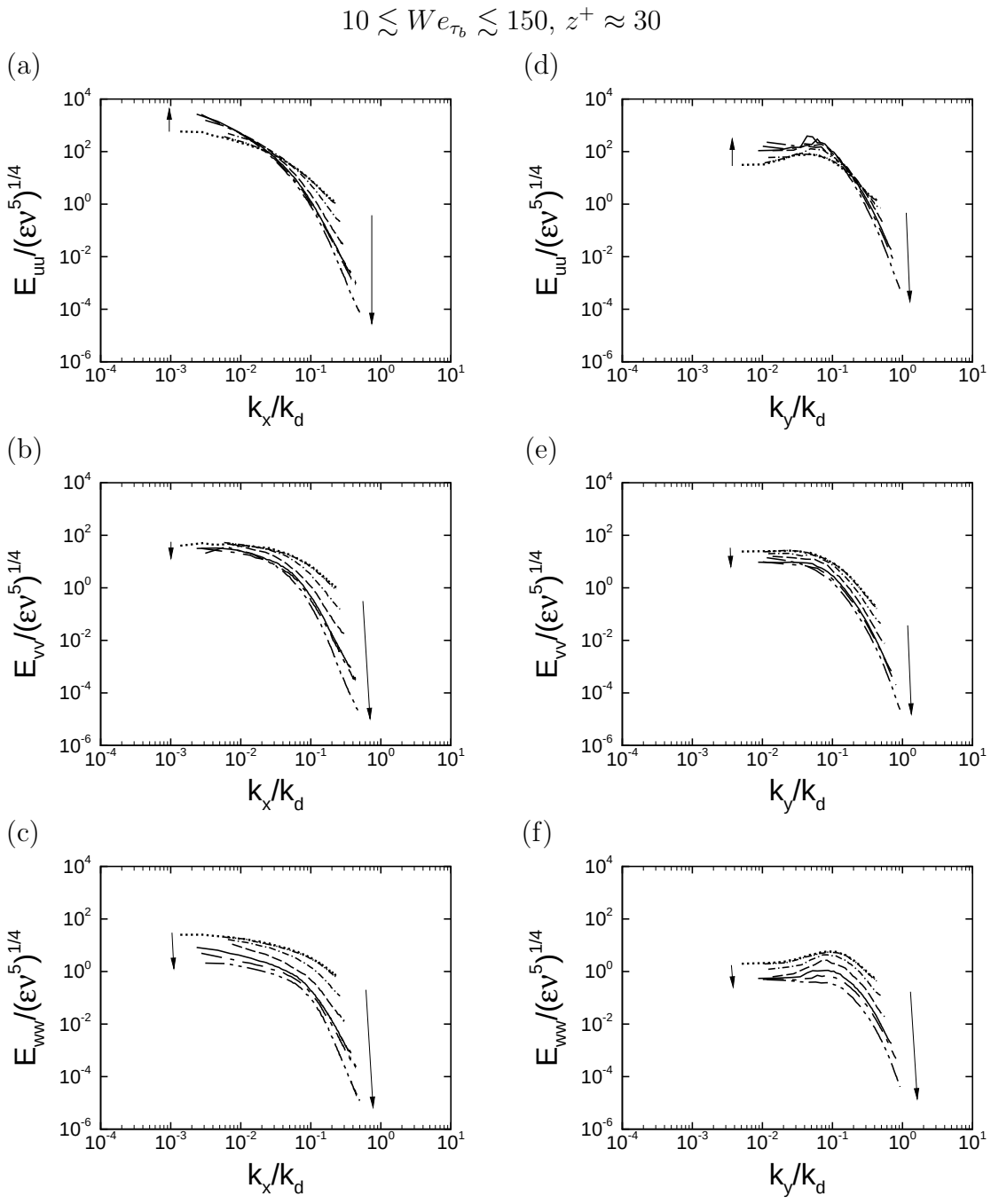

Figure 3.17: Effect of Weissenberg number on the one-dimensional energy spectra at $10 \lesssim We_{\tau_b} \lesssim 150$ and $n_p k_B T/(\rho u_{\tau_b}^2) \approx 1 \times 10^{-3}$: (a-c) streamwise spectra at $z^+ \approx 30$; (d-f) spanwise spectra at $z^+ \approx 30$. Line types same as in figure 3.15.

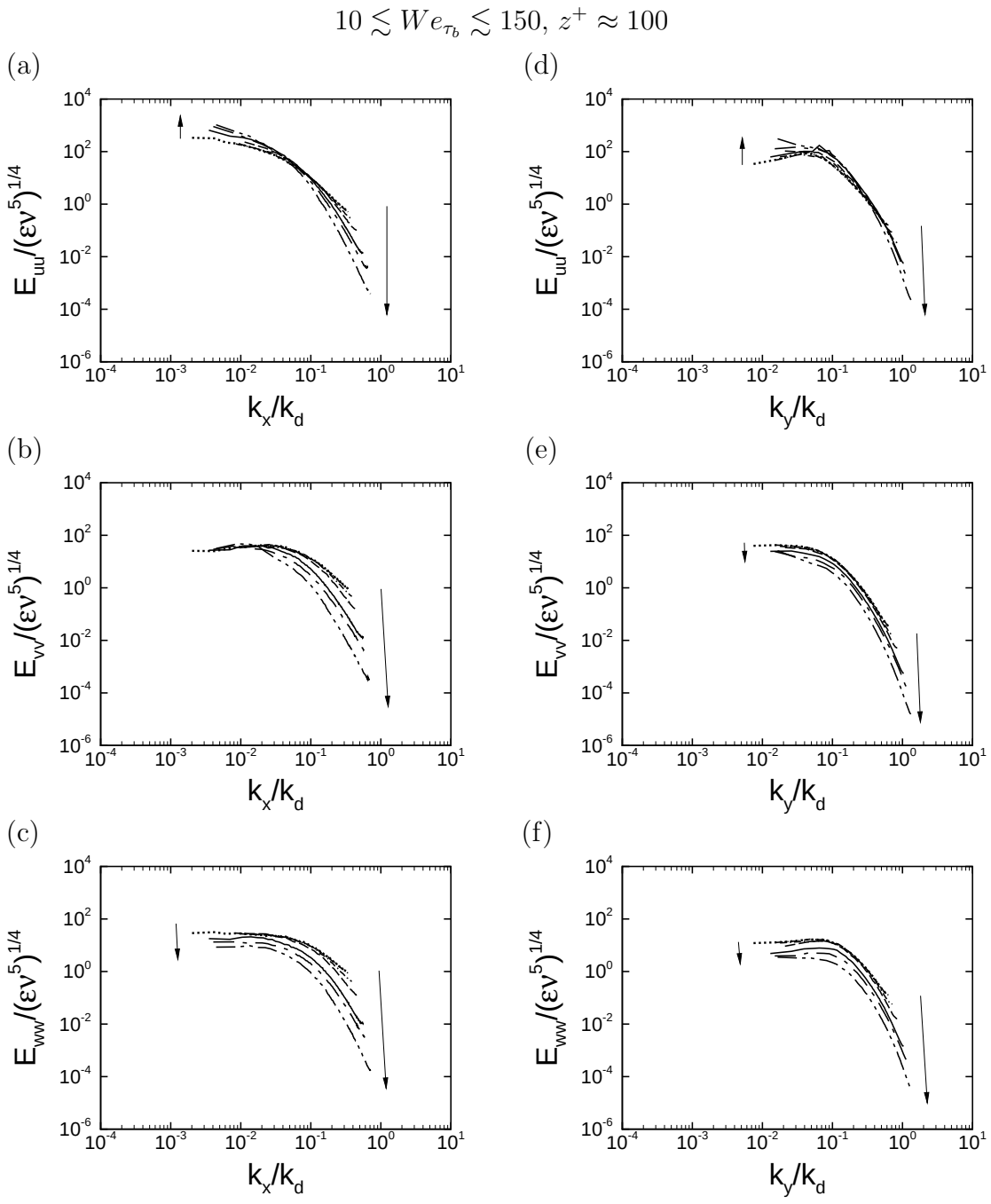

Figure 3.18: Effect of Weissenberg number on the one-dimensional energy spectra at $10 \lesssim We_{\tau_b} \lesssim 150$ and $n_p k_B T/(\rho u_{\tau_b}^2) \approx 1 \times 10^{-3}$: (a-c) streamwise spectra at $z^+ \approx 100$; (d-f) spanwise spectra at $z^+ \approx 100$. Line types same as in figure 3.15.

kinetic energy in the small scales and an enhancement of the turbulence kinetic energy in the largest scales, while in the spectra of the spanwise and wall-normal velocity fluctuations, E_{vv} and E_{ww}, all scales are damped. The degree of attenuation and the range of affected scales is a strong function of z^+ and the Weissenberg number. At $We_{\tau_b} \approx 10$, the spectra are nearly identical to Newtonian flow at both z^+ locations. At $We_{\tau_b} \approx 35$, the spectra are affected at $z^+ \approx 30$, but not so much at $z^+ \approx 100$. At higher Weissenberg numbers, the spectra are affected throughout the cross-section of the channel, although the degree of attenuation and the range of affected scales diminish as z^+ becomes larger.

3.3 Effect of polymer extensibility parameter on the flow statistics

Lastly, we investigate the effect of the polymer extensibility parameter on flow statistics. To this end, simulations were performed at $We_{\tau_b} \approx 35$ and $n_p k_B T/(\rho u_{\tau_b}^2) \approx 1 \times 10^{-3}$ with different values of the polymer extensibility parameter of $b = 4,500$, $45,000$ and $450,000$. A summary of the simulation parameters employed in these computations is provided in table 2.3.

The results are shown in figures 3.19 and 3.20. Increasing the extensibility parameter by two order of magnitude from $b = 4,500$ to $450,000$ results in only a slight increase in the magnitude of drag reduction from $\sim 29\%$ to $\sim 33\%$, as shown in figure 3.19(a) and table 2.3. These small changes in the drag reduction are also reflected as minor variations in the first and second-order turbulence statistics, as shown figures 3.19(b-d) and 3.20(a-b). The biggest change occurs in the magnitude of the polymer

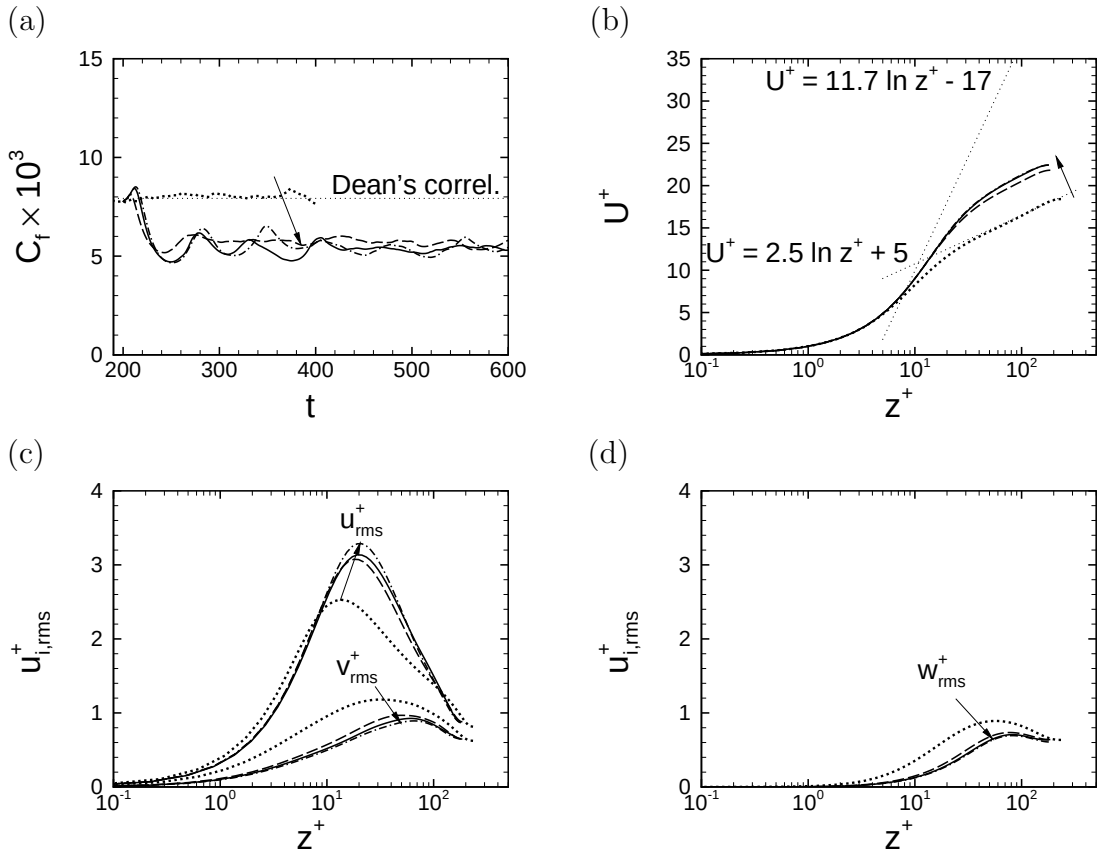

Figure 3.19: Effect of extensibility parameter on the predicted flow statistics at $We_{\tau_b} \approx 35$ and $n_p k_B T/(\rho u_{\tau_b}^2) \approx 1 \times 10^{-3}$: (a) time evolution of the skin friction coefficient; (b) mean velocity profiles; (c) r.m.s. of streamwise and spanwise velocity fluctuations; (d) r.m.s. of wall-normal velocity fluctuations. $\cdots\cdots$, Newtonian (case N); $---$, $b = 4,500$ (case C3.3-l); ——, $b = 45,000$ (case C3-l); $-\cdot-$, $b = 450,000$ (case C3.4-l).

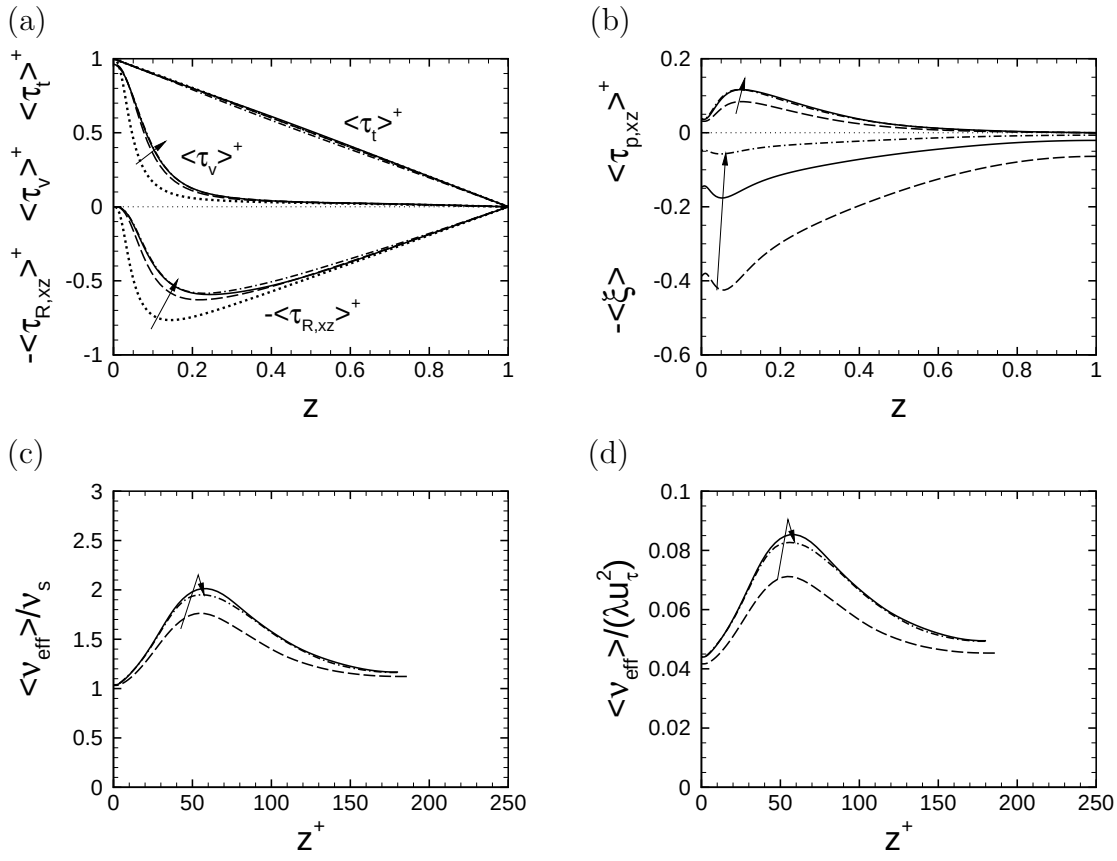

Figure 3.20: Effect of extensibility parameter on the predicted flow statistics at $We_{\tau_b} \approx 35$ and $n_p k_B T/(\rho u_{\tau_b}^2) \approx 1 \times 10^{-3}$: (a) Reynolds shear stresses ($\langle \tau_{R,xz} \rangle^+$), viscous shear stresses ($\langle \tau_v \rangle^+$), and sum of Reynolds, viscous and polymer shear stresses ($\langle \tau_t \rangle^+$); (b) polymer shear stresses ($\langle \tau_{p,xz} \rangle^+$) and polymer extensions; (c) effective viscosities normalized with respect to ν_s; (d) effective viscosities normalized with respect to λu_τ^2. Line types same as in figure 3.19.

extension, which decays from a peak value of $\sim 40\%$ of full extension at $b = 4,500$ to a peak value of $\sim 5\%$ of full extension at $b = 450,000$, as shown in figure 3.20(b). The effective viscosity normalized by ν_s or λu_τ^2 increases with b for $4,500 \leq b \leq 45,000$, but slightly decreases between $45,000 \leq b \leq 450,000$, as shown in figures 3.20(c-d). Overall, the effect of extensibility parameter on the flow statistics (and drag reduction) was found to be negligible in comparison to the effect of Weissenberg number or concentration. In real life, both the polymer extensibility parameter and relaxation time are determined by the polymer molecular weight. The results shown in this and the previous section demonstrate that the beneficial effects of raising the polymer molecular weight arise from the increase in the polymer relaxation time (or Weissenberg number) and not the extensibility parameter.

3.4 Effect of averaging time on the flow statistics at MDR

In their experimental studies, Warholic, Massah & Hanratty (1999) describe different flow statistics than those observed by Ptasinski, *et al.* (2001) and our DNS studies of figures 3.7 and 3.8 at MDR. In the MDR condition observed by Warholic, Massah & Hanratty (1999), the mean velocity profile conformed to Virk's ultimate profile (eqn.1.4), but the peak of the normalized streamwise and cross-stream turbulence intensities were significantly lower than Newtonian values, and the Reynolds shear stress was near-zero. These experimental data were obtained in short channel of length $433h$, where h is the channel half height. Figure 3.21 shows that the same conditions can be obtained from DNS at $We_{\tau_b} \approx 150$ and $n_p k_B T/(\rho u_{\tau_b}^2) \approx 1 \times 10^{-3}$ ($\beta \approx 0.86$) if the statistics are obtained from $450 \leq t \leq 650$. This averaging time corresponds to

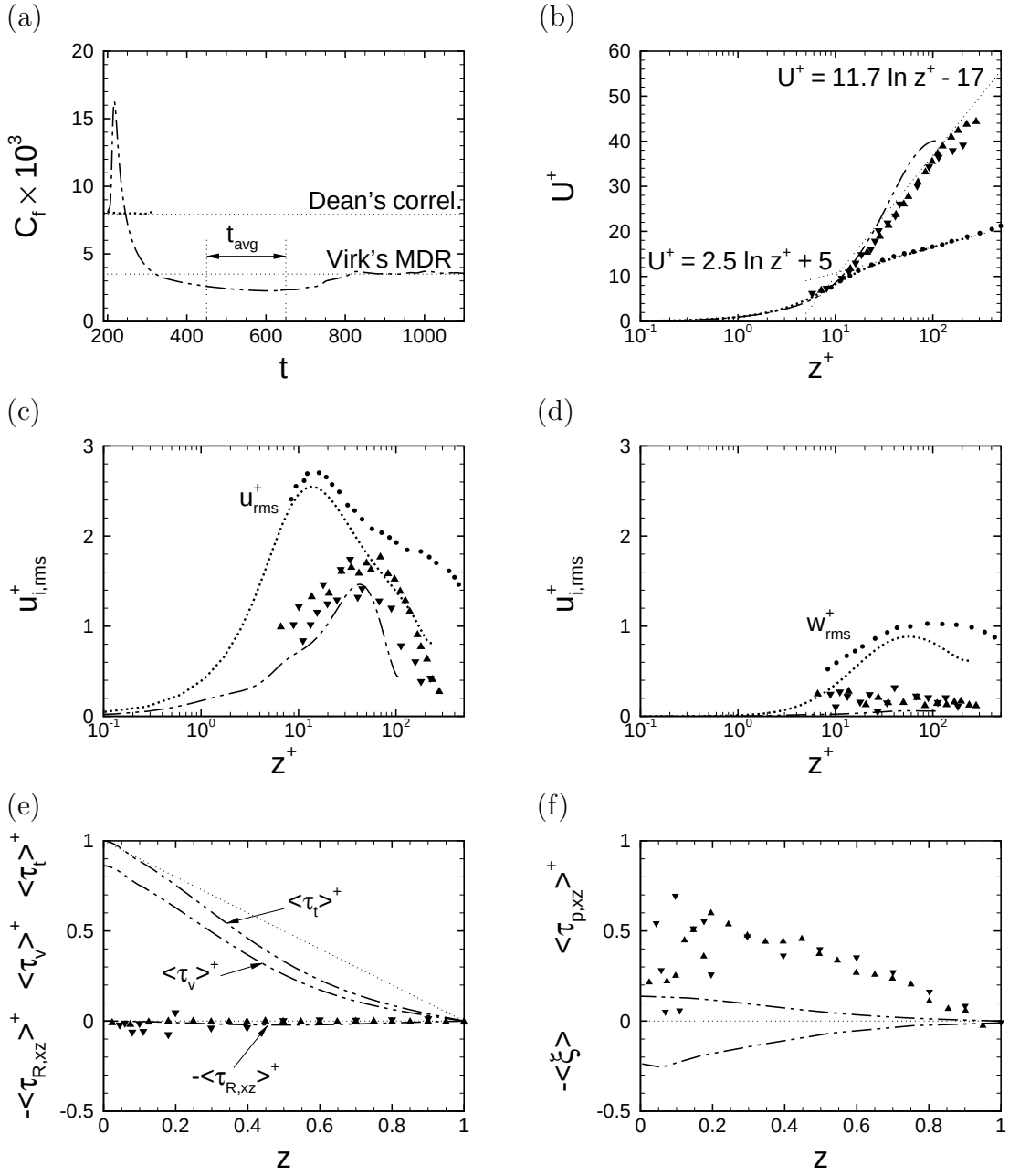

Figure 3.21: Effect of averaging time on the predicted flow statistics at $We_{\tau_b} \approx 150$ and $n_p k_B T/(\rho u_{\tau_b}^2) \approx 1\times10^{-3}$: (a) time evolution of the skin friction coefficient; (b) mean velocity profiles; (c) r.m.s. of streamwise velocity fluctuations; (d) r.m.s. of wall-normal velocity fluctuations; (e) Reynolds shear stresses ($\langle\tau_{R,xz}\rangle^+$), viscous shear stresses ($\langle\tau_v\rangle^+$), and sum of Reynolds, viscous and polymer shear stresses ($\langle\tau_t\rangle^+$); (f) polymer shear stresses ($\langle\tau_{p,xz}\rangle^+$) and polymer extensions. $\cdots\cdots$, Newtonian (case NN); ——··——, $We_{\tau_b} \approx 150$ (case FF3-q with statistics averaged over $450 \leq t \leq 650$); •, experiments of Warholic, *et al.*(1999) Newtonian; ▼, experiments of Warholic, *et al.*(1999) at 64%DR; ▲, experiments of Warholic, *et al.*(1999) at 69%DR.

the travel distance of the flow in the channel between $300h \leq \tilde{t}U_{bulk} \leq 433h$, which is consistent with the position of the test section in Warholic, Massah & Hanratty (1999) experiments ($315h - 433h$). Drag reduction of $\sim 70\%$ was predicted, which is comparable to the 69% drag reduction observed in the experiments of Warholic, Massah & Hanratty (1999). The mean velocity profile shows reasonable agreement with Virk's MDR asymptote and the experimental data of Warholic, Massah & Hanratty (1999) as shown in figure 3.21(b). The normalized turbulence intensities show good agreement with the experimental data of Warholic, Massah & Hanratty (1999) (figures 3.21c & 3.21d). The magnitudes of Reynolds shear stresses in both DNS and experiments are near-zero (figure 3.21e). However, the magnitude of polymer shear stress in DNS is lower than that in the experimental data (figure 3.21f). This is because the polymer shear stresses in Warholic, Massah & Hanratty (1999) experiments were computed using assumption of stationary steady-state viscoelastic flow, in which the sum of Reynolds, viscous and polymer shear stresses linearly decreases from the wall to the center of the channel. However, the total shear stress is not linear in transient state (figure 3.21e), indicating that the magnitudes of polymer shear stresses are overestimated in Warholic, Massah & Hanratty (1999) experiments. All these results indicate that the length of the channel in Warholic, Massah & Hanratty (1999) experiments is not long enough to reach the fully-developed state, and a length of $\gtrsim 600h$ is needed to get accurate statistics at MDR in experimental settings.

Chapter IV

Scaling of Drag Reduction with Polymer and Flow Parameters

Using the databases discussed in the previous section, we investigate the scaling of polymer drag reduction with polymer and flow parameters, and compare our results to the predictions of the theories of Lumley (1969, 1973) and de Gennes (1986).

4.1 Onset of drag reduction

Figure 4.1(a) shows the drag reductions obtained for the runs summarized in table 2.2 as a function of the viscosity ratio, β. For a free-draining FENE-P dumbbell, β is related to the polymer number density, n_p, polymer extensibility parameter, b, and polymer relaxation time, λ, through the relation (Bird, Dotson & Johnson, 1980)

$$\frac{1}{\beta} - 1 = \frac{n_p k_B T}{\mu_s} \lambda \frac{b}{b+3}. \tag{4.1}$$

A value of $\beta = 1$ corresponds to pure solvent, and β decreases monotonically between $0 < \beta < 1$ for increasing polymer number density. To determine the onset condition from the data shown in figure 4.1(a), the onset criteria is set at $0.5\%DR$. This value is chosen because the $\%DR$ cannot be determined to an accuracy greater than about 0.1% in the simulations. The onset parameters corresponding to $0.5\%DR$ in figure

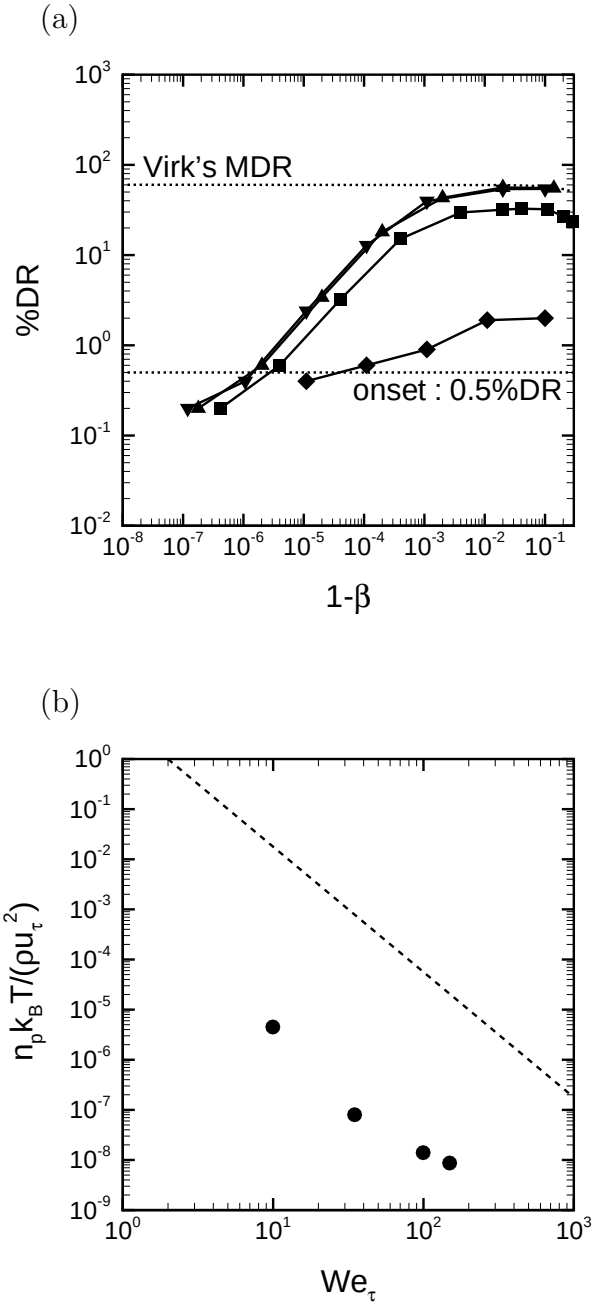

Figure 4.1: (a) Drag reduction as a function of the viscosity ratio, β, from DNS: —♦—, DNS at $We_{\tau_b} \approx 10$; —■—, DNS at $We_{\tau_b} \approx 35$; —▼—, DNS at $We_{\tau_b} \approx 100$; —▲—, DNS at $We_{\tau_b} \approx 150$. (b) Onset conditions observed in DNS compared to predictions of the elastic theory of de Gennes (1986): •, onset data from DNS; ---, $\frac{n_p k_B T}{\rho u_\tau^2}|_{onset} = (z^+)^{(\frac{15n}{8}-\frac{1}{2})} We_\tau^{-\frac{15n}{4}}$ (eqn. 4.2) with $n = 2/3$ and $z^+ = 10$.

4.1(a) are summarized in table 4.1.

Figure 4.1(b) shows $n_p k_B T/(\rho u_\tau^2)$ vs. We_τ corresponding to the onset data of table 4.1. Onset of drag reduction is observed to be a function of both the Weissenberg number and polymer concentration (or number density), as originally suggested by de Gennes (1986). The onset criteria of de Gennes (1986) was reinterpreted for wall-bounded flows by Sreenivasan & White (2000), who showed that in wall-bounded flows, the onset criteria of de Gennes corresponds to

$$\frac{n_p k_B T}{\rho u_\tau^2}|_{onset} = (z^+)^{(\frac{15n}{8}-\frac{1}{2})} We_\tau^{-\frac{15n}{4}} \quad \text{for} \quad z^+ \approx 10, \tag{4.2}$$

where $0 < n \leqslant 2$ is the dimensionality of the polymer stretching. A value of $n = 2/3$ was suggested by Sreenivasan & White (2000) based on analysis of a large body of experimental data, which suggest a scaling of $n_p k_B T/(\rho u_\tau^2) \sim We_\tau^{-2.5}$.

Figure 4.1(b) shows equation (4.2) with $n = 2/3$ compared to DNS data. It can be seen that while the slope of this line is comparable to the DNS data, the line intercept is several orders of magnitude too high.

Lumely's theory (1969, 1973) is of no help in resolving the discrepancy, as it predicts an onset criteria of $We_\tau \sim O(1)$, independent of concentration, in disagreement with the DNS data.

We_{τ_b}	We_τ	b	$1-\beta$	$\frac{n_p k_B T}{\rho u_\tau^2}$
10	9.95	45,000	4.5×10^{-5}	4.5×10^{-6}
35	34.82	45,000	2.8×10^{-6}	8.0×10^{-8}
100	99.50	45,000	1.4×10^{-6}	1.4×10^{-8}
150	149.25	45,000	1.3×10^{-6}	8.7×10^{-9}

Table 4.1: The onset conditions read from figure 4.1(a) at 0.5% drag reduction.

4.2 de Gennes's theory of polymer drag reduction revisited

To resolve the discrepancy between the DNS results and the predictions of the theory of de Gennes (1986), in this section we revisit this theory and develop a revised version of de Gennes's theory.

In the original theory of de Gennes (1986), turbulence dynamics is assumed to be affected by the polymer in turbulent eddies which (i) have a time-scale shorter than the polymer relaxation time λ, and (ii) have redirected "all" their turbulence kinetic energy into the elastic energy of the polymer. Let us denote by r^* the size of an eddy with characteristic time equal to λ, and by r^{**} the largest turbulent eddy of size less then r^* which has redirected all its turbulence kinetic energy to the elastic energy of the polymer.

4.2.1 Estimation of r^*

An expression for r^* can be found using the relation (de Gennes, 1986),

$$r^* = U(r^*)\lambda, \tag{4.3}$$

where $U(r^*)$ is the characteristic velocity at scale r^* and λ is the polymer relaxation time. The characteristic velocity $U(r^*)$ can be defined in terms of the wavenumber $k^* = 1/r^*$ and the spectral energy density $E(k)^*$ at scale k^* or r^* as $U(r^*) = [k^* E(k^*)]^{1/2}$. In the original theory of de Gennes (1986), a Kolmogorov spectrum was assumed for $E(k)$. In this study, we use the form of the spectrum suggested by Pao

(1965). In Pao's spectrum $E(k)$ is given by

$$E(k) = A_k \varepsilon^{2/3} k^{-5/3} F(k/k_d), \tag{4.4}$$

where $A_k = 1.5$ is the Kolmogorov constant and $F(k/k_d) = exp\left[-\frac{3}{2}A_K(k/k_d)^{4/3}\right]$. This gives

$$U(r^*) = A_k^{1/2}(r^*\varepsilon)^{1/3}\left\{F(k^*/k_d)\right\}^{1/2}. \tag{4.5}$$

Combining equations (4.3) and (4.5) gives

$$r^* = A_k^{1/2}(r^*\varepsilon)^{1/3}\lambda\left\{F(k^*/k_d)\right\}^{1/2}. \tag{4.6}$$

In wall-bounded flows, ε can be approximated as $\varepsilon \approx u_\tau^3/(\kappa z)$, where κ is the von Karman constant. Thus, for wall-bounded flows, r^* is given by

$$r^{*+} \equiv \frac{r^* u_\tau}{\nu_w} = \frac{We_\tau^{\frac{3}{2}}}{(\kappa z^+)^{\frac{1}{2}}} A_K^{\frac{3}{4}}\left\{F(k^*/k_d)\right\}^{\frac{3}{4}}, \tag{4.7}$$

where $k_d = (\nu_w^3/\varepsilon)^{-1/4}$, and $k^*/k_d = \kappa^{1/4} z^{+1/4}/r^{*+}$.

4.2.2 Estimation of r^{**}

In the original theory of de Gennes, the expression for r^{**} was found by requiring that the polymer elastic energy per unit volume due to stretching by turbulent scale r^{**} is equal to the turbulence kinetic energy per unit volume at scale r^{**}, or

$$n_p k_B T[\Xi(r^{**})]^{5/2} = \rho U^2(r^{**}), \tag{4.8}$$

where $\Xi(r^{**})$ is the polymer stretching by turbulent scale r^{**}, and $U(r^{**})$ is the characteristic velocity at scale r^{**}. de Gennes (1986) assumed an expression for

$\Xi(r^{**})$ given by

$$\Xi(r^{**}) = (r^*/r^{**})^n, \tag{4.9}$$

where $0 < n \leqslant 2$ is the dimensionality of the polymer stretching, $n = 2$ for three-dimensional flow and $n = 1$ for two-dimensional flow.

Here, we revise some of the assumptions in the original de Gennes's theory (1986) in view of the results observed in DNS:

1. Instead of assuming that the dynamics of turbulence is affected when "all" of the turbulence kinetic energy at a given scale is redirected into the elastic energy of the polymer, as assumed in the original de Gennes's theory (1986), here we assume that the dynamics of turbulence is affected when a minimum fraction, A_E, of the turbulence kinetic energy at a given scale has been redirected into the polymer elastic energy.

2. In addition, in the expression for polymer stretch we include polymer stretching due to the mean flow and turbulent scales other than r^{**}, which were ignored in the original de Gennes's theory (1986).

3. Furthermore, we assume a form of the energy spectrum appropriate for finite Reynolds number instead of the Kolmogorov spectrum appropriate for infinitely long inertial range as assumed by de Gennes (1986).

Under these new assumptions, the elastic energy in the polymer per unit volume due to stretching by turbulent scale r^{**} is no longer equal to $n_p k_B T[\Xi(r^{**})]^{5/2}$, because the polymer is stretched by other scales and by the mean flow as well. The contribution of

scale r^{**} to the total elastic energy is given by $\frac{\Xi(r^{**})}{\langle\Xi\rangle} n_p k_B T \langle\Xi\rangle^{5/2}$, where $\langle\Xi\rangle$ denotes the ensemble-averaged total polymer stretch by all turbulent scales and by the mean flow at location z^+. In addition, the amount turbulence kinetic energy which has been redirected into the polymer elastic energy is no longer $\rho U^2(r^{**})$ but $A_E \rho U^2(r^{**})$. With these assumptions, equation (4.8) is replaced with

$$n_p k_B T \frac{\Xi(r^{**})}{\langle\Xi\rangle} \langle\Xi\rangle^{5/2} \;=\; A_E \rho U^2(r^{**}) \tag{4.10}$$

or

$$n_p k_B T \langle\Xi\rangle^{3/2} [\Xi(r^{**})] \;=\; A_E \rho U^2(r^{**}). \tag{4.11}$$

As with the original derivation of de Gennes (1986), we estimate $\Xi(r^{**}) = (r^*/r^{**})^n$, where n is the dimensionality of the polymer stretching. Thus equation (4.11) reduces to

$$n_p k_B T \langle\Xi\rangle^{3/2} \left(\frac{r^*}{r^{**}}\right)^n \;=\; A_E \rho U^2(r^{**}). \tag{4.12}$$

The characteristic velocity $U(r^{**})$ is defined using Pao's spectrum (Pao, 1965) as

$$U(r^{**}) = A_k^{1/2} (r^{**}\varepsilon)^{1/3} \left\{F(k^{**}/k_d)\right\}^{1/2}, \tag{4.13}$$

where $F(k^{**}/k_d) = exp\left[-\frac{3}{2} A_K (k^{**}/k_d)^{4/3}\right]$, and $k^{**} = 1/r^{**}$ denotes the wavenumber corresponding to scale r^{**}. Taking the ratio of $U(r^{**})$ (eqn.4.13) to $U(r^*)$ (eqn.4.5), gives $U(r^{**})$ in terms of $U(r^*)$, r^* and r^{**} as

$$U(r^{**}) = U(r^*) \left(\frac{r^{**}}{r^*}\right)^{1/3} \left\{\frac{F(k^{**}/k_d)}{F(k^*/k_d)}\right\}^{1/2}. \tag{4.14}$$

Therefore, (4.12) can be rewritten as

$$\frac{n_p k_B T}{\rho U^2(r^*)} = A_E \left(\frac{r^{**}}{r^*}\right)^{n+2/3} \frac{1}{\langle\Xi\rangle^{3/2}} \left\{\frac{F(k^{**}/k_d)}{F(k^*/k_d)}\right\}. \tag{4.15}$$

Substituting $U(r^*)$ (eqn.4.5) into equation (4.15), approximating $\varepsilon \approx u_\tau^3/(\kappa z)$ in wall-bounded flow, and requiring that $r^{**} \leq r^*$, gives r^{**} in wall-bounded flow as

$$r^{**+}(z^+) = \min\left\{\frac{We_\tau^{\left(\frac{3}{2}-\frac{1}{n+2/3}\right)}}{(\kappa z^+)^{\left(\frac{1}{2}-\frac{1}{n+2/3}\right)}}\left[\frac{\langle\Xi\rangle^{\frac{3}{2}}}{A_E} A_K^{\frac{3n-4}{4}} \frac{n_p k_B T}{\rho u_\tau^2} \frac{\{F(k^*/k_d)\}^{\frac{3n}{4}}}{F(k^{**}/k_d)}\right]^{\frac{1}{n+2/3}} \text{ and } \quad r^{*+}\right\}, \tag{4.16}$$

where $r^{**+}(z^+) \equiv \frac{r^{**}u_\tau}{\nu_w}$, $k_d = (\nu_w^3/\varepsilon)^{-1/4} = (\nu_w^3 \kappa z/u_\tau^3)^{-1/4} = (u_\tau/\nu_w)^{3/4}(\kappa z)^{-1/4}$, and $k^{**}/k_d = \kappa^{1/4} z^{+1/4}/r^{**+}$.

4.2.3 Onset criteria based on the revised de Gennes's theory

Onset of drag reduction occurs when r^{**} equals the Kolmogorov scale at the outer edge of the viscous sublayer ($z^+ \approx 10$) or when $r^{**}(z^+) = (\nu_w^3/\varepsilon)^{1/4}|_{z^+\approx 10}$. Substituting for $r^{**+}(z^+)$ from equation (4.16) gives the onset criteria as

$$\langle\Xi\rangle^{3/2} \frac{n_p k_B T}{\rho u_\tau^2}|_{onset} = A_E\,(\kappa z^+)^{(\frac{3n}{4}-\frac{1}{2})} We_\tau^{-\frac{3n}{2}} A_k^{\frac{4-3n}{4}} \frac{F(k^{**}/k_d)}{\{F(k^*/k_d)\}^{\frac{3n}{4}}} \quad \text{at} \quad z^+ \approx 10. \tag{4.17}$$

Gives that at onset, $\langle\Xi\rangle$ is only due to the mean flow and scale r^{**}, and approximating the polymer stretch due to the mean flow with the Hookean dumbbell assumption, $We_\tau \frac{dU^+}{dz^+}$, gives the total polymer stretch at onset as $\langle\Xi\rangle \sim We_\tau \frac{dU^+}{dz^+} + (r^*/r^{**})^n$. With

this assumption, the onset criteria can be rewritten as

$$\frac{n_p k_B T}{\rho u_\tau^2}|_{onset} = \frac{A_E\,(\kappa z^+)^{(\frac{3n}{4}-\frac{1}{2})} We_\tau^{-\frac{3n}{2}} A_k^{\frac{4-3n}{4}}}{\left(We_\tau \frac{dU^+}{dz^+} + \frac{We_\tau^{\frac{3n}{2}}}{(\kappa z^+)^{\frac{3n}{4}}} A_K^{\frac{3n}{4}} \left\{F(k^*/k_d)\right\}^{\frac{3n}{4}}\right)^{3/2}} \frac{F(k^{**}/k_d)}{\left\{F(k^*/k_d)\right\}^{\frac{3n}{4}}}$$

$$\text{at} \quad z^+ \approx 10. \qquad (4.18)$$

4.2.4 Comparison to DNS data

Figure 4.2(a) shows $\langle \Xi \rangle^{3/2} \frac{n_p k_B T}{\rho u_\tau^2}$ plotted as a function of We_τ for onset data of table 4.1, where $\langle \Xi \rangle$ has been input from the DNS data. A least squares fit to the data, shown as the solid line in figure 4.2(a), indicates that the data fits equation (4.17) with $A_E \approx 0.03$ and $n = 2/3$. The value of $A_E \approx 0.03$ observed with this data indicates that the amount of energy which needs to be redirected to the polymer to affect the turbulence dynamics is miniscule, and nowhere near the $A_E = 1$ assumed in the original theory of de Gennes (1986). The dimensionality of the polymer stretching, $n = 2/3$, in the DNS data is consistent with the value of $n = 2/3$ proposed by Sreenivasan & White (2000) based on analysis of experimental data. Furthermore, this value of $n = 2/3$ makes the onset criterion of equation (4.17) independent of the wall-normal location.

Figure 4.2(b) shows the same onset criteria, plotted as $\frac{n_p k_B T}{\rho u_\tau^2}$ vs. We_τ, in comparison to equation (4.18) with $n = 2/3$ and $A_E \approx 0.03$. With $n = 2/3$, equation (4.18) gives the onset criteria as $\frac{n_p k_B T}{\rho u_\tau^2} \propto We_\tau^{-\frac{5}{2}}$. This $-5/2$ slope is also consistent with the value suggested by Sreenivasan & White (2000). However, comparison of figures 4.2(a) and 4.2(b) shows that equation (4.17) (plotted in figure 4.2a) shows better agreement with the DNS data than equation (4.18) (plotted in figure 4.2b).

(a)

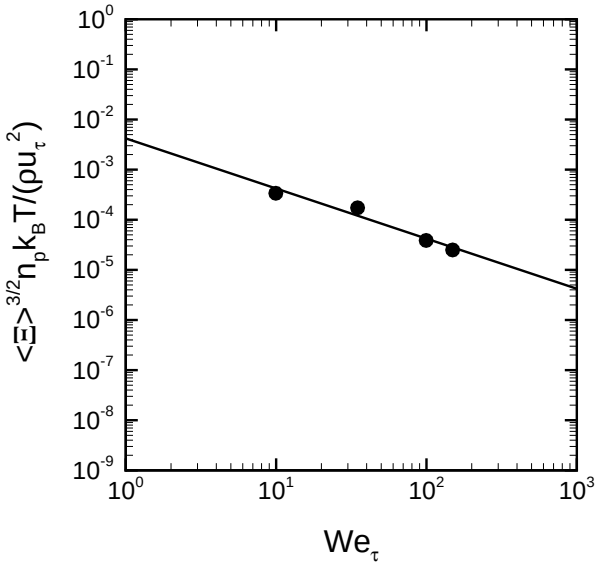

(b)

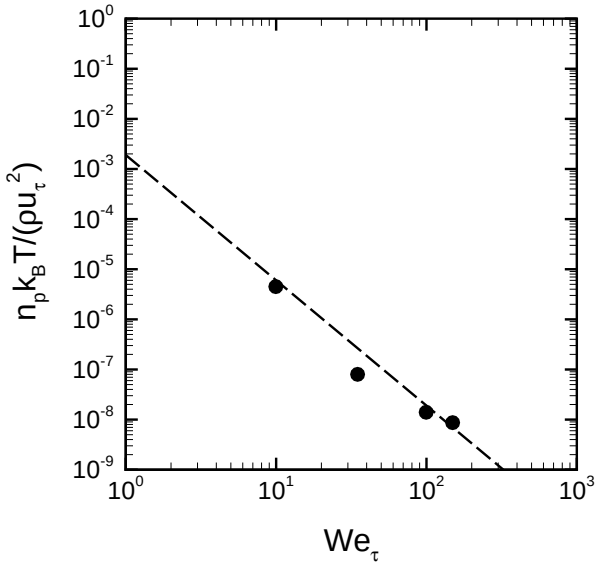

Figure 4.2: (a) Onset of drag reduction observed in DNS compared to revised theory of de Gennes: •, onset data from DNS; ——, $\langle\Xi\rangle^{3/2}\frac{n_p k_B T}{\rho u_\tau^2}|_{onset} = A_E\,(\kappa z^+)^{(\frac{3n}{4}-\frac{1}{2})} We_\tau^{-\frac{3n}{2}} A_k^{\frac{4-3n}{4}} \frac{F(k^{**}/k_d)}{\{F(k^*/k_d)\}^{\frac{3n}{4}}}$ (eqn. 4.17) with $A_E = 0.03$ and $n = 2/3$. (b) Onset of drag reduction observed in DNS compared to revised theory of de Gennes: •, onset data from DNS; – – –, $\frac{n_p k_B T}{\rho u_\tau^2}|_{onset} = \frac{A_E\,(\kappa z^+)^{(\frac{3n}{4}-\frac{1}{2})} We_\tau^{-\frac{3n}{2}} A_k^{\frac{4-3n}{4}}}{\left(We_\tau \frac{dU^+}{dz^+} + \frac{We_\tau^{\frac{3n}{2}}}{(\kappa z^+)^{\frac{3n}{4}}} A_K^{\frac{3n}{4}} \{F(k^*/k_d)\}^{\frac{3n}{4}}\right)^{3/2}} \frac{F(k^{**}/k_d)}{\{F(k^*/k_d)\}^{\frac{3n}{4}}}$ (eqn. 4.18) with $A_E = 0.03$ and $n = 2/3$.

This is because in equation (4.17) and figure 4.2(a) the exact value of $\langle \Xi \rangle$ is used, while in equation (4.18) and figure 4.2(b) $\langle \Xi \rangle$ is estimated based on a Hookean dumbbell, which is not that accurate for a FENE-P dumbbell when the polymer is near full-stretch as is the case in onset data of figures 3.3(f), 3.5(f) and 3.7(f) at onset.

4.3 Saturation of drag reduction

Figures 4.1(a) and 4.3(a) both also show the saturation of drag reduction in DNS. At all Weissenberg numbers, saturation is observed at $1 - \beta \approx 2 \times 10^{-2}$ or $\beta \approx 0.98$. However, the magnitude of drag reduction at saturation is a strong function of the Weissenberg number. At $We_{\tau_b} \approx 10$ and $We_{\tau_b} \approx 35$, only $\sim 2\%$ DR and $\sim 32\%$ DR, respectively, are observed at saturation, while at $We_{\tau_b} \approx 100$ and $We_{\tau_b} \approx 150$, drag reductions of $\sim 54\%$ and $\sim 56\%$ are observed, respectively.

Using the definition of β (eqn.4.1) and for $b \gg 1$, the saturation condition $\beta \approx 0.98$ observed in DNS can be expressed as

$$\frac{n_p k_B T}{\rho u_\tau^2}|_{sat} \approx (1 - \beta) We_\tau^{-1} \approx 0.02 We_\tau^{-1}. \tag{4.19}$$

This criterion has the same scaling as

$$n_p k_B T / (\rho u_\tau^2)|_{sat} \approx \beta We_\tau^{-1} \tag{4.20}$$

suggested by de Gennes (1986) (eqn.1.8), but is lower in magnitude by several orders. Figure 4.3(c) shows the saturation data from DNS compared to equations (4.19) and (4.20). While the saturation criterion (4.19) shows good agreement with the DNS data, the saturation criterion of de Gennes (1986) is higher than DNS by several

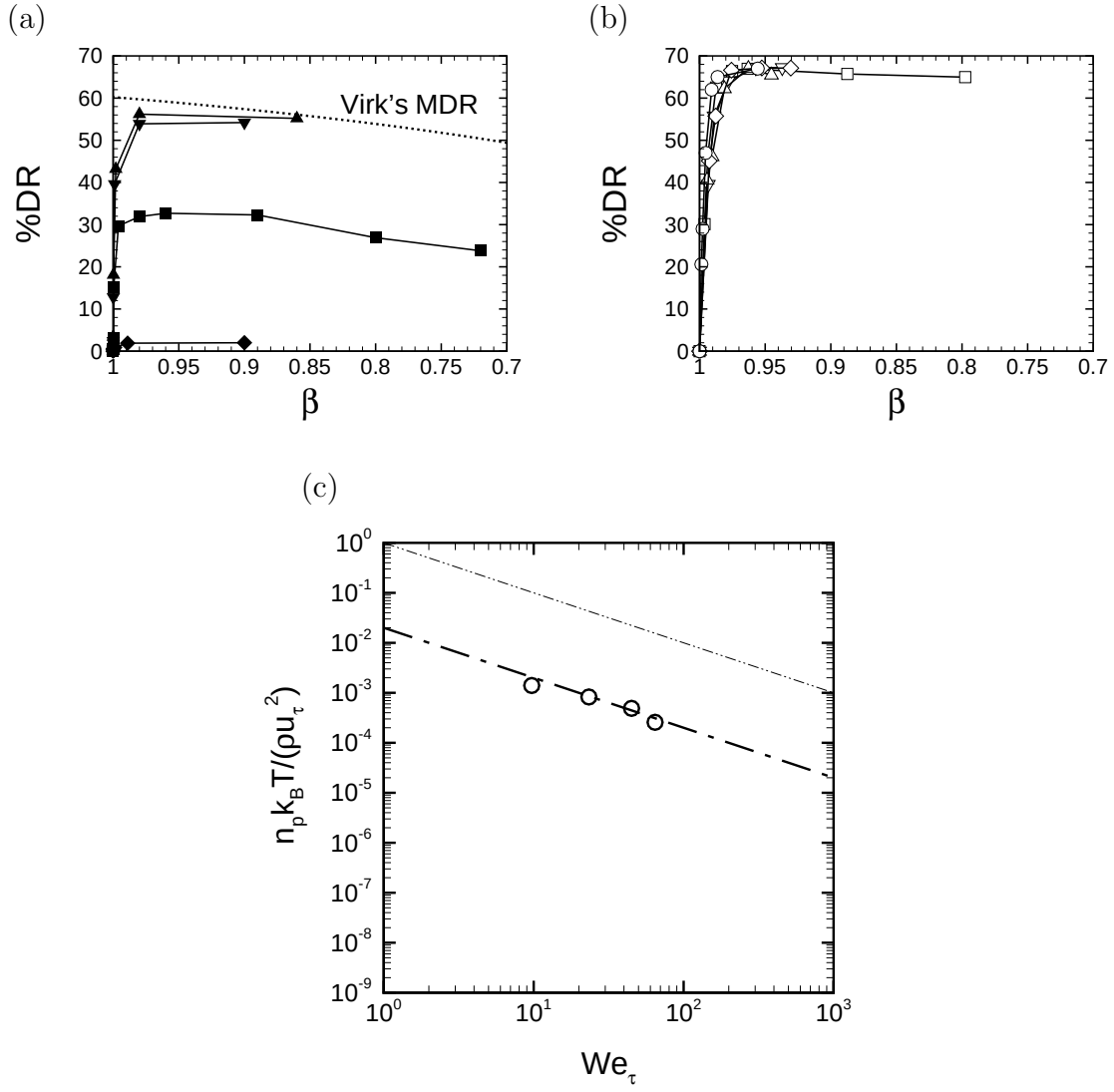

Figure 4.3: Saturation of drag reduction with increasing polymer concentration: (a) drag reduction as a function of the viscosity ratio, β, from DNS; (b) drag reduction as a function of the viscosity ratio, β, from experiments of Hoyt (1966) at $Re_{\tau_b} \approx 420$. —♦—, DNS at $We_{\tau_b} \approx 10$; —■—, DNS at $We_{\tau_b} \approx 35$; —▼—, DNS at $We_{\tau_b} \approx 100$; —▲—, DNS at $We_{\tau_b} \approx 150$; —□—, PEO of $M_w \approx 3.4 \times 10^6$ ($We_{\tau_b} \approx 1360$); —▽—, PEO of $M_w \approx 5.8 \times 10^6$ ($We_{\tau_b} \approx 3520$); —△—, PEO of $M_w \approx 7.0 \times 10^6$ ($We_{\tau_b} \approx 4930$); —◇—, PEO of $M_w \approx 8.0 \times 10^6$ ($We_{\tau_b} \approx 6260$); —○—, PAM of $M_w \approx 1.6 \times 10^6$ ($We_{\tau_b} \approx 230$); (c) Saturation of drag reduction observed in DNS compared to elastic theory of de Gennes (1986) and revised theory of de Gennes: ○, saturation data from DNS; – ·· –, $\frac{n_p k_B T}{\rho u_\tau^2}|_{sat} = We_\tau^{-1}$ (eqn. 4.20); —— · ——, $\frac{n_p k_B T}{\rho u_\tau^2}|_{sat} = (1-\beta) We_\tau^{-1}$ (eqn. 4.19) with $\beta = 0.98$.

orders of magnitude.

The trends in saturation of drag reduction observed in DNS (figure 4.3a) can also be observed in the experimental date (Hoyt, 1966), as shown in figure 4.3(b). Here the experimental data of Hoyt (1966), which were originally plotted as drag reduction vs. polymer molecular weight M_w, have been replotted as $\%DR$ vs. β. The value of $\beta \approx 0.98$ for which saturation is observed in DNS is also observed in experimental data.

In the Lumley's theory (Lumley, 1969, 1973), the saturation value of the effective viscosity, ν_w, in wall-bounded flows is given by (see eqn.1.6)

$$\nu_{eff,sat} \sim (0.2)^{4/3} \lambda u_\tau^2 \sim (0.1) \lambda u_\tau^2. \tag{4.21}$$

This alternative saturation criterion is also consistent with the DNS data, as shown in chapter III.

4.4 Criteria for maximum drag reduction (MDR)

Based on the data tabulated in table 2.2 and shown in figures 4.1(a) and 4.3(a), in the DNS simulations, which were performed at a base Reynolds number of $Re_{\tau_b} \approx 230$, MDR is achieved at saturation concentration ($\beta \approx 0.98$) at $We_{\tau_b} \approx 150$. The drag reduction of $DR \approx 56\%$, observed at MDR in DNS is comparable to the range of $57 - 60\%DR$ predicted by Virk's MDR asymptote (Virk, Mickley & Smith, 1970; Virk, 1975), as shown in figures 4.1(a) and 4.3(a).

The corresponding Re_τ and We_τ values at MDR, based on the values of u_τ and ν_w in viscoelastic flow, as opposed to the base flow, are $Re_\tau \approx 149$ at $We_\tau \approx 65$.

These suggest the MDR criterion as

$$We_\tau \sim O(Re_\tau/2). \tag{4.22}$$

This criterion is consistent with the MDR criterion of $We_\tau \sim O(Re_\tau)$, suggested by Lumley (1969, 1973) and de Gennes (1986).

4.5 Range of affected scales

Another important question in polymer drag reduction concerns the range of turbulent scales which have been affected by the polymer. In wall-bounded flows, Lumely's theory and the revised version of de Gennes's theory identify the size of the largest eddies affected by the polymer as r^* (eqn.4.7) and r^{**} (eqn.4.16), respectively. In DNS, an estimation of the size of the largest eddies attenuated by the polymer can be obtained from the largest damped scale in the spectra of E_{uu} at different wall-normal locations (figures 3.9-3.14). For reasons which will be explained in § 5.4, the E_{vv} and E_{ww} spectra show a decay at all scales and cannot be used for this purpose.

Figure 4.4 shows $r_x = 2\pi/k_{x,c}$ and $r_y = 2\pi/k_{y,c}$, where $k_{x,c}$ and $k_{y,c}$ are the wavenumbers of the largest damped scale compared to Newtonian flow in the spectra of $E_{uu}(k_x)$ and $E_{uu}(k_y)$ (figures 3.9-3.14), respectively, compared to r^* of Lumely's theory (eqn.4.7) and r^{**} of the revised de Gennes's theory (eqn.4.16) for all the runs at $We_{\tau_b} \approx 35$, 100, 150 tabulated in table 2.2. Comparison of r_x and r_y to r^* of Lumely's theory at $We_{\tau_b} \approx 35$, 100, 150 and different concentration (figures 4.4a-4.4c) shows that at saturation concentrations, the r_y/r^* approaches values $\sim O(1)$ at all Weissenberg numbers, while the magnitudes of r_x/r^* is about an order of

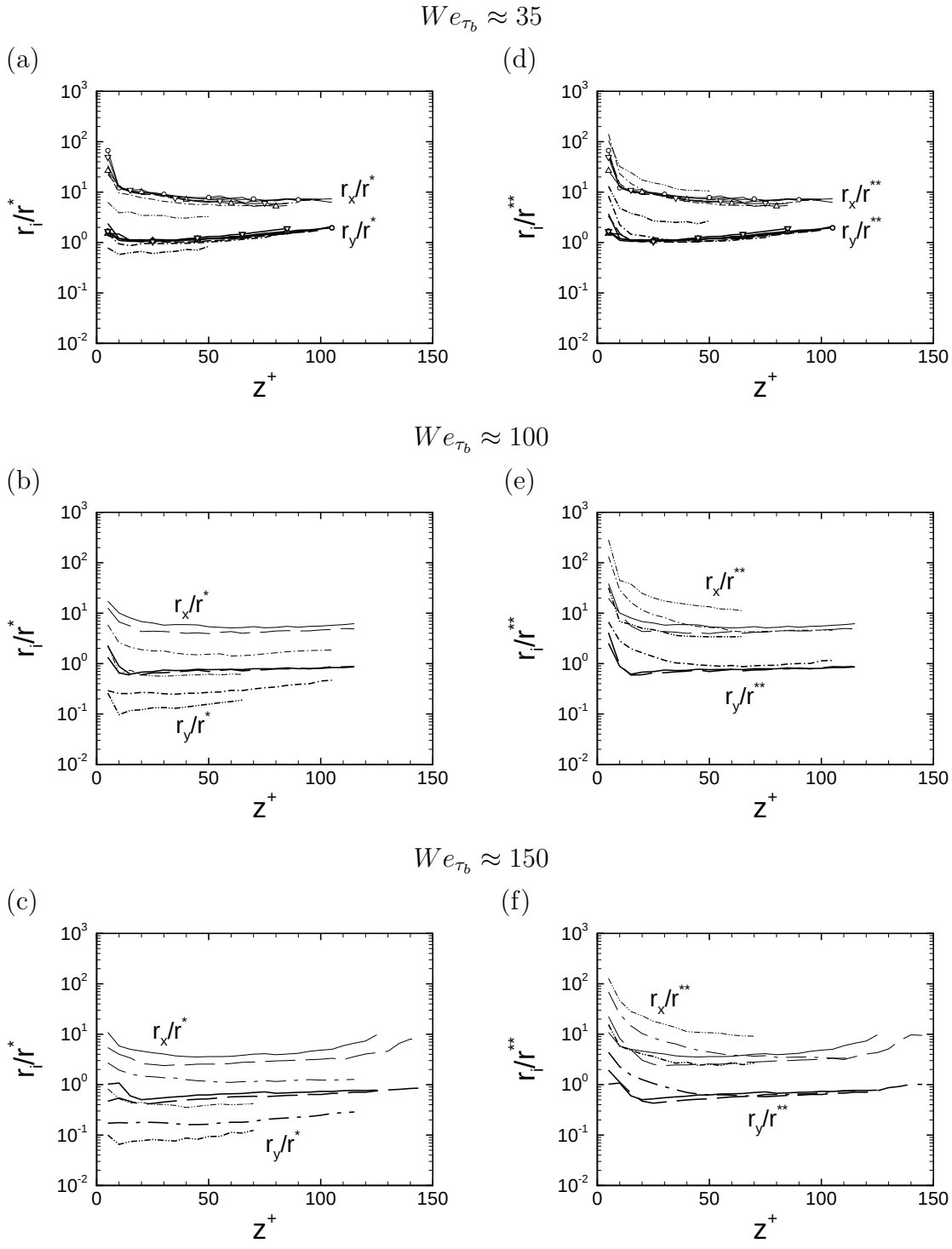

Figure 4.4: The largest streamwise and spanwise scales, r_x and r_y, damped by the polymer in the E_{uu} spectra (a,d) with varying the concentration at $We_{\tau_b} \approx 35$, (b,e) with varying the concentration at $We_{\tau_b} \approx 100$, and (c,f) with varying the concentration at $We_{\tau_b} \approx 150$, compared to predictions of Lumley's theory (Lumley, 1969, 1973) (eqn.4.7) and the revised theory of de Gennes (eqn.4.16): (a-c) r_i compared to r^* (eqn.4.7); (d-f) r_i compared to r^{**} (eqn.4.16) with $n = 2/3$ and $A_E = 0.03$. Line types in (a,d) same as in figure 3.3; line types in (b,e) same as in figure 3.5; line types in (c,f) same as in figure 3.7; thin lines, r_x; thick lines, r_y.

magnitude higher than the predictions of Lumley's theory. At concentration below the saturation concentration, r_i/r^* become lower than $O(1)$ and the data does not collapse at different concentrations.

Figures 4.4(d-f) show the comparison of r_i to r^{**} of the revised de Gennes's theory (eqn.4.16) (with $A_{turb} = 0.03$, $n = 2/3$ and the actual $\langle \Xi \rangle$ from DNS). A better collapse of the data is observed in this scaling at all Weissenberg numbers and concentrations. With the exception of the lowest concentration, the magnitudes of r_y/r^{**} approach values $\sim O(1)$ for all Weissenberg numbers and concentrations. The deviation at the lowest concentration is believed to be due to the polymer being close to full stretch, which makes some of the assumptions in de Gennes's theory (such as eqn.4.9) invalid. The magnitude of r_x/r^{**} is about an order of magnitude higher than r_y/r^{**}, reflecting the inhomogeneity of the turbulence structure in wall-bounded flow.

Figure 4.5 shows the comparison of r_i to r^* and r^{**} for $10 \lesssim We_{\tau_b} \lesssim 150$ at saturation concentration ($n_p k_B T/(\rho u_{\tau_b}^2) \approx 1 \times 10^{-3}$, corresponding to $0.86 \lesssim \beta \lesssim 0.989$). At saturation concentration, r_i/r^{**} and r_i/r^* become nearly identical. The magnitudes of both r_y/r^* and r_y/r^{**} approach values $\sim O(1)$ for all Weissenberg numbers, and r_x/r^* and r_x/r^{**} are about an order of magnitude higher than r_y/r^* and r_y/r^{**}, respectively.

Overall, these results indicate that Lumley's theory (Lumley, 1969, 1973) accurately predicts the range of affected scales at saturation concentration, while the revised theory of de Gennes proposed in this study can predict the range of affected scales at all but the most dilute concentrations. Neither theory accounts for inhomogeneity of the flow, which is a prominent feature in wall-bounded turbulence. As

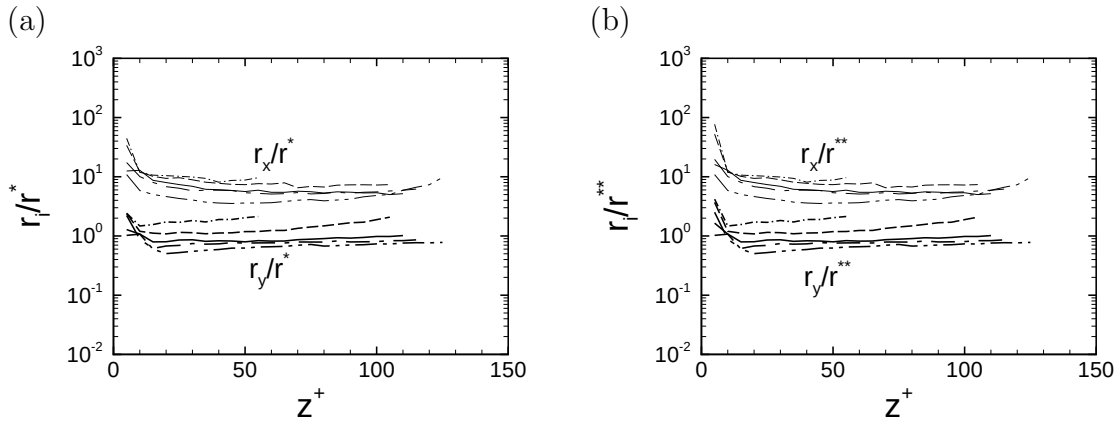

Figure 4.5: Effect of Weissenberg number on the largest streamwise and spanwise scales, r_x and r_y, damped by the polymer in the E_{uu} spectra at $10 \lesssim We_{\tau_b} \lesssim 150$ and saturation concentration of $n_p k_B T/(\rho u_{\tau_b}^2) \approx 1 \times 10^{-3}$: (a) r_i compared to r^* (eqn.4.7); (b) r_i compared to r^{**} (eqn.4.16) with $n = 2/3$ and $A_{turb} = 0.03$. Line types same as in figure 3.15; thin lines, r_x; thick lines, r_y.

such, the predictions of both theories are more directly applicable to the spanwise and, presumably, wall-normal directions, than the streamwise direction. Lumley's theory (Lumley, 1969, 1973) does not attempt to account for the effect of polymer concentration, but correctly accounts for the effect of Weissenberg number at saturation concentrations. The revised theory of de Gennes (eqn.4.16) is more complete and accounts for the effect of both the Weissenberg number and the polymer concentration.

Figures 4.6(a-c) show the r_x and r_y obtained from DNS normalized with respect to the channel half height, h, at $We_{\tau_b} \approx 35$, 100 and 150, respectively. At each Weissenberg number, the magnitudes of r_x and r_y shift to larger values as the polymer number density increases. At MDR, $r_y \sim h$. Figures 4.6(d-f) show the r_i in inner scaling. In the near wall region, the largest damped eddies have a spanwise size, r_y^+, of $\sim (100 - 500)$ wall units and a streamwise size, r_x^+, of $\sim (1000 - 6000)$ wall units, while in the core, the largest damped eddies have a spanwise size, r_y^+, of $\sim (30 - 100)$ wall units and a streamwise size, r_x^+, of $\sim (100 - 1000)$ wall units, depending on the polymer concentration and Weissenberg number.

Figures 4.7(a-c) show the r_i normalized with respect to u_τ and the effective viscosity, ν_{eff}, introduced in equation (3.1) and shown in figures 3.4(c-d), 3.6(c-d) and 3.8(c-d). Normalizing r_i using ν_{eff} does a somewhat better job of collapsing the data for different concentrations and Weissenberg numbers than ν_w used in the definition of $r^+ = ru_\tau/\nu_w$, but is does not fully collapse the data. Figures 4.7(d-f) show r_i normalized with respect to the polymer relaxation time, λ, and the wall friction velocity, u_τ. At the saturation concentration, $r_y \sim 2\lambda u_\tau$ at all Weissenberg numbers.

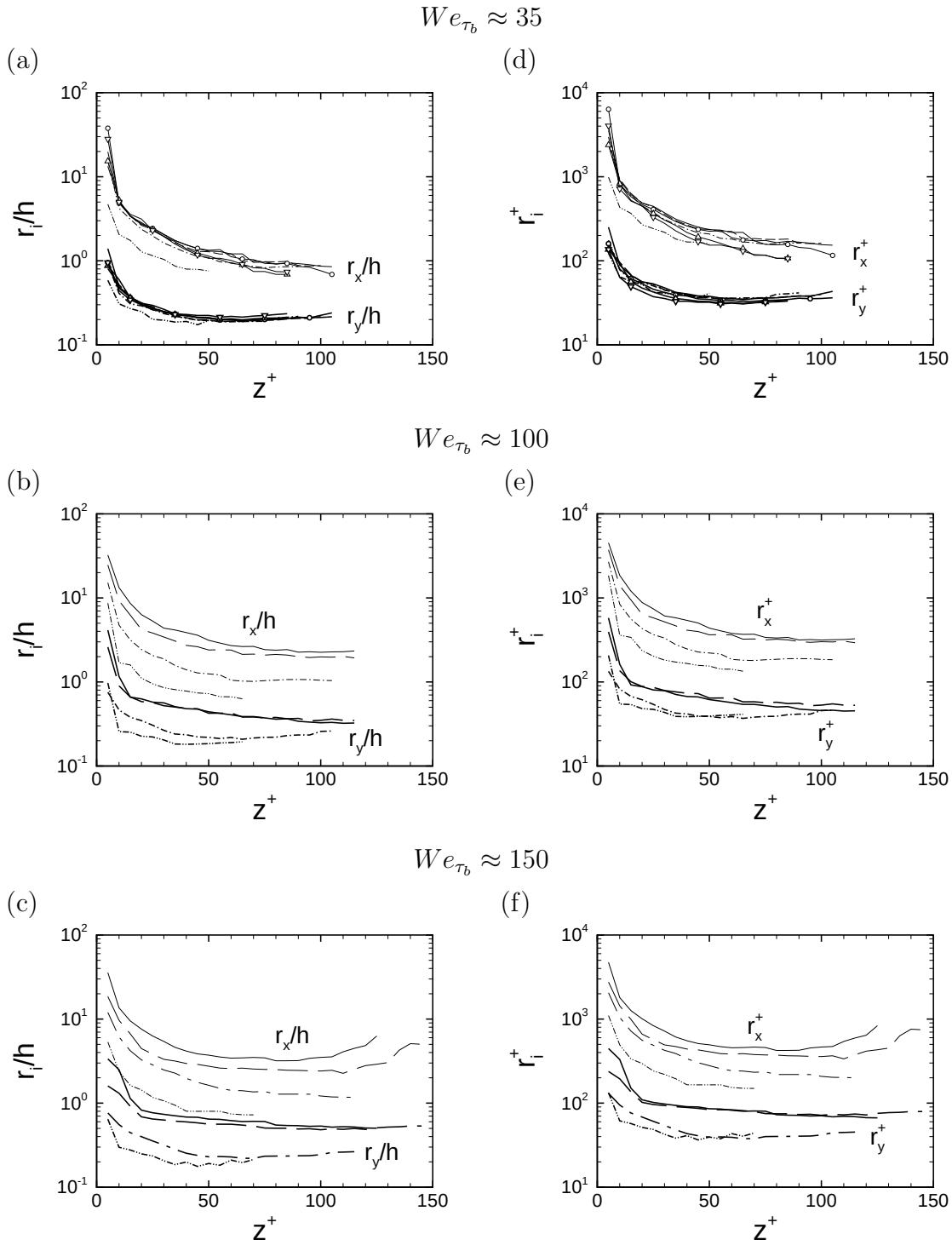

Figure 4.6: Effect of polymer concentration on the largest streamwise and spanwise scales, r_x and r_y, damped by the polymer in the E_{uu} spectra at (a,d) $We_{\tau_b} \approx 35$, (b,e) $We_{\tau_b} \approx 100$, (c,f) $We_{\tau_b} \approx 150$: (a-c) r_i in outer scaling; (d-f) r_i in inner scaling. Line types in (a,d) same as in figure 3.3; line types in (b,e) same as in figure 3.5; line types in (c,f) same as in figure 3.7; thin lines, r_x; thick lines, r_y.

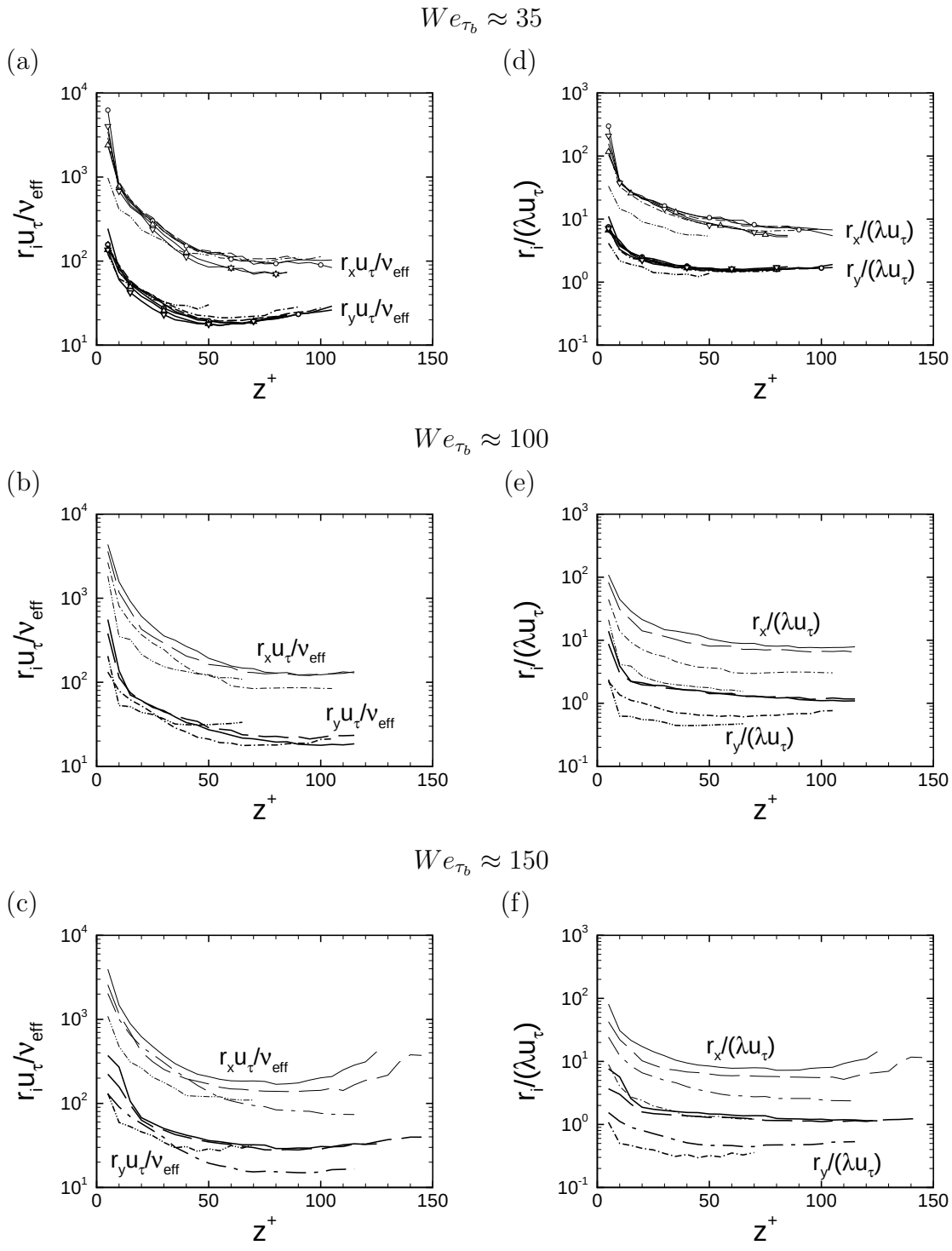

Figure 4.7: Effect of polymer concentration on the largest streamwise and spanwise scales, r_x and r_y, damped by the polymer in the E_{uu} spectra at (a,d) $We_{\tau_b} \approx 35$, (b,e) $We_{\tau_b} \approx 100$, (c,f) $We_{\tau_b} \approx 150$: (a-c) r_i normalized using ν_{eff} and u_τ; (d-f) r_i normalized using λ and u_τ. Line types in (a,d) same as in figure 3.3; line types in (b,e) same as in figure 3.5; line types in (c,f) same as in figure 3.7; thin lines, r_x; thick lines, r_y.

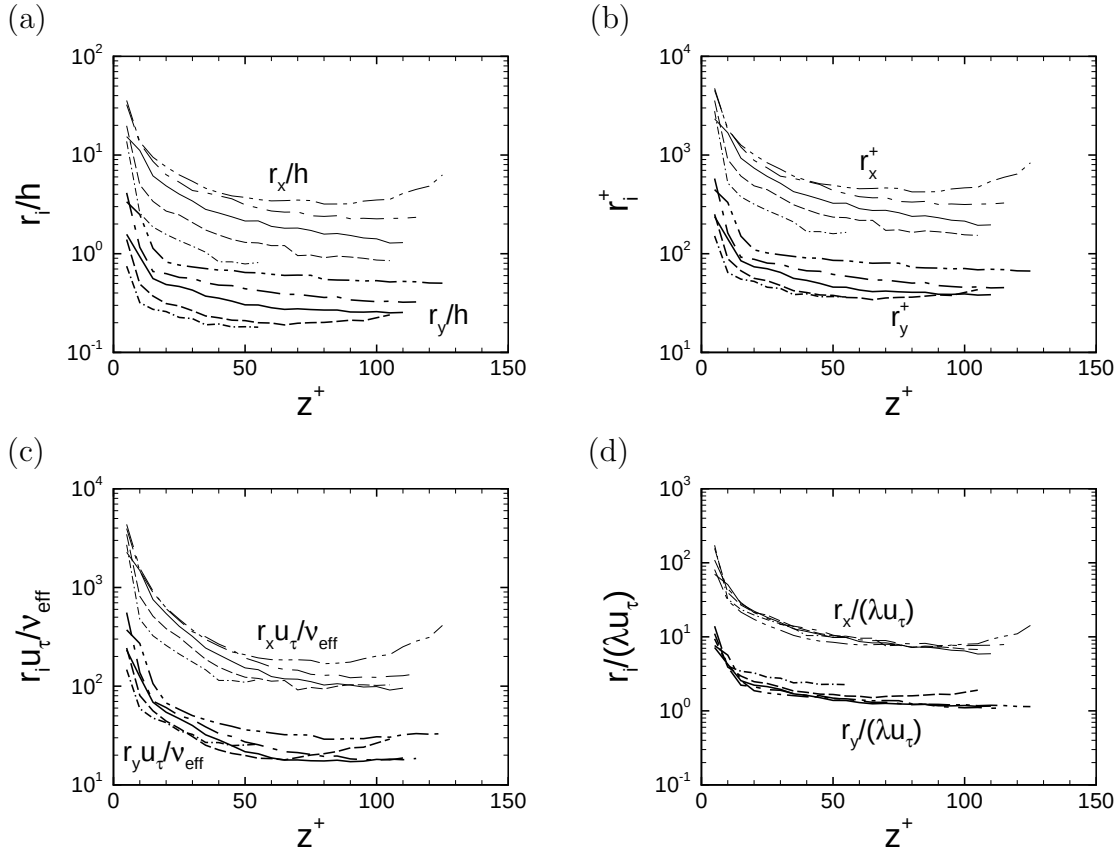

Figure 4.8: Effect of Weissenberg number on the largest streamwise and spanwise scales, r_x and r_y, damped by the polymer in the E_{uu} spectra at $10 \lesssim We_{\tau_b} \lesssim 150$ and saturation concentration of $n_p k_B T/(\rho u_{\tau_b}^2) \approx 1 \times 10^{-3}$: (a) r_i in outer scaling; (b) r_i in inner scaling; (c) r_i normalized using ν_{eff} and u_τ; (d) r_i normalized using λ and u_τ. Line types same as in figure 3.15; thin lines, r_x; thick lines, r_y.

Figure 4.8 shows r_i/h, r_i^+, $r_i u_\tau/\nu_{eff}$ and $r_i/(\lambda u_\tau)$ at saturation concentration ($n_p k_B T/(\rho u_{\tau_b}^2) \approx 1 \times 10^{-3}$, corresponding to $0.86 \lesssim \beta \lesssim 0.989$) for all Weissenberg numbers ($10 \lesssim We_{\tau_b} \lesssim 150$). Both r_i/h and r_i^+ increase with increasing Weissenberg number, with r_x approximately an order of magnitude larger than r_y in all cases (figures 4.8a-4.8b). At MDR, $r_y \sim h$ and $r_y \sim 2\lambda u_\tau$, as shown in figures 4.8(a,d). This gives the MDR criterion as $r_y \sim h \sim 2\lambda u_\tau$ or $\lambda u_\tau \sim O(h/2)$ or $We_\tau \sim O(Re_\tau/2)$, which is consistent with the equation (4.22). In the near wall region, the largest damped eddies have a spanwise size, r_y^+, of $\sim (100 - 600)$ wall units and a streamwise size, r_x^+, of $\sim (2000 - 5000)$ wall units, while in the core, the largest damped eddies have a spanwise size, r_y^+, of $\sim (30 - 70)$ wall units and a streamwise size, r_x^+, of $\sim (100 - 1000)$ wall units, depending on the Weissenberg number, as shown in figure 4.8(b). Normalizing r_i using v_{eff} results in a reasonable collapse of the data, as shown in figure 4.8(c). However, the best collapse of the data is obtained when r_x and r_y are normalized by λu_τ.

Chapter V

Mechanism of Drag Reduction

Using the databases discussed in chapter III and the revised de Gennes's theory introduced in chapter IV, we investigate the detailed mechanism of polymer drag reduction. Our objective is to presenta quantitative theory of polymer drag reduction which can explain all the features observed in the data of chapter III and IV.

5.1 Data analysis

A variety of turbulence measures were employed to clarify the mechanism of polymer drag reduction. These include the polymer and turbulence energetics, anisotropy-invariant maps, and comparisons of DNS results to predictions of classical theories of polymer drag reduction. A brief description of each measure is given below.

5.1.1 Polymer and turbulence energetics

To understand the energy exchanges between the polymer and turbulence, various terms in the turbulence kinetic energy budget and polymer elastic energy budget were examined.

In viscoelastic flow, the energy dynamics in the α-direction is governed by (Ptasin-

ski, *et al.*, 2003)

$$\frac{D\langle E_{\alpha\alpha}\rangle}{Dt} = \langle P_{\alpha\alpha}\rangle - \langle \varepsilon_{\alpha\alpha}\rangle + \langle \Pi_{\alpha\alpha}\rangle - \langle T_{\alpha\alpha}\rangle$$
$$+\langle t^{(v)}_{\alpha\alpha}\rangle + \langle t^{(R)}_{\alpha\alpha}\rangle + \langle t^{(press)}_{\alpha\alpha}\rangle + \langle t^{(p)}_{\alpha\alpha}\rangle \quad , \tag{5.1}$$

where no summation is implied over the index α, $\langle\cdot\rangle$ denotes an ensemble-averaged quantity obtained by averaging the quantity in the homogeneous flow directions and in time, $\langle E_{\alpha\alpha}\rangle = \frac{1}{2}\langle u'_\alpha u'_\alpha\rangle$ is the ensemble-averaged turbulence kinetic energy in the α-direction, $\langle P_{\alpha\alpha}\rangle = -\langle u'_\alpha u'_\gamma\rangle\frac{\partial U_\alpha}{\partial x_\gamma}$, $\langle \varepsilon_{\alpha\alpha}\rangle = \nu_s\langle\left(\frac{\partial u'_\alpha}{\partial x_\gamma}\right)^2\rangle$, $\langle \Pi_{\alpha\alpha}\rangle = \langle p'\frac{\partial u'_\alpha}{\partial x_\alpha}\rangle$, and $\langle T_{\alpha\alpha}\rangle = \langle \tau'_{p,\alpha\gamma}\frac{\partial u'_\alpha}{\partial x_\gamma}\rangle$ are the ensemble-averaged rates of turbulence production, viscous dissipation, pressure-strain correlation, and energy transfer from turbulence to the polymer in the α-direction, respectively, $\langle t^{(v)}_{\alpha\alpha}\rangle = \frac{\partial}{\partial x_\gamma}\left(\frac{\nu_s}{2}\frac{\partial}{\partial x_\gamma}\left(\langle u'_\alpha u'_\alpha\rangle\right)\right)$, $\langle t^{(R)}_{\alpha\alpha}\rangle = \frac{\partial}{\partial x_\gamma}\left(-\frac{1}{2}\langle u'_\alpha u'_\alpha u'_\gamma\rangle\right)$, $\langle t^{(press)}_{\alpha\alpha}\rangle = -\frac{\partial}{\partial x_\alpha}\left(\langle u'_\alpha p'\rangle\right)$, and $\langle t^{(p)}_{\alpha\alpha}\rangle = \frac{\partial}{\partial x_\gamma}\left(\langle u'_\alpha \tau'_{p,\alpha\gamma}\rangle\right)$ are the ensemble-averaged rates of transport by the fluctuating viscous stress, the fluctuating Reynolds stress, the fluctuating pressure, and the fluctuating polymer stress in the α-direction, respectively, u'_α and U_α are the fluctuating and mean velocities in the α-direction, respectively, p' is the fluctuating pressure, and τ'_p is the fluctuating polymer stress.

Summation of equation (5.1) over all α-direction gives the governing equation for the total turbulence kinetic energy as

$$\frac{D\langle E_{ii}\rangle}{Dt} = \langle P_{ii}\rangle - \langle \varepsilon_{ii}\rangle - \langle T_{ii}\rangle$$
$$+\langle t^{(v)}_{ii}\rangle + \langle t^{(R)}_{ii}\rangle + \langle t^{(press)}_{ii}\rangle \quad +\langle t^{(p)}_{ii}\rangle, \tag{5.2}$$

where the pressure-stain correlation term is eliminated because $\sum_\alpha \Pi_{\alpha\alpha} = 0$.

The energetics of the polymer is governed by (Ptasinski, *et al.*, 2003)

$$\frac{D\langle E_p\rangle}{Dt} = \langle T_U\rangle + \langle T_{ii}\rangle - \langle \varepsilon_p\rangle + \langle t_p\rangle, \tag{5.3}$$

where $\langle E_p\rangle$ is the ensemble-averaged elastic energy stored in the polymer due to transfer from the mean flow and turbulence, $\langle T_U\rangle = \langle \tau_{p,ij}\rangle \frac{\partial U_i}{\partial x_j}$ and $\langle T_{ii}\rangle = \langle \tau'_{p,ij}\frac{\partial u'_i}{\partial x_j}\rangle$ are the ensemble-averaged rates of energy transfer from the mean flow to the polymer and from turbulence to the polymer, respectively, $\langle \varepsilon_p\rangle$ is the ensemble-averaged rate of polymer dissipation, $\langle t_p\rangle = \frac{\partial}{\partial x_j}\left(\langle -u'_j E'_p\rangle\right)$ is the ensemble-averaged rate of energy transport by the polymer, τ_p is the polymer stress, and E_p is the total polymer elastic energy and $E'_p = E_p - \langle E_p\rangle$ is the fluctuating polymer elastic energy. For a FENE-P dumbbell model of the polymer, $\langle E_p\rangle = \frac{1}{2}\langle n_p k_B T b \ln(\frac{1}{1-Tr(\mathbf{A})/b})\rangle$, and $\langle \varepsilon_p\rangle = \frac{1}{2\lambda}\langle \frac{\tau_{p,ii}}{1-Tr(\mathbf{A})/b}\rangle$ (Ptasinski, *et al.*, 2003).

In addition to the above ensemble-averaged quantities, in the present study, we also track the time evolution of a number of instantaneous volume-averaged turbulence and polymer quantities, including the volume-averaged turbulence kinetic energy, $\langle E_{ii}(t)\rangle_V$, polymer elastic energy, $\langle E_p(t)\rangle_V$, rate of turbulence production, $\langle P_{ii}(t)\rangle_V$, rate of viscous dissipation, $\langle \varepsilon_{ii}(t)\rangle_V$, and rate of energy transfer from turbulence to the polymer, $\langle T_{ii}(t)\rangle_V$. In all these quantities, $\langle\cdot\rangle_V$ denotes volume average at time t, defined as

$$\langle \phi(t)\rangle_V = \frac{1}{L_x L_y L_z}\int_{L_z}\int_{L_y}\int_{L_x} \phi(t)\, dxdydz. \tag{5.4}$$

Furthermore, to separate the elastic energy stored in the polymer resulting from exchanges with the mean flow, $\langle E_{p,U}(t)\rangle_V$, from the elastic energy stored in the poly-

mer resulting from exchanges with turbulence, $\langle E_{p,tur}(t)\rangle_V$, we compute $\langle E_{p,U}(t)\rangle_V$ and $\langle E_{p,tur}(t)\rangle_V$ by time integration of the respective energy transfer rates minus the respective dissipation rates, as

$$\langle E_{p,U}(t)\rangle_V = \frac{1}{L_x L_y L_z}\int_{t_o}^{t}\int_{L_z}\int_{L_y}\int_{L_x}\left[T_U(t) - \frac{T_U(t)}{T_U(t)+T_{ii}(t)}\varepsilon_p(t)\right]dxdydzdt, \tag{5.5}$$

$$\langle E_{p,tur}(t)\rangle_V = \frac{1}{L_x L_y L_z}\int_{t_o}^{t}\int_{L_z}\int_{L_y}\int_{L_x}\left[T_{ii}(t) - \frac{T_{ii}(t)}{T_U(t)+T_{ii}(t)}\varepsilon_p(t)\right]dxdydzdt, \tag{5.6}$$

where t_o is the time at the start of viscoelastic simulations, $T_U = \tau_{p,ij}\frac{\partial U_i}{\partial x_j}$ is the rate of energy transfer from the mean flow to the polymer, $T_{ii} = \tau_{p,ij}\frac{\partial u_i'}{\partial x_j}$ is the rate of energy transfer from turbulence to the polymer, and $\varepsilon_p = \frac{1}{2\lambda}\frac{\tau_{p,ii}}{1-Tr(\mathbf{A})/b}$ is the rate of polymer dissipation.

5.1.2 Anisotropy-invariant maps

As will be shown in § 5.2.2, anisotropy plays a major role in the mechanism of polymer drag reduction. To quantify the degree of anisotropy in the flow, we examine the anisotropy-invariant maps based on the scalar invariants of the anisotropy tensor, as defined by Lumley & Newman (1977),

$$\mathrm{II} = b_{ij}b_{ji}, \tag{5.7}$$

$$\mathrm{III} = b_{ij}b_{jk}b_{ki}, \tag{5.8}$$

where $b_{ij} = \langle u_i'u_j'\rangle/\langle u_k'u_k'\rangle - \delta_{ij}/3$ is the anisotropy tensor.

All physically realizable turbulence is bound by the three lines given by II =

(a)

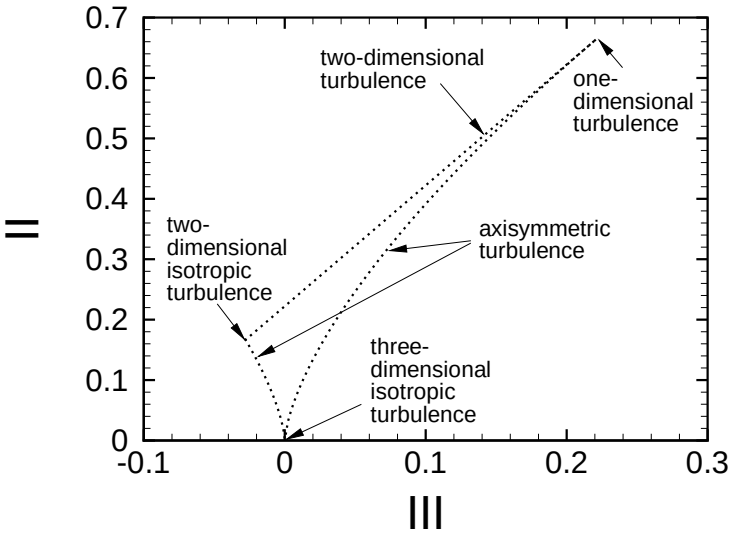

(b)

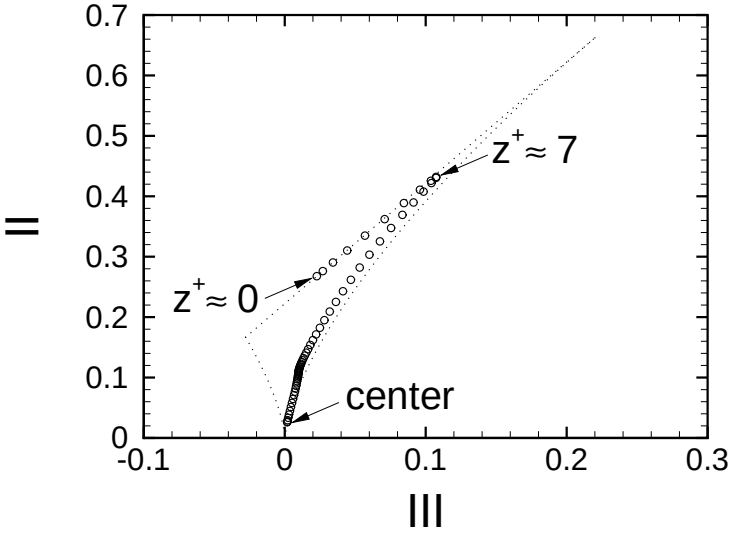

Figure 5.1: Anisotropy-invariant maps showing (a) limiting states of turbulence and (b) data from Newtonian turbulent channel flow at $Re_{\tau_b} \approx 230$ (case NN).

$\frac{2}{9} + 2\text{III}$ and the two branches of $\text{II} = \frac{3}{2}\left(\frac{4}{3}|\text{III}|\right)^{2/3}$, as shown in figure 5.1(a). The line $\text{II} = \frac{2}{9} + 2\text{III}$ represents two-dimensional turbulence, while the two branches of $\text{II} = \frac{3}{2}\left(\frac{4}{3}|\text{III}|\right)^{2/3}$ represent turbulence strained by axisymmetric expansion and axisymmetric contraction, respectively. The intersection of these lines denotes the limiting states of turbulence, corresponding to three-dimensional isotropic turbulence at (0,0), two-dimensional isotropic turbulence at $(-\frac{1}{36},\frac{1}{6})$, and one-dimensional turbulence at $(\frac{2}{9},\frac{2}{3})$, respectively.

In Newtonian turbulent channel flow, the data points corresponding to the viscous sublayer lie along the two-dimensional turbulence line, the data points corresponding to the buffer layer lie close to the axisymmetric expansion line, while at the center of the channel, the data points move towards the three-dimensional isotropic turbulence limit, as shown in figure 5.1(b).

5.1.3 Comparison to predictions of classical theories

A critical unanswered question in polymer drag reduction concerns the range of turbulent scales which are affected by the polymer and the manner in which these scales are affected.

The two principal theories of polymer drag reduction, suggested by Lumley (1969, 1973) and de Gennes (1986), respectively, identify the range of turbulent eddies which are affected by the polymer based on the eddy characteristic times. In the theory of Lumley, it is suggested that the largest eddies affected by the polymer have a

characteristic time, T^*, equal to the polymer relaxation time, λ, or

$$T^{*+} = We_\tau, \tag{5.9}$$

where $T^{*+} \equiv \frac{T^* u_\tau^2}{\nu}$, $We_\tau \equiv \frac{\lambda u_\tau^2}{\nu}$, and u_τ and ν are the wall-friction velocity and kinematic viscosity in the viscoelastic flow, respectively, where ν is commonly defined as either the zero shear viscosity, ν_o, or the wall-shear viscosity, $\nu_w = \frac{\tau_w}{\rho(dU/dz)_w}$, of the viscoelastic flow.

In the theory of de Gennes, it is suggested that the turbulence dynamics is affected in a turbulent eddy when the eddy has a characteristic time shorter than λ and it has redirected "all" its turbulence kinetic energy into the elastic energy of the polymer. In practice, the conditions suggested by de Gennes's original theory have never been observed in either experiments or DNS, the theory gives predictions which are orders of magnitude off from observations in both experiments (Sreenivasan & White, 2000) and DNS, as shown in chapter IV.

A revised version of the theory of de Gennes was proposed in § 4.2, in which it is assumed that the turbulence dynamics is affected in a turbulent eddy when the eddy has a characteristic time shorter than λ and it has redirected a minimum fraction, A_E, of its turbulence kinetic energy into the elastic energy of the polymer. With these assumptions, it can be shown that the largest eddies affected by the polymer have a characteristic time, T^{**}, given by

$$T^{**+}(z^+) = \min\left\{ We_\tau^{\left(1-\frac{2/3}{n+2/3}\right)} \left[\frac{\langle \Xi \rangle^{\frac{3}{2}}}{A_E} \; \frac{n_p k_B T}{\rho u_\tau^2} \; \frac{\kappa z^+}{A_K^{\frac{3}{2}}} \; \frac{\{F(k^*/k_d)\}^{\frac{3n}{4}}}{\{F(k^{**}/k_d)\}^{\frac{3n}{4}+\frac{3}{2}}} \right]^{\frac{2/3}{n+2/3}} \text{and} \quad We_\tau \right\}, \tag{5.10}$$

where A_K is the Kolmogorov constant, $F(k/k_d) = \exp\left[-\frac{3}{2}A_K(k/k_d)^{4/3}\right]$ is the dissipation range correction to the Kolmogorov inertial range spectrum suggested by Pao (1965), $k_d = (\nu^3/\varepsilon)^{-1/4}$ is the Kolmogorov wavenumber, k^* and k^{**} are the wavenumbers of a turbulent eddy with characteristic time equal to T^* and T^{**}, respectively, κ is the von Karman constant, Ξ is the total polymer stretch, A_E is the fraction of turbulence kinetic energy at wavenumber k^{**} redirected into the elastic energy of the polymer, and $0 < n \leqslant 2$ denotes the dimensionality of the polymer stretching. Comparison of the predictions of this theory with DNS results in viscoelastic turbulent channel flow suggested values of $A_E \approx 0.03$ and $n = 2/3$, as shown in chapter IV.

To compare these predictions with DNS results in viscoelastic turbulent channel flow, the characteristic time, $\tau^+(k_i^+, z^+)$, of an eddy with wavenumber k_i^+ in the ith direction at wall-normal location z^+ is defined as the inverse of the eddy characteristic strain-rate, $\tau^+(k_i^+, z^+) \equiv [s^+(k_i^+, z^+)]^{-1}$, where

$$s^+(k_i^+, z^+) \equiv \sqrt{\frac{D^+(k_i^+, z^+)}{2} k_i^+}, \tag{5.11}$$

and $D^+(k_i^+, z^+)$ is the one-dimensional dissipation spectrum at wavenumber k_i^+ and wall-normal location z^+.

5.2 Some key features of polymer drag reduction

To illustrate several key features of polymer drag reduction, in this section, we review some of the DNS studies results from two representative cases of viscoelastic turbulent channel flow described in chapter III; one at low drag reduction (LDR), and the other at high drag reduction (HDR) and approaching maximum drag reduction

(MDR). The LDR case (CC3-q) corresponds to $33\%DR$ and was obtained with the simulation parameters $We_{\tau_b} \approx 35$, $n_p k_B T/\rho u_{\tau_b}^2 \approx 1\times10^{-3}$ ($\beta \approx 0.96$), and $b = 45,000$. The HDR case (FF4-q) corresponds to $56\%DR$ and was obtained with the simulation parameters $We_{\tau_b} \approx 150$, $n_p k_B T/\rho u_{\tau_b}^2 \approx 1 \times 10^{-4}$ ($\beta \approx 0.98$), $b = 45,000$. Both simulations were preformed in channels of size $\frac{320\pi}{27}h \times \frac{16\pi}{5}h \times 2h$, were driven at constant flow rate, and were initialized by introducing the polymer in its coiled state into a fully-developed base Newtonian turbulent flow.

5.2.1 Minimal exchange of energy between turbulence and polymer

Figures 5.2(a) and 5.2(b) show the time histories of the volume-averaged turbulence kinetic energy, $\langle E_{ii}(t)\rangle_V/(U_{bulk}^2/2)$, and polymer elastic energy originating from turbulence, $\langle E_{p,tur}(t)\rangle_V/(U_{bulk}^2/2)$, in the LDR and HDR cases, respectively. Immediately following the introduction of the polymer into the base Newtonian turbulent flow at $t = 200$ (time O), the polymer begins to uncoil, resulting in growth of $\langle E_{p,tur}(t)\rangle_V$ between the times of O and P for a time period corresponding to $\frac{\Delta\tilde{t}U_{bulk}}{h} \sim 11$ ($200 < t < 217$) in the LDR case and $\frac{\Delta\tilde{t}U_{bulk}}{h} \sim 16$ ($200 < t < 224$) in the HDR case, where $\tilde{t}$ denotes the dimensional time. This growth in $\langle E_{p,tur}(t)\rangle_V$ is accompanied by a simultaneous drop in the turbulence kinetic energy, $\langle E_{ii}(t)\rangle_V$, between the times of O and k for a time period corresponding to $\sim 9\lambda$ ($200 < t < 231$) in the LDR case and $\sim 6\lambda$ ($200 < t < 293$) in the HDR case. With the turbulence suppressed, the strain-rates within the flow can no longer sustain a stretched polymer and the polymer relaxes, leading to decay of $\langle E_{p,tur}(t)\rangle_V$, between the times of P and p for a time period corresponding to $\sim 10\lambda$ ($217 < t < 252$) in the LDR case

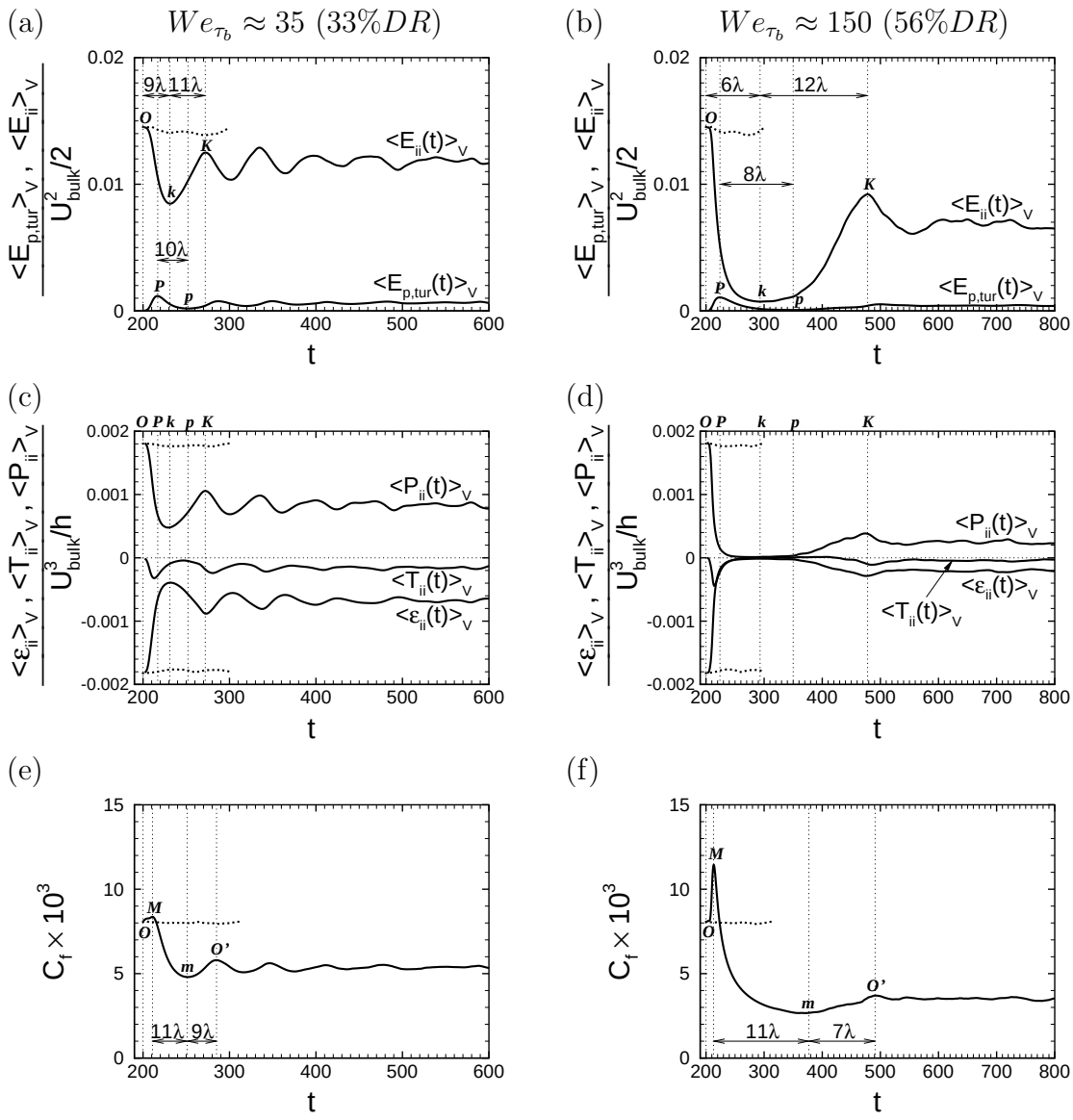

Figure 5.2: (a-b) Time histories of the volume-averaged turbulence kinetic energy, $\langle E_{ii}(t)\rangle_V$, and polymer elastic energy originating from turbulence, $\langle E_{p,tur}(t)\rangle_V$, normalized by $U_{bulk}^2/2$; (c-d) time histories of the volume-averaged rates of turbulence production, $\langle P_{ii}(t)\rangle_V$, viscous dissipation, $\langle \varepsilon_{ii}(t)\rangle_V$, and energy transfer from turbulence to the polymer, $\langle T_{ii}(t)\rangle_V$, normalized by U_{bulk}^3/h; (e-f) time histories of the skin friction coefficient, in (a,c,e) LDR regime (case CC3-q, 33%DR) and (b,d,f) HDR regime (case FF4-q, 56%DR). The times O, k, K, p, P denote start of viscoelastic simulations, minima and maxima of $\langle E_{ii}(t)\rangle_V$, and minima and maxima of $\langle E_{p,tur}(t)\rangle_V$ during the first cycle of turbulence suppression and regeneration, respectively. ——, viscoelastic flow; ·····, Newtonian flow.

and $\sim 8\lambda$ ($224 < t < 350$) in the HDR case. With the polymer relaxed, turbulence is regenerated, resulting in growth of $\langle E_{ii}(t)\rangle_V$ between the times of k and K for a time period corresponding to $\sim 11\lambda$ ($231 < t < 272$) in the LDR case and $\sim 12\lambda$ ($293 < t < 478$) in the HDR case. The first cycle of turbulence suppression and regeneration is thus completed and a new cycle resumes. This cyclic behavior continues for a few cycles, getting weaker with the passage of time until the viscoelastic flow has settled into a stationary turbulent state. In the stationary viscoelastic turbulent flow, the magnitude of the turbulence kinetic energy has dropped to $\sim 82\%$ and $\sim 47\%$ of the Newtonian value in the LDR and HDR cases, respectively, indicating that turbulence has been suppressed. What is noteworthy is that these significant drops in the turbulence kinetic energy are accompanied by only a minimal storage of elastic energy in the polymer due to energy exchanges between the turbulence and the polymer. In the stationary viscoelastic turbulent state, the elastic energy stored in the polymer due to interactions with turbulence amounts to only $\sim 4\%$ and $\sim 3\%$ of the turbulence kinetic energy in the base Newtonian flow, and to $\sim 5\%$ and $\sim 6\%$ of the turbulence kinetic energy in the stationary viscoelastic turbulent flow in the LDR and HDR cases, respectively. These results indicate that suppression of turbulence is not simply due to a redirection of turbulence kinetic energy into the elastic energy of the polymer, as has been suggested by some classical theories (de Gennes, 1986). Rather, a more subtle mechanism is at work.

A similar behavior can also be observed in the time histories of the volume-averaged rates of turbulence production, $\langle P_{ii}(t)\rangle_V/(U_{bulk}^3/h)$, viscous dissipation, $\langle \varepsilon_{ii}(t)\rangle_V/(U_{bulk}^3/h)$, and energy transfer from turbulence to the polymer,

$\langle T_{ii}(t)\rangle_V/(U_{bulk}^3/h)$, as shown in figures 5.2(c) and 5.2(d). In the stationary viscoelastic turbulent flow, the volume-averaged rate of energy transfer from turbulence to the polymer is only $\sim 19\%$ and $\sim 17\%$ of the corresponding volume-averaged rate of turbulence production, and only $\sim 9\%$ and $\sim 2\%$ of the volume-averaged rate of turbulence production in the base Newtonian flow in the LDR and HDR cases, respectively. At the same time, the volume-averaged rate of turbulence production has dropped to $\sim 46\%$ and $\sim 14\%$ of the Newtonian value in the LDR and HDR cases, respectively. These results suggest that suppression of turbulence is also not due to an enhanced dissipation of the turbulence kinetic energy by the elongational viscosity introduced by the polymer (Lumley, 1969, 1973). Rather a more complex mechanism is at work.

The combined effects of the trends in $\langle E_{ii}(t)\rangle_V/(U_{bulk}^2/2)$ and $\langle E_{p,tur}(t)\rangle_V/(U_{bulk}^2/2)$ is also reflected in the time histories of the skin friction coefficient, as shown in figures 5.2(e) and 5.2(f). Immediately following the introduction of the polymer, when the polymer is being uncoiled but the turbulence has not yet been suppressed, the skin friction coefficient rapidly grows between the times of O and M for a time period corresponding to $\frac{\Delta\tilde{t}U_{bulk}}{h} \sim 7$ $(200 < t < 211)$ in the LDR case and $\frac{\Delta\tilde{t}U_{bulk}}{h} \sim 9$ $(200 < t < 213)$ in the HDR case. This is followed by a decay in the skin friction coefficient between the times of M and m for a time period corresponding to $\sim 11\lambda$ in both the LDR $(211 < t < 251)$ and HDR $(213 < t < 377)$ cases, while the turbulence is being suppressed. This decay in C_f is, in turn, followed by an increase in the skin friction coefficient between the times of m and O' for a time period corresponding to $\sim 9\lambda$ $(251 < t < 285)$ in the LDR case and $\sim 7\lambda$ $(377 < t < 491)$

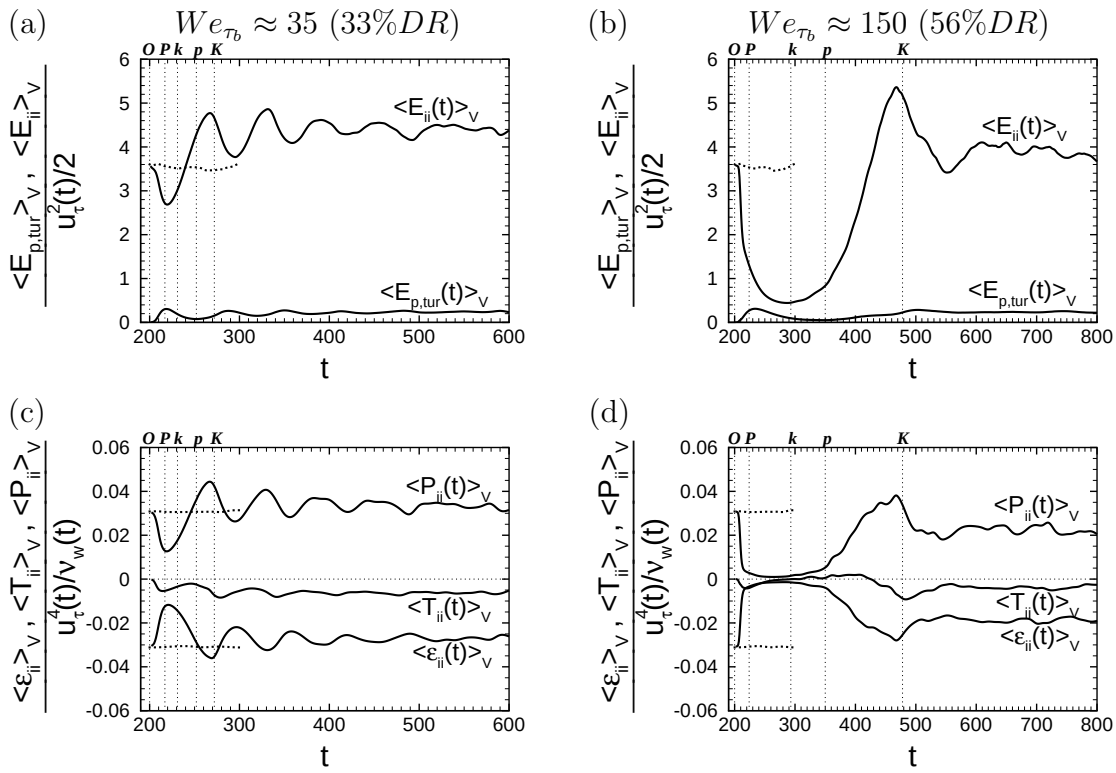

Figure 5.3: (a-b) Time histories of the volume-averaged turbulence kinetic energy, $\langle E_{ii}(t)\rangle_V$, and polymer elastic energy originating from turbulence, $\langle E_{p,tur}(t)\rangle_V$, normalized by $u_\tau^2(t)/2$; (c-d) time histories of the volume-averaged rates of turbulence production, $\langle P_{ii}(t)\rangle_V$, viscous dissipation, $\langle \varepsilon_{ii}(t)\rangle_V$, and energy transfer from turbulence to the polymer, $\langle T_{ii}(t)\rangle_V$, normalized by $u_\tau^4(t)/\nu_w(t)$ in (a,c) LDR regime (case CC3-q, 33%DR) and (b,d) HDR regime (case FF4-q, 56%DR). ——, viscoelastic flow; ·····, Newtonian flow.

in the HDR case, while the turbulence is being regenerated. These periodic trends in the skin friction coefficient also persist for a few cycles until the viscoelastic flow has settled into a stationary turbulent state. In the stationary viscoelastic turbulent flow, the magnitude of the skin friction coefficient has dropped to 67% and 44% of the Newtonian values, corresponding to $33\%DR$ and $56\%DR$ in the LDR and HDR cases, respectively.

Similar trends can also be observed in the time histories of $\langle E_{ii}(t)\rangle_V$, $\langle E_{p,tur}(t)\rangle_V$, and $\langle P_{ii}(t)\rangle_V$, $\langle \varepsilon_{ii}(t)\rangle_V$, $\langle T_{ii}(t)\rangle_V$ when these quantities are normalized by the instantaneous wall-friction velocity, $u_\tau(t)$, and wall-shear viscosity, $\nu_w(t)$, as shown in figure 5.3. What is noteworthy here are the relative magnitudes of the normalized turbulence kinetic energy and rates of turbulence production in the viscoelastic stationary state compared to Newtonian flow. In the LDR and HDR cases, the normalized rates of turbulence production are $\sim 106\%$ and $\sim 72\%$ of the Newtonian values, respectively, while the respective magnitudes of turbulence kinetic energy are $\sim 121\%$ and $\sim 108\%$ of the Newtonian values. These results suggest a pileup of turbulence kinetic energy in the drag-reduced flow.

5.2.2 Highly anisotropic structure of turbulence in drag-reduced flow

To further explore the nature and origin of this pileup of turbulence kinetic energy in drag-reduced flow, in figure 5.4 we compare the one-point flow statistics in the LDR and HDR regimes to Newtonian flow. The mean velocity profiles in viscoelastic flow display the expected thickening of the buffer layer and approach to Virk's MDR profile (Virk, Mickley & Smith, 1970) as shown in figure 5.4(a), while the Reynolds shear

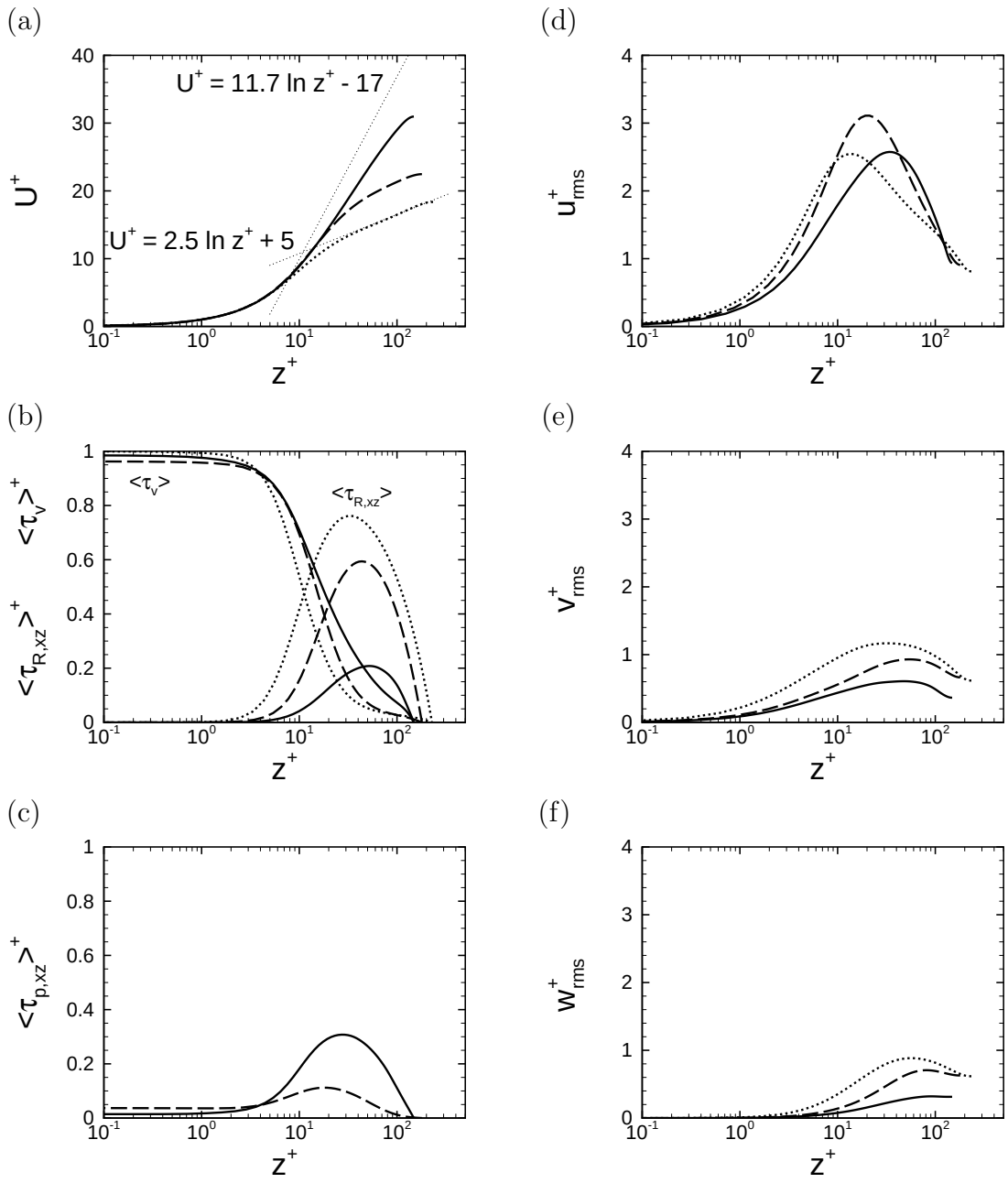

Figure 5.4: One-point flow statistics in stationary viscoelastic flow in LDR and HDR regimes compared to Newtonian flow: (a) mean velocity profiles; (b) Reynolds, $\langle\tau_{R,xz}\rangle^+$, and viscous, $\langle\tau_v\rangle^+$, shear stresses; (c) polymer shear stresses; (d) streamwise turbulence intensities; (e) spanwise turbulence intensities; (f) wall-normal turbulence intensities. ·····, Newtonian flow (case NN); – – –, viscoelastic flow at low drag reduction (case CC3-q, 33%DR); ——, viscoelastic flow at high drag reduction (case FF4-q, 56%DR).

stresses show the expected enhanced decay with increasing drag reduction, as shown in figures 5.4(b). The most remarkable feature in these statistics is in the behavior of the turbulence intensities (figures 5.4d, 5.4e & 5.4f). While the normalized spanwise and wall-normal turbulence intensities (figures 5.4e & 5.4f) show the anticipated decay with increasing drag reduction, the normalized streamwise turbulence intensity (figure 5.4d) shows a pileup of turbulence kinetic energy in this component. The peak magnitude of the normalized streamwise turbulence intensity is $\sim 122\%$ of the Newtonian value in the LDR case and $\sim 101\%$ of the Newtonian value in the HDR case. These results suggest that in drag-reduced flow, turbulence kinetic energy is somehow piled up and trapped in the streamwise component of the velocity. This pileup of turbulence kinetic energy in the streamwise component along with strong decay of turbulence kinetic energy in the spanwise and wall-normal components leads to a highly anisotropic turbulence structure in drag-reduced flow.

To investigate this anisotropy in further detail, in figure 5.5 we show the anisotropy-invariant maps in the LDR and HDR cases compared to Newtonian flow. Two features can be observed in these anisotropy-invariant maps. One is the expected thickening of the viscous sublayer from ~ 7 wall units in Newtonian flow to ~ 11 wall units and ~ 19 wall units in the LDR and HDR cases, respectively. The second, and more important, feature is a shift of the outer layer away from the three-dimensional isotropic limit (point 0,0) towards the one-dimensional turbulence limit with increasing drag reduction. In the LDR case (figure 5.5b), this shift is observed for $11 < z^+ \lesssim 100$, while in the HDR case (figure 5.5c), it is observed throughout the outer layer, $19 < z^+ \lesssim 149$.

A more in depth view of this anisotropy can be gained by examining the spectra

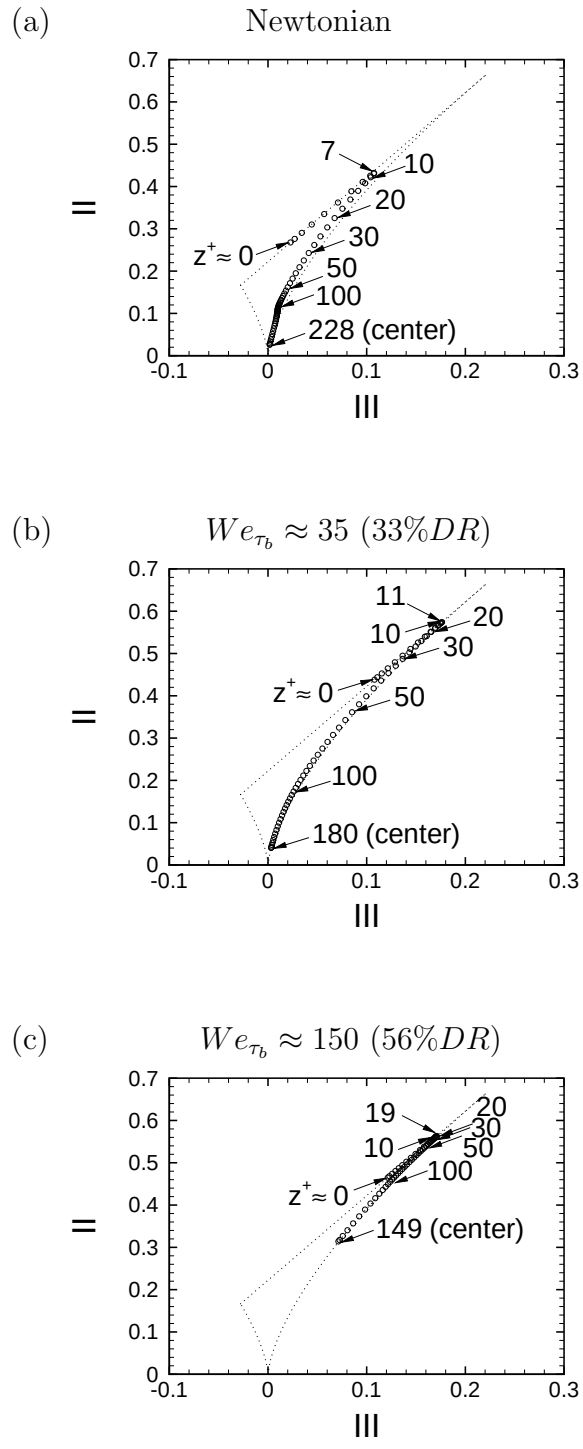

Figure 5.5: Anisotropy-invariant maps for (a) Newtonian flow (case NN), (b) viscoelastic flow in the LDR regime (case CC3-q, 33%DR) and (c) viscoelastic flow in the HDR regime (case FF4-q, 56%DR).

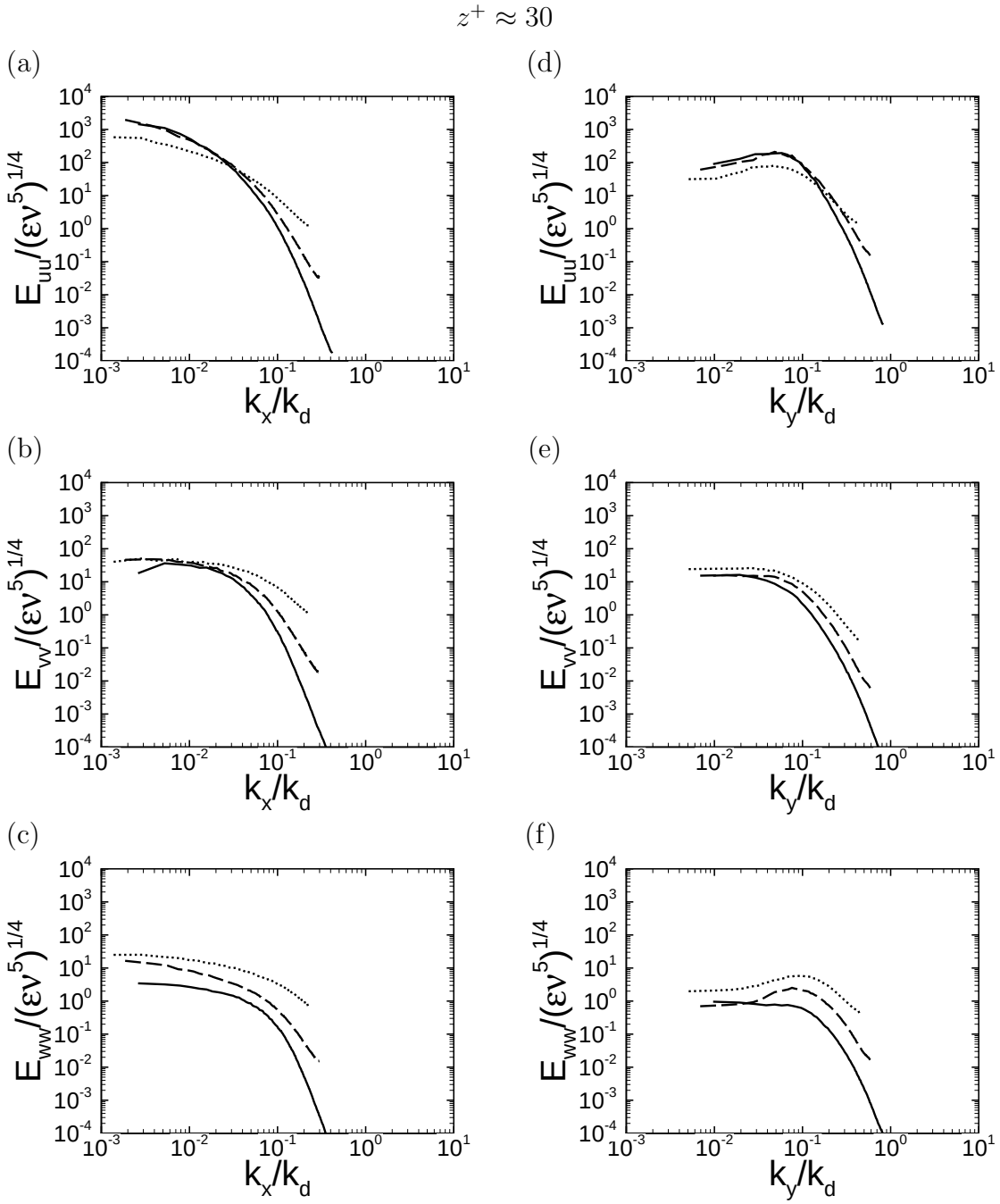

Figure 5.6: The one-dimensional energy spectra in LDR (case CC3-q, 33%DR) and HDR (case FF4-q, 56%DR) regimes compared to Newtonian flow (case NN) at $z^+ \approx 30$. ·····, Newtonian flow (case NN); – – –, viscoelastic flow at low drag reduction (case CC3-q, 33%DR); ——, viscoelastic flow at high drag reduction (case FF4-q, 56%DR).

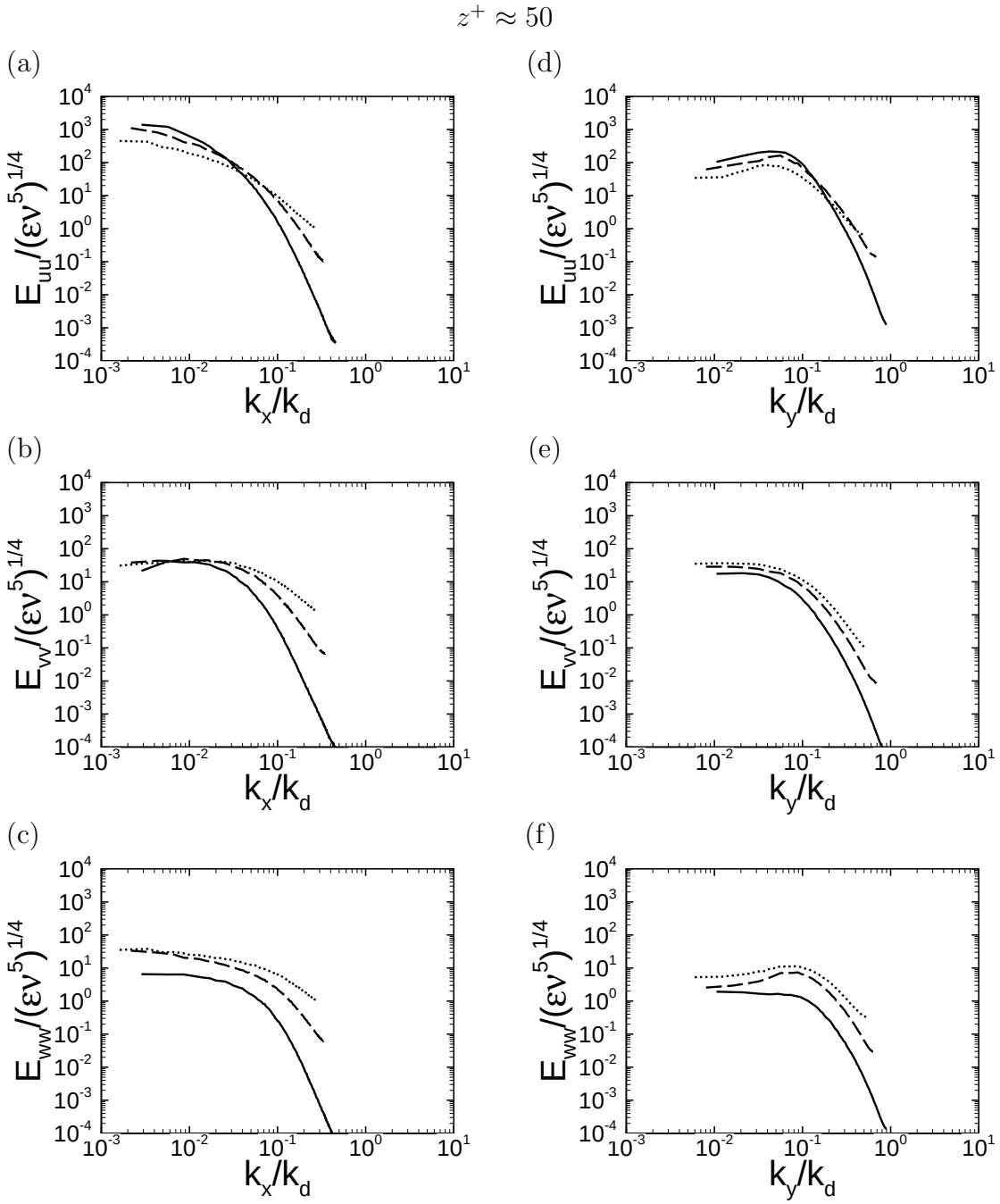

Figure 5.7: The one-dimensional energy spectra in LDR (case CC3-q, 33%DR) and HDR (case FF4-q, 56%DR) regimes compared to Newtonian flow (case NN) at $z^+ \approx 50$. ·····, Newtonian flow (case NN); – – –, viscoelastic flow at low drag reduction (case CC3-q, 33%DR); ——, viscoelastic flow at high drag reduction (case FF4-q, 56%DR).

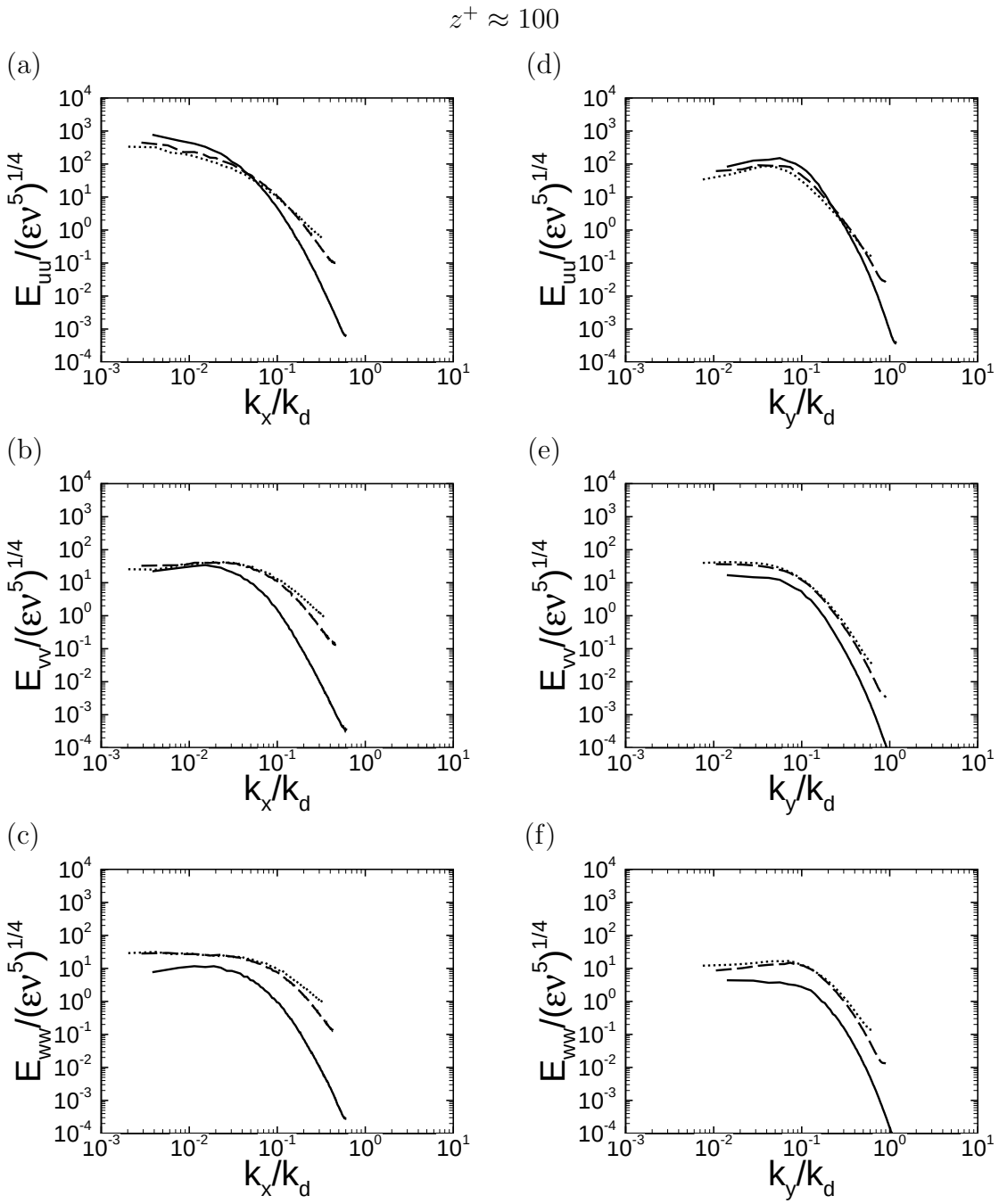

Figure 5.8: The one-dimensional energy spectra in LDR (case CC3-q, 33%DR) and HDR (case FF4-q, 56%DR) regimes compared to Newtonian flow (case NN) at $z^+ \approx 100$. $\cdots\cdots$, Newtonian flow (case NN); $---$, viscoelastic flow at low drag reduction (case CC3-q, 33%DR); ——, viscoelastic flow at high drag reduction (case FF4-q, 56%DR).

of velocity components, $E_{\alpha\alpha}(k_i)$, as shown in figures 5.6-5.8. At wall-normal locations where the turbulence shifts towards the one-dimensional turbulence limit, a decay of turbulence kinetic energy can be observed in the spectra of spanwise and wall-normal velocity components at the small scales in the LDR case and at all scales in the HDR case, while the streamwise kinetic energy shows a pileup of energy at the large scales accompanied by a decay at the small scales. In the LDR case, these features are most prominent for $z^+ \lesssim 50$, while in the HDR case, they are noticeable throughout the cross-section of the channel.

These results suggest that anisotropy of turbulence in drag-reduced flow is due to a pileup of turbulence kinetic energy at the large scales of the streamwise component of velocity along with decay of turbulence at all scales in the cross-stream components at the wall-normal locations affected by the polymer.

5.3 Comparison to classical theories of polymer drag reduction

To gain an understanding of the underlying mechanisms responsible for the features discussed in the previous section, we begin by comparing these features to the predictions of classical theories of polymer drag reduction.

Figures 5.9 and 5.10 show the characteristic strain-rate, $s^+(k_i^+, z^+)$, at the start of viscoelastic simulations (base Newtonian flow) and in the viscoelastic stationary state in the LDR and HDR regimes compared to T^{*+} of Lumley's theory (Lumley, 1969, 1973), and $T^{**+}(z^+)$ of the revised version of de Gennes's theory proposed in this present study, where T^{*+}, $T^{**+}(z^+)$, and $s^+(k_i^+, z^+)$ are defined by (5.9), (5.10) and

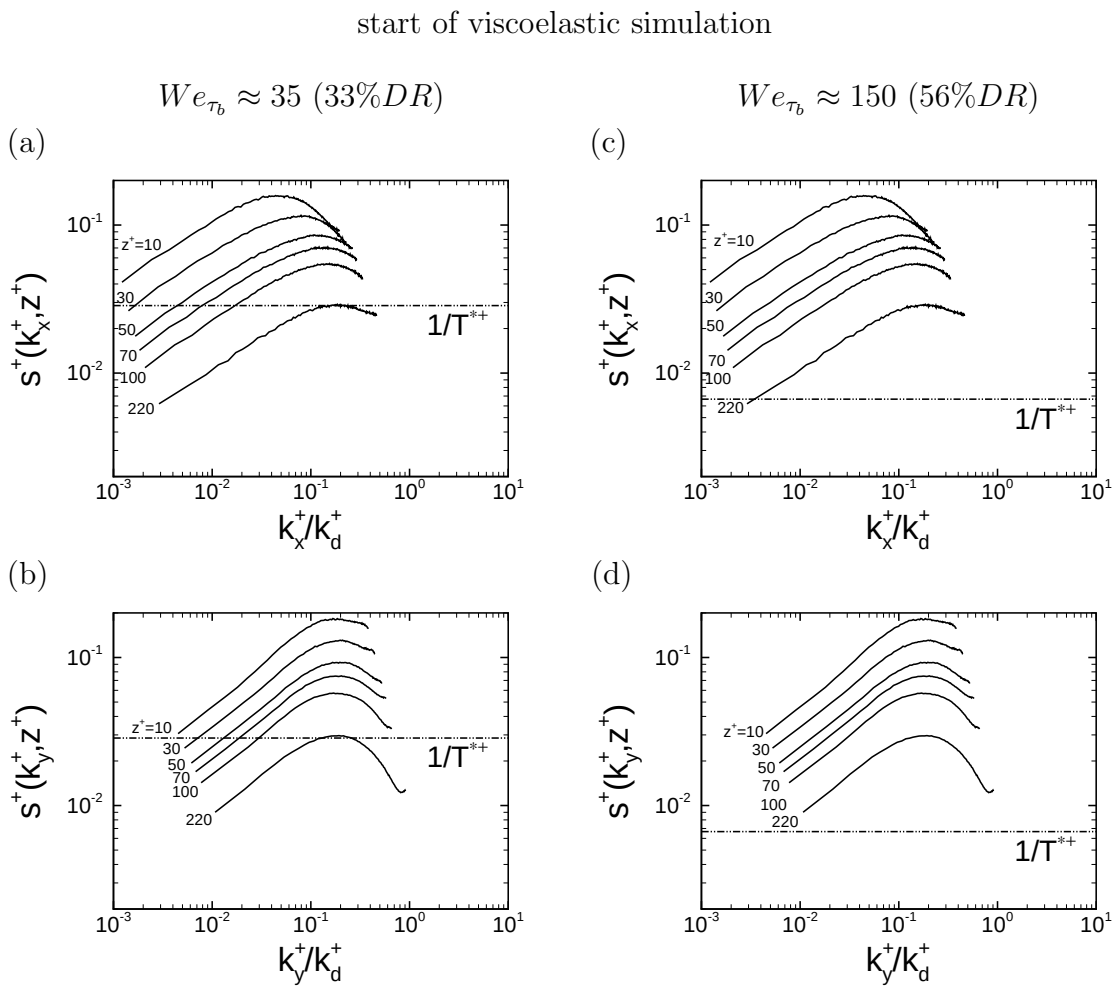

Figure 5.9: The characteristic strain-rate, $s^+(k_i^+, z^+)$, in Newtonian flow (case NN) at (a-b) low drag reduction (case CC3-q, 33%DR) and (c-d) high drag reduction (case FF4-q, 56%DR) compared to $1/T^{*+}$ of Lumley's theory (Lumley, 1969, 1973). $-\cdot\cdot-$, $1/T^{*+}$ from Lumley's theory.

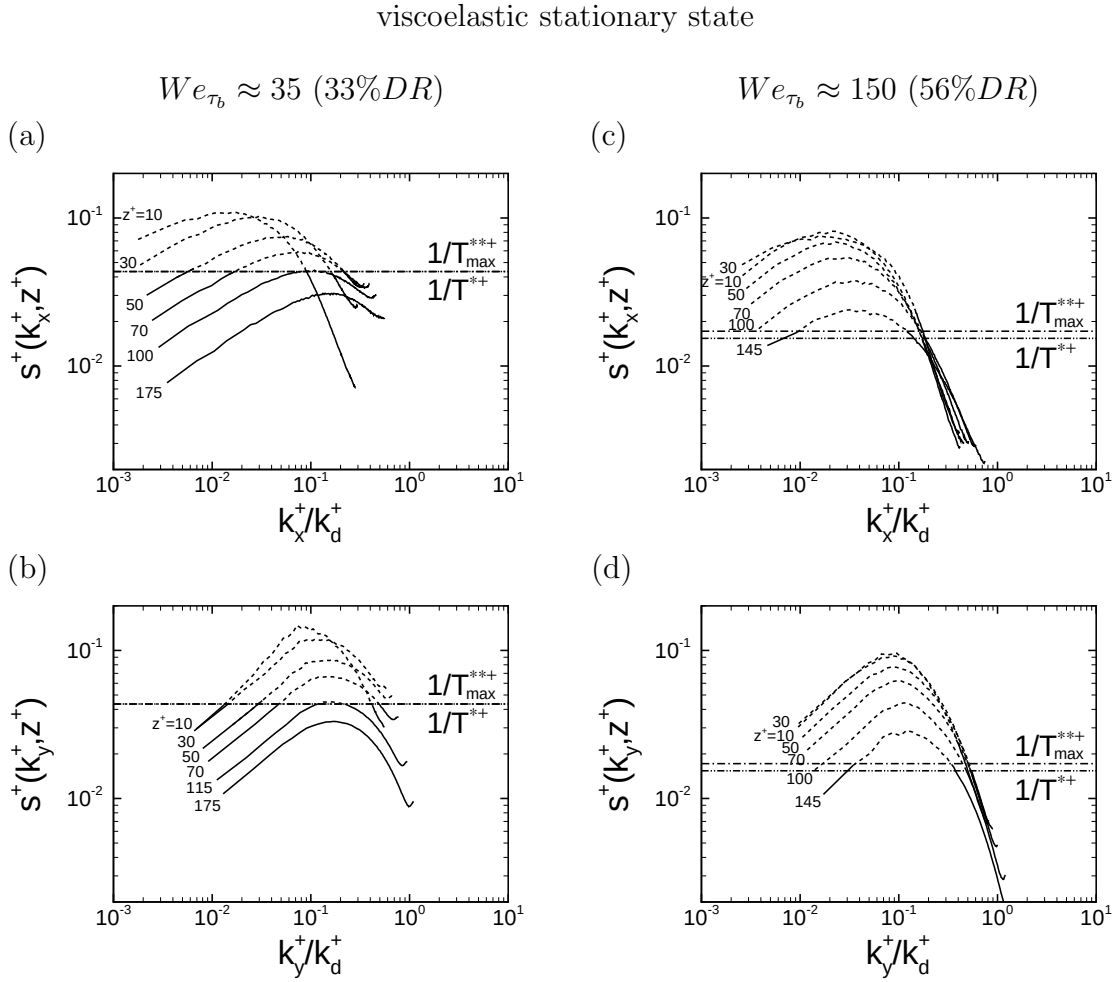

Figure 5.10: The characteristic strain-rate, $s^+(k_i^+, z^+)$, in viscoelastic flow at (a-b) low drag reduction (case CC3-q, 33%DR) and (c-d) high drag reduction (case FF4-q, 56%DR) compared to $1/T^{*+}$ of Lumley's theory (Lumley, 1969, 1973) and $1/T^{**+}(z^+)$ of the revised version of de Gennes's theory. $-\cdots-$, $1/T^{*+}$ from Lumley's theory; $-\cdot-$, lowest $1/T^{**+}(z^+)$ from the revised version of de Gennes's theory; ---, scales with $s^+(k_i^+, z^+) > 1/T^{**+}(z^+)$; ——, scales with $s^+(k_i^+, z^+) < 1/T^{**+}(z^+)$.

(5.11), respectively. In Lumley's theory, it is assumed that all turbulent scales with a characteristic strain-rate, $s^+(k_i^+, z^+) > 1/T^{*+}$ are affected by the polymer through the enhanced elongational viscosity introduced by the polymer at these scales. In the revised theory of de Gennes, it is assumed that all turbulent scales with a characteristic strain-rate, $s^+(k_i^+, z^+) > 1/T^{**+}(z^+)$ are affected by the polymer through redirection of a fraction (greater than or equal to A_E) of their turbulence kinetic energy into the elastic energy of the polymer. From the perspective of turbulence dynamics, both mechanisms represent an additional drain of turbulence kinetic energy at the affected scales. Because $T^{**+}(z^+)$ is a function of z^+, the affected scales based on the revised theory of de Gennes are shown as dashed lines at each wall-normal location in figures 5.10(a-d). These figures also show $1/T^{**+}_{max}(z^+)$, corresponding to the maximum value of $T^{**+}(z^+)$ over all wall-normal locations, compared to $1/T^{*+}$ of Lumley's theory. Since both the LDR and HDR cases shown in figures 5.9 and 5.10 are near saturation concentration (with $\beta \sim 0.96$ and $\beta \sim 0.98$, respectively), and at saturation concentration $T^{**+}(z^+) = T^{*+}$, little difference is observed between T^{*+} of Lumley's theory and $T^{**+}_{max}(z^+)$ of the revised theory of de Gennes in these figures. The differences between the two theories become more pronounced at concentrations below saturation, as will be shown in § 5.5. At the start of the viscoelastic simulation (figure 5.9), $T^{**+}(z^+)$ cannot be defined, because the polymer is still in a coiled state at this time and its elastic energy is still zero. Consequently, only $1/T^{*+}$ is shown in figures 5.9(a-d)

Comparison of $s^+(k_i^+, z^+)$ and $1/T^{*+}$ in figures 5.9(a-d) shows that according to Lumley's theory, when the polymer is first introduced into the base Newtonian flow

in the LDR case (figures 5.9a-5.9b), all turbulent scales at $z^+ \leq 10$, all but the very largest of the turbulent scales at $10 < z^+ \leq 30$, and all the mid-range to small scales at $30 < z^+ \leq 220$ are affected by the polymer, while in the HDR case (figures 5.9c-5.9d), all turbulent scales at all z^+ locations are affected.

In the stationary viscoelastic flow in the LDR case (figures 5.10a-5.10b), both Lumley's theory and the revised theory of de Gennes predict that the polymer affects nearly all wavenumbers at $z^+ \leq 30$, the mid-range to high wavenumbers at $30 < z^+ \leq 115$, and has no effect at $z^+ > 115$. In the HDR case (figures 5.10c-5.10d), both theories predict that all turbulent scales are affected at $z^+ \leq 100$, while for $100 < z^+ \leq 145$ the effect of the polymer is limited to the mid-range to high wavenumbers.

These predictions of the classical theories for wall-normal ranges where the polymer has any effect on dynamics of turbulence are consistent with observations in the anisotropy-invariant maps of figure 5.5 and the energy spectra of figures 5.6-5.8, which both show deviations from Newtonian dynamics at $z^+ \lesssim 100$ in the LDR case, and throughout the cross-section of the channel in the HDR case. The main effect of the polymer, according to classical theories, is a drain of energy at the affected scales. This drain of energy can indeed be observed in the DNS results shown in figures 5.6-5.8, 5.11 and 5.12. Over the affected range of scales, both the energy spectra and the characteristic stain-rates show a sharp decay compared to Newtonian flow, with both the magnitude of decay and the range of affected scales increasing with enhanced drag reduction. This enhanced decay, which can also be viewed as an enhanced dissipation, leads to a shift of the dissipation peak towards larger wavenumbers, as originally suggested by Lumley (1969) and shown in figures 5.11 and 5.12. However, both the

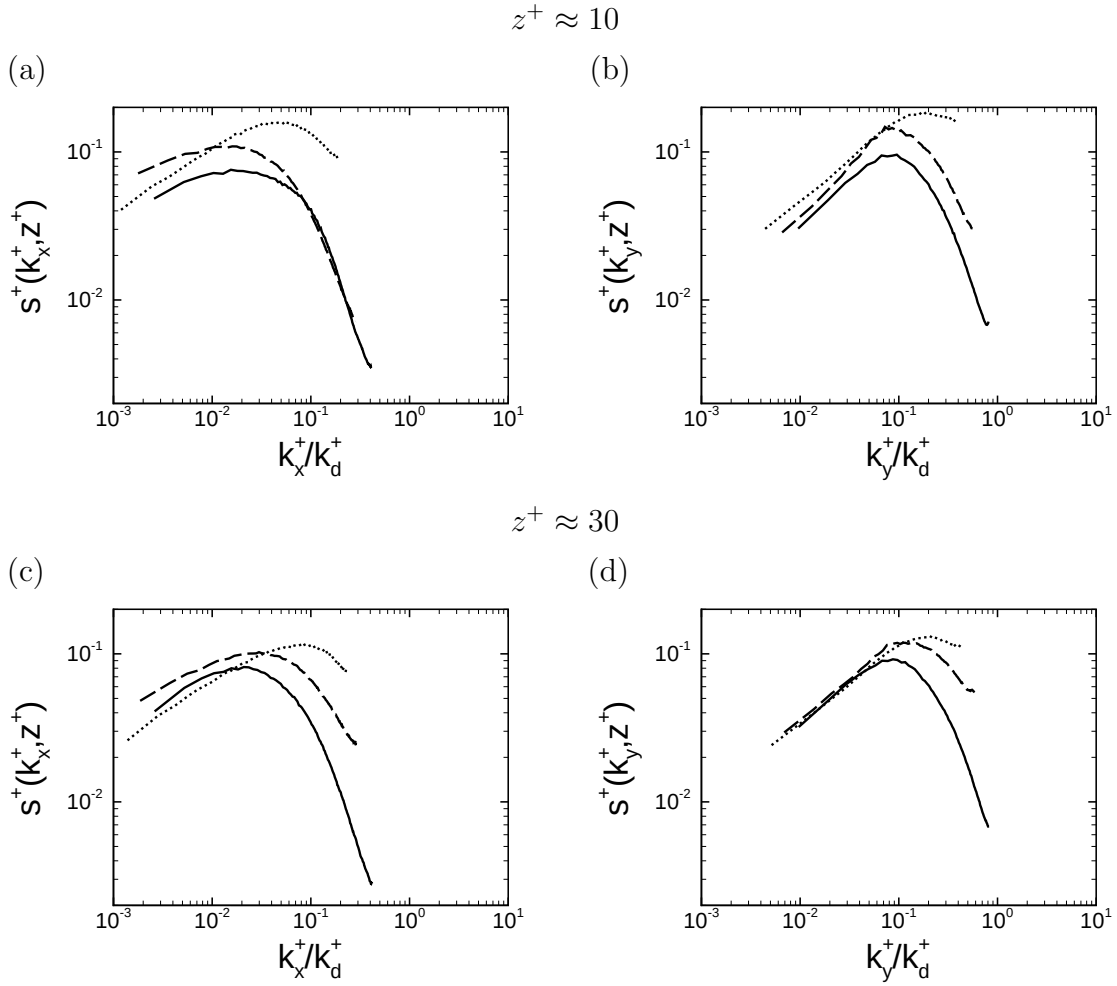

Figure 5.11: The characteristic strain-rates in LDR (case CC3-q, 33%DR) and HDR (case FF4-q, 56%DR) regimes compared to Newtonian flow (case NN) at (a-b) $z^+ \approx 10$ and (c-d) $z^+ \approx 30$. $\cdots\cdots$, Newtonian flow (case NN); $--$, viscoelastic flow at low drag reduction (case CC3-q, 33%DR); ——, viscoelastic flow at high drag reduction (case FF4-q, 56%DR).

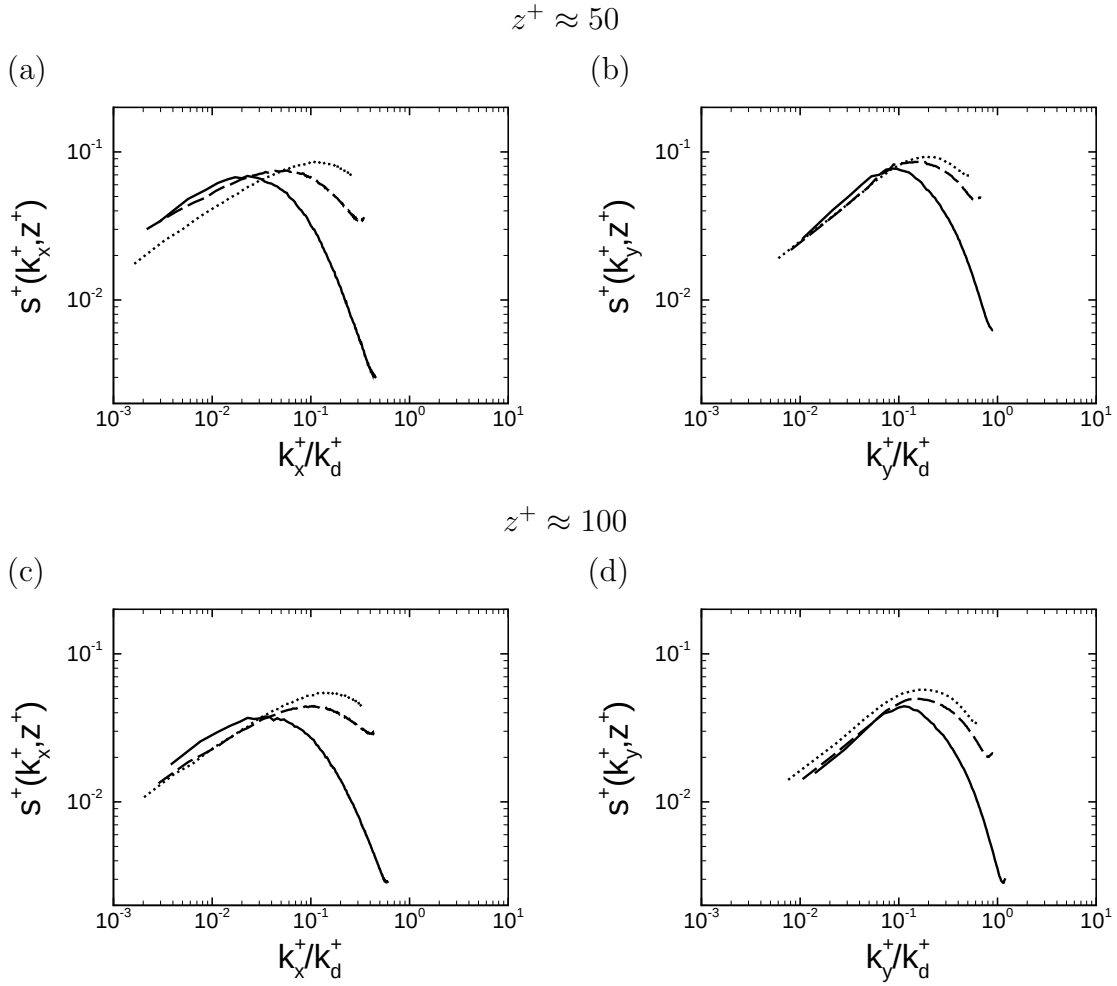

Figure 5.12: The characteristic strain-rates in LDR (case CC3-q, 33%DR) and HDR (case FF4-q, 56%DR) regimes compared to Newtonian flow (case NN) at (a-b) $z^+ \approx 50$ and (c-d) $z^+ \approx 100$. ·····, Newtonian flow (case NN); – – –, viscoelastic flow at low drag reduction (case CC3-q, 33%DR); ——, viscoelastic flow at high drag reduction (case FF4-q, 56%DR).

energy spectra of figures 5.6-5.8 and the characteristic strain-rate of figures 5.11 and 5.12 show a feature which is not predicted by classical theories, namely, a pileup of the streamwise kinetic energy and an enhanced characteristic strain-rate at the large scales in drag reduced flow.

This pileup of streamwise turbulence kinetic energy in the large scales is observed both when these scales are supposed to experience a decay according to classical theories (as with $z^+ < 30$ in the LDR case or $z^+ < 100$ in the HDR case) or when the scales are supposed to be unaffected by the polymer according to the classical theories (as with $z^+ = 50$ in the LDR case). These features indicate that a more subtle mechanism is at work in polymer drag reduction than that suggested by classical theories.

5.4 Role of pressure-strain in establishing anisotropy

The key to mechanism of polymer drag reduction lies in a secondary feature of the drain of energy from the turbulent scales which are affected by the polymer according to classical theories. In these affected scales, the drain of energy results in a drop in all components of the strain-rate tensor, including the diagonal components, as shown in figures 5.13-5.15. This drop in the strain-rate results in a proportionate drop in the pressure-strain correlation at these and neighboring scales, which inhibits the transfer of turbulence kinetic energy from the streamwise component to the cross-stream components at these scales. When this drop in pressure-strain correlation extends to the largest energy containing eddies, the turbulence kinetic energy which is transferred from the mean flow to turbulence is trapped in the streamwise component

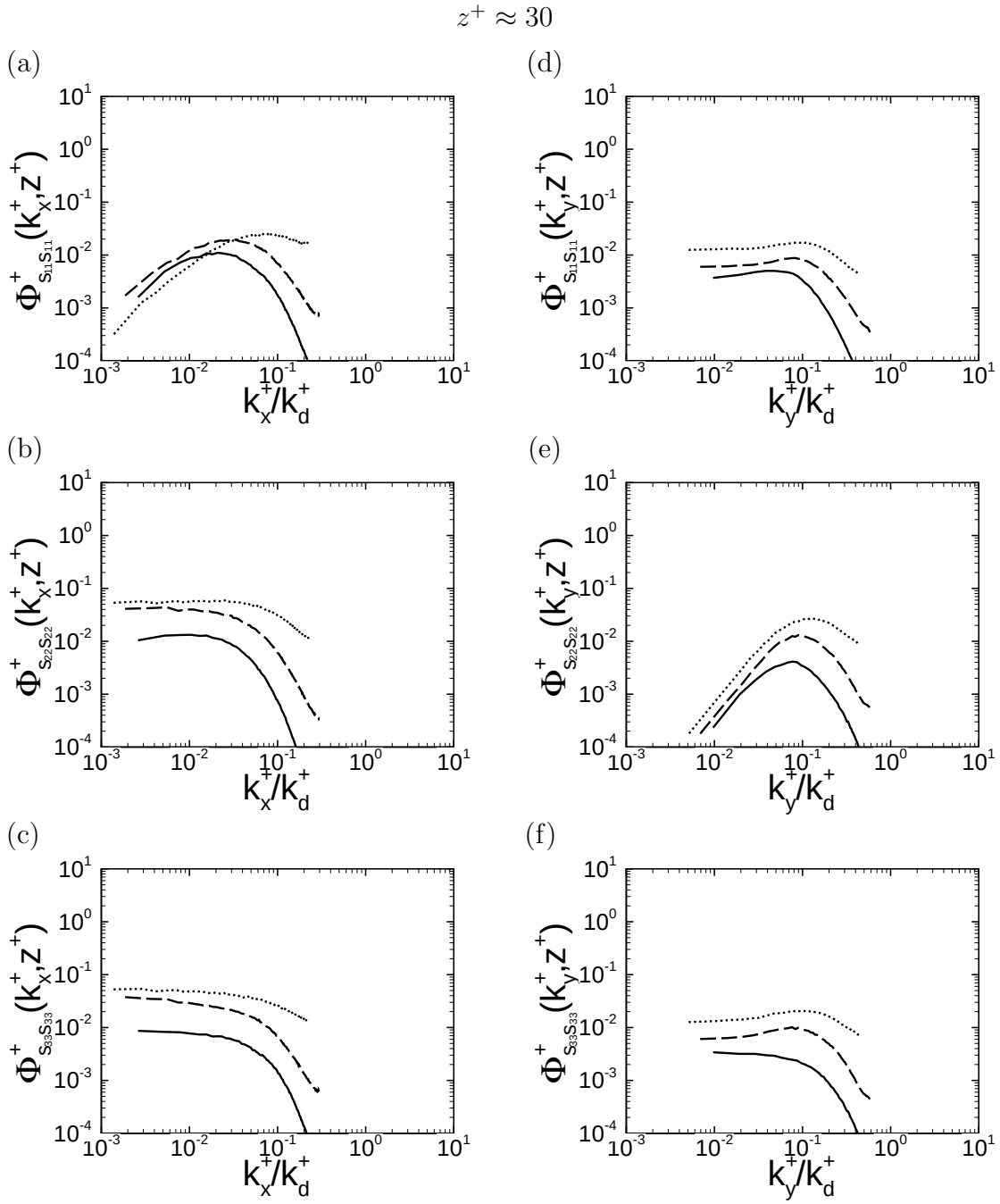

Figure 5.13: The normalized one-dimensional spectral density of the diagonal components of strain-rate in LDR (case CC3-q, 33%DR) and HDR (case FF4-q, 56%DR) regimes compared to Newtonian flow (case NN) at $z^+ \approx 30$. $\cdots\cdots$, Newtonian flow (case NN); $---$, viscoelastic flow at low drag reduction (case CC3-q, 33%DR); ——, viscoelastic flow at high drag reduction (case FF4-q, 56%DR).

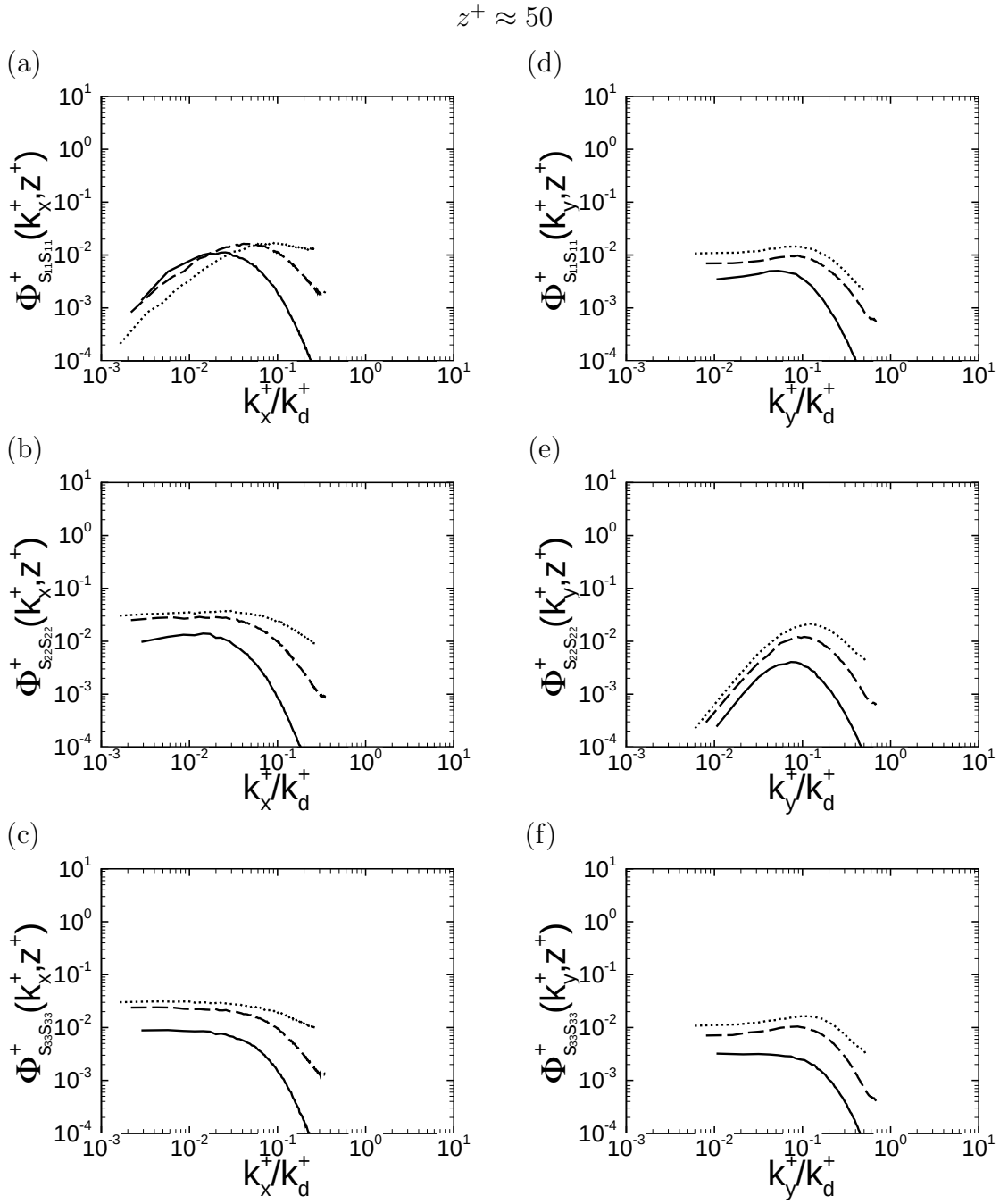

Figure 5.14: The normalized one-dimensional spectral density of the diagonal components of strain-rate in LDR (case CC3-q, 33%DR) and HDR (case FF4-q, 56%DR) regimes compared to Newtonian flow (case NN) at $z^+ \approx 50$. $\cdots\cdots$, Newtonian flow (case NN); $---$, viscoelastic flow at low drag reduction (case CC3-q, 33%DR); ——, viscoelastic flow at high drag reduction (case FF4-q, 56%DR).

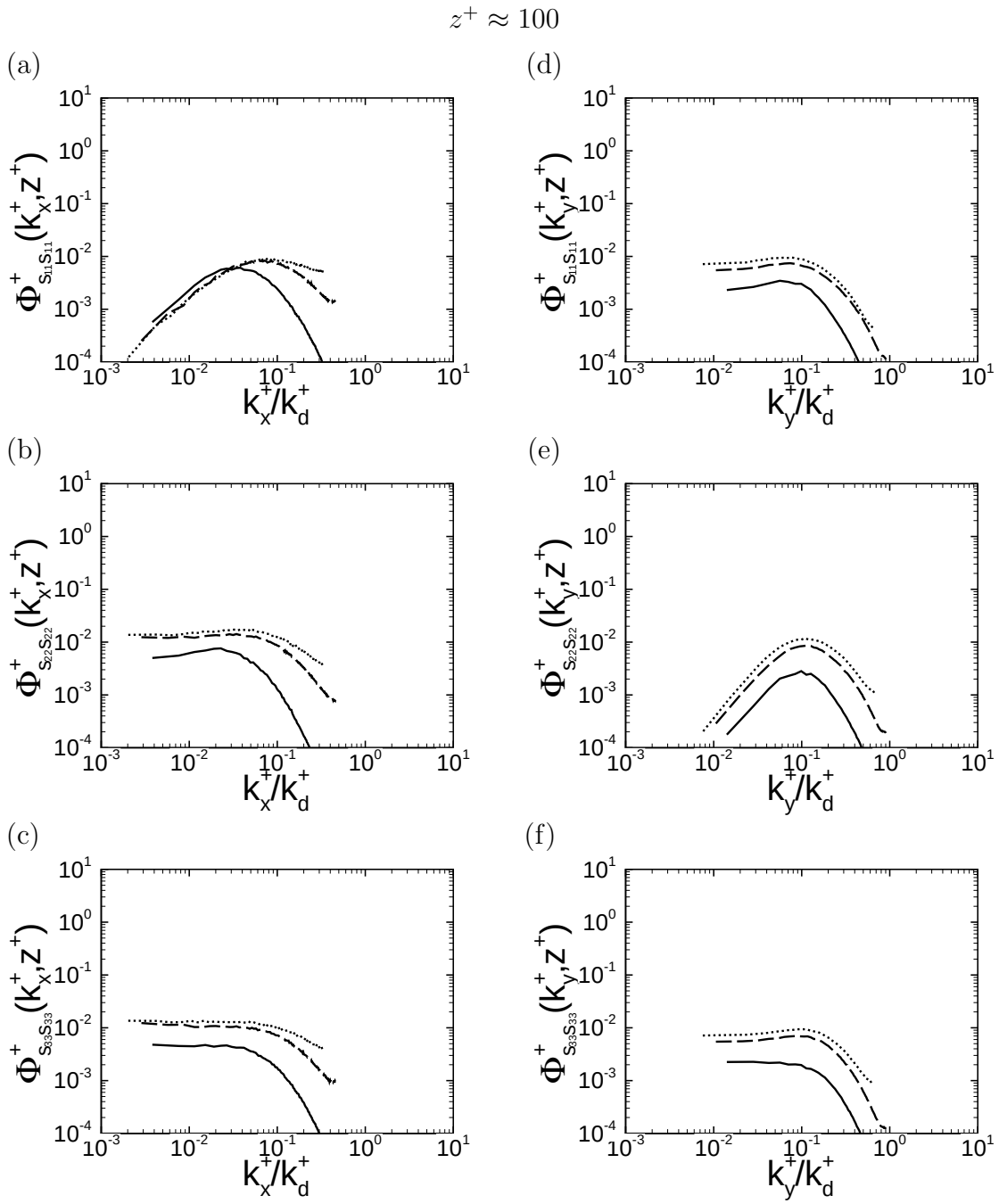

Figure 5.15: The normalized one-dimensional spectral density of the diagonal components of strain-rate in LDR (case CC3-q, 33%DR) and HDR (case FF4-q, 56%DR) regimes compared to Newtonian flow (case NN) at $z^+ \approx 100$. $\cdots\cdots$, Newtonian flow (case NN); $---$, viscoelastic flow at low drag reduction (case CC3-q, 33%DR); ——, viscoelastic flow at high drag reduction (case FF4-q, 56%DR).

of these large scale eddies and cannot be redistributed to the cross-stream directions. This results in a sharp drop in the wall normal turbulence intensity and the Reynolds shear stress, as seen in figures 5.4 and 5.6-5.8. This drop in the Reynolds shear stress, in turn, results in a drop in the rate of turbulence production and leads to drag reduction. Furthermore, the energy trapped in the streamwise component can no longer cascade to the small scales, leading to further decay of $E_{\alpha\alpha}(k_i)$ (figures 5.6-5.8) and $s^+(k_i^+, z^+)$ (figures 5.10, 5.11 & 5.12) in the small scales. This decay further amplifies the features described above. Thus the miniscule extraction of energy by the polymer at the affected turbulent scales starts a self-amplifying sequence of events, which leads to cessation of turbulence production and results in drag reduction. For effective drag reduction, the initial minute extraction of energy by the polymer needs to extend to the largest turbulent scales at wall-normal locations where the peak of production occurs, as seen in the $We_{\tau_b} \approx 150$ data in figures 5.6-5.8 and 5.10.

Examination of the various terms in the turbulence kinetic energy budget (eqn.5.1 & 5.2) gives a picture consistent with the above, as shown in figures 5.16, 5.17 and 5.18. The pressure-strain correlation, $\langle \Pi_{\alpha\alpha} \rangle^+$, in drag reduced flow shows a significant drop compared to Newtonian flow, as shown in figures 5.16(a-c). In the LDR case, this attenuation is most prominently observed for $z^+ < 70$, where the characteristic strain-rate (figures 5.9, 5.10, 5.11 & 5.12) shows a noticeable decay compared to Newtonian flow. In the HDR case, $\langle \Pi_{\alpha\alpha} \rangle^+$ is reduced throughout the cross-section of the channel, which is again consistent with the range of affected scales at $We_{\tau_b} \approx 150$ in figures 5.10, 5.11 and 5.12. These observations are consistent with the assumption that the drop in the strain-rate is the source of the drop in the pressure-strain correlation.

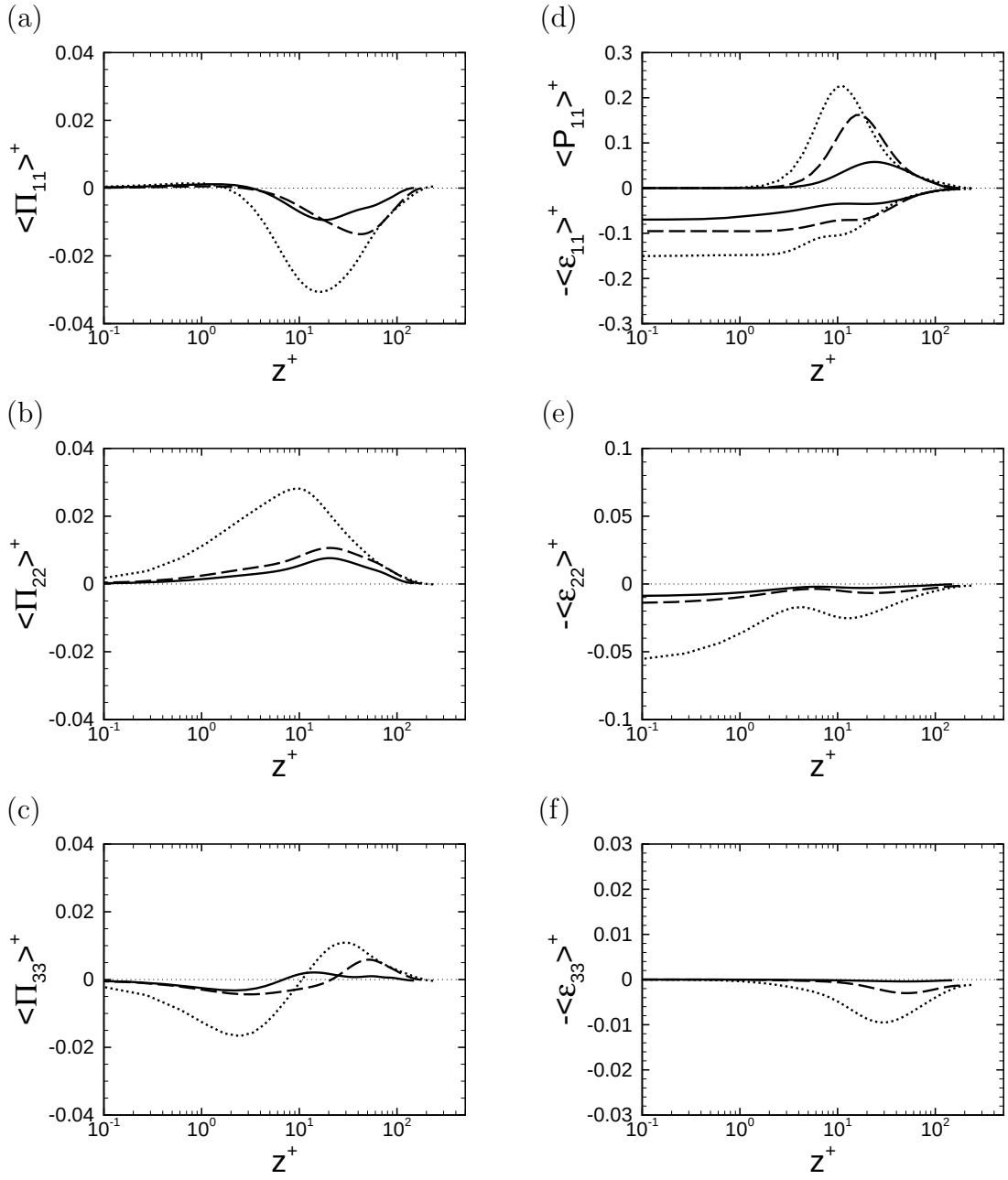

Figure 5.16: Components of turbulence kinetic energy budgets in LDR (case CC3-q, 33%DR) and HDR (case FF4-q, 56%DR) regimes compared to Newtonian flow (case NN): (a-c) pressure-strain correlation, $\langle\Pi_{\alpha\alpha}\rangle^+$; (d-f) turbulence production, $\langle P_{\alpha\alpha}\rangle^+$, and viscous dissipation, $\langle\varepsilon_{\alpha\alpha}\rangle^+$. (a,d) streamwise direction; (b,e) spanwise direction; (c,f) wall-normal direction. ·····, Newtonian flow (case NN); − − −, viscoelastic flow at low drag reduction (case CC3-q, 33%DR); ——, viscoelastic flow at high drag reduction (case FF4-q, 56%DR).

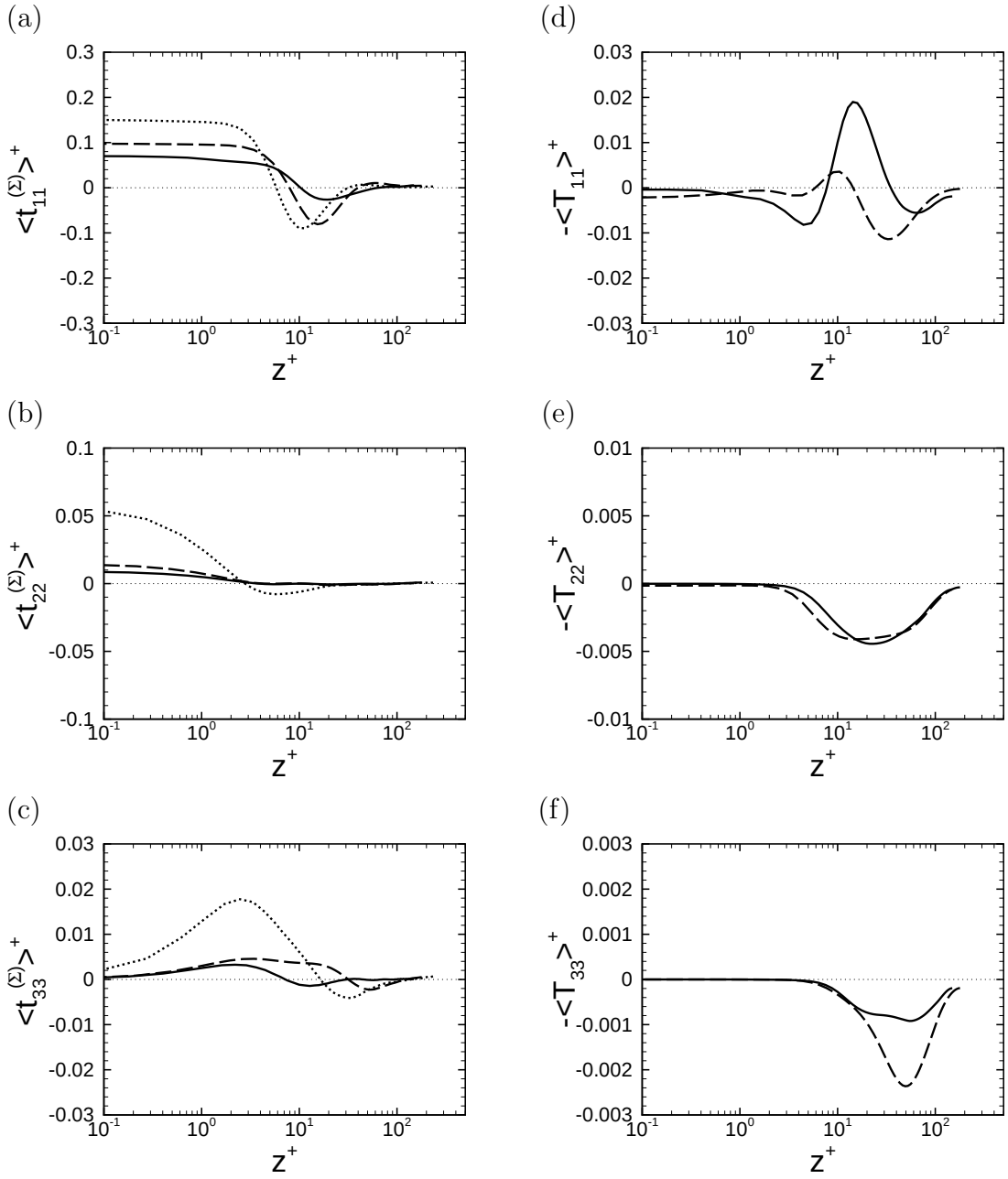

Figure 5.17: Components of turbulence kinetic energy budgets in LDR (case CC3-q, 33%DR) and HDR (case FF4-q, 56%DR) regimes compared to Newtonian flow (case NN): (a-c) sum of transport terms, $\langle t_{\alpha\alpha}^{(\Sigma)} \rangle^+ = \langle t_{\alpha\alpha}^{(v)} + t_{\alpha\alpha}^{(press)} + t_{\alpha\alpha}^{(R)} + t_{\alpha\alpha}^{(p)} \rangle^+$; (d-f) energy transfer from turbulence to the polymer, $\langle T_{\alpha\alpha} \rangle^+$. (a,d) streamwise direction; (b,e) spanwise direction; (c,f) wall-normal direction. ····, Newtonian flow (case NN); – – –, viscoelastic flow at low drag reduction (case CC3-q, 33%DR); ——, viscoelastic flow at high drag reduction (case FF4-q, 56%DR).

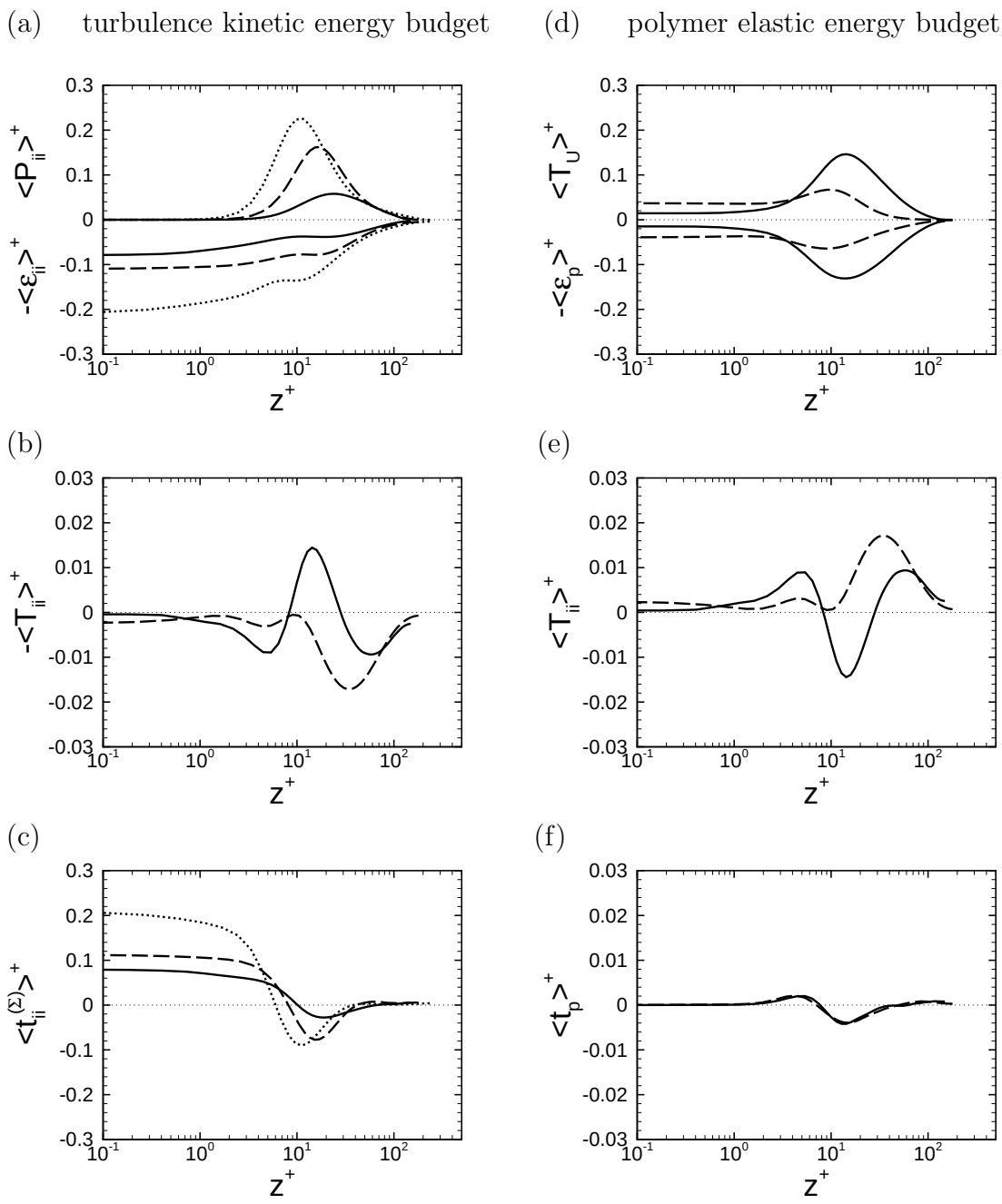

Figure 5.18: Turbulence kinetic energy and polymer elastic energy budgets in LDR (case CC3-q, 33%DR) and HDR (case FF4-q, 56%DR) regimes compared to Newtonian flow (case NN): (a) turbulence production, $\langle P_{ii}\rangle^+$, and viscous dissipation, $\langle \varepsilon_{ii}\rangle^+$; (b) energy transfer from turbulence to the polymer, $\langle T_{ii}\rangle^+$; (c) sum of transport terms, $\langle t_{ii}^{(\Sigma)}\rangle^+ = \langle t_{ii}^{(v)} + t_{ii}^{(press)} + t_{ii}^{(R)} + t_{ii}^{(p)}\rangle^+$; (d) energy transfer from the mean flow to the polymer, $\langle T_U\rangle^+$, and polymer dissipation, $\langle \varepsilon_p\rangle^+$; (e) energy transfer from turbulence to the polymer, $\langle T_{ii}\rangle^+$; (f) polymer energy transport, $\langle t_p\rangle^+$. $\cdots\cdots$, Newtonian flow (case NN); $--$, viscoelastic flow at low drag reduction (case CC3-q, 33%DR); ——, viscoelastic flow at high drag reduction (case FF4-q, 56%DR).

The drop in the pressure-strain correlation leads to a drop in the rate of turbulence production, $\langle P_{11} \rangle^+$, as shown in figures 5.16(d) and 5.18(a). In the LDR case, this drop in the rate of turbulence production is observed for $z^+ < 20$, while in the HDR case it is observed for $z^+ < 70$. These z^+ ranges are consistent with the z^+ ranges for which the largest turbulent eddies are affected by the polymer in figures 5.10(a-d). The drop in the turbulence production results in a proportionate drop in the rate of viscous dissipation, $\langle \varepsilon_{\alpha\alpha} \rangle^+$, as shown in figures 5.16(d-f) and 5.18(a), as well as in transport terms, $\langle t_{\alpha\alpha}^{(\Sigma)} \rangle^+$, as shown in figures 5.17(a-c) and 5.18(c). Figures 5.17(d-f) and 5.18(b) show the rates of energy transfer from turbulence to the polymer, $\langle T_{\alpha\alpha} \rangle^+$. The most noticeable feature of $\langle T_{\alpha\alpha} \rangle^+$ (figures 5.17d-5.17f) and its sum, $\langle T_{ii} \rangle^+$ (figure 5.18b), is their insignificant magnitude compared to the rates of turbulence production or dissipation. In the outer region ($z^+ > 20$ in the LDR case and $z^+ > 30$ in the HDR case), $-\langle T_{\alpha\alpha} \rangle^+$ is negative in all components, indicating a transfer of energy from turbulence to the polymer on average. However, in the near-wall region, energy is observed to transfer from the polymer to turbulence in the streamwise component on average. This is simply a reflection of the biaxial flow which is set up by the streamwise vortices in the near-wall region, and is not believed to be dynamically significant. This biaxial flow stretches the polymer in the cross-stream directions, while forcing the polymer to recoil in streamwise direction. Through the stretching process, the polymer absorbs energy from the cross-stream components of turbulence, while through recoiling process it releases its energy into the streamwise component of turbulence.

Figures 5.18(a-c) and 5.18(d-f) show the total turbulence kinetic energy and poly-

mer elastic energy budgets in the LDR and HDR cases compared to Newtonian flow. The total kinetic energy is dominated by the streamwise component, and thus its behavior is similar to that discussed for the streamwise kinetic energy in figures 5.16 and 5.17. In addition to the small transfer of energy $\langle T_{ii} \rangle^+$ from turbulence to the polymer, the polymer energy budget also shows a transfer of energy $\langle T_U \rangle^+$ from the mean flow to the polymer. The magnitude of the energy transfer $\langle T_U \rangle^+$ from the mean flow to the polymer is much larger than the energy transfer $\langle T_{ii} \rangle^+$ from turbulence to the polymer. But the effect on drag reduction of this transfer from the mean flow is not believed to be dynamically significant. The polymer dissipation, $\langle \varepsilon_p \rangle^+$, mostly reflects the transfer of energy from the mean flow $\langle T_U \rangle^+$, while the polymer transport $\langle t_p \rangle^+$ is insignificant in magnitude.

The drop in pressure-strain correlation, which we have identified as the key to polymer drag reduction has been mentioned as a possible source of polymer drag reduction going back to Tiederman (1990). Several recent computational studies (Ptasinski, *et al.*, 2003; Stone, *et al.*, 2004; Li & Graham, 2007) have also attributed polymer drag reduction to a drop in pressure-strain correlation. However, in these studies the drop in pressure-strain correlation has been attributed to a drop in the fluctuating pressure, not the fluctuating strain-rate as argued in the present study.

To investigate this issue, in figures 5.19(a) and figures 5.19(d-f) we show the normalized r.m.s. pressure fluctuation, p^+_{rms}, and the normalized r.m.s. strain-rate fluctuation, $s^+_{ii,rms}$, in the LDR and HDR regimes compared to Newtonian flow. It can be seen that while in the LDR case p^+_{rms} is lower than Newtonian, in the HDR case it is actually higher. In contrast, all diagonal components of $s^+_{ii,rms}$ are observed to

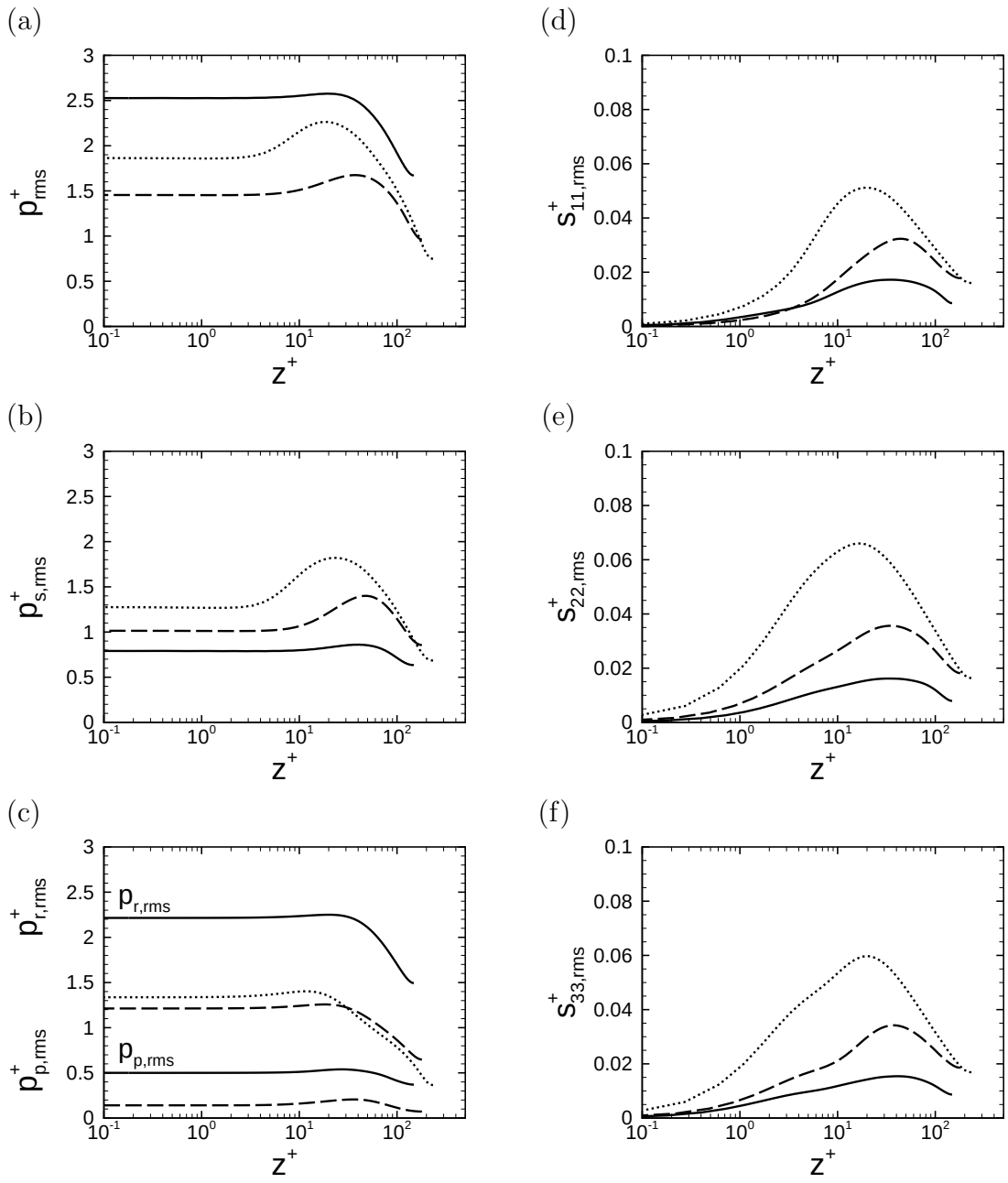

Figure 5.19: (a) total r.m.s. pressure fluctuations, (b) slow part of r.m.s. pressure fluctuations, (c) rapid and polymer parts of r.m.s. pressure fluctuations, (d-f) The diagonal components of normalized r.m.s. strain-rate fluctuation in LDR (case CC3-q, 33%DR) and HDR (case FF4-q, 56%DR) regimes compared to Newtonian flow (case NN). ·····, Newtonian flow (case NN); −−−, viscoelastic flow at low drag reduction (case CC3-q, 33%DR); ——, viscoelastic flow at high drag reduction (case FF4-q, 56%DR).

drop with the magnitude of the drop increasing with increasing drag reduction with magnitude similar to the drops observed in $\langle \Pi_{\alpha\alpha} \rangle^+$ in figures 5.16(a-c). To investigate the behavior of p^+_{rms} in more detail, in figures 5.19(b-c), we plot the slow, rapid and polymer contributions to p^+_{rms} as defined by Kim (1989) and Ptasinski, *et al.* (2003) as

$$\frac{\partial^2 p'_r}{\partial x_i^2} = \frac{\partial^2}{\partial x_i \partial x_j}(-u'_i U_j - U_i u'_j) \qquad \text{B.C. } \| \frac{\partial p'_r}{\partial z} = 0, \tag{5.12}$$

$$\frac{\partial^2 p'_s}{\partial x_i^2} = \frac{\partial^2}{\partial x_i \partial x_j}(-u'_i u'_j + \langle u'_i u'_j \rangle) \qquad \text{B.C. } \| \frac{\partial p'_s}{\partial z} = \nu_s \frac{\partial^2 w'}{\partial z^2}, \tag{5.13}$$

$$\frac{\partial^2 p'_p}{\partial x_i^2} = \frac{\partial^2}{\partial x_i \partial x_j}(\tau'_{p,ij}) \qquad \text{B.C. } \| \frac{\partial p'_p}{\partial z} = \frac{\partial \tau'_{p,zj}}{\partial x_j}. \tag{5.14}$$

With increasing drag reduction, the slow part of r.m.s. pressure fluctuation, $p^+_{s,rms}$ (figure 5.19b), is observed to monotonically drop, while the polymer part of r.m.s. pressure fluctuation, $p^+_{p,rms}$ (figure 5.19c), is observed to monotonically grow. In contrast, the rapid part of r.m.s. pressure fluctuation, $p^+_{r,rms}$ (figure 5.19c), drops in the LDR case, but becomes higher than Newtonian in the HDR case. These results suggest that the growth of p^+_{rms} is due to the growth of $p^+_{p,rms}$ and $p^+_{r,rms}$. All these results indicate that the drop in the rate of pressure-strain correlation is due to the reduced strain-rate rather than the change in pressure fluctuations.

5.5 Effect of polymer concentration

To verify that the mechanism of drag reduction described in the previous sections for saturation concentrations also applies to concentrations below saturation in this section. We investigate the effect of polymer concentration on the features described in § 5.2 through § 5.4 for $We_{\tau_b} \approx 35$ and $We_{\tau_b} \approx 150$. At both Weissenberg numbers,

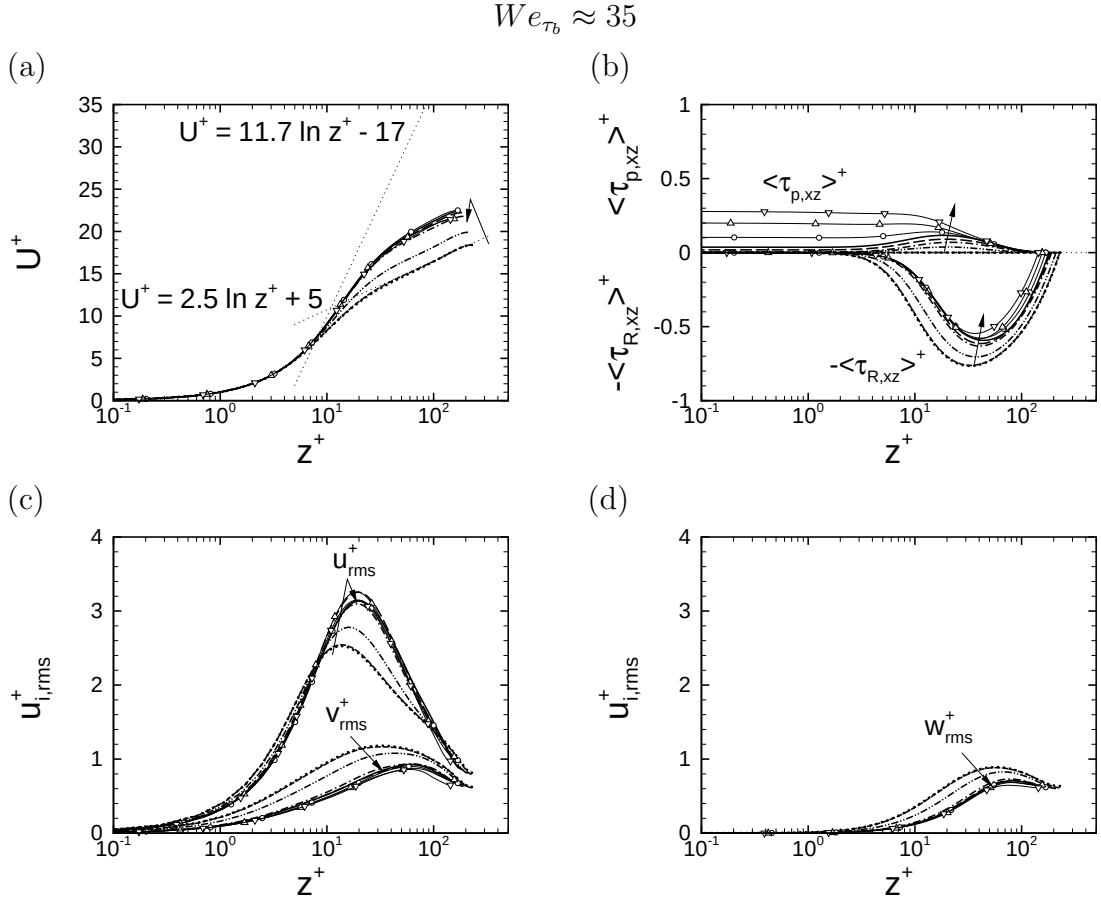

Figure 5.20: Effect of polymer concentration on the predicted second-order turbulence statistics at $We_{\tau_b} \approx 35$: (a) mean velocity profiles; (b) Reynolds shear stresses and polymer shear stresses; (c) streamwise and spanwise turbulence intensities; (d) wall-normal turbulence intensities. $\cdots\cdots$, Newtonian (case N); ---, $\beta \approx 0.999996$ (case C7-l); $-\cdots-$, $\beta \approx 0.9996$ (case C5-l); $-\cdot-$, $\beta \approx 0.996$ (case C4-l); $--$, $\beta \approx 0.98$ (case C4.1-l); ——, $\beta \approx 0.96$ (case C3-l); —○—, $\beta \approx 0.89$ (case C3.1-l); —△—, $\beta \approx 0.80$ (case C3.2-l); —▽—, $\beta \approx 0.72$ (case C2-l).

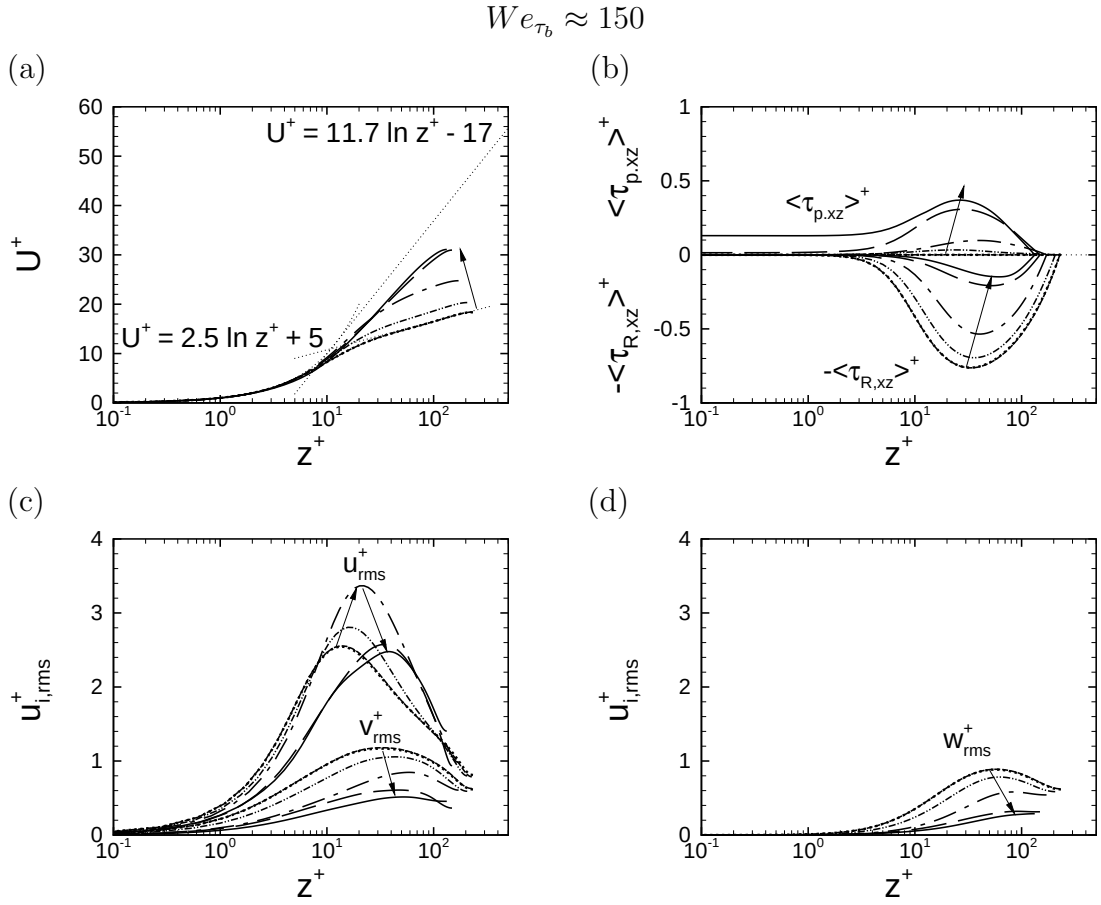

Figure 5.21: Effect of polymer concentration on the predicted second-order turbulence statistics at $We_{\tau_b} \approx 150$: (a) mean velocity profiles; (b) Reynolds shear stresses and polymer shear stresses; (c) streamwise and spanwise turbulence intensities; (d) wall-normal turbulence intensities. $\cdots\cdots$, Newtonian (case NN); ---, $\beta \approx 0.999998$ (case F8-q); $-\cdots-$, $\beta \approx 0.9998$ (case F6-q); ——·——, $\beta \approx 0.998$ (case FF5-q); —— ——, $\beta \approx 0.98$ (case FF4-q); ——, $\beta \approx 0.86$ (case FF3-q).

drag reduction monotonically increases for $0.98 \lesssim \beta < 1$, plateaus for $0.9 \lesssim \beta \lesssim 0.98$, and slowly decays for $\beta \lesssim 0.9$. A summary of the simulation parameters for these simulations is given in table 2.2.

Figures 5.20 and 5.21 show the one-point flow statistics in stationary viscoelastic turbulent flow at various concentrations for $We_{\tau_b} \approx 35$ and $We_{\tau_b} \approx 150$, respectively. At $We_{\tau_b} \approx 35$, increasing the concentration up to the saturation concentration leads to a thickening of the buffer layer and an upward shift of the mean velocity profile from Newtonian values as shown in figure 5.20(a). These changes are accompanied by a drop in the Reynolds shear stress, as shown in figure 5.20(b). The streamwise turbulence intensity shows a monotonic increase in the magnitude of its peak and a shift of the peak away from the wall with increasing concentration up to the saturation concentration, while the cross-stream turbulence intensities decay, as shown in figures 5.20(c-d). Increasing the concentration beyond the saturation concentration leads to a slight drop in the magnitude of drag reduction which is reflected in all the flow statistics, as shown in table 2.2 and figure 5.20. At $We_{\tau_b} \approx 150$, the mean velocity profile adjusts from the Newtonian profile to the ultimate profile with increasing polymer concentration, while the Reynolds shear stress monotonically decays, as shown in figures 5.21(a-b). The streamwise turbulence intensity shows an increase in its peak magnitude with increasing polymer concentration for $0.998 \lesssim \beta < 1$, but the magnitude of the peak in the streamwise turbulence intensity drops back to values comparable to the Newtonian value at higher concentrations ($\beta \gtrsim 0.98$). Furthermore, the peak of the streamwise turbulence intensity shifts towards the center of the channel with increasing concentration, while the cross-stream turbulence inten-

sities monotonically decay (figures 5.21c & 5.21d). Overall, the features observed in the turbulence intensities at both Weissenberg numbers indicate that the turbulence structure at both Weissenberg numbers becomes more anisotropic with increasing polymer concentration up to the saturation concentration.

To investigate the effect of concentration on the anisotropy state of turbulence, figures 5.22 and 5.23 show the anisotropy-invariant maps at $We_{\tau_b} \approx 35$ for $0.72 \lesssim \beta \lesssim 0.9996$ and at $We_{\tau_b} \approx 150$ for $0.86 \lesssim \beta \lesssim 0.9998$, respectively. At $We_{\tau_b} \approx 35$, the degree of anisotropy rapidly increases with increasing polymer concentration up to the saturation concentration ($\beta \approx 0.96$), but remains nearly unchanged at higher concentrations, as shown in figure 5.22. The shift towards the one-dimensional turbulence limit is confined to $9 \lesssim z^+ \lesssim 50$ at the lowest concentration ($\beta \approx 0.9996$), but extends to $11 \lesssim z^+ \lesssim 100$ at the saturation concentration ($\beta \approx 0.96$). Increasing the concentration beyond the saturation concentration only slightly modifies the anisotropy state of turbulence in the channel. Similar trends are also observed at $We_{\tau_b} \approx 150$ as shown in figure 5.23, although the features are more enhanced than those at $We_{\tau_b} \approx 35$. The degree of anisotropy of turbulence rapidly increases with increasing concentration. The shift towards the one-dimensional turbulence limit is observed for $9 \lesssim z^+ \lesssim 100$ at the lowest concentration ($\beta \approx 0.9998$) and it extends to $12 \lesssim z^+ \lesssim 132$ (center of the channel) at the highest concentration ($\beta \approx 0.86$).

We next examine the effect of polymer concentration on the characteristic strain-rate and compare the DNS results with the predictions of classical theories. Figures 5.24 and 5.25 show the characteristic strain-rate at $We_{\tau_b} \approx 35$ with varying polymer concentration for $0.72 \lesssim \beta \lesssim 0.9996$ compared to $1/T^{*+}$ of Lumley's theory (eqn.5.9)

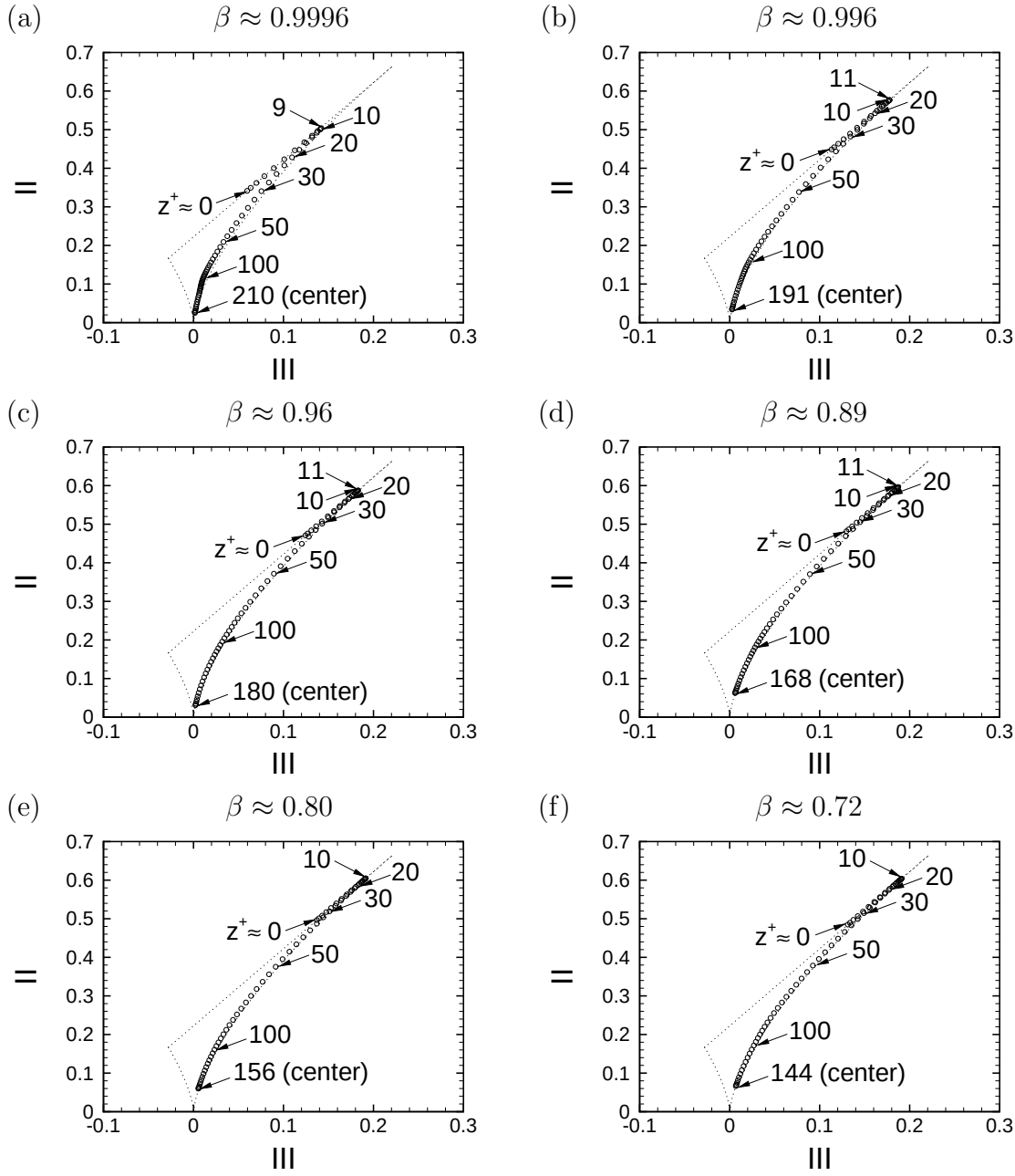

Figure 5.22: Effect of polymer concentration on anisotropy-invariant maps at $We_{\tau_b} \approx 35$: (a) $\beta \approx 0.9996$ (case C5-l); (b) $\beta \approx 0.996$ (case C4-l); (c) $\beta \approx 0.96$ (case C3-l); (d) $\beta \approx 0.89$ (case C3.1-l); (e) $\beta \approx 0.80$ (case C3.2-l); (f) $\beta \approx 0.72$ (case C2-l).

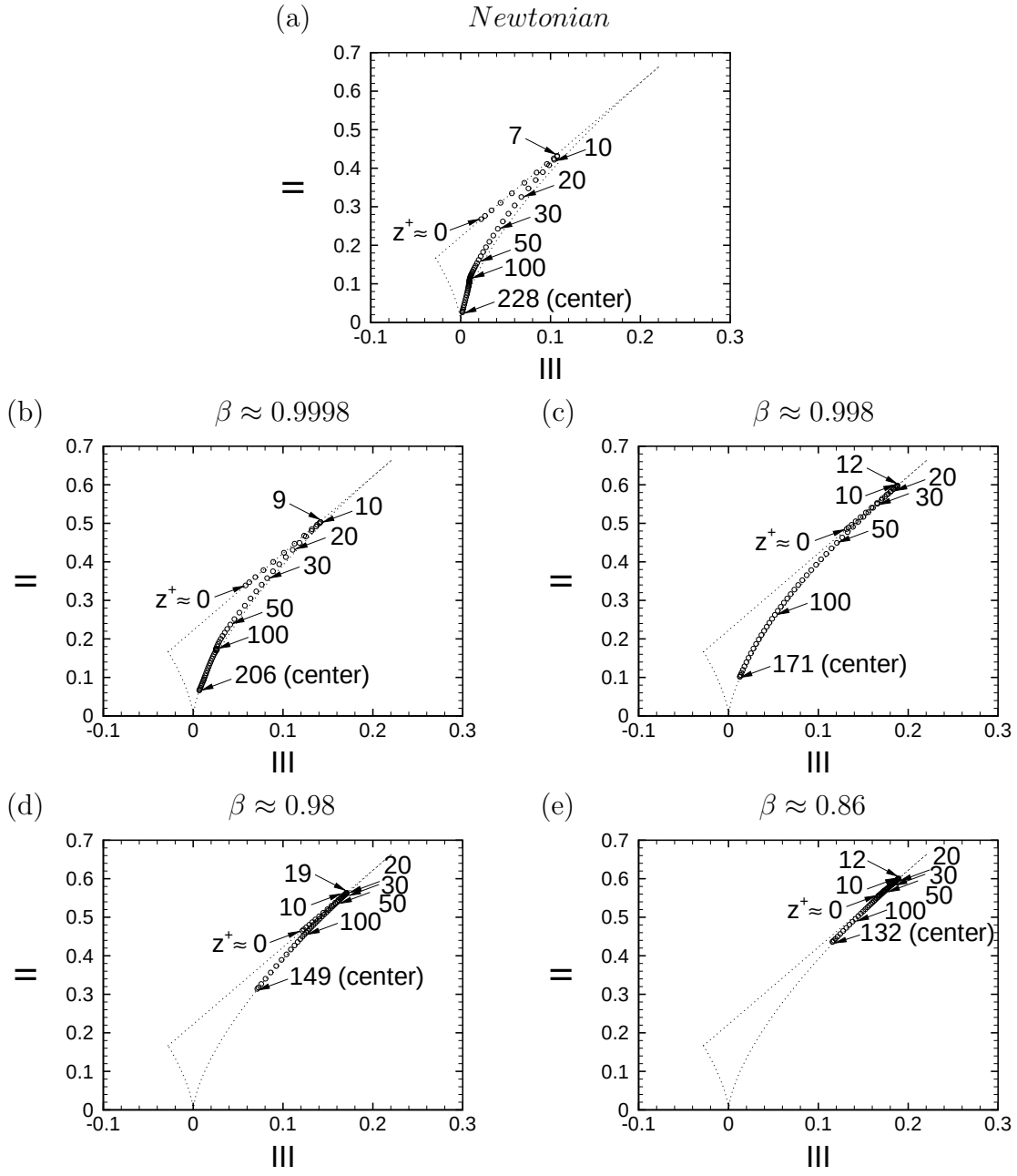

Figure 5.23: Effect of polymer concentration on anisotropy-invariant maps at $We_{\tau_b} \approx 150$: (a) Newtonian (case NN); (b) $\beta \approx 0.9998$ (case F6-q); (c) $\beta \approx 0.998$ (case FF5-q); (d) $\beta \approx 0.98$ (case FF4-q); (e) $\beta \approx 0.86$ (case FF3-q).

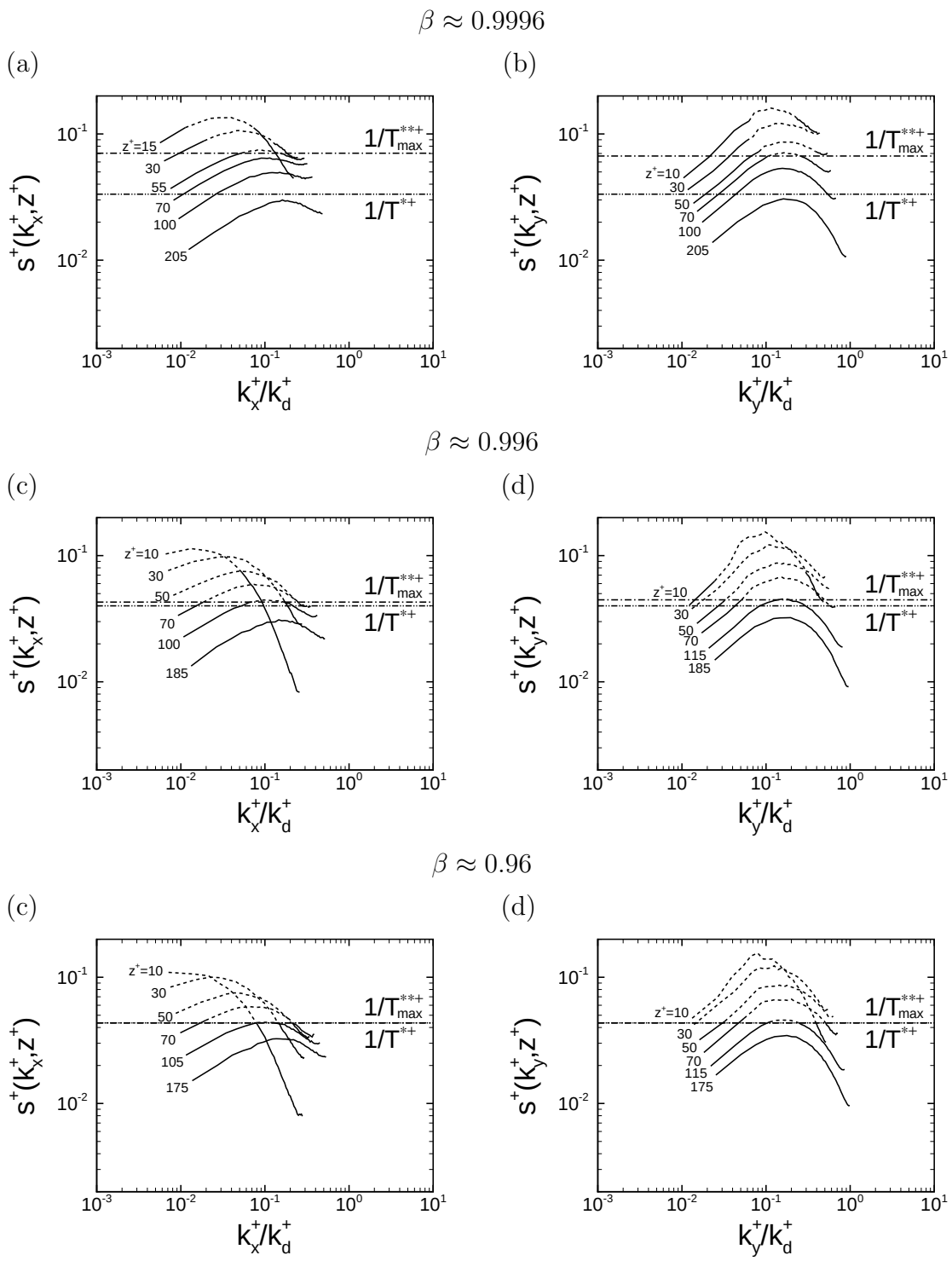

Figure 5.24: Effect of polymer concentration on the characteristic strain-rate at $We_{\tau_b} \approx 35$: (a-b) $\beta \approx 0.9996$ (case C5-l); (c-d) $\beta \approx 0.996$ (case C4-l); (e-f) $\beta \approx 0.96$ (case C3-l). (a,c,e) streamwise spectra; (b,d,f) spanwise spectra. $-\cdots-$, $1/T^{*+}$ from Lumley's theory; $-\cdot-$, lowest $1/T^{**+}(z^+)$ from the revised version of de Gennes's theory; ---, scales with $s^+(k_i^+, z^+) > 1/T^{**+}(z^+)$; ——, scales with $s^+(k_i^+, z^+) < 1/T^{**+}(z^+)$.

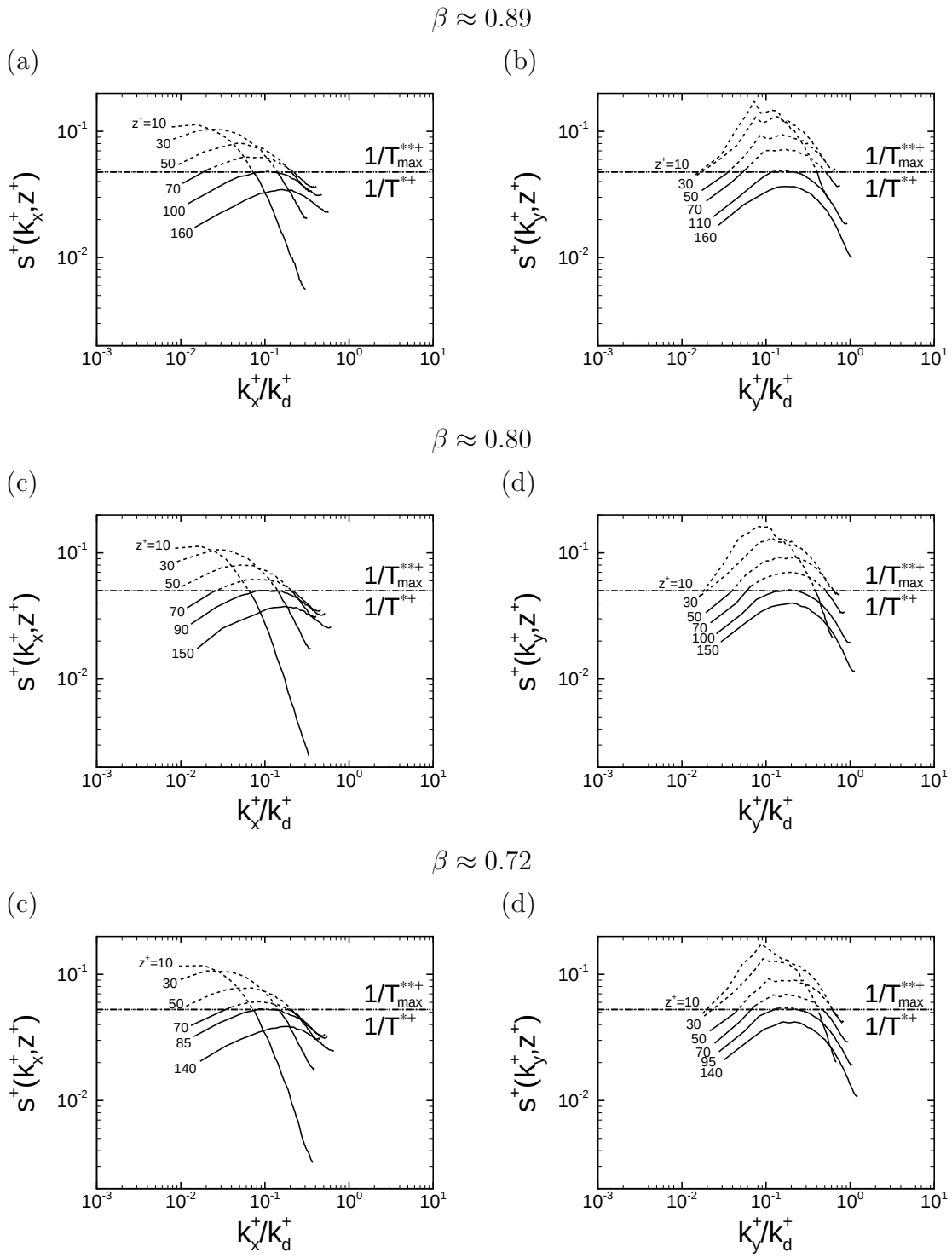

Figure 5.25: Effect of polymer concentration on the characteristic strain-rate at $We_{\tau_b} \approx 35$: (a-b) $\beta \approx 0.89$ (case C3.1-l); (c-d) $\beta \approx 0.80$ (case C3.2-l); (e-f) $\beta \approx 0.72$ (case C2-l). (a,c,e) streamwise spectra; (b,d,f) spanwise spectra. $-\cdots-$, $1/T^{*+}$ from Lumley's theory; $-\cdot-$, lowest $1/T^{**+}(z^+)$ from the revised version of de Gennes's theory; ---, scales with $s^+(k_i^+, z^+) > 1/T^{**+}(z^+)$; ——, scales with $s^+(k_i^+, z^+) < 1/T^{**+}(z^+)$.

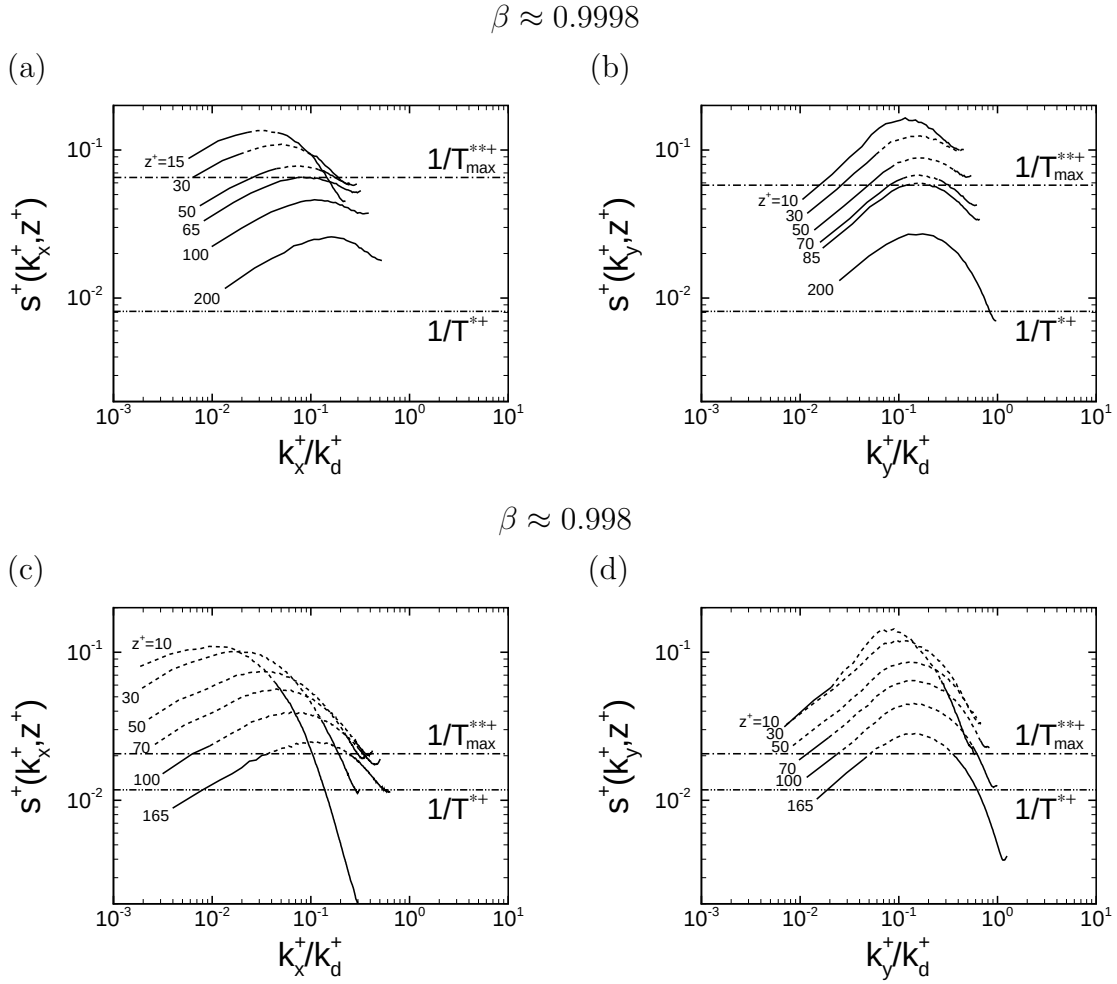

Figure 5.26: Effect of polymer concentration on the characteristic strain-rate at $We_{\tau_b} \approx 150$: (a-b) $\beta \approx 0.9998$ (case F6-l); (c-d) $\beta \approx 0.998$ (case FF5-q). (a,c) streamwise spectra; (b,d) spanwise spectra. $-\cdots-$, $1/T^{*+}$ from Lumley's theory; $-\cdot-$, lowest $1/T^{**+}(z^+)$ from the revised version of de Gennes's theory; ---, scales with $s^+(k_i^+, z^+) > 1/T^{**+}(z^+)$; ——, scales with $s^+(k_i^+, z^+) < 1/T^{**+}(z^+)$.

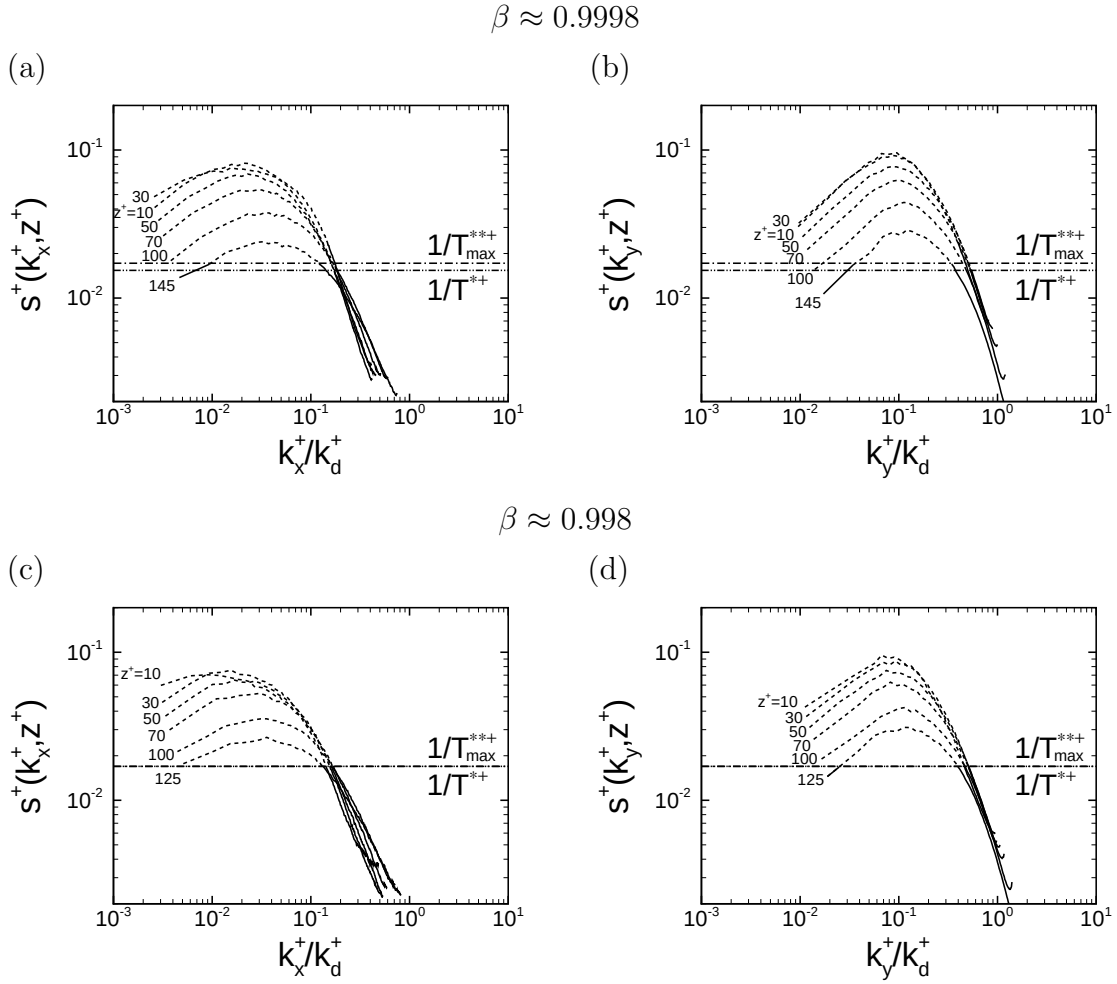

Figure 5.27: Effect of polymer concentration on the characteristic strain-rate at $We_{\tau_b} \approx 150$: (a-b) $\beta \approx 0.98$ (case FF4-q); (c-d) $\beta \approx 0.86$ (case FF3-q). (a,c) streamwise spectra; (b,d) spanwise spectra. $-\cdots-$, $1/T^{*+}$ from Lumley's theory; $-\cdot-$, lowest $1/T^{**+}(z^+)$ from the revised version of de Gennes's theory; ---, scales with $s^+(k_i^+, z^+) > 1/T^{**+}(z^+)$; ——, scales with $s^+(k_i^+, z^+) < 1/T^{**+}(z^+)$.

and $1/T^{**+}(z^+)$ of the revised de Gennes's theory (eqn.5.10). At concentrations below saturation, Lumley's theory and the revised de Gennes's theory give very different predictions for the range of affected scales. At the lowest concentration ($\beta \approx 0.9996$), the revised de Gennes's theory predicts an effect of polymer on turbulence only for the mid-range and small scales at $z^+ \lesssim 70$, while Lumley's theory predicts an effect at all scales for $z^+ \lesssim 50$ and at mid-range to small scales for $50 \lesssim z^+ < 205$. The difference between the two theories becomes less pronounced at saturation concentrations ($\beta \approx 0.96$) and beyond. At all concentrations, the predictions of de Gennes's revised theory for the range of affected scales are consistent with the ranges of z^+ in the anisotropy-invariant maps (figure 5.22) where the turbulence shifts towards the one-dimensional turbulence limit, while the prediction of Lumley's theory agree with the data from anisotropy-invariant maps only at concentration near saturation. Furthermore, the characteristic strain-rate for only the z^+ ranges at which the revised de Gennes's theory predicts an effect of the polymer on turbulence shows enhanced dissipation. Similar trends are also observed at $We_{\tau_b} \approx 150$ with varying the polymer concentration for $0.86 \lesssim \beta \lesssim 0.9998$ as shown in figures 5.26 and 5.27. At the lowest concentration ($\beta \approx 0.9998$), the Lumley's theory predicts an effect of the polymer at all scales throughout the channel. In contrast, the revised de Gennes's theory predicts the effect of the polymer to be limited to mid-range and small scales for $z^+ \lesssim 85$ at the lowest concentration ($\beta \approx 0.9998$). The difference between the two theories becomes smaller with increasing concentration and becomes identical at the highest concentration ($\beta \approx 0.86$). Once again, only the z^+ ranges predicted by the revised theory of de Gennes are consistent with observations in anisotropy-invariant maps

(figure 5.23) at lower concentrations. Similarly, only the characteristic strain-rate at z^+ ranges for which the revised theory of de Gennes predicts an effect of the polymer on turbulence shows enhanced dissipation.

Lastly, we examine the effect of polymer concentration on the turbulence and polymer energetics. Figures 5.28 and 5.29 show the effect of polymer concentration on the pressure-strain correlation, the total turbulence kinetic energy budget and the polymer elastic energy budget at $We_{\tau_b} \approx 35$, respectively. All the components of the pressure-strain correlation drop with increasing concentration up to the saturation concentration, as shown in figures 5.28(a-c). At the lowest concentration ($\beta \approx 0.999996$), no noticeable change is observed in the pressure-strain correlation compared to Newtonian flow. At $\beta \approx 0.9996$, the pressure-strain correlation drops relative to Newtonian for $z^+ < 50$. At higher concentrations ($\beta \gtrsim 0.996$), a drop of pressure-strain correlation compared to Newtonian is observed for $z^+ < 70$. These z^+ ranges are consistent with the ranges where the polymer affects the turbulence according to the revised de Gennes's theory in the characteristic strain-rate plots of figures 5.24 and 5.25. The rate of turbulence production also rapidly drop for $0.96 \lesssim \beta \leq 1$, and shows little change at higher concentrations, as shown in figure 5.28(d). Once again, no noticeable change is observed in the turbulence production at the lowest concentration ($\beta \approx 0.999996$), while a drop of turbulence production compared to Newtonian is observed for $z^+ < 15$ at $\beta \approx 0.9996$, and for $z^+ < 20$ at higher concentrations ($\beta \gtrsim 0.996$). The trends in these z^+ ranges are consistent with the trends in z^+ ranges for which the largest turbulent scales are affected by the polymer according to the revised de Gennes's theory shown in figures 5.24 and 5.25.

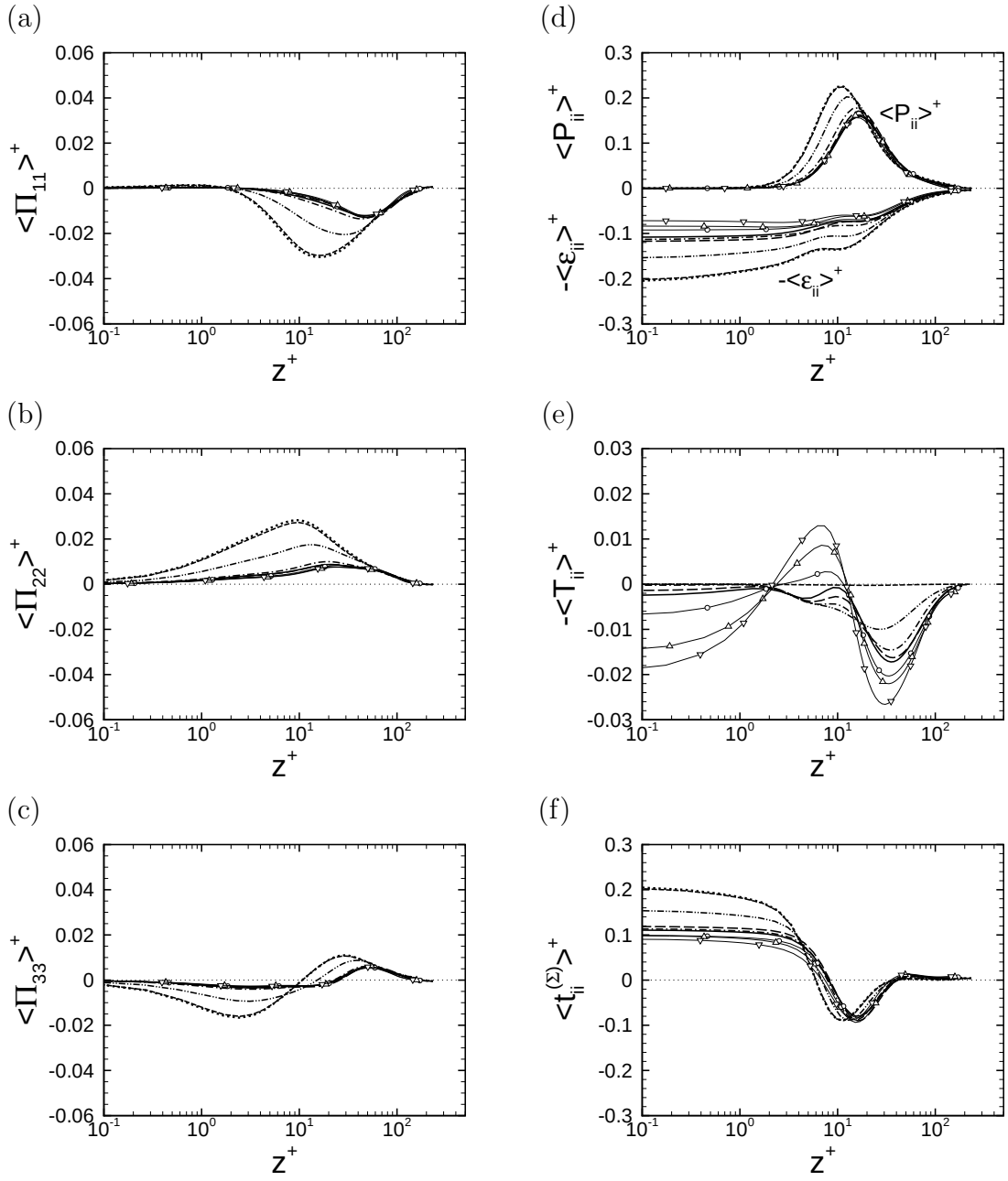

Figure 5.28: Effect of polymer concentration on the predicted turbulence kinetic energy budgets at $We_{\tau_b} \approx 35$: (a-c) pressure-strain correlation, $\langle \Pi_{\alpha\alpha} \rangle^+$; (d) turbulence production, $\langle P_{ii} \rangle^+$, and viscous dissipation, $\langle \varepsilon_{ii} \rangle^+$; (e) energy transfer from turbulence to the polymer, $\langle T_{ii} \rangle^+$; (f) sum of transport terms, $\langle t_{ii}^{(\Sigma)} \rangle^+$. $\cdots\cdots$, Newtonian (case N); ---, $\beta \approx 0.999996$ (case C7-l); $-\cdot\cdot-$, $\beta \approx 0.9996$ (case C5-l); $-\cdot-$, $\beta \approx 0.996$ (case C4-l); $---$, $\beta \approx 0.98$ (case C4.1-l); ——, $\beta \approx 0.96$ (case C3-l); —○—-, $\beta \approx 0.89$ (case C3.1-l); —▲—, $\beta \approx 0.80$ (case C3.2-l); —▼—, $\beta \approx 0.72$ (case C2-l).

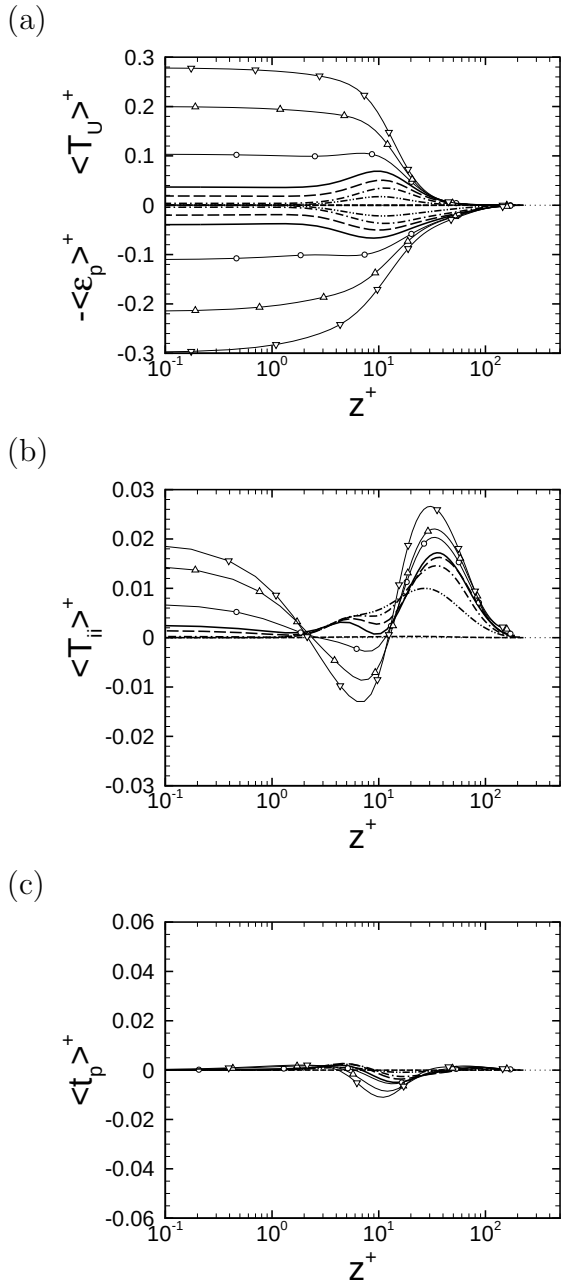

Figure 5.29: Effect of polymer concentration on the predicted polymer elastic energy budgets at $We_{\tau_b} \approx 35$: (a) energy transfer from the mean flow to the polymer, $\langle T_U \rangle^+$, and polymer dissipation, $\langle \varepsilon_p \rangle^+$; (b) energy transfer from turbulence to the polymer, $\langle T_{ii} \rangle^+$; (c) polymer energy transport, $\langle t_p \rangle^+$. $\cdots\cdots$, Newtonian (case N); ---, $\beta \approx 0.999996$ (case C7-l); $-\cdots-$, $\beta \approx 0.9996$ (case C5-l); $-\cdot-$, $\beta \approx 0.996$ (case C4-l); $---$, $\beta \approx 0.98$ (case C4.1-l); ——, $\beta \approx 0.96$ (case C3-l); —○—, $\beta \approx 0.89$ (case C3.1-l); —▲—, $\beta \approx 0.80$ (case C3.2-l); —▼—, $\beta \approx 0.72$ (case C2-l).

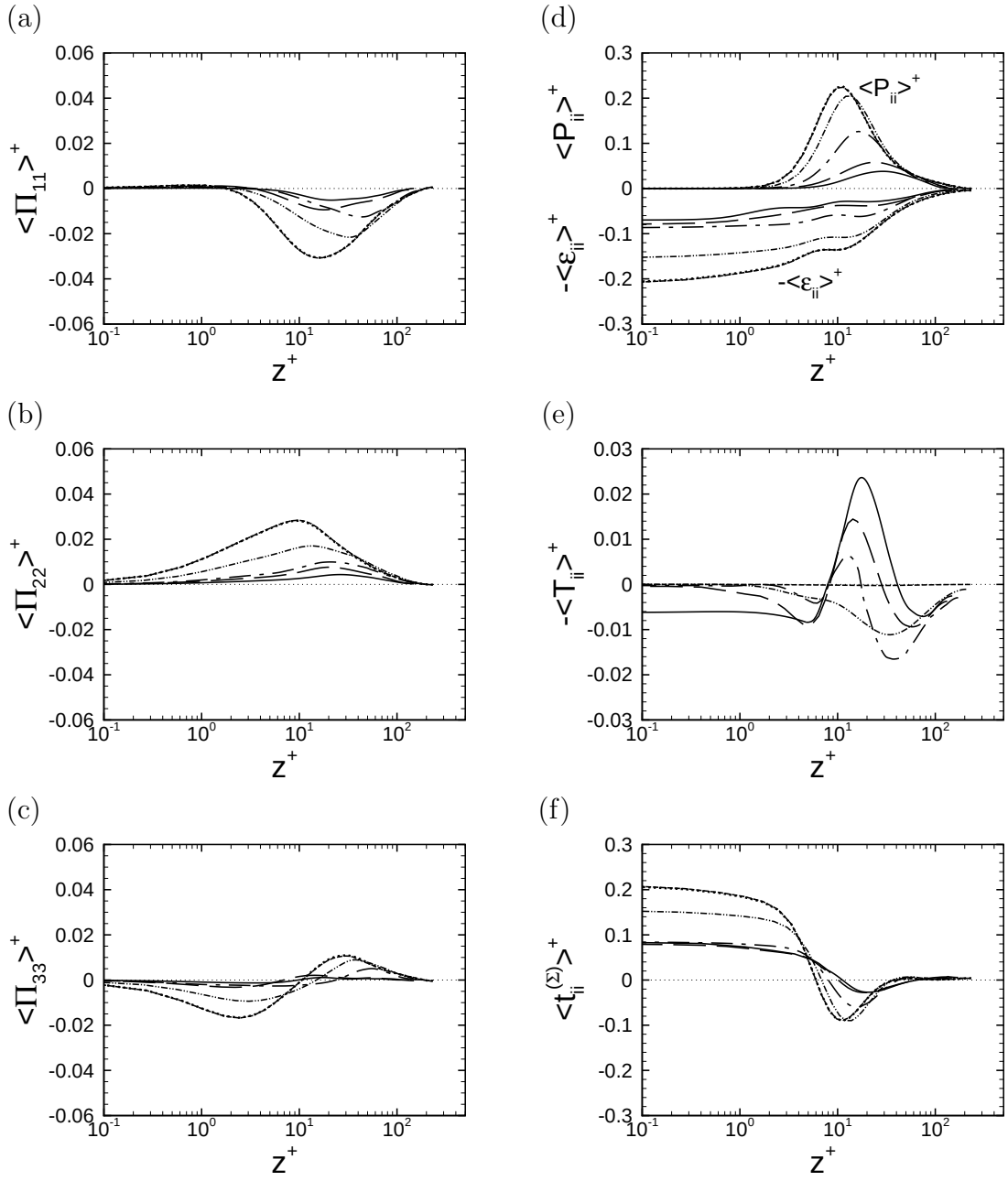

Figure 5.30: Effect of polymer concentration on the predicted turbulence kinetic energy budgets at $We_{\tau_b} \approx 150$: (a-c) pressure-strain correlation, $\langle \Pi_{\alpha\alpha} \rangle^+$; (d) turbulence production, $\langle P_{ii} \rangle^+$, and viscous dissipation, $\langle \varepsilon_{ii} \rangle^+$; (e) energy transfer from turbulence to the polymer, $\langle T_{ii} \rangle^+$; (f) sum of transport terms, $\langle t_{ii}^{(\Sigma)} \rangle^+$. $\cdots\cdots$, Newtonian (case NN); ---, $\beta \approx 0.999998$ (case F8-q); $-\cdots-$, $\beta \approx 0.9998$ (case F6-q); ——$\cdot$——, $\beta \approx 0.998$ (case FF5-q); —— ——, $\beta \approx 0.98$ (case FF4-q); ——, $\beta \approx 0.86$ (case FF3-q).

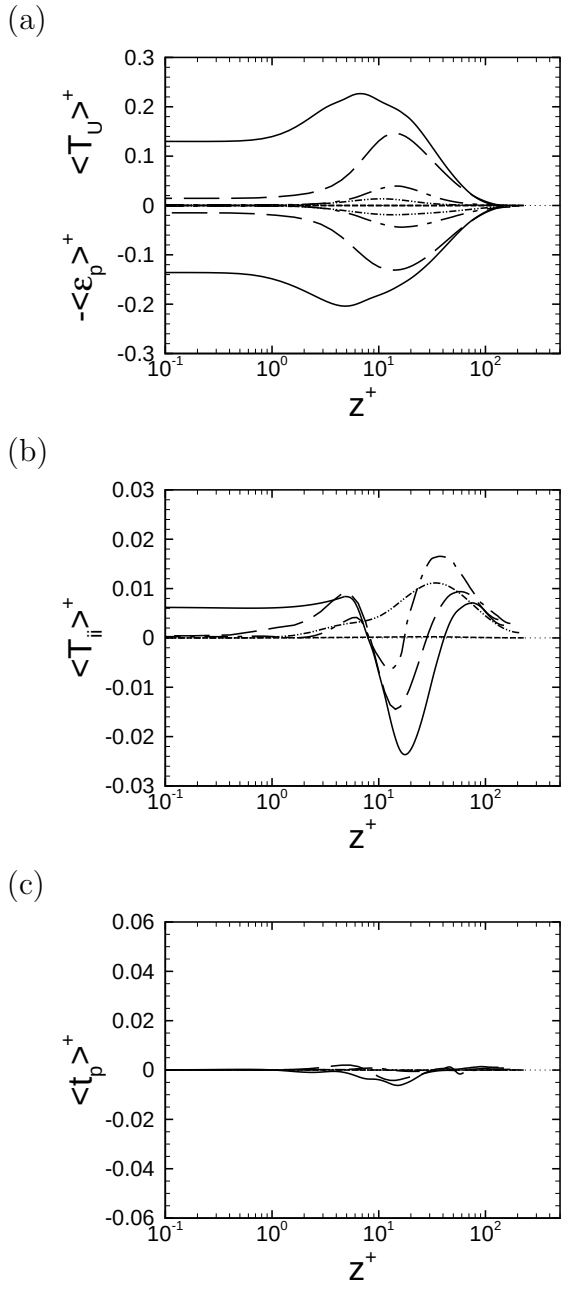

Figure 5.31: Effect of polymer concentration on the predicted polymer elastic energy budgets at $We_{\tau_b} \approx 150$: (a) energy transfer from the mean flow to the polymer, $\langle T_U \rangle^+$, and polymer dissipation, $\langle \varepsilon_p \rangle^+$; (b) energy transfer from turbulence to the polymer, $\langle T_{ii} \rangle^+$; (c) polymer energy transport, $\langle t_p \rangle^+$. $\cdots\cdots$, Newtonian (case NN); ---, $\beta \approx 0.999998$ (case F8-q); $-\cdot\cdot-$, $\beta \approx 0.9998$ (case F6-q); ——$\cdot$——, $\beta \approx 0.998$ (case FF5-q); —— ——, $\beta \approx 0.98$ (case FF4-q); ——, $\beta \approx 0.86$ (case FF3-q).

The drop in turbulence production is also reflected in the rate of viscous dissipation, $\langle \varepsilon_{ii} \rangle^+$ (figure 5.28d) and the sum of transport terms, $\langle t_{ii}^{(\Sigma)} \rangle^+$ (figure 5.28f). In the polymer elastic energy budget shown in figure 5.29, the magnitudes of all the terms in the polymer elastic energy budget including the energy transfer from the mean flow to the polymer, $\langle T_U \rangle^+$ (figure 5.29a), polymer dissipation, $\langle \varepsilon_p \rangle^+$ (figure 5.29a), energy transfer from turbulence to the polymer, $\langle T_{ii} \rangle^+$ (figure 5.29b), and polymer energy transport, $\langle t_p \rangle^+$ (figure 5.29c) monotonically increase with increasing concentration. The energy transfer from the mean flow to the polymer is an order of magnitude larger than the energy transfer from turbulence to the polymer and dominates polymer dissipation at all concentrations. However, this transfer from the mean flow to the polymer is not believed to be significant, because even though it keeps rising at concentrations above the saturation concentration it does not lead to any additional drag reduction.

Figures 5.30 and 5.31 show the effect of the polymer concentration on the pressure-strain correlation, the total turbulence kinetic energy budget and the polymer elastic energy budget at $We_{\tau_b} \approx 150$, respectively. The pressure-strain correlation monotonically drops with increasing polymer concentration, as shown in figures 5.30(a-c). No noticeable drop in pressure-strain correlation occurs at the lowest concentration ($\beta \approx 0.999998$). At higher concentrations, the pressure-strain correlation shows a drop relative to Newtonian for $z^+ < 40$ at $\beta \approx 0.9998$, for $z^+ < 80$ at $\beta \approx 0.998$, and throughout the channel at $\beta \approx 0.98$ and 0.86. These z^+ ranges are consistent with the $z+$ ranges in which de Gennes's revised theory predicts an effect by the polymer on the flow in characteristic strain-rate of figures 5.26 and 5.27. The rate

of turbulence production (figures 5.30d) also monotonically drops with increasing concentration. No noticeable drop in turbulence production occurs at the lowest concentration ($\beta \approx 0.999998$). The turbulence production shows a drop in magnitude compared to Newtonian for $z^+ < 15$ at $\beta \approx 0.9998$, for $z^+ < 30$ at $\beta \approx 0.998$, and throughout the channel at higher concentrations. Once again, the trends in these z^+ ranges are consistent with the trends in z^+ ranges for which the largest turbulent scales are affected by the polymer according to the revised de Gennes's theory in figures 5.26 and 5.27. As a result of the reduced turbulence production, the rate of viscous dissipation, $\langle \varepsilon_{ii} \rangle^+$ (figure 5.30d) and the sum of transport terms, $\langle t_{ii}^{(\Sigma)} \rangle^+$ (figure 5.30f) monotonically drop with increasing concentration. The magnitudes of the energy transfer from the mean flow to the polymer, $\langle T_U \rangle^+$ (figure 5.31a), polymer dissipation, $\langle \varepsilon_p \rangle^+$ (figure 5.31a), energy transfer from turbulence to the polymer, $\langle T_{ii} \rangle^+$ (figure 5.31b), and polymer energy transport, $\langle t_p \rangle^+$ (figure 5.31c) are also observed to increase monotonically with increasing polymer concentration.

These results suggest that the revised theory of de Gennes can correctly predict the range of affected scales by the polymer at all concentrations, while the prediction of Lumley's theory are valid only at or near saturation concentrations.

5.6 Summary of the mechanism of drag reduction

The results of § 5.2 through § 5.5 show that the main effect of the polymer is extraction of a small amount, of no more than $\sim 5\%$ on a volume averaged basis, of turbulence kinetic energy from turbulent scales which have a timescale shorter than the polymer relaxation time. This extraction of energy leads to a decrease in the

fluctuating strain-rate at scales which have redirected a minimum fraction ($\sim 3\%$) of their turbulence kinetic energy to the elastic energy of the polymer. The reduction of the fluctuating strain-rate at these scales, in turn, reduces the magnitude of the pressure-strain correlation at these and neighboring scales, thus inhibiting the ability of turbulence to transfer energy from the streamwise to the cross-stream directions at these scales. When this drop in the pressure-strain correlation extends to the largest energy-containing turbulent scales, the turbulence kinetic energy which has transferred from the mean flow to turbulence is trapped in the streamwise component and cannot be redistributed to the cross-stream directions. This results in a sharp drop in the wall-normal turbulence intensity and the Reynolds shear stress. This drop in the Reynolds shear stress, in turn, results in a drop in the rate of turbulence production and leads to drag reduction. Furthermore, the energy trapped in the streamwise direction can no longer cascade to the small scales due to the anisotropy of these scales, leading to further decay of the fluctuating strain-rate and turbulence kinetic energy in the small scales. This decay further amplifies the features described above. Thus the miniscule extraction of energy by the polymer at the affected turbulent scales starts a self-amplifying sequence of events, which leads to cessation of turbulence production and results in drag reduction. For effective high drag reduction, the initial minute extraction of energy by the polymer needs to extend to the largest turbulent scales at wall-normal locations where the peak of turbulence production occurs.

Chapter VI

Summary and Conclusions

The present study was initiated with the following objectives in mind: (i) Develop the required numerical methods for accurate and efficient Direct Numerical Simulation (DNS) of drag reduction by dilute polymer solutions in wall-bounded flows; (ii) Perform DNS of drag reduction by homogeneous, dilute polymer solutions in turbulent channel flow, and validate the DNS results through 'quantitative' comparisons with the available experimental data; (iii) Use the DNS results to investigate the scaling of drag reduction with polymer and flow parameters, such that the 'optimal' polymer parameters for drag reduction in a given turbulent flow can be determined *a priori*; (iv) Using the DNS results, clarify the detailed mechanism of drag reduction by dilute polymer solutions.

To this end, a novel mixed Eulerian-Lagrangian scheme has been developed. In this scheme, the hydrodynamics equations are solved in an Eulerian representation using standard pseudo-spectral methods (Canuto, *et al.*, 1988), while the polymer dynamics equations are solved in a Lagrangian framework using the Backward-tracking Lagrangian Particle Method (BLPM) suggested by Wapperom, Keunings & Legat (2000). The scheme can handle realistic polymer parameters and incurs a polymeric

artificial stress diffusivity smaller than those needed to stabilize the calculations in conventional Eulerian schemes. The main advantage of the scheme over conventional Eulerian scheme is cost. The computational cost of the mixed Eulerian-Lagrangian scheme is one-fifth of that associated with conventional Eulerian scheme when a tri-linear interpolation scheme is used for backward-tracking the position of polymer particle, and one-third of that associated with conventional Eulerian scheme when a quadratic interpolation scheme is used. This has allowed us to preform detailed parametric studies over a range of polymer parameters, which would be prohibitive with conventional Eulerian schemes.

Using the numerical methods described above, we have performed a series of parametric studies to clarify the role of the three polymer parameters, namely, the polymer relaxation time or Weissenberg number, $We_{\tau_b} \equiv \lambda u_{\tau_b}^2/\nu_s$, the polymer number density, $n_p k_B T/\rho u_{\tau_b}^2$ (or concentration), and the polymer extensibility parameter, b, on drag reduction, where λ denotes the polymer relaxation time, u_{τ_b} is the friction velocity in the base Newtonian flow, ν_s is the solvent viscosity, ρ is the density, n_p is the polymer number density, k_B is the Boltzmann constant, and T is the absolute temperature. All DNS studies were performed in turbulent channel flows at a base Reynolds number of $Re_{\tau_b} \equiv u_{\tau_b} h/\nu_s \approx 230$. The DNS studies covered the range of Weissenberg numbers corresponding to $10 \leq We_{\tau_b} \leq 150$, polymer extensibility parameters corresponding to $4500 \leq b \leq 450,000$ (corresponding to PEO of $3 \times 10^5 < M_w < 10^8$), and polymer number densities corresponding to $1 \times 10^{-8} \leq n_p k_B T/\rho u_{\tau_b}^2 \leq 1 \times 10^{-2}$ (or viscosity ratios of $0.72 \leq \beta \leq 0.99999999$), where $\beta = \mu_s/\mu_o$ denotes the ratio of the solvent viscosity to the zero-shear viscosity of the polymer solution). In the Low Drag Re-

duction (LDR) regime, computations were performed in channels of size $10h \times 5h \times 2h$ with a resolution of $128 \times 128 \times 129$ in the streamwise, spanwise and wall-normal directions, respectively. In the High Drag Reduction (HDR) regime, computations were performed in channels of size $40h \times 10h \times 2h$ with a resolution of $512 \times 256 \times 129$. All computations were performed with a FENE-P dumbbell model of the polymer, were driven at constant flow rate, and were initialized by introducing the polymer in its coiled state into the fully-developed base Newtonian turbulent flow. The results show that the full range of drag reduction from onset of drag reduction to Maximum Drag Reduction (MDR) can be reproduced in DNS using realistic polymer parameters and dilute concentrations ($0.9 < \beta < 1.0$), with statistics in quantitative agreement with the available experimental data.

Using the above DNS results, we have investigated the scaling of drag reduction with polymer and flow parameters. Onset of drag reduction was found to be a function of both the polymer concentration and Weissenberg number, as originally suggested by de Gennes (1986). However, the onset criteria suggested by de Gennes (1986) was found to be several orders of magnitude off from the DNS onset data. To remedy this problem, a revised version of de Gennes's theory was developed. In this revised theory, (i) it is assumed that the dynamics of turbulence at a given scale is affected by the polymer when a minimal fraction, of $\sim 3\%$, of the turbulence kinetic energy at that scale is redirected into the elastic energy of the polymer, as opposed to the 100% assumed in the original de Gennes's theory (1986); (ii) the polymer stretching due to the mean flow and other turbulent scales, which were ignored in the original theory of de Gennes (1986), are included in the expression for the polymer stretch; (iii) a form

of the energy spectrum appropriate for finite Reynolds numbers is assumed instead of the Kolmogorov spectrum used by de Gennes (1986). This revised theory gives good agreement with the onset data observed in DNS, accurately predicts the range of turbulent scales affected by the polymer at all values of drag reduction ranging from onset to MDR, and gives a dimensionality of polymer stretching in agreement with experiments.

Investigation of the dependence of drag reduction on the flow and polymer parameters shows that the $\%DR$ can be expressed as a set of universal functions of β. At all We_{τ_b}, the magnitude of drag reduction increases monotonically with increasing polymer concentration for $1.0 > \beta > 0.98$, and saturates at $\beta \approx 0.98$. The magnitude of drag reduction at saturation is a strong function of the Weissenberg number. A $We_\tau \sim O(Re_\tau/2)$ is needed to achieve MDR. These results indicate that the Weissenberg number is the most critical parameter in determining the magnitude of drag reduction, with the polymer concentration playing only a secondary role at concentrations below saturation. The results also suggest that in poly-disperse polymer solutions, drag reduction is primarily due to trace amounts of the highest molecular weight polymers which give rise to the highest Weissenberg numbers.

Using the above databases, we have identified the detailed mechanism of drag reduction by dilute polymer solutions in wall-bounded flow. It is found that the main effect of the polymer is extraction of a small amount, of no more than $\sim 5\%$ on a volume averaged basis, of turbulence kinetic energy from turbulent scales which have a timescale shorter than the polymer relaxation time. This extraction of energy leads to a decrease in the fluctuating strain-rate at scales which have redirected a

minimum fraction ($\sim 3\%$) of their turbulence kinetic energy to the elastic energy of the polymer. The reduction of the fluctuating strain-rate at these scales, in turn, reduces the magnitude of the pressure-strain correlation at these and neighboring scales, thus inhibiting the ability of turbulence to transfer energy from the streamwise to the cross-stream directions at these scales. When this drop in the pressure-strain correlation extends to the largest energy-containing turbulent scales, the turbulence kinetic energy which has transferred from the mean flow to turbulence is trapped in the streamwise component and cannot be redistributed to the cross-stream directions. This results in a sharp drop in the wall-normal turbulence intensity and the Reynolds shear stress. This drop in the Reynolds shear stress, in turn, results in a drop in the rate of turbulence production and leads to drag reduction. Furthermore, the energy trapped in the streamwise direction can no longer cascade to the small scales due to the anisotropy of these scales, leading to further decay of the fluctuating strain-rate and turbulence kinetic energy in the small scales. This decay further amplifies the features described above. Thus the miniscule extraction of energy by the polymer at the affected turbulent scales starts a self-amplifying sequence of events, which leads to cessation of turbulence production and results in drag reduction. For effective high drag reduction, the initial minute extraction of energy by the polymer needs to extend to the largest turbulent scales at wall-normal locations where the peak of turbulence production occurs.

The above understanding of mechanism of polymer drag reduction opens up exciting new possibilities for deriving novel turbulence control strategies with high drag reduction.

Bibliography

Baron, A. & Sibilla, S. 1998 DNS of the turbulent channel flow of a dilute polymer solution. *App. Scientific Research* **59**, 331–352.

Benzi, R., L'vov, V. S., Procaccia, I. & Tiberkevich, V. 2004 Saturation of turbulnet drag reduction in dilute polymer solution. *Europhys. Lett.* **68**, 825–831.

Benzi, R., de Angelis, E., L'vov, V. S., Procaccia, I. & Tiberkevich, V. 2006 Maximum drag reduction asymptotes and the cross-over to the Newtonian plug. *J. Fluid Eng.* **551**, 185–195.

Beris, A. N. & Dimitropoulos, C. D. 1999 Pseudospectral simulation of turbulent viscoelastic channel flow. *Comput. Methods Appl. Mech. Engrg.* **180**, 365-392.

Berman, N. S. 1977 Flow time scales and drag reduciton. *Phy. of Fluids* **20**, s168–s174.

Bird, R. B., Dotson, P. J. & Johnson, N. L. 1980 Polymer solution rheology based on a finitely extensible bead spring chain model. *J. Non-Newtonian Fluid Mech.* **7**, 213–235.

Bird, R. B., Curtiss, C. F., Armstrong, R. C. and Hassager, O. 1987

Dynamics of Polymeric Liquids, Vol. 2: Kinetic Theory, 2nd ed. *Wiley*, New York, 1987.

Canuto, C., Hussaini, M. Y., Quarteroni, A. & Zang, T. A. 1988 Spectral Methods in Fluid Dynamics. *Springer-Verlag*, New York, 1988.

Dean, R. B. 1978 Reynolds Number Dependence of Skin Friction and Other Bulk Flow Variables in Two-Dimensional Rectangular Duct Flow. *J. Fluid Eng.* **100**, 215–223.

de Angelis, E., Casciola, C., & Piva, R. 2002 DNS of wall turbulence: dilute polymers and self-sustaining mechanisms. *Comput. Fluids* **31**, 495–507.

de Angelis, E., Casciola, C., L'vov, V. S., Piva, R. & Procaccia, I. 2003 Drag reduction by polymers in turbulent channel flows: Energy redistribution between invariant empirical modes. *Phys. Rev. E* **67**, 056312.

de Angelis, E., Casciola, C., L'vov, V. S., Pomyalov, A., Procaccia, I. & Tiberkevich, V. 2004 Drag reduction by a linear viscosity profile. *Phys. Rev. E* **70**, 055301.

de Angelis, E., Casciola, C. M., Benzi, R. & Piva R. 2005 Homogeneous isotropic turbulece in dilute polymers. *J. Fluid Mech.* **531**, 1–10.

de Gennes, P. G. 1986 Towards a scaling theory of drag reduction. *Physica* **140A**, 9–25.

den Toonder, J. M. J., Hulsen, M. A., Kuiken, G. D. C. & Nieuwstadt,

F. T. M. 1997 Drag reduction by polymer additives in a turbulent pipe flow: numerical and laboratory experiments. *J. Fluid Mech.* **337**, 193–231.

Dimitropoulos, C. D., Sureshkumar, R. & Beris, A. N. 1998 Direct numerical simulation of viscoelastic turbulent channel flow exhibiting drag reduction: effect of the variation of rheological parameters. *J. Non-Newtonian Fluid Mech.* **79**, 433-468.

Dimitropoulos, C. D., Sureshkumar, R., Beris, A. N. & Handler, R. A. 2001 Budgets of Reynolds stress, kinetic energy and streamwise enstrophy in viscoelastic turbulent channel flow. *Phys. Fluids* **13**, 1016–1027.

Dimitropoulos, C. D., Dubief, Y., Shaqfeh, E. S. G., Moin, P. & Lele, S. K. 2005 Direct numerical simulation of polymer-induced drag reduction in turbulent boundary layer flow. *Phy. of Fluids* **17**, 011705.

Dimitropoulos, C. D., Dubief, Y., Shaqfeh, E. S. G. & Moin, P. 2006 Direct numerical simulation of polymer-induced drag reduction in turbulent boundary layer flow of inhomogeneous polymer solutions. *J. Fluid Mech.* **566**, 153–162.

Domaradzki, J. A. 1990 An Analytic Green's functions Method in Pseudo-Spectral Navier-Stokes Solvers for Boundary Layer and Channel Flows. *Journal of Computaional Physics* **88**, 232–242.

Dubief, Y., White, M. C., Terrapon, V. E., Shaqfeh, E. S. G., Moin, P. & Lele, S. K. 2004 On the coherent drag-reducing and turbulenc-enhancing behaviour of polymers in wall flows. *J. Fluid Mech.* **514**, 271–280.

Dubief, Y., Terrapon, V. E., White, M. C., Shaqfeh, E. S. G., Moin, P. & Lele, S. K. 2005 New answers on the interaction between polymers and vortices in turbulent flows. *Flow Turbul. Combust.* **74**, 311–329.

Flory, P.J. 1971 Principles of Polymer Chemistry. *Cornell Universwity Press*, 1971.

Fontaine, A. A., Petrie, H. L. & Brungart, T. A. 1992 Velocity profile statistics in a turbulent boundary layer with slot-inected polymer. *J. Fluid Mech.* **238**, 435-446.

Frederick, P. S. 1975 Structure of turbulent boundary laters at maximum drag reduction. *Nature* **256**, 30-31.

Frohnapfel, B., Lammers, P., Jovanovic, J. & Durst, F. 2007 Interpretation of the mechanism associated with turbulent drag redcutino in terms of anisotropy invariants. *J. Fluid Mech.* **577**, 457–466.

Gampert, B. & Yong, C. K. 1990 The influence of polymer additives on the coherent structure of turbulent channel flow. In *Structure of turbulence and drag reduction.* ed. Gyr, A., *Springer-Verlag*, New York, 223–232.

Gyr, A. & Bewersdorff, H. -W. 1990 Changes of structure close to the wall of a turbulent flow in drag-reducing fluids. In *Structure of turbulence and drag reduction.* ed. Gyr, A., *Springer-Verlag*, New York, 215–222.

Gyr, A. & Bewersdorff, H. -W. 1995 Drag reduction of Turbulent flow by additives. *Kluwer Academic Publ.*, 1995.

Harder, K. J. & Tiederman, W. G. 1991 Drag reduction and turbulent structure in two dimensional channel flows. *Philos. Trans. Roy. Soc.* London A 336 (1991) 19–34.

Hershey, H. C. & Zakin, J. L. 1967 A moelcular approach to predicting the onset of drag reduction in the turbulence flow of dilute polymer solutions. *Chem. Engng Sci.* **22** 1847–1857.

Hou, Y. X, Somandepalli, V. S. R. & Mungal, M. G. 2008 Streamwise development of turbulent boundary-layer drag reduction with polymer injection. *J. Fluid Mech.* **597**, 31–66.

Housiadas, K. D. & Beris, A. N. 2003 Polymer-induced drag reduction: Effects of the variations in elasticity and inertia in turbulent viscoelastic channel flow. *Phys. Fluids* **15**, 2369–2384.

Hoyer, K. & Gyr, A. 1996 Turbulent velocity field in heterogeneously drag reduced pipe flow. *J. Non-Newtonian Fluid Mech.* **65**, 221–240.

Hoyt, J. W. 1966 Friction reduction as an estimator of molecular weight. *Polymer Letters.* **4**, 713–716.

Hoyt, J. W. 1971 Drag reduction effectiveness of polymer solution in the turbulent flow rheometer. *A catalog, Polymer Lett.* **9**, 851–862.

Hoyt, J. W. 1972 The effect of additives on fluid friction. *Trans. ASME J. Basic Engng* **94**, 258–285.

Hoyt, J. W. 1990 Drag reduction by polymers and surfactants. In *Viscous drag reduction boundary layers* **123** ed. Bushnell, D. M. & Hefner, J. N., *Progress in Astronautics and Aeronautics, Inc.*, Washington, D.C., 413–432.

Hunston, D. L. 1974 Drag reduction in polymer mixtures and the effect of molecular weight distribution. *Nature* **251**, 697–698.

Jimenez, J. & Moin, P. 1986 The minimal flow unit in near-wall turbulence. *J. Fluid Mech* **225**, 213–240.

Kenis, P. R. & Hoyt, J. W. 1971 Friction reduction by alga l and bacterial polymers. *Report TP-240, Naval Undersea Research and Development Center, Sna Diego, Ca*

Kim, J., Moin, R. & Moser, R. 1987 Turbulence statistics in fully developed channel flow at low Reynolds number. *J. Fluid Mech.* **177**, 133–166.

Kim, J. 1989 On the structure of pressure fluctuations in simulated turbulent channel flow. *J. Fluid Mech.* **205**, 421–451.

Kim, K., Li, C., Sureshkumar, R., Balachandar, S. & Adrian, R. J. 2007 Effects of polymer stresses on eddy structures in drag-reduced turbulent channel flow. *J. Fluid Mech.* **584**, 281–299.

Kim, K., Adrian, R. J., Balachandar, S. & Sureshkumar, R. 2008 Dynamics of hairpin vortices and polymer-induced turbulent drag reduction. *Phys. Rev. Lett.* **100**, 134504.

Kolmogorov, A. N. 1971 The local structure of turbulence in incompressible viscous fluid for very large Reynolds number. *Dokl. Akad. Nauk. SSSR* **30**, 299-303 (reprinted in *Proc. R. Soc. Lond. A* **434**, 9-13, 1991).

Koskie, J. E. & Tiederman, W. G. 1991 Polymer drag reduction af a zero-pressure-gradient boundary layer. *Phys. Fluids* A **3(10)**, 2471–2473.

Larson, R.G. 1999 The structure and rheology of complex fluids. *Oxford University Press*, 1999.

Li, Wei & Graham, M. D. 2007 Polymer induced drag reduction in exact coherent structures of plane Poiseuille flow. *Phys. Fluid* **19**, 83101.

Li, C.-F., Sureshkumar, R. & Khomami, B. 2006 Influence of rheological parameters on polymer induced turbulent drag reduction. *J. Non-Newtonian Fluid Mech.* **140**, 23–40.

Lumley, J. L. 1969 Drag reduction by additives. *Annu. Rev. Fluid Mech.* **1**, 367–384.

Lumley, J. L. 1973 Drag reduction in turbulent flow by polymer additives. *J. Polymer Sci.* **7**, 263–290.

Lumley, J. L. & Newman, G. 1977 The return to isotropy of homogeneous turbulence. *J. Fluid Mech.* **82**, 161–178.

Luchik, T. S. & Tiederman, W. G. 1988 Turbulent structure in low-concentration drag-reducing channel flows. *J. Fluid Mech.* **190**, 241–263.

L'vov, V. S., Pomyalov, A., Procaccia, I. & Tiberkevich, V. 2004 Drag reduction by polymers in wall bounded turbulence. *Phys. Rev. Lett.* **70**, 026304.

Mangiavacchi, N. & Akhavan, R. 1993 Direct numerical simulation of turbulent shear flows on distributed memeory parallel architectures. *Proc. Sixth SIAM Conf. on Parallel Processong for Scientific Computing* **1**, 61–64.

McComb, W. D. & Rabie, L. H. 1979 Development of local turbulent drag reduction due to nonuniform polymer concentration. *Phys. Fluids* **22**, 183–185.

McComb, W. D. & Rabie, L. H. 1982 Local drag reduction due to injection of polymer solutions into turbulent flow in a pipe. *AIChE J.* **28**, 547–565.

Min, T., Yoo, J. Y., Choi, H. & Joseph, D. D. 2003 Drag reduction by polymer additives in a turbulent channel flow. *J. Fluid Mech.* **486**, 213–238.

Min, T., Yoo, J. Y. & Choi, H. 2003 Maximum drag reduction in a turbulent channel flow by polymer additives. *J. Fluid Mech.* **492**, 91–100.

Moser, R. D., Kim, J., & Mansour, N. N. 2007 Direct numerical simulation of turbulent channel flow up to $Re_\tau = 590$. *Phys. Fluid* **11**, 943.

Nadolink, R. H. 1987 Friction reduction in dilute polystyrene solutions. PhD thesis, Univsersity of California at San Deigo, La Jolla, CA.

Nieuwstadt, F. T. M. & den Toonder, J. M. J. 2001 Drag reduction by additives: a review. In *Turbulence Structure and Motion,* ed. Soldati, A. & Monti, R., *Springer-Verlag*, New York, 269–316.

Oldaker, D. K. & Tiederman, W. G. 1977 (Spatial structure of the viscous sublayer in drag-reducing channel flow.) *Phys. Fluid* **20**, S133.

Orlandi, P. 1995 A tentative approach to direct numerical simulation of drag reduction by polymers. *J. Non-Newtonian Fluid Mech.* **60**, 277–301.

Orszag, S. A. 1971 Accurate solution of the Orr-Sommerfeld stability equation. *J. Fluid Mech.* **50**, 689–703.

Pao, Y. H. 1965 Structure of turbulent velocity and scalar fields at large wavenumbers. *Phys. Fluids* **8**, 1063–1075.

Patterson, R. W. & Abernathy, F. H. 1970 Turbulent flow drag reduction and degradation with dilute polymer solutions. *J. Fluid Mech.* **43**, 689–710.

Pierce, C. D. & Moin, P. 2004 Progress-variable approach for large-eddy simulation of non-premixed turbulent combustion. *J. Fluid Mech.* **504**, 73–97.

Pincus, P. 1976 Excluded volume effects and stretched polymer chains. *Macromolecules* **9**, 386–388.

Pinho, F. T. & Whitelaw, J. H. 1990 Flow of non-newtonian fluid in a pipe. *J. Non-Newtonian Fluid Mech.* **34**, 129–144.

Ptasinski, P. K., Nieuwstadt, F. T. M., Van Den Brule, B. H. A. A.& Hulsen, M. A. 2001 Experiments in Turbulent Pipe Flow with Polymer Additives at Maximum Drag Reduction. *Flow, Turbulence and Combustion* **66**, 159–182.

Ptasinski, P. K., Boersma, B. J., Nieuwstadt, F. T. M., Hulsen, M. A., Van Den Brule, B. H. A. A. & Hunt, J. C. R. 2003 Turbulent channel flow near maximum drag reduction: simulations, experiments and mechanisms. *J. Fluid Mech.* **490**, 251–291.

Robinson, S. K. 1991 Coherent motions in theturbulent boundary layer. *Annu. Rev. Fluid Mech.* **23**, 601–639.

Sreenivasan, K. R. & White, C. M. 2000 The onset of drag reduction by dilute polymer additives, and the maximum drag reduction asymptote. *J. Fluid Mech.* **409**, 149–164.

Stone, P. A., Roy, A., Larson, R.G., Waleffe, F. & Graham, M.D 2004 Polymer drag reduction in exact coherent structures of plane shear flow. *Phys. Fluid* **16**, 3470–3482.

Sureshkumar, R. & Beris, A. N. 1995 Effect of artificial stress diffusivity on the stability of numerical calcualtions and the flow dynamics of time-dependent viscoelastic flow. *J. Non-Newtonian Fluid Mech.* **60**, 53–80.

Sureshkumar, R., Beris, A. N. & Handler, R. A. 1997 Direct numerical simulation of the turbulent channel flow of a polymer solution. *Phys. Fluids* **9**, 743–755.

Tamanoa, S., Itoh, M., Hoshizaki, K. & Yokota, K. 2007 Direct numerical simulation of the drag-reducing turbulent boundary layer of viscoelastic fluid. *Phys. Fluids* **19**, 075106.

Tiederman, W. G., Luchik, T. S. & Bogard, D. G. 1985 Wall-layer structure and drag reduction. *J. Fluid Mech.*, **156**, 419–437.

Tiederman, W. G. 1990 The effect of dilute polymer solutions on viscous drag and turbulence structure. In *Structure of Turbulence and Drag Reduction,* ed. Gyr., A., *Springer*, New York, 187–200.

Toms, B. Q. 1949 Some observations on the flow of linear ploymer solutions through straight tubes at large Reynolds numbers. *In Proc. 1st Int. Congress on Rheology* , **2**, North-Holland, Amsterdam 1949, 135–141.

Usui, H., Maeguchi, K. & Sano, Y. 1988 Drag reductin caused by the injection of polymer thread into a turbulent pipe flow. *Phys. Fluids* **31**, 2518–2523.

Vaithianathan, T., Robert, A., Brasseur, J. G. & Collins, L. R. 2007 Polymer mixing in shear-driven turbulence. *J. Fluid Mech.* **585**, 487–497.

Virk, P. S., Mickley, H. S. & Smith, K. A. 1970 The ultimate asymptote and mean flow structure in Tom's Phenomenon. *Trans. ASME* **37**, 488–493.

Virk, P. S. 1975 Drag reduction fundamentals. *AlChE Journal* **21**, 625–656.

Walker, D. T. & Tiederman, W. G. 1990 Turbulent structure in a channel flow with polymer injection at the wall. *J. Fluid Mech.* **218**, 377–403.

Wapperom, P., Keunings, R. & Legat, V. 2000 The backward-tracking Lagrangian particle method for transient viscoelastic flows. *J. Non-Newtonian Fluid Mech.* **91**, 273–295.

Warholic, M. D., Massah, H. & Hanratty, T. J. 1999 Influence of drag-reduction polymers on turbulence: effects of Reynolds number, concentration and mixing. *Exps Fluids.* **27**, 461–472.

Wei T. & Willmarth, W. W. 1992 Modifying turbulent structure with drag-reducing polymer additives in turbulent channel flows. *J. Fluid Mech.* **245**, 619–641.

Wells, C. S., Jr. & Spangler, J. G. 1967 Injection of a drag-reducing fluid into turbulent pipe flow of a Newtonian fluid. *Phys. Fluid* **10**, 1890–1894.

White, C. M., Somandepalli, V. S. R. & Mungal, M. G. 2004 The turbulence structure of drag-reduced boundary layer flow. *Exps Fluids.* **36**, 62–69.

White, C. M. & Mungal, M. G. 2008 Mechanics and prediction of turbulent drag reduction with polymer additives. *Ann. Rev. Fluid Mech.* **40**, 235–256.

Willmarth, W. W., Wei, T. & Lee, C. 1987 Laser anemometer measurments of Reynolds stress in a turbulent channel flow with drag reducing polymer additives. *Phys. Fluid* **30**, 933–935.